

REPORT DOCUMENTATION PAGE			Form Approved OMB NO. 0704-0188		
<p>The public reporting burden for this collection of information is estimated to average 1 hour per response, including the time for reviewing instructions, searching existing data sources, gathering and maintaining the data needed, and completing and reviewing the collection of information. Send comments regarding this burden estimate or any other aspect of this collection of information, including suggestions for reducing this burden, to Washington Headquarters Services, Directorate for Information Operations and Reports, 1215 Jefferson Davis Highway, Suite 1204, Arlington VA, 22202-4302. Respondents should be aware that notwithstanding any other provision of law, no person shall be subject to any penalty for failing to comply with a collection of information if it does not display a currently valid OMB control number.</p> <p>PLEASE DO NOT RETURN YOUR FORM TO THE ABOVE ADDRESS.</p>					
1. REPORT DATE (DD-MM-YYYY) 24-01-2015		2. REPORT TYPE Final Report		3. DATES COVERED (From - To) 1-Sep-2010 - 31-Aug-2014	
4. TITLE AND SUBTITLE Final Report: Use of Spherical Nanoindentation to Characterize the Anisotropic Properties of Microscale Constituents and Interfaces in Hierarchically Structured Composite Materials			5a. CONTRACT NUMBER W911NF-10-1-0409		
			5b. GRANT NUMBER		
			5c. PROGRAM ELEMENT NUMBER 611102		
6. AUTHORS Surya R. Kalidindi, Ulrike G.K. Wegst			5d. PROJECT NUMBER		
			5e. TASK NUMBER		
			5f. WORK UNIT NUMBER		
7. PERFORMING ORGANIZATION NAMES AND ADDRESSES Drexel University 3201 Arch Street Suite 100 Philadelphia, PA 19104 -2875			8. PERFORMING ORGANIZATION REPORT NUMBER		
9. SPONSORING/MONITORING AGENCY NAME(S) AND ADDRESS (ES) U.S. Army Research Office P.O. Box 12211 Research Triangle Park, NC 27709-2211			10. SPONSOR/MONITOR'S ACRONYM(S) ARO		
			11. SPONSOR/MONITOR'S REPORT NUMBER(S) 56046-MS.8		
12. DISTRIBUTION AVAILABILITY STATEMENT Approved for Public Release; Distribution Unlimited					
13. SUPPLEMENTARY NOTES The views, opinions and/or findings contained in this report are those of the author(s) and should not be construed as an official Department of the Army position, policy or decision, unless so designated by other documentation.					
14. ABSTRACT A major impediment to the development of physics-based multi-scale homogenization (composite) theories is the lack of appropriate methods to characterize the local anisotropic elastic-plastic properties of microscale constituents and interfaces at various hierarchical length scales in composite material systems. This work aims to address this gap by combining the information obtained from spherical nanoindentation with different indenter sizes, structure characterization methods (e.g., Orientation Image Mapping in Scanning Electron Microscopy, X-ray micro-tomography), and sophisticated finite element models to arrive at reliable estimates of the					
15. SUBJECT TERMS spherical nanoindentation stress-strain curves, freeze cast Ti foams, polymer-ceramic composites, viscoelastic indentation analysis, strain hardening near grain boundaries					
16. SECURITY CLASSIFICATION OF:			17. LIMITATION OF ABSTRACT UU	15. NUMBER OF PAGES	19a. NAME OF RESPONSIBLE PERSON Surya Kalidindi
a. REPORT UU	b. ABSTRACT UU	c. THIS PAGE UU			19b. TELEPHONE NUMBER 215-895-1311

Report Title

Final Report: Use of Spherical Nanoindentation to Characterize the Anisotropic Properties of Microscale Constituents and Interfaces in Hierarchically Structured Composite Materials

ABSTRACT

A major impediment to the development of physics-based multi-scale homogenization (composite) theories is the lack of appropriate methods to characterize the local anisotropic elastic-plastic properties of microscale constituents and interfaces at various hierarchical length scales in composite material systems. This work aims to address this gap by combining the information obtained from spherical nanoindentation with different indenter sizes, structure characterization methods (e.g., Orientation Image Mapping in Scanning Electron Microscope, X-ray micro-tomography), and sophisticated finite element models to arrive at reliable estimates of the elusive local properties. The methods developed have been critically validated in a series of material systems with increasingly complex internal structures, starting with single-phase cubic and hexagonal metals and progressing to multi-phase metals, freeze-cast polymer-ceramic composite systems with novel but highly complex hierarchical internal structures, and various biomaterials. Using these novel approaches, we were able to quantify reliably for the first time the local mechanical properties exhibited by various microscale constituents and interfaces.

Enter List of papers submitted or published that acknowledge ARO support from the start of the project to the date of this printing. List the papers, including journal references, in the following categories:

(a) Papers published in peer-reviewed journals (N/A for none)

<u>Received</u>	<u>Paper</u>
01/14/2015	5.00 Dipen K. Patel, Hamad F. Al-Harbi, Surya R. Kalidindi. Extracting single-crystal elastic constants from polycrystalline samples using spherical nanoindentation and orientation measurements, <i>Acta Materialia</i> , (10 2014): 108. doi: 10.1016/j.actamat.2014.07.021
01/14/2015	7.00 Siddhartha Pathak, Jessica L. Riesterer, Surya R. Kalidindi, Johann Michler. Understanding pop-ins in spherical nanoindentation, <i>Applied Physics Letters</i> , (10 2014): 161913. doi: 10.1063/1.4898698
01/14/2015	6.00 Surya R. Kalidindi, Shraddha J. Vachhani. Mechanical characterization of grain boundaries using nanoindentation, <i>Current Opinion in Solid State and Materials Science</i> , (08 2014): 196. doi: 10.1016/j.cossms.2014.05.002
08/15/2012	2.00 Siddhartha Pathak, Shraddha J. Vachhani, Karl J. Jepsen, Haviva M. Goldman, Surya R. Kalidindi. Assessment of lamellar level properties in mouse bone utilizing a novel spherical nanoindentation data analysis method, <i>Journal of the Mechanical Behavior of Biomedical Materials</i> , (09 2012): 102. doi: 10.1016/j.jmbbm.2012.03.018
08/15/2012	3.00 Brendan R. Donohue, Adrian Ambrus, Surya R. Kalidindi. Critical evaluation of the indentation data analyses methods for the extraction of isotropic uniaxial mechanical properties using finite element models, <i>Acta Materialia</i> , (05 2012): 3943. doi: 10.1016/j.actamat.2012.03.034
08/23/2013	4.00 S.J. Vachhani, R.D. Doherty, S.R. Kalidindi. Effect of the continuous stiffness measurement on the mechanical properties extracted using spherical nanoindentation, <i>Acta Materialia</i> , (06 2013): 3744. doi: 10.1016/j.actamat.2013.03.005
08/28/2011	1.00 Siddhartha Pathak, Johann Michler, Kilian Wasmer, Surya R. Kalidindi. Studying grain boundary regions in polycrystalline materials using spherical nano-indentation and orientation imaging microscopy, <i>Journal of Materials Science</i> , (8 2011): 0. doi: 10.1007/s10853-011-5859-z
TOTAL:	7

Number of Papers published in peer-reviewed journals:

(b) Papers published in non-peer-reviewed journals (N/A for none)

Received Paper

TOTAL:

Number of Papers published in non peer-reviewed journals:

(c) Presentations

Invited Talk, Establishing correlations between local mechanical properties and local structure in hierarchical materials using spherical nanoindentation, MRS Meeting, Boston, December 2013.

Invited Talk, New Data Analyses Protocols for Extracting Spherical Indentation Stress-Strain Curves, MS&T, Montreal, October 2013.

Number of Presentations: 2.00

Non Peer-Reviewed Conference Proceeding publications (other than abstracts):

Received Paper

TOTAL:

Number of Non Peer-Reviewed Conference Proceeding publications (other than abstracts):

Peer-Reviewed Conference Proceeding publications (other than abstracts):

Received Paper

TOTAL:

Number of Peer-Reviewed Conference Proceeding publications (other than abstracts):

(d) Manuscripts

Received Paper

TOTAL:

Number of Manuscripts:

Books

Received Book

TOTAL:

Received Book Chapter

TOTAL:

Patents Submitted

Patents Awarded

Awards

1. Fellow of TMS, 2015.
2. Invited as TMS MGI Ambassador, (Inaugural Class) 2014.
3. Alexander von Humboldt Award, 2013.
4. Finalist for the Journal of Materials Science Robert W. Cahn Best Paper Prize, 2012.
5. Research featured on the cover of Issue 5 of Modelling and Simulation in Materials Science and Engineering, 2012.
6. Elected Fellow of ASM International, 2011.
7. Elected Fellow of American Society of Mechanical Engineers, 2011.

Graduate Students

<u>NAME</u>	<u>PERCENT SUPPORTED</u>	Discipline
Jordan Weaver	0.75	
Mohammed Abba	0.75	
Dipen Patel	0.50	
FTE Equivalent:	2.00	
Total Number:	3	

Names of Post Doctorates

<u>NAME</u>	<u>PERCENT SUPPORTED</u>
FTE Equivalent:	
Total Number:	

Names of Faculty Supported

<u>NAME</u>	<u>PERCENT SUPPORTED</u>	National Academy Member
Surya R. Kalidindi	0.08	
FTE Equivalent:	0.08	
Total Number:	1	

Names of Under Graduate students supported

<u>NAME</u>	<u>PERCENT SUPPORTED</u>
FTE Equivalent:	
Total Number:	

Student Metrics

This section only applies to graduating undergraduates supported by this agreement in this reporting period

The number of undergraduates funded by this agreement who graduated during this period: 0.00

The number of undergraduates funded by this agreement who graduated during this period with a degree in science, mathematics, engineering, or technology fields:..... 0.00

The number of undergraduates funded by your agreement who graduated during this period and will continue to pursue a graduate or Ph.D. degree in science, mathematics, engineering, or technology fields:..... 0.00

Number of graduating undergraduates who achieved a 3.5 GPA to 4.0 (4.0 max scale):..... 0.00

Number of graduating undergraduates funded by a DoD funded Center of Excellence grant for Education, Research and Engineering:..... 0.00

The number of undergraduates funded by your agreement who graduated during this period and intend to work for the Department of Defense 0.00

The number of undergraduates funded by your agreement who graduated during this period and will receive scholarships or fellowships for further studies in science, mathematics, engineering or technology fields:..... 0.00

Names of Personnel receiving masters degrees

NAME

Total Number:

Names of personnel receiving PHDs

NAME

Shraddha Vachhani

Total Number:

1

Names of other research staff

NAME

PERCENT SUPPORTED

FTE Equivalent:

Total Number:

Sub Contractors (DD882)

1 a. Georgia Institute of Technology

1 b. 225 NORTH AVENUE

ATLANTA GA 303320357

Sub Contractor Numbers (c): 202282

Patent Clause Number (d-1): 10

Patent Date (d-2): 1/1/13 12:00AM

Work Description (e): The PI moved from Drexel University to Georgia Tech. So a subaward was made so the F

Sub Contract Award Date (f-1): 1/1/13 12:00AM

Sub Contract Est Completion Date(f-2): 8/31/14 12:00AM

1 a. Georgia Institute of Technology

1 b. 225 NORTH AVENUE

ATLANTA GA 303320357

Sub Contractor Numbers (c): 202282

Patent Clause Number (d-1): 10

Patent Date (d-2): 1/1/13 12:00AM

Work Description (e): The PI moved from Drexel University to Georgia Tech. So a subaward was made so the F

Sub Contract Award Date (f-1): 1/1/13 12:00AM

Sub Contract Est Completion Date(f-2): 8/31/14 12:00AM

Inventions (DD882)

Scientific Progress

Statement of the Problem

Reliable and validated protocols are currently lacking for characterization of the local anisotropic elastic-plastic properties of microscale constituents and interfaces at various hierarchical length scales in composite material systems. This information is critically needed for advancing multiscale materials models and inverse solutions to materials and process design problems. This work aims to address this critical gap by combining the information obtained from spherical nanoindentation (with different indenter sizes), structure characterization methods (e.g., Orientation Image Mapping in Scanning Electron Microscope, X-ray micro-tomography), and sophisticated finite element models to arrive at reliable estimates of the elusive local properties.

Summary of Significant Results (August 1, 2011 to July, 31 2014)

We have investigated three different classes of material systems in this project: (i) Metals/alloys, (ii) polymers/polymer composites, and (iii) biomaterials. Significant results in each class of materials systems are described next.

Metals/Alloys

We have developed and validated new protocols to characterize the mechanical response of regions within individual grains (both in the grain interior as well as near the grain boundary) in annealed and deformed polycrystalline metal samples using a combination of spherical nanoindentation and orientation imaging microscopy. Significant results from these studies include:

1.1 We have demonstrated the application of our novel spherical nanoindentation-OIM (orientation image mapping) data analysis protocols to study the mechanical response of grain boundary regions in as-cast and 30% deformed polycrystalline Fe-3%Si steel. In particular, we demonstrated that it is possible to investigate the role of grain boundaries in the mechanical deformation of polycrystalline samples by systematically studying the changes in the indentation stress-strain curves as a function of the distance from the grain boundary. These results have already been published [1], and this paper has been uploaded with this report.

1.2 We have critically validated the novel data analyses protocols for spherical indentation developed in this work using finite element models. Currently, two different definitions of indentation strain and two different definitions of contact radius are being used in literature, leading to inconsistent estimates of mechanical properties (especially plastic properties). In particular, we are able to establish important connections between the indentation stress-strain curves and the conventional uniaxial stress-strain curves. The journal paper from this work is already published [2], and has been uploaded with this report.

1.3 The effects of the superimposed oscillating load while using the continuous stiffness measurement (CSM) technique on the extracted indentation stress-strain curves were systematically investigated using spherical nanoindentation tests performed on a variety of samples using probes of 1 and 100 μm radii. The CSM signal with a 45Hz oscillation frequency and 2nm amplitude appears to produce the most reasonable values of stiffness and is therefore the best choice for reliably extracting indentation stress-strain curves for the materials studied. The journal paper from this work is already published [3], and has been uploaded with this report.

1.4 Our interest in estimating grain scale properties of materials using spherical nanoindentation has led us to develop inverse protocols for predicting single crystal elastic constants, C_{11} , C_{12} , and C_{44} for a selected material phase in a polycrystalline material. We have accomplished this inversion using novel spectral approaches (built on results developed in a prior ARO funded project on the development of a microstructure sensitive design (MSD) framework). The developed protocol to estimate the single crystal elastic constants involves a two-step process. The first task of this approach involves capturing the functional dependence of the indentation modulus, E_{ind} on the lattice orientation (g) using selected results from finite element simulations. The unknown single crystal elastic constants in a given sample are then established via a regression technique that minimizes the difference between the measured indentation modulus, $E_{\text{ind}}^m(g)$ on differently oriented grains in a polycrystalline sample and the function established in the first step. These novel methods were demonstrated on indentation measurements obtained from a cubic polycrystalline, as-cast, Fe-3%Si sample. The journal paper from this work is already published [4], and has been uploaded with this report.

1.5 A review article was written to summarize the tremendous potential of the nanoindentation protocols developed in this work in serving as a high-throughput technique for robust and quantitative assessment of the mechanical role of various mesoscale interfaces. This review is already published, and has been uploaded with this report [5].

1.6 Pop-ins, or sudden displacement-bursts at constant load in a nanoindentation test, are typically attributed to the difficulty of setting up potent dislocation sources in the very small indentation zones in these experiments. In order to understand the physical processes underlying pop-ins, we utilize a combination of interrupted spherical indentation tests along with depth profiling of the residual indentation surfaces using in-situ atomic force microscopy (AFM). A plausible sequence of physical processes (related to metal plasticity) occurring underneath the indenter during and immediately after the occurrence of the pop-in is proposed to explain these observations. The journal paper from this work is already published [6], and has been

uploaded with this report.

1.7 We employed the novel protocols developed in this work for studies on the evolution of local properties within individual grains as a consequence of macroscopically imposed plastic deformation on a polycrystalline sample. These measurements, made possible for the first time because of the novel protocols developed in this work, showed a significant variation in the strain hardening rates in the individual grains of the polycrystalline sample. A positive correlation was observed between the percentage increase in the local slip resistance and the value of the Taylor factor computed for the local crystal orientation at the indentation site subjected to the macroscale imposed deformation. A journal paper describing these results has been submitted for publication, and is enclosed here as Appendix A.

1.8 The studied described above was extended to a focused study on grain boundary regions in deformed polycrystalline samples of Al. In this study, we demonstrated that grains with a lower Taylor factor (soft grains), when present next to a grain with a high Taylor factor (Taylor hard grain) show a hardened layer in the vicinity on the grain boundary; whereas, the Taylor hard grain shows no change in the yield behavior as compared to the grain interior. Near a boundary where the grains on either side have very similar Taylor factors, there is again no change in the local yield behavior as compared to the grain interior. It should be noted that insights such as these are extremely hard to obtain with any other characterization tool, and to the best of our knowledge such datasets have never been successfully obtained and reported in prior literature. A journal paper describing these results is currently being prepared for publication, and is enclosed here as Appendix B.

1.9 We have written a comprehensive review paper outlining all of the main advances made in the extraction of indentation stress-strain curves from spherical nanoindentation. This review is currently under review, and is enclosed here as Appendix C.

1.10 Spherical Nanoindentation was applied to characterize the microscale properties of commercial and high purity titanium. This is the first extension of the spherical nanoindentation stress-strain technique to a hexagonal crystal system. We have demonstrated that the indentation stress-strain curve captures the increase in yield strength between high and commercial purity titanium due to the increase in oxygen content (see Appendix D).

1.11 Process-structure-property relationships were explored for directionally aligned porous titanium alloy (Ti-6Al-4V) using freeze-casting. This technique is largely untapped for metal structures which have potential lightweight, energy absorbing applications primarily because the structure-property tunability and hierarchy demonstrated in polymer and ceramic systems has proven challenging for larger, denser particles. We overcame this challenge by adjusting the particle volume fraction, freezing rate, solution viscosity, and adding ethanol to produce samples with 65-34 % porosity, 7-29 GPa compressive stiffness, and 83-412 MPa yield strength. We have also more than doubled the specific crushing energy absorption measured up to 50% strain previously published in literature for similar porous titanium structures. These successes should provide a path forward to produce freeze-cast metals for different functional and structural applications. The full results of this study are in preparation for publication and can be found in Appendix E. In an effort to further increase the toughness (crushing energy) of the freeze-cast titanium, a multistep polymer infiltration process was successfully performed (see Year 3 Progress Report, Appendix C). This novel Ti-6Al-4V – Polymethyl methacrylate (PMMA) had an average density, strength, and stiffness of 2.28 g cm⁻³, 193 MPa, and 4.86 GPa respectively. The specific crushing energy was increased by nearly a factor of two from 17.3 J g⁻¹ to 33.2 J g⁻¹. We have proven that a lightweight titanium alloy-PMMA composite can be constructed from freeze casting and infiltration which shows good crushing energy absorption and potentially excellent crushing energy absorption through the hierarchical materials design obtainable in the freeze-casting and infiltration process.

Polymers/Polymers Composites

2.1 Hybrid thin films with a nacre-like microstructure were fabricated in a straightforward and reproducible manner through manual shear casting using the biopolymer chitosan as the matrix material and alumina platelets as the reinforcing particles. The ratio of inorganic to organic content was varied from 0% to 15% and the relative humidities from 36% to 75% to determine their effects on the mechanical properties. It was found that increasing the volume fraction of alumina from 0% to 15% results in a twofold increase in the modulus of the film but decreases the tensile strength by up to 30% when the volume fraction of alumina is higher than 5%. Additionally, this study quantifies and illustrates the critical role of the relative humidity on the mechanical properties of the hybrid film. Increasing the relative humidity from 36% to 75% decreases the modulus and strength by about 45% and triples the strain at failure. This study has been completed, and the manuscript to be submitted for publication can be found in Appendix F.

2.2 To be able to reliably use spherical nanoindentation on polymer composites or hybrids that contain soft constituents, we have to first develop analysis techniques that will work for materials that exhibit viscoelasticity. Current methods that are used for viscoelastic materials are usually applied after the material has experienced some significant deformation. This does not give an accurate representation of the material properties of the undeformed sample. This study develops analysis protocols to extract stress-strain curves and viscoelastic properties from the load-displacement data generated from nanoindentation materials exhibiting time-dependent response. Once these protocols are developed they can then be applied, in the future, to study viscoelastic and viscoplastic properties of the constituents of composite material systems. We plan to demonstrate the

validity of these new protocols through selected case studies on a range of materials including polymers, polymer blends, and a biopolymer used in novel hybrid thin films with highly aligned microstructures that our group has recently fabricated to mimic natural materials. A brief summary of our completed work and future plans are included in Appendix G.

Biomaterials

3.1 We have demonstrated the applicability of our recently developed data analysis procedures for spherical nanoindentation in conjunction with Raman spectroscopy for studying the lamellar level correlations between the local mechanical properties and local composition in mouse bone. [7]. In particular, two different inbred strains of mouse, A/J and C57BL/6J (B6) were studied to successfully demonstrate the correlations between the local mineral-to-matrix ratio and the local indentation modulus and yield properties at the indentation site. These results have already been published [7], and the journal paper has been uploaded with this report.

3.2 Continued work involving a larger sample size has concluded that there is also a significant difference between the two mouse strains. Our results demonstrate that the overall bone composition (mineral to matrix ratio), the mineral maturity and substitutions in the lattice of apatite, are significantly different between the two mice strains. The differences are not very significant in the new bone; whereas, in old, mature bone, except for the mineral maturity, the bone composition is significantly different between the two strains. Our investigations also found strong correlations between the local mechanical properties (elastic modulus and indentation yield strength) and the mineral to matrix ratios. These results are being prepared for a journal paper, and are enclosed here in Appendix H.

References (current journal publications from this project)

1. Pathak, S., et al., Studying grain boundary regions in polycrystalline materials using spherical nano-indentation and orientation imaging microscopy. *Journal of Materials Science*, 2012. 47(2): p. 815-823.
2. Donohue, B.R., A. Ambrus, and S.R. Kalidindi, Critical evaluation of the indentation data analyses methods for the extraction of isotropic uniaxial mechanical properties using finite element models. *Acta Materialia*, 2012. 60(9): p. 3943-3952.
3. Vachhani, S.J., R.D. Doherty, and S.R. Kalidindi, Effect of the continuous stiffness measurement on the mechanical properties extracted using spherical nanoindentation. *Acta Materialia*, 2013. 61(10): p. 3744-3751.
4. Patel, D.K., H.F. Al-Harbi, and S.R. Kalidindi, Extracting single-crystal elastic constants from polycrystalline samples using spherical nanoindentation and orientation measurements. *Acta Materialia*, 2014. 79: p. 108-116.
5. Kalidindi, S.R. and S.J. Vachhani, Mechanical characterization of grain boundaries using nanoindentation. *Current Opinion in Solid State and Materials Science*, 2014.
6. Pathak, S., et al., Understanding pop-ins in spherical nanoindentation. *Applied Physics Letters*, 2014. 105(16): p. -.
7. Pathak, S., et al., Assessment of lamellar level properties in mouse bone utilizing a novel spherical nanoindentation data analysis method. *Journal of the Mechanical Behavior of Biomedical Materials*, 2012. 13: p. 102-117.

Technology Transfer

The spherical nanoindentation protocols developed in this project have now been adopted by Dr. Nathan Mara's group at Los Alamos National Laboratory on a range of projects, including studies on irradiated materials.

Table of Contents

Appendix A: Grain-Scale Measurement of Slip Resistances in Aluminum Polycrystals using Spherical Nanoindentation

Appendix B: Studies of Grain Boundary Regions in Deformed Polycrystalline Aluminum Using Spherical Nanoindentation

Appendix C: Spherical Nanoindentation Stress-Strain Curves

Appendix D: Nanoindentation Stress-Strain Curves for Titanium

Appendix E: Structure-Processing Correlations and Mechanical Properties in Freeze-Cast Ti-6Al-4V with Highly Aligned Porosity

Appendix F: Nacre-Like Hybrid Films: Structure, Properties, and the Effect of Relative Humidity

Appendix G: Spherical Nanoindentation Protocols for Extracting Micro-scale Mechanical Properties in Viscoelastic Materials

Appendix H: Lamellar level correlations between mechanical behavior and composition in mouse bone

Appendix A: Grain-Scale Measurement of Slip Resistances in Aluminum Polycrystals using Spherical Nanoindentation

Shraddha J. Vachhani^{1,2} and Surya R. Kalidindi^{1*}

¹Woodruff School of Mechanical Engineering, Georgia Institute of Technology, Atlanta, GA 30332, USA

²Currently at Materials Science and Technology Division, Los Alamos National Laboratories, Los Alamos, NM 87545, USA

*corresponding author

Abstract

In this work, we develop and demonstrate novel protocols based on spherical nanoindentation and orientation image mapping (OIM) for quantifying the local increases in slip resistances in the individual grains of a deformed (or strain hardened) polycrystalline sample. These new protocols utilize the recently developed data analyses methods for extracting indentation stress-strain (ISS) curves in conjunction with the measurements of the local crystal orientations at the indentation sites using the OIM technique. The proposed protocols involve two main steps. In the first step, spherical nanoindentation measurements are conducted on fully annealed samples of the material of interest to map out the functional dependence of the indentation yield strength (Y_{ind}) on the crystal lattice orientation in the annealed condition. In the second step, spherical nanoindentation and OIM measurements are conducted on the deformed samples of the same material and are analyzed rigorously to reliably estimate the increase in the local slip resistance at the indentation sites. The function established in the first step is utilized in the second step to properly account for the influence of the local crystal orientation on the measured Y_{ind} in the deformed sample. This novel measurement and data analysis protocol is demonstrated in this paper on polycrystalline samples of high purity aluminum. From this study, it was noted that the influence of the crystal lattice orientation on the measured Y_{ind} in Al crystals can be as high as 40%, with the lowest values corresponding to the [100] (cube) orientation and highest values corresponding to the [111] orientation. The measurements on the deformed samples showed a significant variation in the strain hardening rates in the individual grains of the polycrystalline sample. A positive correlation was observed between the percentage increase in the local slip resistance and the value of the Taylor factor computed for the local crystal orientation at the indentation site subjected to the macroscale imposed deformation.

Keywords: Spherical Nanoindentation, Orientation Imaging, Indentation Yield, Taylor Factor, Indentation Stress-Strain Curves

Introduction

Over the last decade, nanoindentation [1-4] has emerged as a tool of choice for investigating mechanical behavior of hierarchical materials, since the interrogation volume under the indenter can be varied systematically by roughly three orders of magnitude in length scales in the range of 50 nms to 50 μ ms. While the indentation experiments are easy to perform and require minimal sample preparation (compared to other small scale mechanical testing options such as micro-pillar testing [5-7]), the data analysis and interpretation is quite complicated, mainly due to the complex continuously evolving stress state under the indenter tip. Traditionally, indentation experiments have been carried out with sharp tips [8-10], and the values of local elastic modulus and hardness were extracted mainly from an analysis of the unloading portion of the test segment [11-13]. However, recent advances in instrumentation (e.g., the availability of the continuous stiffness measurement (CSM) [14]) have now made it possible to convert the measured load-displacement data from spherical nanoindentation into highly reproducible and consistent indentation stress-strain (ISS) curves [15]. Examining the indentation data in the form of ISS curves provides better insights into the local mechanical response in the sample (although it still needs to be interpreted as an average over the indentation zone experiencing highly heterogeneous stress/strain fields). More specifically, it was demonstrated that these new protocols produce meaningful information such as the local indentation modulus and the local indentation yield strength (Y_{ind}). In recent work, the use of ISS curves for nanoindentation data analysis has demonstrated tremendous promise in providing new insights into material behavior, including the role of grain boundaries during macroscale deformation in metals [16], buckling behavior of carbon nanotube forests [17], and lamellar level properties in bone [18].

In this work, we build on prior work from our research group that focused on the characterization of the changes in the local slip resistance in deformed polycrystalline samples of cubic metals [19]. The main concept underlying these new protocols was already introduced in our earlier paper, and involved the utilization and combined analysis of measured data from both spherical nanoindentation and orientation imaging microscopy (OIM) [20, 21]. This particular analysis protocol was prompted by the recognition that the measured Y_{ind} in deformed samples is influenced by both the local crystal lattice orientation and the local dislocation density in a multiplicative manner (details presented later). In order to isolate the contribution from the local dislocation density, it becomes essential to establish a protocol that correctly accounts for the effect of the crystal lattice orientation at the indentation site. Consequently, in our prior work, we establish a new protocol that approached the task in two distinct steps. In the first step, the focus was placed on the annealed samples of the material system of interest (even though our interest is really in the deformed samples), where there is negligible dislocation density in the samples. In this way, one can map out the functional dependence of the Y_{ind} on the local crystal orientation in the indentation zone. Subsequently, in the second step of the protocols, the focus is shifted to the deformed samples of actual interest. However, the information gathered from the first step (on the annealed samples) is critically important in relating the measured Y_{ind} to the local percentage

increase in the slip resistance at the indentation site. It should be noted that this protocol provides a single value for the effective (or the averaged) slip resistance at the indentation site and is therefore most easily interpreted for cubic metals, where it is reasonable to assume that the slip resistance of the different slip systems at the material point of interest are roughly equal to each other. Extension of this protocol to hexagonal metals (with a multitude of slip and twin systems with large variations in their corresponding slip and twin resistances even at a single material point) needs a more detailed analysis.

Our prior work [19] explored these new concepts on polycrystalline Fe-Si samples that exhibit a body-centered cubic (bcc) structure. Although the earlier work established a strong foundation, much additional development is needed to improve the fidelity and robustness of these novel protocols. In this study, we have undertaken a much more extensive effort with the following salient distinctions from the earlier work: (i) The present study was performed on polycrystalline samples of high purity Aluminum (Al), which exhibits a face-centered cubic (fcc) structure. The main reasons for the selection of Aluminum was the relatively simple set of well-defined slips systems (the bcc metals exhibit pencil glide where multiple planes possessing the (111) directions could serve as potential slip systems) and very low elastic anisotropy. Both of these factors are expected to simplify significantly the subsequent analyses of the data presented here. (ii) The samples selected for the present study have been much more systematically processed, corresponding to 0, 10, and 20 percent reductions in plane strain compression. In the earlier work, the samples corresponded to 0, 30, and 80 percent reductions, which made it very difficult to correlate the increases in slip resistances to the amount of cold work imposed on the sample. (iii) The number of measurements performed within a single orientation as well as the number of orientations tested in both annealed and deformed conditions are both substantially larger in this study. Consequently, the present study allowed for a much more meaningful statistical investigation of the correlations sought in the study. (iv) A number of the steps involved in the protocols have been refined to increase the reliability and robustness of the method. For example, it was discovered that the use of a 100 μ m radius indenter tip in the measurements on the annealed sample helped minimize the uncertainty introduced into the analyses as a consequence of the unavoidable pop-ins in these tests. In a similar vein, the protocols for extracting the Y_{ind} and for capturing mathematically the functional dependence of the Y_{ind} on the crystal lattice orientation were both substantially refined in the present study.

The overall study presented here is aimed at gaining quantitative insights into the strain hardening rates in the individual grains of a polycrystalline sample. These measurements are critical for maturing physics-based crystal plasticity models [22-25]. Towards this goal, we present our measurements from the study and our analyses of these results. The measurements are provided as tables in this paper to allow other researchers to conduct their own analyses of the main experimental results obtained here using different assumptions, approximations, and crystal plasticity models.

Indentation Stress-Strain (ISS) Curves

The procedures used in this study to convert the raw load-displacement data in spherical nanoindentation into ISS curves have been detailed in prior publications [15, 26], and are briefly reviewed here. The procedure, based on Hertz theory [27, 28], involves the accurate determination of the effective zero point and the computation of the indentation stress and strain values. The effective point of initial contact (may or may not correspond to the actual point of contact) [15] is identified such that the initial elastic loading data segment immediately following this point provides the best agreement with the Hertz theory for all three measured signals: the load (\tilde{P}), the displacement (\tilde{h}), and the contact stiffness (S). For spherical nanoindentation, this search for the effective initial point can be accomplished using the following relationship based on Hertz theory:

$$S = \frac{3P}{2h_e} = \frac{3(\tilde{P} - P^*)}{(\tilde{h} - h^*)} \quad (1)$$

where P^* and h^* denote the load and displacement values respectively at the point of initial contact. Linear regression can be used to determine the effective point of initial contact or the so-called effective zero-point (i.e., the values of P^* and h^*).

The radius of contact (a) can be estimated as

$$a = \frac{S}{2E_{eff}}, \quad \frac{1}{E_{eff}} = \frac{1 - \nu_s^2}{E_s} + \frac{1 - \nu_i^2}{E_i} \quad (2)$$

where S is the harmonic contact stiffness. E_{eff} is the effective stiffness of the sample-indenter system, E and ν are the Young's modulus and Poisson's ratio, and the subscripts i and s denote the indenter and sample, respectively. The term $\frac{E_s}{1 - \nu_s^2}$ is generally referred to as the sample

indentation modulus, denoted by E_{ind} . The value of E_{ind} is estimated from an analyses of the initial loading segment (identified in the zero-point analyses described above) using the Hertz theory. The values of the indentation stress (σ_{ind}) and the indentation strain (ϵ_{ind}) for the initial elastic loading segment are then computed as

$$\sigma_{ind} = \frac{P}{\pi a^2}, \quad \epsilon_{ind} = \frac{4}{3\pi} \frac{h_e}{a} \approx \frac{h_e}{2.4a}, \quad \sigma_{ind} = E_{ind} \epsilon_{ind}, \quad (3)$$

where h_e is the elastic indentation depth at load P . The use of Eq. (3) produces a linear relationship between the indentation stress and indentation strain values for the initial elastic loading regime. Beyond this initial elastic regime, the definition of indentation stress is kept the

same, but the definition of the indentation strain is extended by replacing the elastic indentation depth (h_e) by the total indentation depth (h_t) in Eq. (3).

Note that the protocols described above rely on the CSM to obtain a continuous estimate of the radius of contact, a , at every point on the load-displacement curve. Studies have shown that the use of CSM is most reliable within certain windows of frequency and amplitude for the superimposed oscillations [29, 30]. It has been shown [30] that the most reliable (ISS) curves for aluminum can be obtained using the CSM at 45 Hz oscillation frequency and a 2 nm oscillation amplitude. These test conditions were utilized in all of the measurements reported in this paper.

Materials and Methods

Polycrystalline samples of high purity aluminum (99.999%) were used in this study. Since our interest here is mainly on the hardening rates within grains (not on the grain boundary regions) we produced fully annealed, large grained, samples of aluminum for this study. This was accomplished by sectioning out samples from a heavily rolled block of high purity aluminum and annealing them for 72 hours at 640°C. These large-grained samples make it easier to validate the novel protocols being developed in this effort by allowing several measurements within selected grains (of specific orientations) without being influenced by the grain boundaries. As mentioned earlier, the annealed samples are critical for establishing the functional dependence of the Y_{ind} on the crystal lattice orientation. Some of the annealed samples were subsequently deformed in plane strain compression to two reduction levels of 10% and 20%. These reduction levels correspond to true strains of -0.11, and -0.22, respectively. The deformed samples were studied using the protocols described in this paper to quantify the increases in slip resistances in the grains of different lattice orientations.

As mentioned earlier, one of the reasons for choosing pure aluminum was that it exhibits very little elastic anisotropy ($A = 1.22$) [31]. This is desirable, since the data analysis protocols for nanoindentation are based on Hertz theory, which is based on a frictionless contact between two elastically isotropic surfaces. A modified form of Hertz theory [32] does exist to account for elastic anisotropy in cubic crystals. This theory predicts the sample indentation modulus for Al grains of different orientations to be in the range of 68.8 - 70.6 GPa. Therefore, there should be very little effect of the crystal orientation on the sample indentation modulus in the present study. Additionally, the oxide film on aluminum is exceedingly thin, making its contribution to the indentation response negligible. Absence of solute also eliminates complications due to segregation and precipitation during plastic deformation.

For both the indentation and OIM measurements, the samples were mounted in epoxy and prepared by mechanical grinding using Si-C papers followed by polishing using the 9 μm , 3 μm and 1 μm diamond suspensions on a Buehler grinding and polishing machine. Mechanical polishing was followed by electropolishing using a mixture of perchloric acid (10%) and methanol for 45 seconds at -20°C and 12V [33]. It is emphasized that a high quality surface

finish is extremely critical for the indentation measurements [34], especially since we intend to extract mechanical properties from the very small initial elastic loading segments.

Grain orientation maps for the samples were obtained using orientation imaging microscopy (OIM), which is based on the automatic indexing of electron back-scattered diffraction (EBSD) patterns. Orientation at each measurement voxel was denoted using the Bunge-Euler angles [35], as an ordered set of three angles (ϕ_1 , Φ , ϕ_2), which describe the rotations for the transformation from the sample reference frame to the crystal reference frame. The grains tested on the sample surfaces were numbered for convenience and will be referred to using their assigned grain numbers. The grain maps were used to identify regions of interest to perform the indentation testing. After the indentation tests were performed, the regions of interest were imaged again in the SEM using OIM, to confirm the location of the indents and determine the local crystal orientation at the indentation site.

Nanoindentation tests were then carried out at selected locations in the annealed and deformed samples using the MTS nanoindenter XP® equipped with the CSM attachment. Care was taken to ensure that the indents were placed well away from the grain boundaries. Twenty seven grains of different orientations, spread out over the inverse pole figure (IPF) triangle were identified on the surfaces of the fully annealed samples for the indentation measurements. Between 9 and 18 indentation tests were performed on each of the selected grains using the protocols outlined in the previous section, and the (ISS) curves were plotted for each test. In the case of the deformed samples, at least 15 indents were performed in each grain due to the increased heterogeneity in the microstructure of deformed samples and the higher expected scatter within each grain.

As reported in prior studies [34] indentation measurements performed on annealed metal samples using a small radius indenter tip almost always produce pop-ins. In fact, this observation was utilized in this study to ensure that the surface preparation during the polishing steps left an undisturbed surface on the sample (i.e., the surface is still representative of the original sample and has not been tainted by the polishing steps). In other words, the efficacy of the surface preparation protocols on the annealed samples used in this study was verified by ensuring that large pop-ins were produced when indents were carried out with the 1 μm indenter tip (see Figure 1). These pop-ins are attributed to the difficulty of establishing a potent dislocation source (e.g., a Frank-Reed source) in the very small indentation zone sizes ($\ll 1 \mu\text{m}$) associated with these measurements.

The main challenge with using the smaller indenter tips (desired because they can lead to higher spatial resolution of the indentation measurements) is that the pop-ins manifest themselves as strain bursts near theoretical strengths in the ISS curves followed by an unloading part before the indentation stresses approach values that represent indentation flow stresses in the absence of the pop-in [34]. Thus, the occurrence of pop-ins masks the yield behavior and the extraction of Y_{ind} becomes somewhat unreliable. The effect of indenter tip size on the occurrence and size of the pop-ins is shown in Figure 1. Since the indentation zone is much larger for a larger indenter tip, the probability of establishing the necessary dislocation sources to accommodate the imposed

deformation is significantly higher, and hence the probability of the occurrence of the pop-in is greatly reduced. Because of these advantages, it was decided to conduct the measurements in this study using the 100 μm radius indenter tip.

Since the occurrence of pop-ins is a stochastic process, even with the 100 μm radius indenter tip and small pop-ins were occasionally observed in the measurements on the annealed samples, as shown in Figure 2. Therefore, Y_{ind} was extracted by back-extrapolating from the post-elastic segment shown between the two vertical dashed lines in Figure 2. In this study, Y_{ind} was determined as the point of intersection between the modulus line (i.e., the elastic portion of the initial loading segment) and the best-fit line for the stress-strain curve within the strain range of 0.0065 and 0.013. This protocol was standardized for all the tests reported in this paper. Macroscale deformation increases the dislocation density, and hence, in the deformed samples, the pop-ins are almost completely absent. In order to maintain consistency, the same back-extrapolation method was still used to extract the indentation yield point in the deformed samples as well.

Results and Discussion

The OIM scans of one of the four samples tested in the fully annealed condition is shown in Figure 3(a). All of the grain orientations tested in the three annealed samples (only one is shown in Figure 3(a)) are plotted in the standard [001] IPF (inverse pole figure) map shown in Figure 3(d). In other words, the color in the OIM scan is mapped to the crystal direction in the grain that is perpendicular to the sample surface (i.e., parallel to the indentation direction). Note that since the indenter tip is axisymmetric, in-plane rotations of the sample (and the corresponding rotations of the crystal orientations with respect to a fixed reference frame) will not alter the nanoindentation response. Consequently, the nanoindentation response is only a function of two of the three Bunge Euler angles used to represent the grain orientation, denoted as (Φ, ϕ_2) .

Representative load-displacement and corresponding ISS curves for two selected grain orientations are plotted in Figure 4. Grain #1 is close to the [001] corner of the IPF triangle, meaning that the [001] crystal direction for this grain is close to the indentation direction. On the other hand, Grain #27 is close to the [111] corner and therefore has the [111] crystal direction almost parallel to the indentation direction. As expected, these two orientations show a very large difference in their nanoindentation response. Multiple (9-18) indentation measurements were performed on each grain to quantify the experimental scatter in the extracted Y_{ind} values. A total of twenty seven grain orientations were tested in the annealed samples using the 100 μm spherical tip. These grains were selected so that their orientations covered the fundamental stereographic triangle in a uniform manner (see Figure 3(d)). The results from all of these tests are summarized in Table 1. It was observed that the nanoindentation responses within each grain exhibited relatively low deviations in the extracted values of both E_{ind} and the Y_{ind} (see Table 1).

As noted earlier, the measured values of E_{ind} do not exhibit any significant dependence on the grain orientation. However, the measured values of Y_{ind} exhibit a strong dependence on the grain lattice

orientation. In fact, Y_{ind} can vary by as much as 40% depending on the orientation of the grain. Figure 5 is a contour plot showing the dependence of the Y_{ind} on the local crystal lattice orientation at the indentation site in the standard IPF plot. This plot was generated by interpolating between the measured Y_{ind} values for the 27 grains provided in Table 1 (see also Figure 3(d)). This interpolation was accomplished using generalized spherical harmonics (GSH) [35][ref]. This contour plot indicates that the lowest value of Y_{ind} would be for a cube-oriented grain (~ 40 MPa), while the highest value of Y_{ind} would correspond to a [111] oriented grain (~ 65 MPa). Since the dislocation density in an annealed material is expected to be very low and independent of the crystal lattice orientation, all of this variation in the Y_{ind} with respect to the crystal orientation is fully attributable to the differences in the orientations of the active slip systems with respect to the indentation direction. Since all fcc crystals exhibit the same set of slip systems in plastic deformation at low temperatures (where plastic response is close to a rate-independent response), we should expect the contour plots of Y_{ind} in the orientation space should look alike for all fcc crystals, except for a constant scaling factor. This hypothesis, however, needs to be verified experimentally.

A similar indentation yield map has been previously reported [19] for annealed grains of Fe-3 wt% Si (a bcc metal). Interestingly, the range in the values of Y_{ind} is significantly higher in the fcc metal reported here. This can be explained as a natural consequence of the availability of a much larger number of potential slip systems in the bcc crystals, which reduces the plastic anisotropy at the single crystal level. It is also noted that the softest orientations and the hardest orientations for indentation are the same (i.e., [001] and [111] orientations, respectively) in both fcc and bcc metals. The main difference in the Y_{ind} plots measured in the bcc and fcc crystals appears to be in the relative (i.e., percentage) difference in the Y_{ind} values for the [111] and [101] orientations. This difference appears to be more significant in the fcc crystals compared to the bcc crystals. However, it is very important to recognize that only a limited number of measurements have been reported to date in both systems, and additional measurements are critically needed to verify and confirm these fairly limited observations.

The yield contour presented in Figure 5 has tremendous value in studies on deformed polycrystalline samples. Using this interpolation plot, Y_{ind} for any given orientation of pure aluminum in the fully annealed condition can now be estimated. As noted earlier, measurements of Y_{ind} within the grains in deformed polycrystalline samples are likely to be influenced by both the local orientation at the indentation site and the local accumulated dislocation density. It can be argued that the percentage increase in the Y_{ind} from a reference annealed state for any selected lattice orientation should directly reflect the percentage increase in the local slip resistance (also referred as critical resolved shear strength or CRSS). In this type of analysis, it is implicitly assumed that the slip resistance is the same on all slip systems in the indentation zone. This is a reasonable assumption for cubic polycrystalline metals. We shall now focus on characterizing the local mechanical behavior in the deformed samples using this approach, with the goal of obtaining insights into strain hardening rates in the grains of different orientations in the plastically deformed samples of Al.

As described earlier, two high purity aluminum samples were subjected to light deformation (10% reduction in height) and another was subjected to moderate deformation (20% reduction in height); both these reductions were applied in a channel-die to attain plane strain conditions at the sample scale. Representative OIM maps of the sample deformed to 10% reduction in height and 20% reduction in height are shown in Figures 3(b) and 3(c), respectively. The orientations of all grains studied at these reduction levels are shown in Figures 3(e) and 3(f), respectively. It is immediately apparent from the OIM maps that there is a much larger spread in the orientations within the grains in the deformed samples. Furthermore, the orientation spread is significantly higher for the sample with higher amount of deformation (20% reduction in height) as compared to the lightly deformed sample (10% reduction in height). However, no significant grain fragmentation was observed in either of these samples. All of these observations are consistent with observations reported in earlier studies [36, 37]. Indeed, the heterogeneity of both structure and local properties is a characteristic feature of deformed polycrystalline metal samples, and is responsible for important phenomena such as recrystallization [38, 39]. One can qualitatively explain this evolving heterogeneity (both between the grains and within the grains) as a natural consequence of the need to accommodate the overall imposed plastic deformation in ways that satisfy the governing field equations (i.e., equilibrium equations) while utilizing only the available slip systems in each grain (in fcc metals there are only twelve $(111)[\bar{1}\bar{1}0]$ potential slip systems in each grain). However, to develop a more quantitative understanding of the physics controlling the evolution of the microstructure in deformed polycrystalline metals, it would be necessary to develop and employ the novel characterization techniques described in this paper. One of the significant gaps in our current understanding of the grain-scale plasticity comes from a lack of reliable quantitative information on how the individual crystals harden in the process of accommodating the macroscale imposed plastic deformation. In other words, as noted earlier, we expect different grains to undergo different amounts of plastic deformation locally in response to the macroscale imposed plastic deformation (in this study, this was selected as 10% and 20% reduction levels in plane strain compression). Consequently, they should harden by different amounts in the process of accommodating the imposed plastic deformation. The novel techniques described in this paper are specifically aimed at measuring the increases in local yield strength in individual grains in a deformed sample and correlating these increases to the crystal orientation.

Spherical nanoindentation tests were performed on selected regions within the individual grains (well away from visible grain boundaries) using the same protocols that were used on the annealed samples. In this case, the pop-ins were almost always completely absent. The results obtained from the deformed samples are summarized in Tables 2 and 3 for the two different reduction levels. It was once again observed that multiple indentations performed on same grains produced fairly consistent measurements. As noted earlier, at the low reduction levels studied here, the grains have not yet fragmented in any significant manner (see Figures 3(b) and 3(c)). Consequently, the variance in the measurements within a single grain is still relatively low in the measurements reported in this study.

As a specific example of the effect of plastic deformation on Y_{ind} , we show in Figure 6 ISS curves for two grains of almost the same orientation, where one was tested in the fully annealed condition and the other in the 10% deformed sample. As seen here, the increment in the Y_{ind} due to the imposed deformation is quite significant. For each of the grains tested in the deformed condition, the Y_{ind} in the fully annealed condition was estimated using the indentation yield map presented in Figure 5, and the values are presented in Tables 2 and 3. This is the Y_{ind} value that would have been measured for the orientations studied in the deformed sample, if they were tested in the fully annealed condition. It is important to reliably establish this value since the Y_{ind} in the annealed condition can vary by as much as 40%, depending on the local crystal lattice orientation at the indentation site. A reliable estimate of the increment in Y_{ind} (i.e., ΔY_{ind}) for any given orientation can then be determined as the difference between the measured indentation yield point in the deformed condition ($Y_{ind}(g,d)$) and the estimated indentation yield point in the fully annealed condition, $Y_{ind}(g,0)$, as

$$\Delta Y_{ind}(g,d) = Y_{ind}(g,d) - Y_{ind}(g,0) \quad (4)$$

where d refers to the amount of deformation (i.e., 10% or 20% reduction in height by plane strain compression) and g refers to the local crystal lattice orientation at the indentation site.

The simplest relationship that one can try to establish between Y_{ind} and the local dislocation content (ρ) is through the critical resolved shear strength (τ_{crss}) of the slip system. In a highly simplified manner, this relationship can be expressed as

$$Y_{ind}(g,d) = M(g) \tau_{crss}(d) \quad (5)$$

$$\Delta \tau_{crss}(d) = \tau_{crss}(d) - \tau_{crss}(0) \propto \sqrt{\rho} \quad (6)$$

where M is a Taylor factor for indentation that depends only on the grain orientation with respect to the indentation direction (in this case, only two of the three Bunge-Euler angles describing local crystal orientation), τ_{crss} is the critical resolved shear strength in the crystal, $\Delta \tau_{crss}$ is the increment in the local averaged critical resolved shear strength between the annealed and deformed conditions, and ρ is the local dislocation density. The Taylor factor M is defined as

$$M = \frac{\sum \Delta \gamma}{\Delta \epsilon} \quad (7)$$

where $\Delta \gamma$ is the sum of the slip shears on all the slip systems, and $\Delta \epsilon$ is the imposed macroscopic plastic strain increment. In other words, a grain with a higher value of M is expected to require a higher amount of total slip on its available slip systems to accommodate the imposed macroscopic plastic deformation. Grains with higher values of M are generally referred as hard (oriented) grains, and those with lower values of M are generally referred as soft grains.

Based on the highly simplified crystal plasticity theory presented above for indentation, grains with higher values of M (i.e., hard grains) are expected to produce more amounts of total slip and

therefore harden more than the grains with lower values of M . This is the fundamental hypothesis we aim to critically evaluate in this study using the novel protocols described here.

A convenient measure for comparing the relative hardening rates in the differently oriented grains in a given deformed sample is to express the increase in the slip resistance as a percentage of the initial critical resolved shear stress in the material in the annealed condition. Combining Eqs. (4)-(6), the percentage increase in the critical resolved shear stress is expressed as

$$\% \tau_{crss} = \frac{\Delta \tau_{crss}(d)}{\tau_{crss}(0)} * 100 = \frac{\Delta Y_{ind}(g, d)}{Y_{ind}(g, 0)} * 100 \quad (8)$$

As noted earlier, $\% \tau_{crss}$ provides an indirect measure of the local dislocation content or local hardening in the deformed samples (cf. Eq. (6)).

From Tables 2 and 3 it is clear that $\% \tau_{crss}$ (reflecting the local hardening rates) does vary significantly with the grain orientation. Also reported in the Tables 2 and 3 are values of the Taylor factor for plane strain compression for each of the orientation of interest. The definition of the Taylor factor provided in Eq. (7) is general and can be applied to any imposed deformation mode. The values presented in Tables 2 and 3 are for plane strain compression, and are not to be confused with the Taylor factors for the indentation mode of deformation used in Eq. (5). Taylor factors shown in Tables 2 and 3 indicate how the specific orientations will accommodate an imposed plane strain compression (there is an implicit assumption here that the grain will experience locally the same deformation as the macroscale imposed deformation; this assumption is usually referred to as the Taylor assumption [40]). As noted earlier, our main hypotheses from the simple model presented earlier is that the grains with higher Taylor factors for plane strain compression are expected to require a larger amount of total slip, and consequently harden more than the grains with lower Taylor factors.

Figures 7(a) and 7(b) show the variation of $\% \tau_{crss}$ (estimated from the nanoindentation measurements conducted in this study) with the Taylor factors for all grain orientations studied at both reduction levels (i.e., 10% and 20% reduction by plane strain compression), respectively. It is seen that there is a strong positive correlations between the local strain hardening levels in the individual grains and the Taylor factors computed for their lattice orientations. In fact, in both sets of measurements shown in Figures 7(a) and 7(b), there is a strong suggestion for a linear relationship between $\% \tau_{crss}$ and M .

The positive correlations between $\% \tau_{crss}$ and M is a very important finding and supports the main hypothesis laid out earlier. The data presented here confirms that orientations with a lower Taylor factor (soft grains) harden at a lower rate compared to grains with a higher Taylor factor (hard grains). This dependence has been discussed in various books and has been probed previously within a limited scope [41, 42]. To the best of our knowledge, the dataset presented in

this paper represents the most comprehensive set of measurements conducted to date in support of this expected correlation.

Interestingly enough, and as noted earlier, Figures 7(a) and 7(b) actually suggest a linear relationship between $\% \tau_{crss}$ and M . The observed linear dependence can be reconciled using a highly simplified model for the hardening rate in each grain. If we assume that the initial hardening rate in the differently oriented crystals in their annealed condition is constant (denoted by h) and relatively independent of the grain orientation, we can express the increase in slip resistance as

$$\Delta \tau_{crss} = h \sum \Delta \gamma \quad (9)$$

Combining Eq. (9) with Eq. (7) we can show that

$$\% \tau_{crss} = M \left(\frac{h^* \Delta \varepsilon}{\tau_{crss}(0)} \right) \quad (10)$$

Eq. (10) is consistent with the linear correlations observed in Figures 7(a) and 7(b).

The simple model presented above, however, assumes that the initial hardening rate (i.e., the stage II hardening rate) in the individual crystals is constant for all grain orientations. It is indeed remarkable that very simple models discussed above correctly predict the main trends in the measurements obtained in this study. It is also anticipated that the measurement dataset produced in this study would be of high value to experts engaged in the development of refined crystal plasticity theories and simulation tools. We have therefore presented all of the relevant details of the measurements in this paper (see Tables 1-3), so that the broader scientific community can re-analyze this dataset using their own favorite models, and draw their own conclusions and correlations.

From Tables 1-3, it is also seen that the scatter in the measured Y_{ind} values for individual grains is higher for the deformed samples as compared to the scatter observed for the annealed samples. This is expected because, for the deformed samples, in addition to the experimental scatter in the Y_{ind} values, there is also a real variation in the dislocation density from one location to another within individual grains which contributes to the scatter.

Conclusions

A new set of protocols have been developed to reliably measure the local percentage increases in slip resistance (from their values in the annealed condition) in individual grains of a deformed cubic polycrystal sample. In the present study, the protocols were specifically demonstrated for Al polycrystals. However, we believe that the same set of protocols can be applied to a range of cubic metals deforming by crystallographic slip. The overall approach combines the use of spherical nanoindentation stress-strain curves with electron-backscattered diffraction for orientation imaging. The proposed protocol is essentially a two-step process. In the first step, the dependence of the indentation yield strength (Y_{ind}) on the crystal lattice orientation is mapped out

in the fully annealed condition. In the second step, this function is utilized to carefully isolate the contribution from the increase in the critical resolved shear strength (due to increased dislocation density) to the Y_{ind} measured in deformed samples. The protocols developed here were applied to deformed samples of polycrystalline Al and the results showed a remarkable agreement with a highly simplified theory. These new protocols have the potential to open several new lines of investigations in fundamental studies of deformation and recrystallization in polycrystalline metals.

Acknowledgements

Authors wish to thank Prof. R. D. Doherty for the many insightful discussions during the course of this work. Authors acknowledge funding from ARO grant W911NF-10-1-0409 (David Stepp, Program Manager). The MTS nanoindenter XP® and the TSL-OIM system (integrated with the ESEM Philips XL-30) used in this study is maintained and operated by the Centralized Research Facilities in the College of Engineering at Drexel University. SJV is currently at Los Alamos National Laboratory, operated by LANS for the NNSA of the US Department of Energy under Contract No. DE-AC52-06NA25396.

References

1. Hay, J.L. and G.M. Pharr, *Instrumented indentation testing*. ASM Handbook.
2. Hay, J.C., A. Bolshakov, and G.M. Pharr, *A critical examination of the fundamental relations used in the analysis of nanoindentation data*. Journal of Materials Research, 1999. **14**(6): p. 2296-2305.
3. Fischer-Cripps, A.C., *Nanoindentation*. Mechanical Engineering Series, ed. F.F. Ling. 2002, New York: Springer.
4. Fischer-Cripps, A.C., *A review of analysis methods for sub-micron indentation testing*. Vacuum, 2000. **58**(4): p. 569-585.
5. Uchic, M.D., et al., *Sample dimensions influence strength and crystal plasticity*. Science, 2004. **305**(5686): p. 986-989.
6. Shan, Z.W., et al., *Mechanical annealing and source-limited deformation in submicrometre-diameter Ni crystals*. Nat Mater, 2008. **7**(2): p. 115-119.
7. Kunz, A., S. Pathak, and J.R. Greer, *Size effects in Al nanopillars: Single crystalline vs. bicrystalline*. Acta Materialia, 2011. **59**(11): p. 4416-4424.
8. Bucaille, J.L., et al., *Determination of plastic properties of metals by instrumented indentation using different sharp indenters*. Acta Materialia, 2003. **51**(6): p. 1663-1678.
9. Rho, J.-Y., T.Y. Tsui, and G.M. Pharr, *Elastic properties of human cortical and trabecular lamellar bone measured by nanoindentation*. Biomaterials, 1997. **18**(20): p. 1325-1330.
10. Poole, W.J., M.F. Ashby, and N.A. Fleck, *Micro-hardness of annealed and work-hardened copper polycrystals*. Scripta Materialia, 1996. **34**(4): p. 559-564.
11. Oliver, W.C. and G.M. Pharr, *Improved technique for determining hardness and elastic modulus using load and displacement sensing indentation experiments*. Journal of Materials Research, 1992. **7**(6): p. 1564-1580.
12. Oliver, W.C. and G.M. Pharr, *Measurement of hardness and elastic modulus by instrumented indentation: Advances in understanding and refinements to methodology*. Journal of Materials Research, 2004. **19**: p. 3-20.
13. Fischer-Cripps, A.C., *Study of analysis methods of depth-sensing indentation test data for spherical indenters*. Journal of Materials Research, 2001. **16**: p. 1579-1584.

14. Li, X. and B. Bhushan, *A review of nanoindentation continuous stiffness measurement technique and its applications*. Materials Characterization, 2002. **48**(1): p. 11-36.
15. Kalidindi, S.R. and S. Pathak, *Determination of the effective zero-point and the extraction of spherical nanoindentation stress-strain curves*. Acta Materialia, 2008. **56**: p. 3523-32.
16. Pathak, S., et al., *Studying grain boundary regions in polycrystalline materials using spherical nano-indentation and orientation imaging microscopy*. Journal of Materials Science, 2012. **47**(2): p. 815-823.
17. Pathak, S., et al., *Viscoelasticity and high buckling stress of dense carbon nanotube brushes*. Carbon, 2009. **47**: p. 1969-1976.
18. Pathak, S., et al., *Assessment of lamellar level properties in mouse bone utilizing a novel spherical nanoindentation data analysis method*. Journal of the Mechanical Behavior of Biomedical Materials, 2012. **13**(0): p. 102-117.
19. Pathak, S., D. Stojakovic, and S.R. Kalidindi, *Measurement of the local mechanical properties in polycrystalline samples using spherical nanoindentation and orientation imaging microscopy*. Acta Materialia, 2009. **57**: p. 3020-3028.
20. Adams, B.L. *Measurement and representation of polycrystalline microstructure*. in Winter Annual Meeting of the American Society of Mechanical Engineers, Nov 8-13 1992. 1992. Anaheim, CA, USA: Publ by ASME, New York, NY, USA.
21. Adams, B.L., *Orientation imaging microscopy: Emerging and future applications*. Ultramicroscopy Proceedings of the 1996 6th Conference on Frontiers in Electron Microscopy in Materials Science, Jun 4-7 1996, 1997. **67**(1-4): p. 11-17.
22. Asaro, R.J., *Crystal Plasticity*. Journal of Applied Mechanics, 1983. **50**(4b): p. 921-934.
23. Bronkhorst, C.A., S.R. Kalidindi, and L. Anand, *Polycrystalline plasticity and the evolution of crystallographic texture in FCC metals*. Philosophical Transactions of the Royal Society of London Series A-Mathematical Physical and Engineering Sciences, 1992. **341**(1662): p. 443-477.
24. Kalidindi, S.R., *Incorporation of deformation twinning in crystal plasticity models*. Journal of the Mechanics and Physics of Solids, 1998. **46**(2): p. 267-271.
25. Van Houtte, P., L. Delannay, and S.R. Kalidindi, *Comparison of two grain interaction models for polycrystal plasticity and deformation texture prediction*. International Journal of Plasticity, 2002. **18**(3): p. 359-377.
26. Pathak, S., J. Shaffer, and S.R. Kalidindi, *Determination of an effective zero-point and extraction of indentation stress-strain curves without the continuous stiffness measurement signal*. Scripta Materialia, 2009. **60**: p. 439-442.
27. Hertz, H., *Miscellaneous Papers*. New York: MacMillan and Co., Ltd, 1896.
28. Johnson, K.L., *Indentation Contact Mechanics*. 1985: Cambridge University Press, Cambridge.
29. G.M. Pharr, J.H.S.a.W.C.O., *Critical issues in making small-depth mechanical property measurements by nanoindentation with continuous stiffness measurement*. Journal of Materials Research, 2009. **24**: p. 653-666.
30. Vachhani, S.J., R.D. Doherty, and S.R. Kalidindi, *Effect of the continuous stiffness measurement on the mechanical properties extracted using spherical nanoindentation*. Acta Materialia, 2013. **61**(10): p. 3744-3751.
31. Gene Simmons, H.W., *Single Crystal Elastic Constants and Calculated Aggregate Properties*. 1971, Cambridge MIT Press.
32. Vlassak, J.J. and W.D. Nix, *Measuring the elastic properties of anisotropic materials by means of indentation experiments*. Journal of the Mechanics and Physics of Solids, 1994. **42**(8): p. 1223-1245.
33. *Metallography and Microstructures*, in ASM handbooks Online, G.F.V. Voort, Editor. 2004.
34. Pathak, S., et al., *Importance of surface preparation on the nano-indentation stress-strain curves measured in metals*. Journal of Materials Research, 2009. **24**: p. 1142-1155.
35. Bunge, H., *Texture Analysis in Materials Science*. Butterworths, 1982.
36. Kalidindi, S.R., A. Bhattacharya, and R. Doherty, *Detailed Analysis of Plastic Deformation in Columnar Polycrystalline Aluminum Using Orientation Image Mapping and Crystal Plasticity Models*.

- Proceedings of the Royal Society of London: Mathematical, Physical and Engineering Sciences., 2004. **460**(2047): p. 1935 - 1956
37. Bhattacharyya, A., et al., *Evolution of grain-scale microstructure during large strain simple compression of polycrystalline aluminum with quasi-columnar grains: OIM measurements and numerical simulations*. International Journal of Plasticity, 2001. **17**(6): p. 861-883.
 38. Humphreys, F.J. and M. Hatherly, *Recrystallization and Related Annealing Phenomena*. 2nd ed. 2004, Amsterdam: Elsevier.
 39. Doherty, R.D., et al., *Current issues in recrystallization: a review*. Materials Science & Engineering A, 1997. **238**: p. 214-274.
 40. Taylor, G.I., *Plastic strain in metals*. Journal of the Institute of Metals, 1938. **62**: p. 307-324.
 41. Dillamore, I.L., Morris P. L., Smith C. J. E. , Hutchinson W. B., *Transition Bands and Recrystallization in Metals*. Proceedings of the Royal Society A, 1972. **329**: p. 405-420.
 42. Stojakovic, D., *Microstructure Evolution in Deformed and Recrystallized Electrical Steel*, in *Materials Science and Engineering*. 2008, Drexel University: Philadelphia. p. 101.

Figures

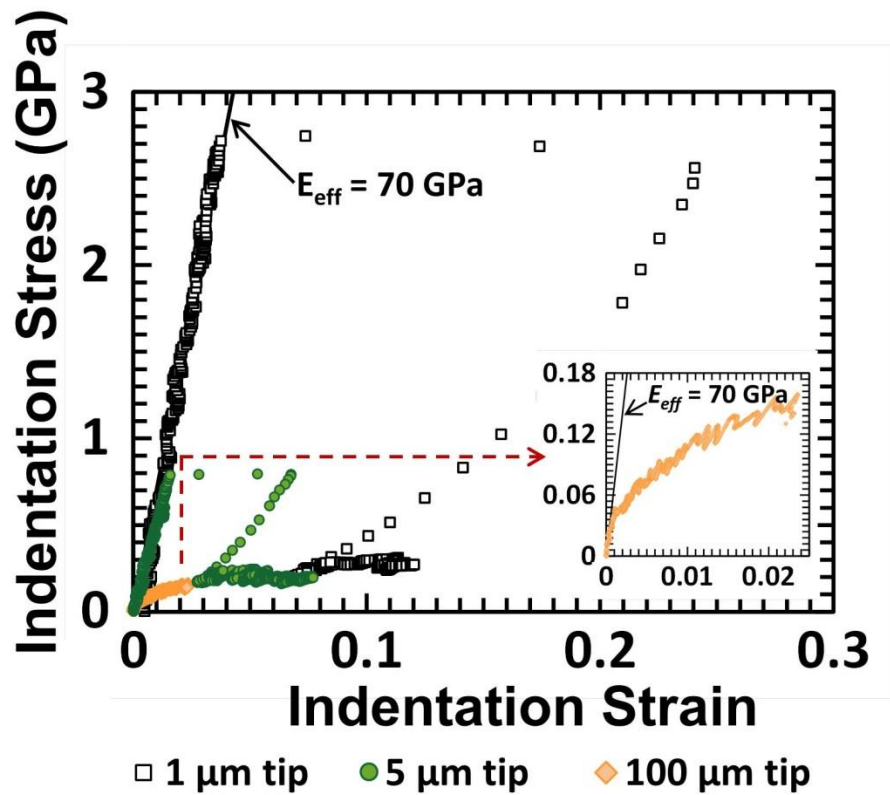


Figure 1. Representative ISS curves for tests performed within the same grain in the fully annealed aluminum sample using the 1, 5 and 100 μm indenter tips. Pop-ins mask the conventional elastic-plastic transition and make the determination of the Y_{ind} difficult. The size of the pop-in reduces rapidly with an increase in the indenter tip size and is absent for the test with the 100 μm indenter tip (expanded in the inset).

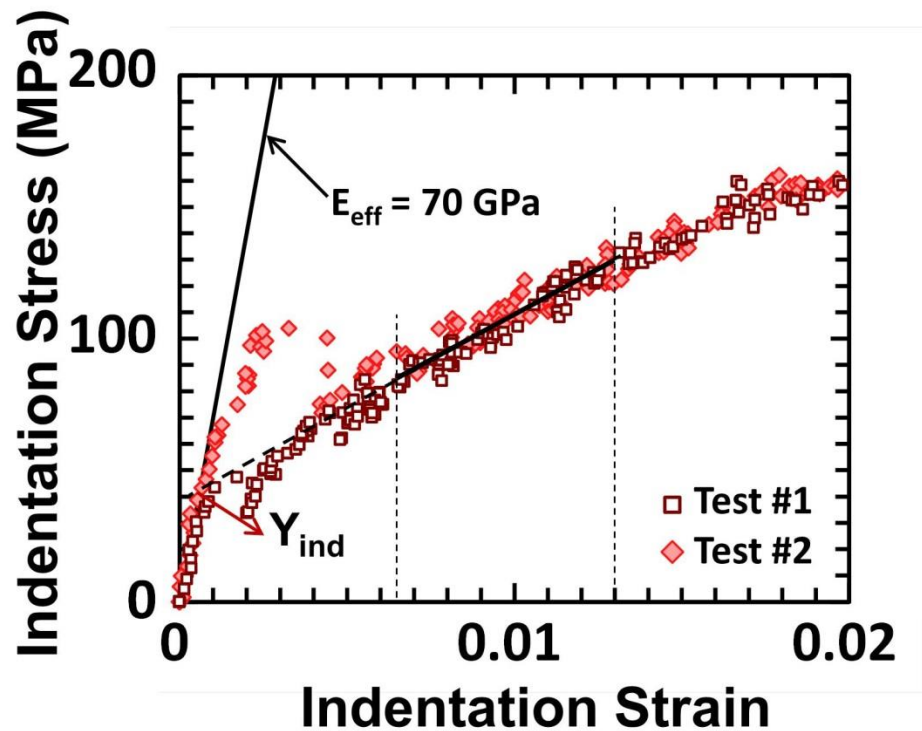


Figure 2: ISS curves for two tests carried out within the same grain in the fully annealed aluminum sample using the 100 μm indenter tip. As seen here, the pop-ins are occasionally observed but are small enough that the back-extrapolation method can be reliably used to extract Y_{ind} values. The dashed vertical lines show the segment of the stress-strain curve used for the back extrapolation. This segment is carefully selected to be just outside the pop-in segment.

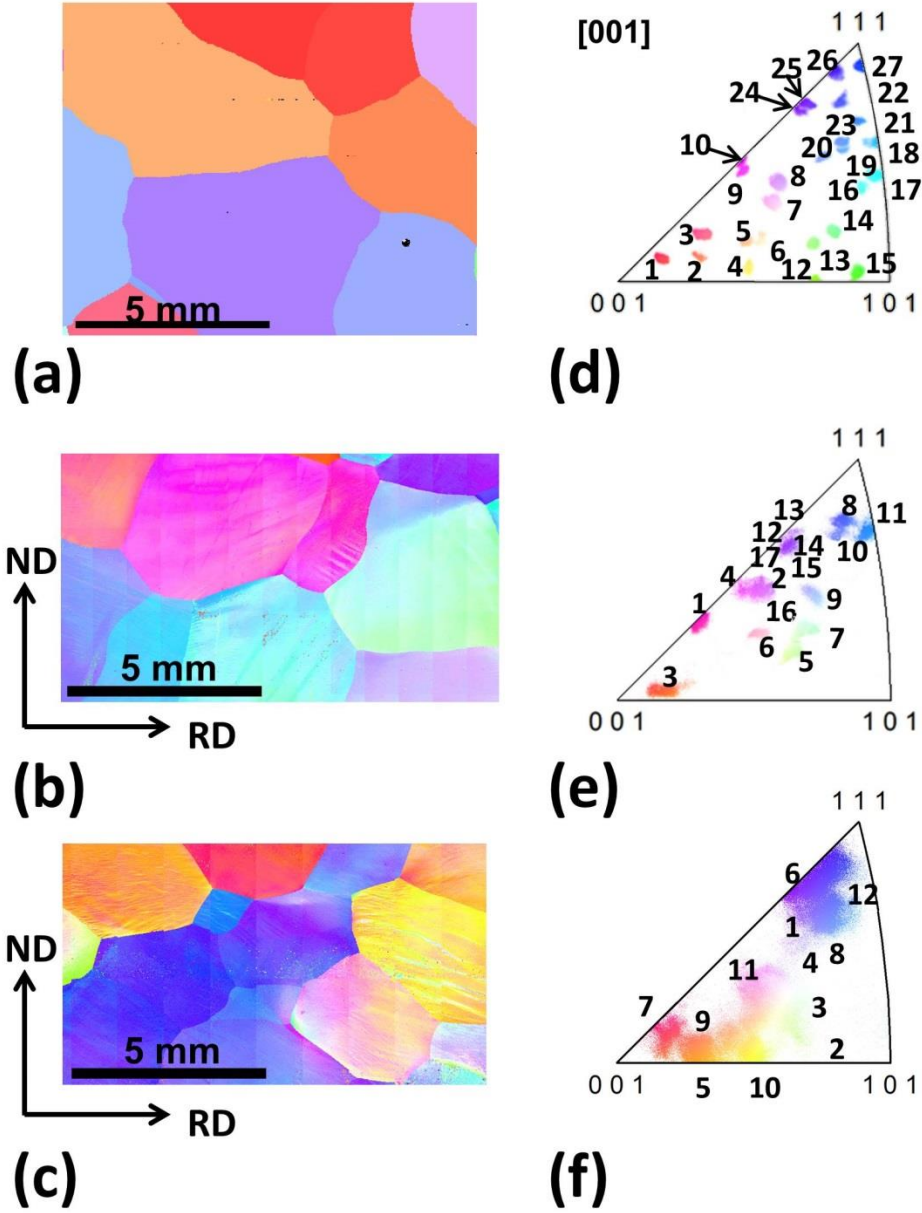


Figure 3: Representative OIM maps from the pure aluminum samples studied in the (a) fully annealed condition, (b) after 10% and (c) 20% reduction in height by plane strain compression. The IPF maps showing the positions of all the grains tested in the (d) fully annealed condition, after (e) 10% and (f) 20% reduction in height respectively. Since the grains are very large (~2-3 mm) only a limited number of orientations are present in each sample and multiple samples were employed to gather adequate amount of data for the study.

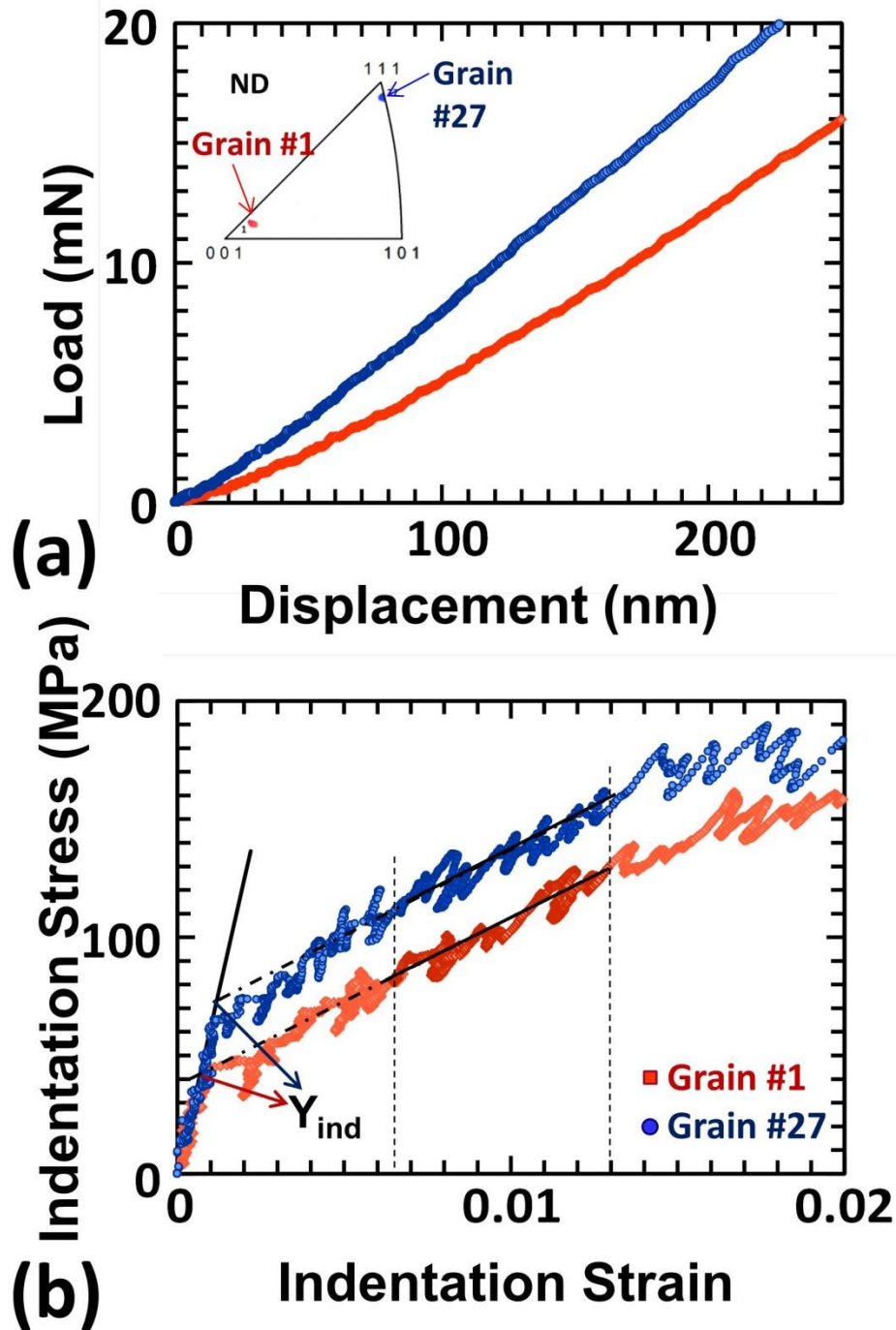


Figure 4: The measured load-displacement data for two grains (grain #1 and grain #27) in the fully annealed condition. The inset shows the IPF map which indicates the orientation of the grains with respect to the indentation axis. The corresponding ISS curves are in (b). Note that the Y_{ind} values vary quite significantly between the two orientations.

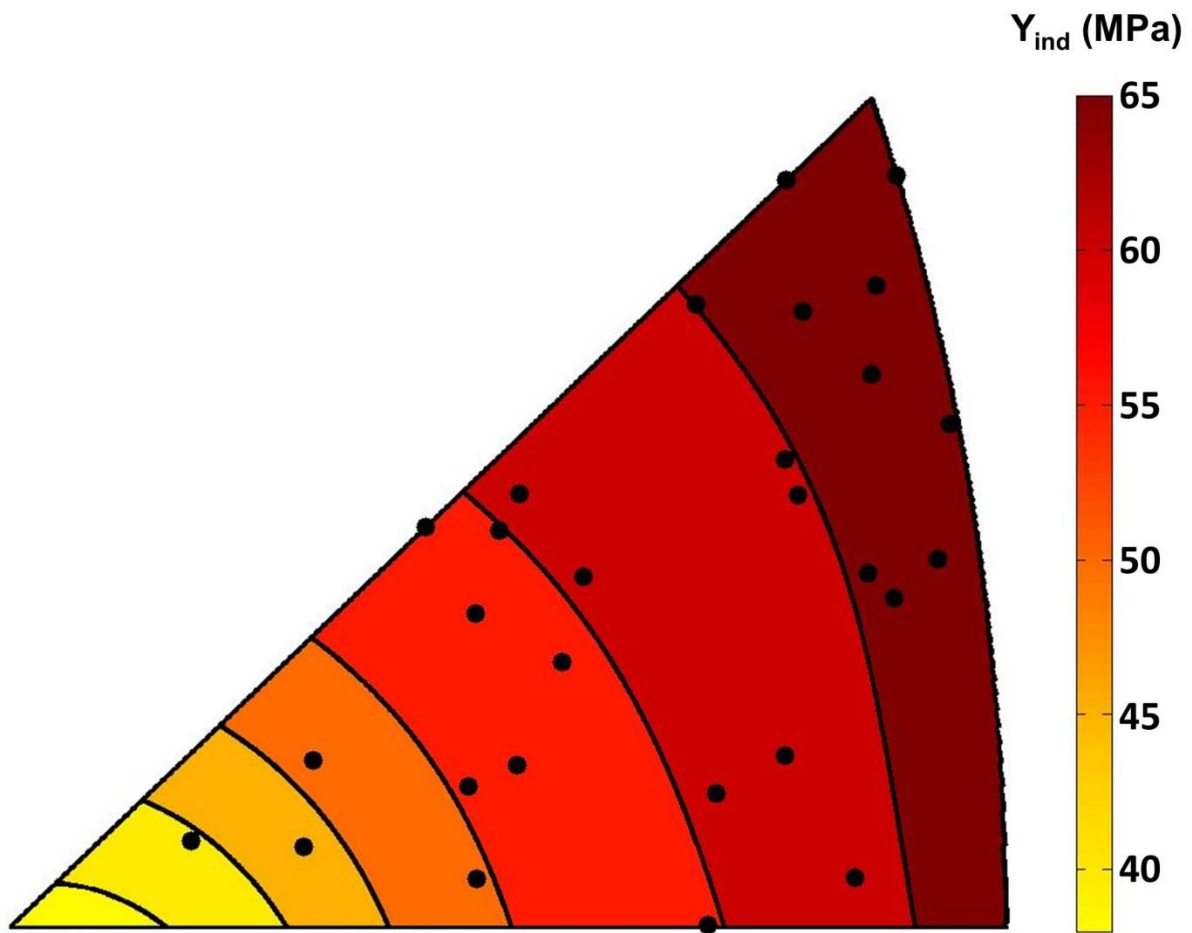


Figure 5: Contour plot generated by interpolating between the average Y_{ind} values extracted for the 27 grains in the annealed condition. The black circles represent the positions of the tested grains on the standard IPF plot.

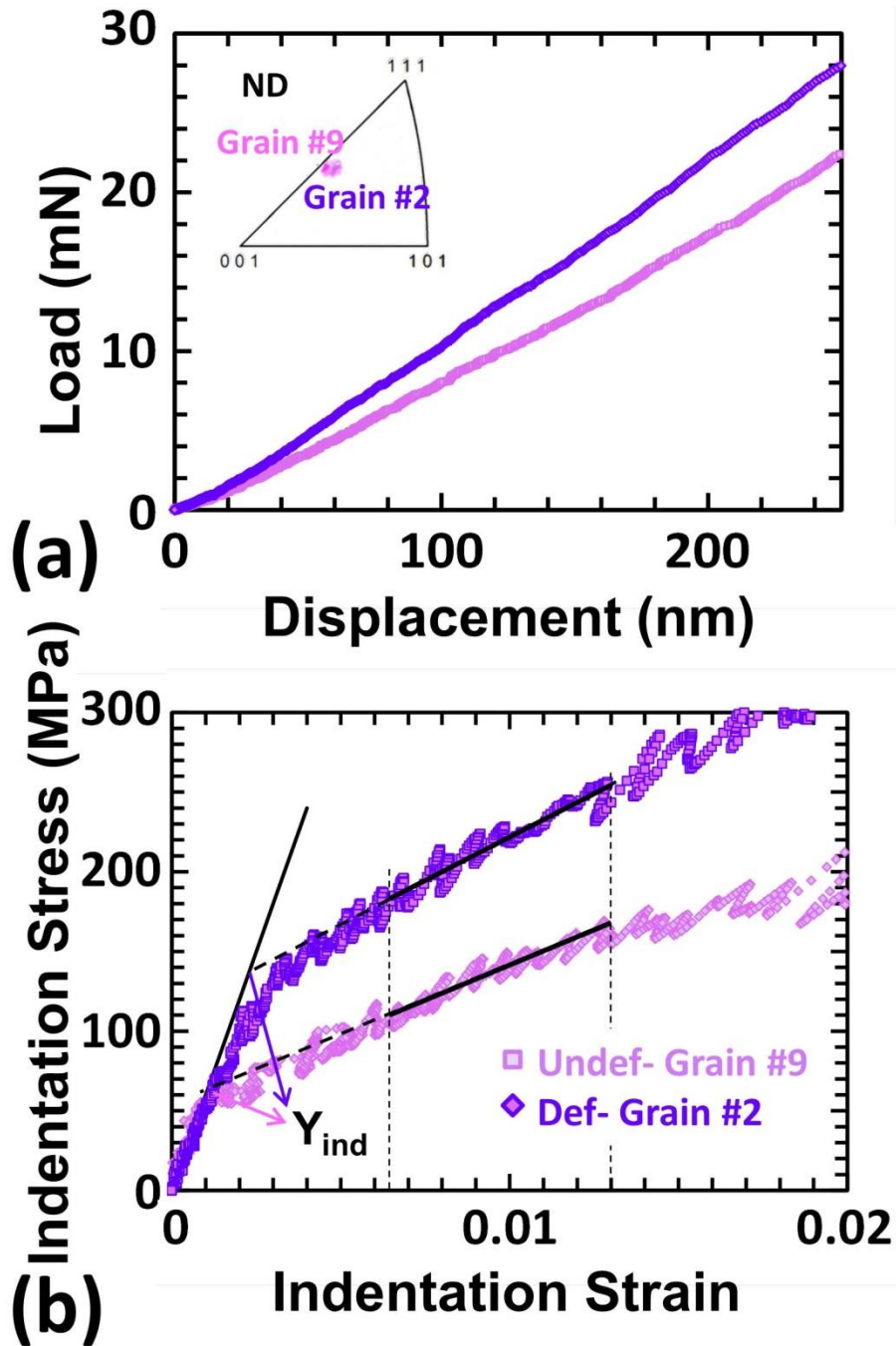


Figure 6: (a) The load-displacement data, and (b) corresponding indentation stress-strain curves, for two almost identically oriented grains (4.3° misorientation), showing the effect of deformation on the ISS response. Grain #9 was tested in the fully annealed condition and Grain #2 was tested after the sample was deformed to 10% reduction in height by plane strain compression.

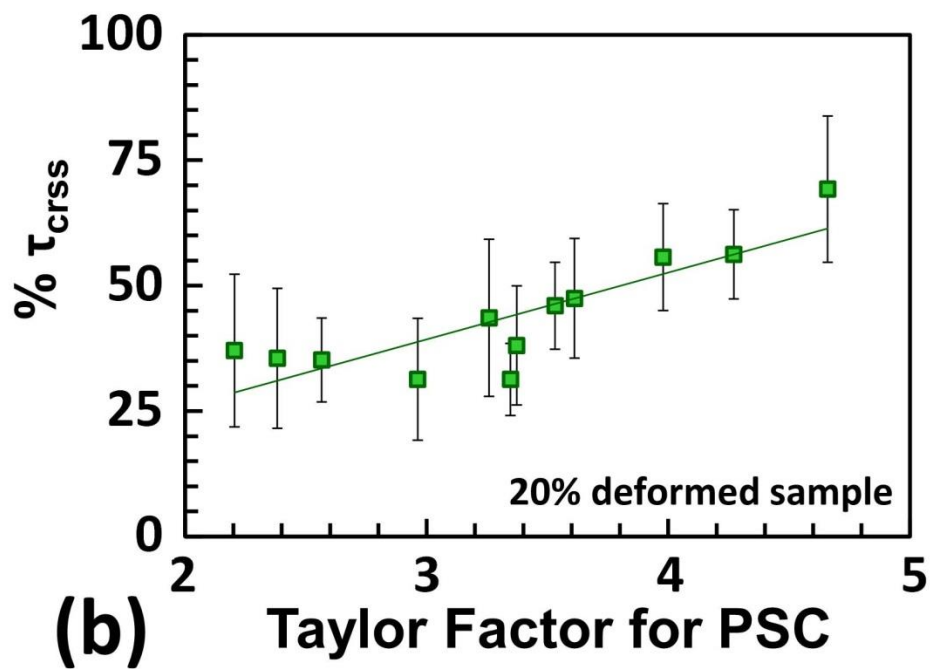
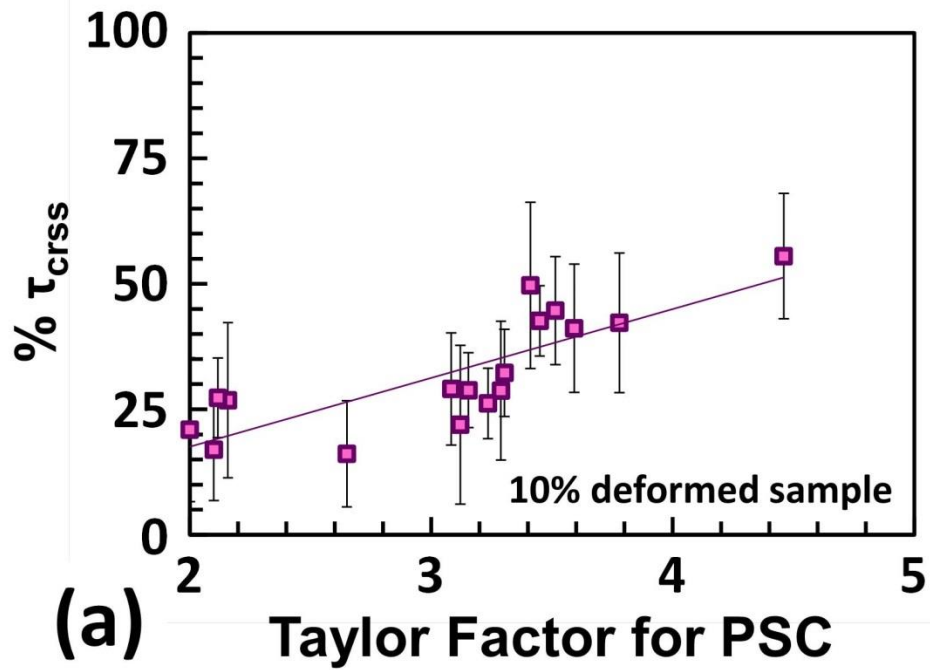


Figure 7: Plot of the percentage increase in the measured critical resolved shear stress, for individual grains, as a function of the Taylor factor in plane strain compression computed for the grains. (a) 10% reduction level, and (b) 20% reduction level.

Tables

Grain No.	Orientation (Euler Angles)			E_{ind} (GPa)	Y_{ind} (MPa)
	Φ_1	Φ	Φ_2		
1	73.1	9.8	63.4	74.3 ± 0.9	46.2 ± 8.0
2	224.9	14.7	73.9	75.0 ± 1.0	52.4 ± 5.1
3	219.9	16.8	60.3	75.8 ± 0.3	47.6 ± 7.4
4	143	22.4	83.7	75.4 ± 0.2	61.0 ± 5.7
5	347.9	23	72.2	74.8 ± 1.0	61.7 ± 5.7
6	29	25.4	71.6	74.8 ± 1.9	53.6 ± 5.3
7	60.9	29.2	63.4	75.1 ± 1.0	58.0 ± 9.9
8	348.5	32	57.6	75.1 ± 1.1	63.5 ± 9.2
9	190.1	30.2	49.9	75.1 ± 0.5	59.9 ± 9.9
10	347.2	27.9	45	74.2 ± 0.5	60.4 ± 8.3
11	280.5	32	48.5	74.2 ± 0.3	59.5 ± 8.5
12	23	32.8	89.7	75.1 ± 0.1	53.4 ± 8.2
13	13.7	33.8	78.8	74.3 ± 2.5	58.7 ± 4.4
14	306.5	37.1	77	74.1 ± 0.2	61.9 ± 6.9
15	299.7	39.3	86.5	75.1 ± 0.9	62.4 ± 7.8
16	273.4	43.6	68.8	75.3 ± 1.1	62.3 ± 9.9
17	167.3	45.9	67.6	74.3 ± 0.7	61.1 ± 9.5
18	182.5	48.8	60.9	74.9 ± 0.5	66.8 ± 9.4
19	232.2	42.2	57.9	75.4 ± 1.1	67.1 ± 9.2
20	15	41.9	60.3	75.6 ± 1.2	59.8 ± 6.1
21	207.7	47.2	56.3	74.6 ± 1.1	67.7 ± 7.9
22	187.6	49.5	52.4	75.2 ± 0.1	61.2 ± 4.5
23	185.6	46.5	51.1	74.7 ± 1.8	67.0 ± 8.4
24	288.6	43	66.8	74.8 ± 0.1	60.3 ± 7.1
25	241.3	43.4	46.7	75.5 ± 1.5	61.0 ± 9.6
26	45	49.7	45	74.7 ± 1.0	72.5 ± 9.8
27	45.4	53	48.6	74.6 ± 1.8	64.3 ± 7.1

Table 5.1: Summary of the measurements on the 27 grains tested in the fully annealed condition. Orientation of the grains are presented as Bunge-Euler angles. The indentation modulus (E_{ind}) and the indentation yield strength (Y_{ind}) were extracted from nanoindentation tests carried out using the 100 μ m spherical tip.

Grain No	Orientation (Euler Angles)			Taylor Factor for PSC	Predicted Y_{ind} (undef)	Y_{ind} (MPa)	% τ_{crss}
	ϕ_1	Φ	ϕ_2				
1	70.4	44.7	269.7	4.46	54.8	85.5 ± 6.9	55.5 ± 12.5
2	32.5	29.1	304	3.12	61.1	74.4 ± 9.8	22.0 ± 15.2
3	290.1	24.5	69.9	3.41	46.3	68.9 ± 7.6	49.7 ± 16.5
4	203.1	17.6	181.7	2.16	62.2	78.6 ± 9.6	26.8 ± 15.5
5	254.4	29.5	133.5	3.45	60.5	87.0 ± 4.3	42.6 ± 7.0
6	250.7	35.5	130.6	3.51	58.0	83.9 ± 6.2	44.66 ± 10.8
7	255.1	45.5	132.5	3.59	61.5	86.1 ± 7.8	41.15 ± 12.8
8	53	49.8	335.7	3.08	66.3	85.2 ± 7.4	29.1 ± 11.2
9	150.7	37.7	195.5	2.65	64.3	74.3 ± 6.8	16.2 ± 10.6
10	208.4	41.3	115.7	3.30	66.1	87.3 ± 5.7	32.3 ± 8.7
11	196.4	42.4	123.7	3.29	66.5	86.3 ± 9.3	28.7 ± 13.8
12	198.1	29.4	187.1	2.10	064.4	74.8 ± 6.5	16.9 ± 10.1
13	298.5	55.7	44.6	3.78	63.1	89.6 ± 8.8	42.3 ± 13.9
14	190.5	25.7	203	2.12	65.5	84.0 ± 5.2	27.3 ± 7.9
15	185.4	28.1	201.9	2.00	64.3	82.6 ± 9.2	20.9 ± 14.3
16	307.2	29.1	344	3.15	60.1	77.3 ± 4.5	28.0 ± 7.4
17	307.2	40.8	42.1	3.23	63.5	80.8 ± 4.5	26.2 ± 7.0

Table 2: The grain orientations, corresponding Taylor factor for PSC, the predicted Y_{ind} values in the fully annealed condition for the orientations, Y_{ind} in the deformed condition, measured using indentation, and percentage increase in the critical resolved shear stress, as a result of the imposed macroscopic strain for the sample deformed to 10% reduction in height by plane strain compression.

Grain No	Orientation (Euler Angles)			Taylor Factor for PSC	Predicted Y_{ind} (undef)	Y_{ind} (MPa)	% τ_{crss}
	Φ_1	Φ	Φ_2				
1	162.3	35.3	175.2	2.20	65.8	90.4 ± 10.0	37.1 ± 15.2
2	155.4	8.6	167.1	2.38	64.5	88.1 ± 9.9	35.5 ± 14.0
3	226.4	37.4	116	3.53	59.1	86.1 ± 5.1	46.0 ± 8.7
4	46.3	33.4	10.6	3.26	63.0	90.5 ± 9.9	43.6 ± 15.7
5	111.6	44.5	259.4	4.66	50.8	86.1 ± 7.4	69.2 ± 14.6
6	141.1	35.6	195.7	2.96	64.9	85.4 ± 7.9	31.4 ± 12.1
7	80.8	24.4	288.5	3.37	47.7	66.3 ± 5.7	38.1 ± 12.1
8	127.4	34	187.6	3.35	65.9	86.7 ± 4.7	31.3 ± 7.2
9	61.3	45.7	298.7	4.27	53.6	84.4 ± 4.8	56.2 ± 8.9
10	275.1	39.2	62.8	3.98	53.9	84.1 ± 5.8	55.7 ± 10.7
11	106.2	34.5	283.2	3.61	39.3	87.0 ± 7.0	47.46 ± 11.9
12	147.7	34	180.1	2.57	65.9	89.2 ± 5.5	35.2 ± 8.4

Table 3: The grain orientations, corresponding Taylor factor for PSC, the predicted Y_{ind} values for the orientation in the fully annealed condition, Y_{ind} measured in the as deformed condition and percentage increase in the critical resolved shear stress, as a result of the imposed macroscopic strain for the sample deformed to 20% reduction in height by plane strain compression.

Appendix B: Studies of Grain Boundary Regions in Deformed Polycrystalline Aluminum Using Spherical Nanoindentation

1. Introduction

The importance of grain boundaries and other mesoscale interfaces in controlling the mechanical properties of structural metals and alloys is widely recognized and reported in published literature [1-13]. However, there is currently very little quantitative information and understanding on the precise roles of various different types and kinds of mesoscale interfaces in the overall mechanical behavior of the material. In this regard, it should be noted that the well-known Hall-Petch rule [7, 8] provides a robust relationship between the average grain size and the macroscale yield strength of the material. It is important to recognize that this linkage captures only an average effect by treating all grain boundaries alike. Based on the current understanding of the physics of the grain boundaries, however, it is fully expected that the mechanical role of grain boundaries should depend on the grain boundary character, which includes information on the misorientation across the grain boundary and the orientation of the grain boundary with respect to a sample reference frame. However, these dependencies are not yet established quantitatively. It is emphasized this understanding is critical to developing physics-based models for strain hardening and recrystallization processes in all polycrystals.

One of the main impediments to establishing the fundamental science underlying the mechanical role of mesoscale interfaces is the lack of validated and cost-effective protocols for measuring mechanical properties at the small length scales of interest. One approach explored in current literature involves the fabrication of micro-pillars [14-17] using focused ion-beam and testing them in a scanning electron microscope. However, this approach requires access to highly sophisticated equipment and is very effort intensive. It is not particularly well suited for characterizing the local mechanical properties of a large number of mesoscale constituents and interfaces in a high throughput approach. The other emerging alternative approach for addressing this challenge is instrumented indentation (both nano and micro) combined with improvements in data analyses protocols.

Recent advances in the analysis of spherical nanoindentation data now provide a means of extracting very reliable and repeatable measurements of local mechanical properties at a sub-

micron length scale [18-21] This local mechanical behavior data can be combined with local structure information obtained using complementary techniques such as orientation imaging microscopy (OIM) to further our understanding of local structure-property relationships in metallic materials and their evolution during macroscopically imposed plastic deformation. In previous work [22], we studied the evolution of slip-resistances within individual grains (i.e. in the grain interiors) during deformation in polycrystalline aluminum (Al). As a natural progression of this work, we have conducted a detailed study into the evolution of local mechanical properties in the grain boundary regions in plastically deformed samples of polycrystalline Al. In a previous study, Pathak et al. [23] have demonstrated the viability of the combined spherical nanoindentation-OIM testing and analysis protocols in quantifying changes in mechanical properties in the grain boundary regions of a deformed Fe- 3% Si steel sample. In that prior work, three specifically selected grain boundaries were studied in 30% deformed samples. Building on this previous experience, in this work, we have systematically investigated regions around eight grain boundaries in a high purity aluminum sample deformed by plane-strain compression to obtain a 20% reduction in height. The smaller strain level and the larger number of grain boundaries were selected for the present study with the specific goal of quantitatively relating the grain boundary parameters to the measured changes in the local mechanical properties in the grain boundary regions.

2. Spherical Nanoindentation and Indentation Stress Strain Curves

Indentation is a versatile tool for measuring the mechanical properties from small material volumes[24]. Traditionally, indentation experiments have been carried out with sharp tips [25-27], and the values of local elastic modulus and hardness were extracted mainly from an analysis of the unloading portion of the test segment [19, 28, 29]. However, recent advances in instrumentation (e.g., the availability of the continuous stiffness measurement (CSM) [30]) have now made it possible to convert the measured load-displacement data from spherical nanoindentation into highly reproducible and consistent indentation stress-strain (ISS) curves [31]. It has been demonstrated that these new protocols produce meaningful information such as the local indentation modulus and the local indentation yield strength (Y_{ind}). The procedures used to convert raw indentation data into ISS curves and extract Y_{ind} from the ISS data have been detailed in prior publications [22, 31]. A brief overview of the same is provided here.

The methodology for converting raw spherical nanoindentation data into ISS curves is largely based on Hertz Theory [32-34]. The first step involves the determination of the effective point of initial contact or the effective zero point, such that all the measured signals provide the best agreement with the Hertz theory beyond this point. If \tilde{P} , \tilde{h} and S are the measured load, displacement and stiffness signals, and P^* and h^* denote the raw load and displacement values at the effective zero point, the expected relationship between all these variables in the initial elastic loading segment can be shown as [31]

$$S = \frac{3P}{2h_e} = \frac{3(\tilde{P} - P^*)}{2(\tilde{h} - h^*)} \quad (1)$$

where h_e is the elastic indentation depth at load P . Linear regression can be used to determine the values of P^* and h^* , i.e., the effective zero point [add refs]. The second step involves the determination of the radius of contact (a) as [31]

$$a = \frac{S}{2E_{eff}}, \quad \frac{1}{E_{eff}} = \frac{1 - \nu_s^2}{E_s} + \frac{1 - \nu_i^2}{E_i} \quad (2)$$

where E_{eff} is the effective stiffness of the indenter-sample system, E and ν are the Young's modulus and Poisson's ratio respectively and the subscripts i and s refer to the indenter and the sample respectively. As the last step, the values of indentation stress (σ_{ind}) and indentation strain (ϵ_{ind}) are extracted from the raw data using [31]

$$\sigma_{ind} = \frac{P}{\pi a^2}, \quad \epsilon_{ind} = \frac{4h_t}{3\pi a} \quad (3)$$

From the ISS curves, Y_{ind} was determined as the point of intersection between the modulus line (i.e., the elastic portion of the initial loading segment) and the best-fit line for the stress-strain curve within the strain range of 0.0065 and 0.013 [22]. This approach was necessary in our prior work so as to minimize the effect of pop-ins (strain jumps) caused by inability to produce potent dislocation sources in the indentation zone in the tests on annealed samples. Although pop-ins are almost completely absent in the deformed samples[22, 35, 36], the protocols need the indentation yield strengths in the annealed conditions in order to estimate the percentage changes in the local slip resistances at the indentation sites. These protocols have been described in detail in prior papers [22, 36] and are briefly reviewed later in this paper.

Because of the need to utilize the measured values of the indentation yield strengths in the annealed condition where the pop-ins are mostly unavoidable, we have employed consistently the same back-extrapolation method to extract the indentation yield point in the deformed samples as well.

3. Materials and Methods

High purity, polycrystalline aluminum (99.999%) was used for this work. Pure aluminum exhibits low elastic anisotropy ($A=1.22$) [37] and hence the effect of crystal orientation on the indentation modulus is very small. A modified form of Hertz theory [32, 33] predicts the sample indentation modulus for grains of different orientations to be in the range of 68.8 to 70.6 GPa. The surface oxide film in aluminum is extremely thin, thus making its interference with our measurements negligible.

Since we intend to interrogate regions near grain boundaries, a fully annealed, large grained sample was used for this study, so that the grain boundary segments were long enough to allow a large number of measurements while staying away from triple junctions. In order to achieve these large grains, a sample was cut out from a heavily rolled block of high purity aluminum and annealed at 640°C for 72 hours. The sample was then deformed by plane strain compression in a channel-die at room temperature to achieve 20% reduction in height. The sample was then mounted in epoxy and the surface was prepared using mechanical grinding and polishing. Since a high quality surface finish is extremely important for indentation measurements [35], electropolishing was used as the final sample preparation step.

An orientation map of the polished surface was obtained using orientation imaging microscopy (OIM), which is based on the automated indexing of electron backscatter diffraction patterns (EBSD). Bunge-Euler angles [38] were used to denote the orientation at each point on the surface. These are an ordered set of three rotations (ϕ_1, Φ, ϕ_2) that transform the sample reference frame to the crystal reference frame. The grains on the surface were numbered for convenience and will be henceforth referred to using the assigned grain numbers. From this OIM map, eight grain boundaries were selected for this study. These were selected to include a broad range of grain boundaries, including low and high angle boundaries as well as low, moderate, and high deviations in the Taylor factors of the grains on either side of the boundary.

With an aim to obtain better spatial resolution and also place as many indents as possible close to the grain boundary, a 20 μm spherical indenter tip was used). Note that using a indenter tip with a smaller diameter increased the probability of the occurrence of pop-ins. As mentioned in the previous sections and discussed in detail in our prior work[22], pop-ins are displacement jumps during an indentation test and produce a discontinuity in the ISS curves. This makes the determination of Y_{ind} difficult and thus needed to be avoided. Occurrence of pop-ins is related to difficulty of establishing potent dislocation sources in the small indentation zones and is almost always observed when indentation measurements are carried out on annealed samples using indenter tips of a small radius. Therefore, in our prior work [22] where the effect of orientation on Y_{ind} for the high purity aluminum was characterized, a 100 μm spherical indenter tip was used. The effect of the indenter tip size on the indentation response of the 20% deformed sample is shown in Figure 1. All the data used for comparisons was obtained within the same grain. As seen from the figure, although there is significant difference in the post elastic behavior, the values of Y_{ind} are in excellent agreement in the two indentation stress-strain curves. This observation is in agreement with the findings discussed in [23] regarding the effect of indenter tip size on the indentation stress strain curves. For this work, since we are interested only in the Y_{ind} values, switching the indenter tip size between 20 μm and 100 μm did not affect the extracted values.

Indentation tests were performed along lines inclined to the selected grain boundary at shallow angles to allow for acquisition of more data points as a function of the distance from the grain boundary [39]. The long grain boundary segments, which are a result of the large grains in our samples allowed us to place multiple rows (6-9) of indents close to the boundary. Each row contained 12 to 13 indents spaced 20 μm apart. This resulted in approximately 80 to 120 indents across each grain boundary. The large number of indents used in this study allows us to ensure that the trends observed in our investigations can be distinguished from the inherent noise in the nanoindentation response. It should be noted that such a high number of data-points would be almost impossible to obtain using other small-scale mechanical testing techniques such as micro-pillar testing. High resolution OIM maps as well as optical micrographs were used to image the indents near the grain boundaries of interest after the indentations were performed. These were used to extract crystallographic information in the vicinity of the grain boundary as well as accurately determine the position of the indents with respect to the grain boundary. The

perpendicular distance from the center of each indent to the grain boundary was calculated from these micrographs and will hence forth be referred to as the distance from the grain boundary.

The combined indentation-OIM analysis protocols developed in our prior work [22] were based on the assumption that the effect of the crystal lattice orientation on the measured indentation yield point can be expressed by the same multiplicative factor (very similar to a Taylor factor) for both undeformed and deformed samples. As argued in our earlier work [22], this is a reasonable assumption for the high symmetry cubic crystals with a relatively large number of slips systems with roughly the same slip resistance. In order to implement these protocols, a contour plot showing the dependence of the Y_{ind} on the local crystal lattice orientation at the indentation site in the annealed sample was already experimentally established for high purity aluminum [22]. This same plot is used here to predict the effect of local crystal orientation on Y_{ind} , since the exact same material was used in the present study.

For each of the indentations performed in the deformed condition, the expected Y_{ind} in the fully annealed condition was extracted from the indentation yield strength presented in our previous work [22]. This is the indentation yield strength that would have been measured for the same orientations, if they were tested in the fully annealed condition. A reliable estimate of the increment in Y_{ind} (i.e., ΔY_{ind}) as a consequence of the macroscopically imposed plastic deformation (i.e. 20% reduction by plane strain compression) can then be determined as the difference between the measured indentation yield point in the deformed condition (denoted as $Y_{ind}(g,d)$) and the estimated indentation yield point in the fully annealed condition (denoted as $Y_{ind}(g,0)$) as

$$\Delta Y_{ind}(g,d) = Y_{ind}(g,d) - Y_{ind}(g,0) \quad (4)$$

In Eq. (4) d refers to the amount of macroscopically imposed plastic deformation and g refers to the local crystal lattice orientation at the indentation site.

The simplest relationship that one can try to establish between Y_{ind} and the local dislocation content (ρ) is through the critical resolved shear strength (τ_{crss}) of the slip system. In a highly simplified manner, this relationship can be expressed as

$$Y_{ind}(g,d) = M(g)\tau_{crss}(d) \quad (5)$$

$$\Delta\tau_{crss}(d) = \tau_{crss}(d) - \tau_{crss}(0) \propto \sqrt{\rho} \quad (6)$$

where M is similar to a Taylor factor for indentation that depends only on the grain orientation with respect to the indentation direction (in this case, only two of the three Bunge-Euler angles describing local crystal orientation), τ_{crss} is the critical resolved shear strength in the crystal, $\Delta\tau_{crss}$ is the increment in the local averaged critical resolved shear strength between the annealed and deformed conditions, and ρ is the local dislocation density.

A convenient measure for comparing the relative hardening levels in the differently oriented regions in a given deformed sample is to express the increase in the slip resistance as a percentage of the initial critical resolved shear stress in the material in the annealed condition. Combining Eqs. (4)-(6), the percentage increase in the critical resolved shear stress is expressed as

$$\% \tau_{crss} = \frac{\Delta\tau_{crss}(d)}{\tau_{crss}(0)} * 100 = \frac{\Delta Y_{ind}(g,d)}{Y_{ind}(g,0)} * 100 \quad (8)$$

As noted earlier, $\% \tau_{crss}$ provides an indirect measure of the local dislocation content or local hardening in the deformed samples (cf. Eq. (6)).

The $\% \tau_{crss}$ are expected to correlate to the Taylor factors associated with the macroscopically imposed plastic deformation on the sample. The Taylor factor M is defined as

$$M = \frac{\sum \Delta\gamma}{\Delta\epsilon} \quad (7)$$

where $\Delta\gamma$ is the sum of the slip shears on all the slip systems, and $\Delta\epsilon$ is the imposed macroscopic plastic strain increment. In other words, a grain with a higher value of M is expected to require a higher amount of total slip on its available slip systems to accommodate the imposed macroscopic plastic deformation. Grains with higher values of M are generally referred as hard (oriented) grains, and those with lower values of M are generally referred as soft grains.

In our most recent work [22], we provided strong experimental evidence suggesting that grains with higher values of M (i.e., hard grains) harden more than the grains with lower values of M because they demand higher amounts of total slip in the grain. This previous study focused on grain interior regions to acquire the needed datasets. In this paper, we explore the grain boundary regions with the exact same toolsets.

4. Results and Discussion

The eight grain boundaries studied here are identified on the OIM map of the 20% deformed high purity aluminum sample shown in Figure 2. Each grain in the OIM map is color coded to represent its position on the standard [ND] inverse pole figure (IPF). In other words, the color represents the crystal direction in the grain that was perpendicular to the sample surface and parallel to the loading direction during the plane strain compression. Note however that the sample surface that was used for the nanoindentation testing is the TD section. The rolling direction (RD) for the section in the OIM map is horizontal and the normal direction (ND) is vertical.

About 80-120 indentation tests across each of the eight boundaries were carried out and the raw indentation data was converted into ISS curves. Representative ISS curves for indents close to and far away from the boundary, for the two grains (Grain #5 and #12) on either side of grain boundary #1 (GB #1) are shown in Figure 3. As discussed previously in Section 3, pop-ins are mostly absent in the indentation tests carried out on the deformed samples using the 20 μm spherical tip, suggesting that it is relatively easy to set up the necessary dislocation sources in the indentation zones using the existing network of forest dislocations. Also clear from this figure is the fact that, even for the same grain boundary, the grains on either side behave very differently in the immediate vicinity of the boundary as compared to the response measured away from the boundary. As seen in Figure 3, for grain #5, there is little difference between the indentation response measured close to the grain boundary and away whereas on the other side of GB #1, in grain #12, the measured indentation stress-strain curve and the Y_{ind} exhibit significant increases in the immediate vicinity of the grain boundary than far away.

The indentation test results for five of the eight boundaries studied are presented in Figures 4-8; these five represent the most interesting results from the total set of eight. The OIM map showing the grain boundary, the orientation on a standard [ND] inverse pole figure map and the position of the indents with respect to the grain boundaries are provided for each grain boundary in Figures 4-8 (a). The summaries of the measured Y_{ind} and the percentage increase in τ_{crss} due to the imposed macroscopic deformation are given in Figures 4-8 (b) and (c) respectively.

Table 1 summarizes the details of the OIM and nanoindentation measurements away from the grain boundaries for the eight boundaries of interest. The orientation away from the grain boundary represents the average orientation in the region of about 500 μm around the grain boundary where the indentation tests were performed. Δg across the boundary is the misorientation between the average orientations measured in the region of about 500 μm on either side of the grain boundary and GOS represents the grain orientation spread measured in the same region. The Taylor factors presented are for plane strain compression for the average orientations measured in the region of about 500 μm on either side of the grain boundary. $Y_{ind}(g,d)$ and $Y_{ind}(g,0)$ represent the indentation yield strength values measured within the grains (well away from the grain boundaries) and the indentation yield strength values extracted from the indentation yield surface for aluminum, which represent the expected Y_{ind} , if the orientations were tested in the fully annealed condition.

Table 2 summarizes the details of the OIM and nanoindentation measurements in the vicinity of the grain boundaries, for the eight boundaries of interest. The orientation at the grain boundary represents the average orientation in the region of about 60 μm around the grain boundary where the indentation tests were performed. Δg across the boundary is the minimum calculated misorientation between the average orientations measured in the region of about 60 μm on either side of the grain boundary. The Taylor factors (at GB) presented are for plane strain compression for the average orientations in the grain boundary region and GOS represents the grain orientation spread measured in the region of about 60 μm on either side of the grain boundary. Δg (center to GB) is the calculated misorientation between the average orientations away from the boundary (reported on Table 1) and average orientation in the grain boundary region (reported in Table 2). $Y_{ind}(g,0)$ represents the indentation yield strength values extracted

from the indentation yield surface of aluminum, which represents the expected Y_{ind} , if the orientations at the grain boundary were tested in the fully annealed condition.

From Figures 4-8 and Tables 1 and 2, it is clear that all grain boundaries do not behave in the same manner. For GB-1 (See Figure 4), there is a substantial transition zone on one side of the boundary where the measured values of Y_{ind} near the boundary are higher than those measured within the grains (away from the boundary region). The immediate vicinities of GB-2, GB-3 and GB-4 (See Figure 5), also exhibit hardened layers, at least on one side of the grain boundary, although it appears to be significantly less pronounced as compared to GB-1. For GB-5 (see Figure 6) and GB-6, the presence of a grain boundary appears to have a negligible effect on the Y_{ind} values measured in the vicinity of the grain boundary. In other words, the Y_{ind} measured very close to the grain boundary is very similar to the Y_{ind} measured well away from the boundary (but within the respective grains). All these boundaries (GB-1 to GB-6) were high angle grain boundaries. GB-7 is a low angle grain boundary, and once again, the presence of a grain boundary appears to have a negligible effect on the Y_{ind} values measured in the vicinity of the grain boundary (See Figure 7).

Looking at the Taylor factors in plane strain compression for each of the orientation of interest, it is seen that away from the grain boundaries, the orientations with a higher Taylor factor show more hardening as a result of the 20% height reduction. This is consistent with the findings reported previously [22].

However, in the immediate vicinity of the grain boundary, a grain with a low Taylor factor (soft grain) when present next to a grain with relatively high Taylor factor (hard grain) showed much more hardening at the boundary. The difference in the Taylor factor between adjacent grains is highest across GB-1, where grain #12 is a very soft grain with a Taylor factor of 2.80 next to a very hard grain (Taylor factor of 4.55). From Figure 4 and Table 1 and 2, it is seen that grain #12, in the immediate vicinity of GB-1 shows the most significant amount of hardening both in terms of the percentage change in the Y_{ind} as well as the thickness of the hardened layer. GB-2, GB-3 and GB-4 show progressively lesser difference in the Taylor factors for the orientations on either side of the boundary and also progressively lesser amount of hardening on the 'soft grain' side. GB-5 has two moderately hard grains of almost the same Taylor factor on either side of the boundary and GB-6 has two soft grains of very similar Taylor

factors next to each other. In both these cases, the hardened layer is completely absent. GB-7 is a low angle grain boundary with two relatively hard grains next to one another across the boundary. Consistent with previous observations (GB-5 and GB-6), here again, there is little effect of the boundary on the hardening near the grain boundary. Note that all low angle grain boundaries will have grains of very similar orientation and Taylor factors next to each other and thus are a special case in that there is little effect of the low angle grain boundaries on the hardening at the grain boundary.

In order to quantify the changes in the hardening levels in the grain boundary regions, we need to define suitable parameters. In this study, we define two such parameters, which are shown in Figure 8(a). The first parameter is $\%Y_{ind}(at\ GB)$ which is the change in the $Y_{ind}(at\ GB)$ with respect to the Y_{ind} measured in the grain interior. Here $Y_{ind}(at\ GB)$ is the y-intercept for the best fit line through all the Y_{ind} values measured between 2 μm and 8-15 μm from the grain boundary, on a plot of Y_{ind} vs. distance from the boundary. The second parameter is the thickness of hardened layer calculated as the distance from the grain boundary where the best fit line through all the Y_{ind} values measured between 2 μm and 8-15 μm from the grain boundary intersects the horizontal line that represents, on a plot of Y_{ind} vs. distance from the boundary plot, Y_{ind} (away from the boundary). Note here that the extrapolated value of Y_{ind} and the calculated thickness of the hardened layer are both strongly affected by the number of data points used for the interpolation and hence it is important to have a sufficiently large number of data points in the ‘hardened region’ in order to be confident about the numbers extracted.

Figure 8(b) shows the variation of the thickness of the hardened layer in the ‘soft’ grain as well as the percentage increase in the indentation yield strength (Y_{ind}) with respect to the Y_{ind} measured in the grain interior as a function of the difference in the Taylor Factor of the grains on either side of the grain boundary in question. There appears to be a very strong relationship between the difference in Taylor factor at the grain boundary and the extent of hardening at the grain boundary. Although more data points need to be added to this plot in order to reliably quantify the relationship, this is a very important observation. It supports the hypothesis [40] of the presence of hardened layer at grain boundaries in deformed materials, due to the mismatch in the mechanical properties across the boundaries. The measurements reported in this work indicate that these hardened layers are predominantly on the side of the softer (lower Taylor factor) grain. Note that the thickness of the hardened layer observed near these grain boundaries

is comparable to the average grain sizes in most commercially used metals and alloys. This would mean that for grain boundaries in a sample that are between hard and soft grains, there will be significant hardening within the entire soft grain, due to the presence of the boundary.

While the 7 grain boundaries discussed here seem to follow the trends discussed above, the last grain boundary, GB-8 appears to be an exception. GB-8 has a soft grain #12 (Taylor factor of 2.34) adjacent to a hard grain #3, that has a Taylor factor of 4.03. According to previous observation, one would expect a hardened layer on the side of grain #12. However in this case, as seen in Figure 9, there is a significant hardened layer present on either side of the grain boundary. Interestingly, this grain boundary has a sharp curvature (See Figure 9a) and significant spread in the orientation is observed close to this sharp bend in the boundary. Although indentation tests were performed at least 500 μm away from the curvature (measured along the boundary), during bulk deformation, the presence of the curvature is likely to have affected the region of the grain boundary that was tested. Also, grain #3 is at the free surface of the sample during plane strain compression and consequently underwent significant shear. Note the significant spread in the orientation within the grain (See Figure 2). A combination of these two factors is likely to have led to GB-8 behaving differently compared to the trends seen at the other grain boundaries.

Measures of the grain orientation spread in the vicinity of the grain boundary and the calculated misorientations between the average orientations measured within the grains and in the vicinity of the boundaries (See Table 2) both seem to provide an indication of the presence of a hardened layer in the immediate vicinity of the boundary. This is not surprising because if the ‘soft’ grain is forced to undergo additional deformation in the immediate vicinity of the boundary, due to the presence of a ‘hard’ grain as in neighbor, the spread in the orientation is going to be larger due to the varying extent of deformation in the vicinity of the grain boundary. The difference in the dislocation activity in different regions near the boundary is likely to produce a larger spread in the orientations in this region. This additional deformation near the grain boundary region is also likely to change the orientation in this region as compared to the orientation within the grains and grains with a hardened boundary layer are therefore likely to have a higher degree of misorientation between orientation measured in grain and at the grain boundary regions. These measures are only indications and from Table 2 it is clear that there are exceptions to this trend. Long range interactions between neighboring grains, the stability of the

orientation with respect to the imposed deformation are probably causes for this. A more detailed investigation involving a more uniform grain size distribution within the sample, larger number of boundaries as well as one where the grain orientations are tracked during the imposed macroscopic deformation will shed more light on this matter.

Note here again that the grains in these samples were grown after the samples were cut out. As the grains grow very large during the long annealing treatment (72 hours at 640°C), the grain boundaries very close to the surfaces, will migrate very slowly and will have time to orient themselves at almost right angles to the free surface. Therefore we expect the grain boundaries we are investigating to be nominally perpendicular to the sample surface, particularly within the relatively shallow depths that we are interested in here. This was also verified by removing a top layer of about 100 μm and re-imaging the sample surface using OIM. Thus, the possibility of a grain boundary being inclined to the sample surface is very remote. Another concern in the interpretation of the observed changes in local mechanical properties near the grain boundaries is these there might be artifacts resulting from curvatures on the sample surface at the grain boundary regions due to sample preparation, particularly, electropolishing. In order to exclude this as a possibility, the topography of the sample surface around two grain boundaries of interest (GB-1 and GB-5) was imaged with a sharp Berkovich tip using Hysitron's TI 950 TriboIndenter[®] in the SPM imaging mode. For both these boundaries, it was observed that the sample surface was very smooth and that the maximum height difference at the grain boundary was ~ 8 nm and occurred within a distance of ~ 2 μm around the boundary. Any data points affected by such steps (if present) at the boundary would lie within a region of ± 1 μm from the grain boundary (grey-ed out on the plots and excluded during the analysis). This region of ± 1 μm from the boundary is also the region where the indentation zone at the point of yield might be directly intersecting the grain boundary which makes the interpretation of tests within these regions difficult.

5. Conclusions

A novel approach to characterizing the mechanical behavior of grain boundary regions in deformed polycrystalline materials using combined OIM-spherical nanoindentation is demonstrated in this study. From the regions studied around eight selected grain boundaries, it is concluded that 'soft' grains when present next to 'hard' grains harden significantly more in the immediate vicinity of the boundary. The extent of hardening increases with the increase in the

difference in the Taylor factor for the adjacent grains. In other words, spatial variations in stored energy are significant in the vicinity of the boundary when a ‘hard’ grain is present adjacent to a ‘soft’ one. However, sharp curvatures in the boundary or additional shear due to the proximity of a boundary to the free sample surface mask these trends.

References

1. Kobayashi, S., S. Tsurekawa, and T. Watanabe, *Roles of structure-dependent hardening at grain boundaries and triple junctions in deformation and fracture of molybdenum polycrystals*. Materials Science and Engineering: A, 2008. **483–484**(0): p. 712-715.
2. Zaefferer, S., et al., *On the influence of the grain boundary misorientation on the plastic deformation of aluminum bicrystals*. Acta Materialia, 2003. **51**(16): p. 4719-4735.
3. Wang, Z.G., et al., *Orientation dependence of the cyclic deformation behavior and the role of grain boundaries in fatigue damage in copper crystals*. Materials Science and Engineering: A, 2001. **319–321**(0): p. 63-73.
4. Aifantis, K.E. and J.R. Willis, *The role of interfaces in enhancing the yield strength of composites and polycrystals*. Journal of the Mechanics and Physics of Solids, 2005. **53**(5): p. 1047-1070.
5. Kalidindi, S.R., A.A. Salem, and R.D. Doherty, *Role of deformation twinning on strain hardening in cubic and hexagonal polycrystalline metals*. Advanced Engineering Materials, 2003. **5**(4): p. 229-+.
6. Li, J.C.M., *Petch relation and grain boundary sources*. Transactions of the Metallurgical Society of AIME, 1963. **227**(1): p. 239-247.
7. Petch, N.J., *Cleavage strength of polycrystals*. Iron and Steel Institute -- Journal, 1953. **174**(Part 1): p. 25-28.
8. Hall, E.O., *The deformation and ageing of mild steel III. Discussion of results*. Proceedings of the Physical Society. Section B, 1951. **64**: p. 747-753.
9. Lasalmonie, A. and J.L. Strudel, *Influence of grain size on the mechanical behaviour of some high strength materials*. Journal of Materials Science, 1986. **21**(6): p. 1837-1852.
10. Kubota, K., M. Mabuchi, and K. Higashi, *Review Processing and mechanical properties of fine-grained magnesium alloys*. Journal of Materials Science, 1999. **34**(10): p. 2255-2262.
11. Suwas, S., A. Bhowmik, and S. Biswas, *Ultra-fine Grain Materials by Severe Plastic Deformation: Application to Steels*, in *Microstructure and Texture in Steels*, A. Halder, S. Suwas, and D. Bhattacharjee, Editors. 2009, Springer London. p. 325-344.
12. Vinogradov, A., S. Hashimoto, and V.I. Kopylov, *Enhanced strength and fatigue life of ultra-fine grain Fe–36Ni Invar alloy*. Materials Science and Engineering: A, 2003. **355**(1–2): p. 277-285.
13. Vinogradov, A., *Fatigue limit and crack growth in ultra-fine grain metals produced by severe plastic deformation*. Journal of Materials Science, 2007. **42**(5): p. 1797-1808.
14. Shan, Z.W., et al., *Mechanical annealing and source-limited deformation in submicrometre-diameter Ni crystals*. Nat Mater, 2008. **7**(2): p. 115-119.
15. Uchic, M.D., et al., *Sample Dimensions Influence Strength and Crystal Plasticity*. Science, 2004. **305**(5686): p. 986-989.

16. Li, N., et al., *Compressive flow behavior of Cu thin films and Cu/Nb multilayers containing nanometer-scale helium bubbles*. Scripta Materialia, 2011. **64**(10): p. 974-977.
17. Kunz, A., S. Pathak, and J.R. Greer, *Size effects in Al nanopillars: Single crystalline vs. bicrystalline*. Acta Materialia, 2011. **59**(11): p. 4416-4424.
18. Fischer-Cripps, A.C., *A review of analysis methods for sub-micron indentation testing*. Vacuum, 2000. **58**(4): p. 569-585.
19. Fischer-Cripps, A.C., *Study of analysis methods of depth-sensing indentation test data for spherical indenters*. Journal of Materials Research, 2001. **16**: p. 1579-84.
20. Fischer-Cripps, A.C., *Nanoindentation*. Mechanical Engineering Series, ed. F.F. Ling. 2002, New York: Springer.
21. Fischer-Cripps, A.C., *Critical review of analysis and interpretation of nanoindentation test data*. Surface and Coatings Technology, 2006. **200**(14–15): p. 4153-4165.
22. Shraddha J. Vachhani, S.R.K., *Grain-Scale Measurement of Slip Resistances in Aluminum Polycrystals using Spherical Nanoindentation* Acta Materialia, 2015. Submitted.
23. Pathak, S., et al., *Studying grain boundary regions in polycrystalline materials using spherical nano-indentation and orientation imaging microscopy*. Journal of Materials Science, 2012. **47**(2): p. 815-823.
24. Tabor, D., *The hardness of metals*. 1951: Clarendon Press, Oxford University Press. ix + 176.
25. Bucaille, J.L., et al., *Determination of plastic properties of metals by instrumented indentation using different sharp indenters*. Acta Materialia, 2003. **51**(6): p. 1663-1678.
26. Rho, J.-Y., T.Y. Tsui, and G.M. Pharr, *Elastic properties of human cortical and trabecular lamellar bone measured by nanoindentation*. Biomaterials, 1997. **18**(20): p. 1325-1330.
27. Poole, W.J., M.F. Ashby, and N.A. Fleck, *Micro-hardness of annealed and work-hardened copper polycrystals*. Scripta Materialia, 1996. **34**(4): p. 559-564.
28. Oliver, W.C. and G.M. Pharr, *Improved technique for determining hardness and elastic modulus using load and displacement sensing indentation experiments*. Journal of Materials Research, 1992. **7**(6): p. 1564-1580.
29. Oliver, W.C. and G.M. Pharr, *Measurement of hardness and elastic modulus by instrumented indentation: Advances in understanding and refinements to methodology*. Journal of Materials Research, 2004. **19**: p. 3-20.
30. Li, X. and B. Bhushan, *A review of nanoindentation continuous stiffness measurement technique and its applications*. Materials Characterization, 2002. **48**(1): p. 11-36.
31. Kalidindi, S.R. and S. Pathak, *Determination of the effective zero-point and the extraction of spherical nanoindentation stress-strain curves*. Acta Materialia, 2008. **56**: p. 3523-32.
32. Hertz, H., *Miscellaneous Papers*. New York: MacMillan and Co., Ltd, 1896.
33. Johnson, K.L., *Indentation Contact Mechanics*. 1985: Cambridge University Press, Cambridge.
34. Sneddon, I.N., *Relation between load and penetration in axisymmetric Boussinesq problem for punch of arbitrary profile*. International Journal of Engineering Science, 1965. **3**: p. 47-57.
35. Pathak, S., et al., *Importance of surface preparation on the nano-indentation stress-strain curves measured in metals*. Journal of Materials Research, 2009. **24**: p. 1142-55.

36. Pathak, S., D. Stojakovic, and S.R. Kalidindi, *Measurement of the local mechanical properties in polycrystalline samples using spherical nanoindentation and orientation imaging microscopy*. Acta Materialia, 2009. **57**: p. 3020-8.
37. Gene Simmons, H.W., *Single Crystal Elastic Constants and Calculated Aggregate Properties*. 1971, Cambridge MIT Press.
38. Bunge, H., *Texture Analysis in Materials Science*. Butterworths, 1982.
39. Pathak, S., et al., *Studying grain boundary regions in polycrystalline materials using spherical nano-indentation and orientation imaging microscopy*. Journal of Materials Science, 2012. **47**(2): p. 815-823.
40. Meyers MA, A.E., *A model for the effect of grain size on the yield stress of metals*. Philosophical Magazine A, 1982. **46**: p. 737.

Figures

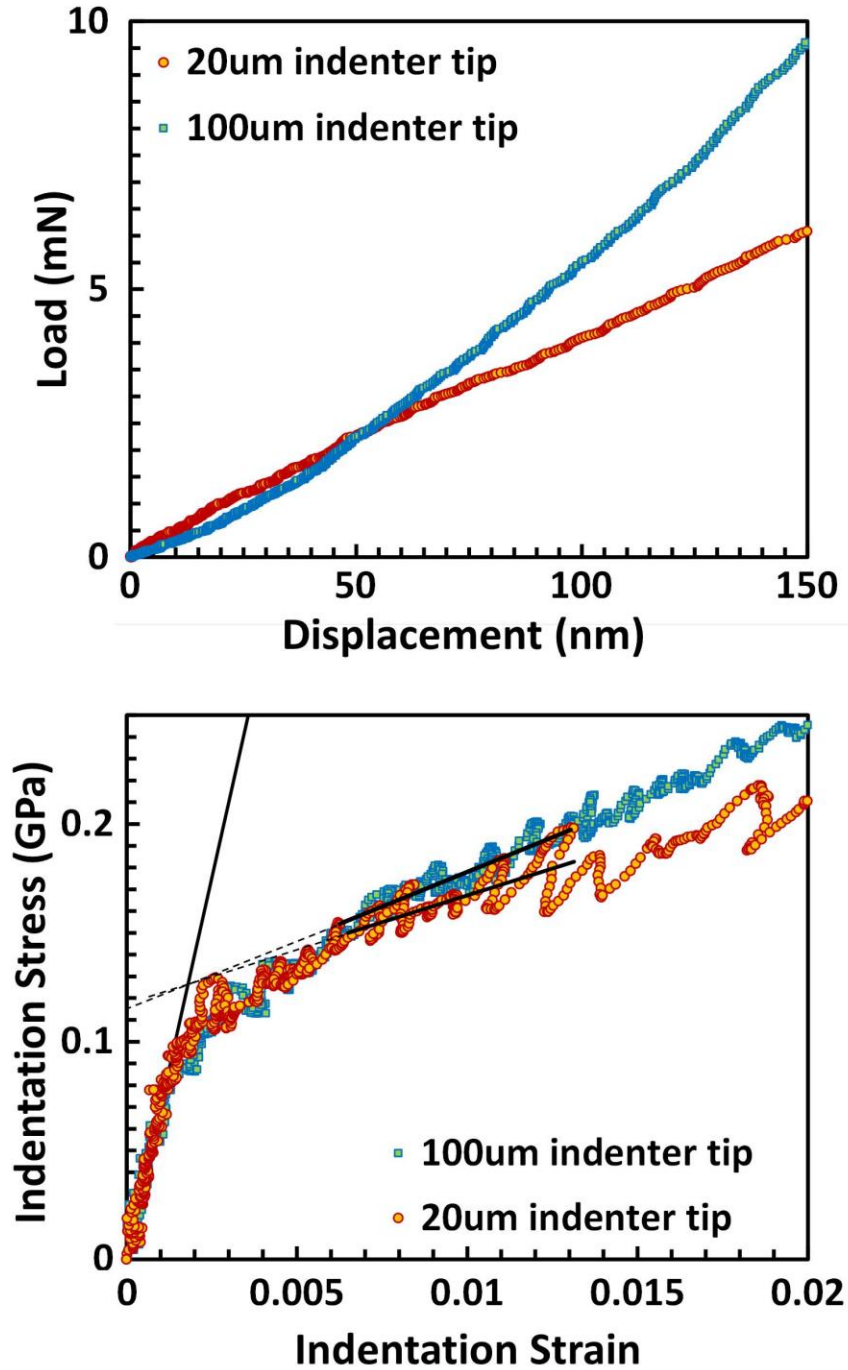


Figure 1: Representative (a) Load-displacement and (b) ISS curves for tests performed with the 20um and 100um spherical indenter tip showing that the extracted Y_{ind} values are not effected by the indenter tip size

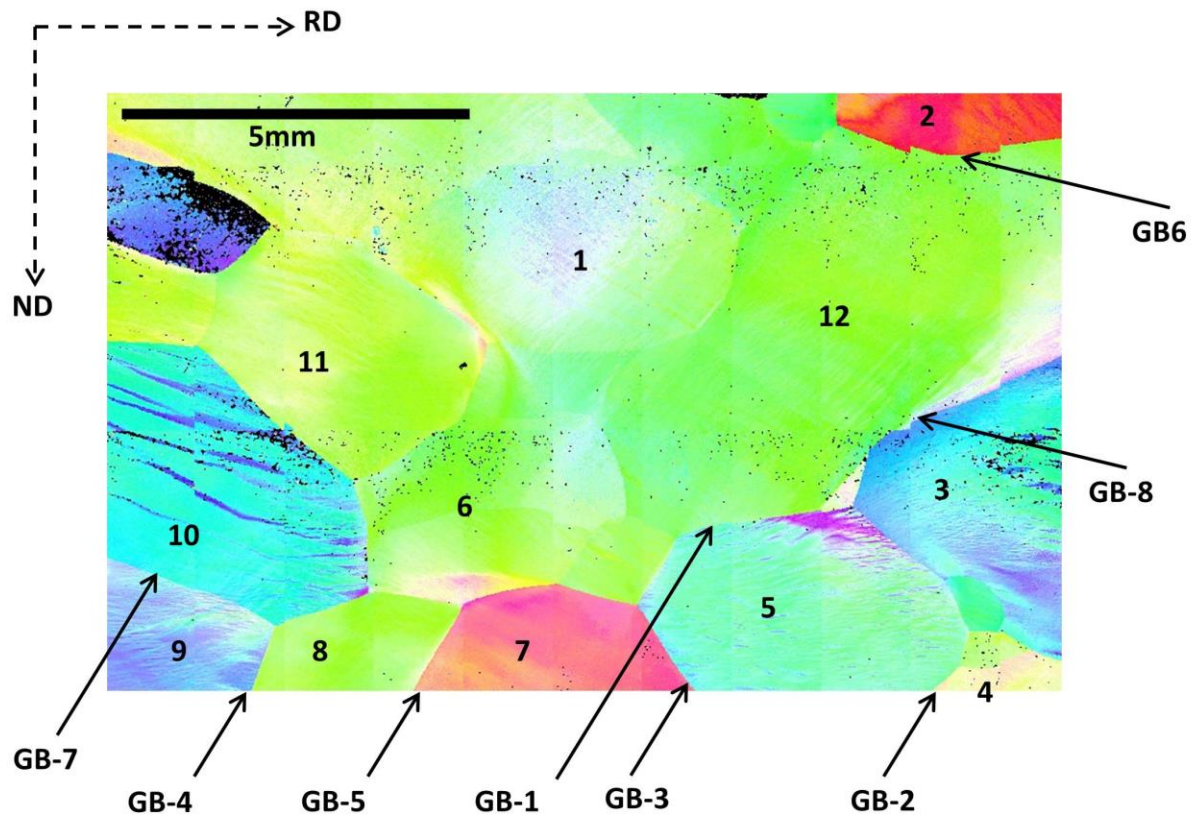


Figure 2: OIM map of the sample deformed to 20% reduction in height, by plane strain compression showing the grain boundaries studied using nanoindentation. (Note that the discontinuities seen in grain boundaries 6 (GB-6) and 8 (GB-8) are only artifacts that show up as the OIM image is a composite of many small scans)

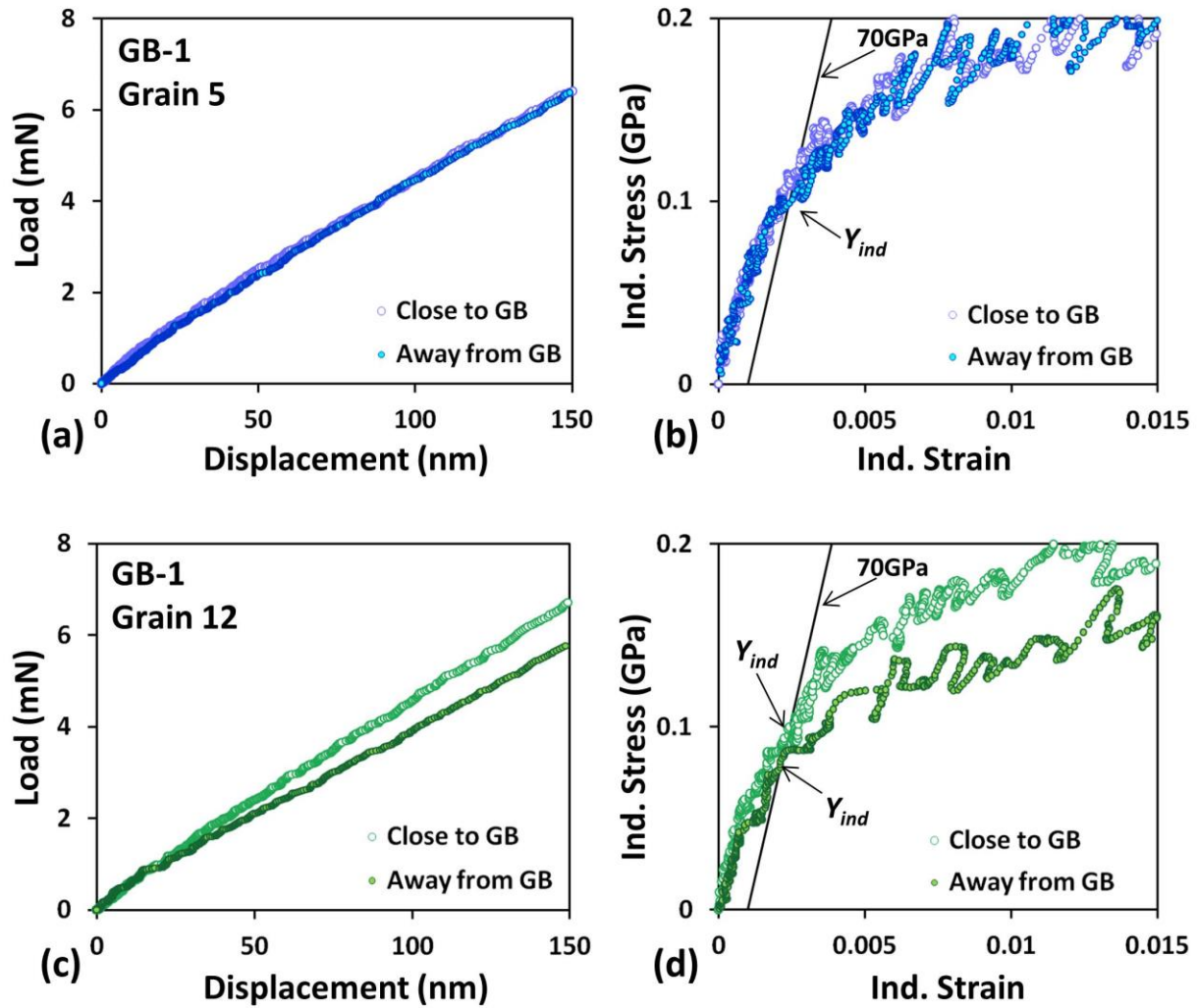


Figure 3: Representative (a) and (c) load-displacement curves and (b) and (d) corresponding indentation stress-strain curves obtained for grains #5 and #12 respectively, adjoining the grain boundary 1 (GB-1). The open circles represent data from close to the boundary ($\sim 8 \mu\text{m}$) and the closed circles represent data obtained away from the boundary ($\sim 40\text{-}50 \mu\text{m}$).

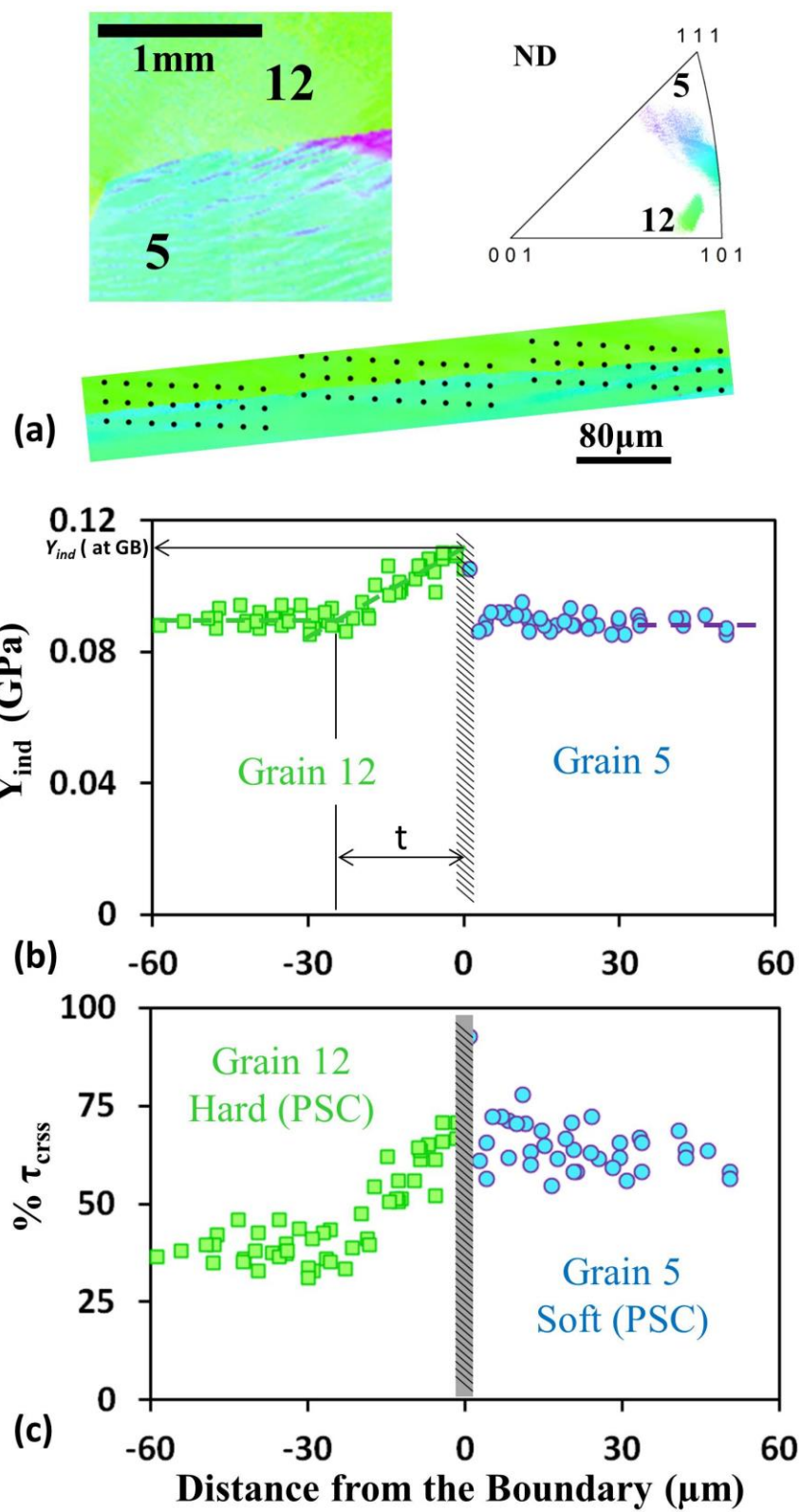


Figure 4: (a) Crystallographic details of grain boundary 1 (GB-1) and the location of indents across the boundary. (b) The measured Y_{ind} across GB-1 between grain #12 and #5. (c) Percentage change in the Y_{ind} , with respect to the annealed condition.

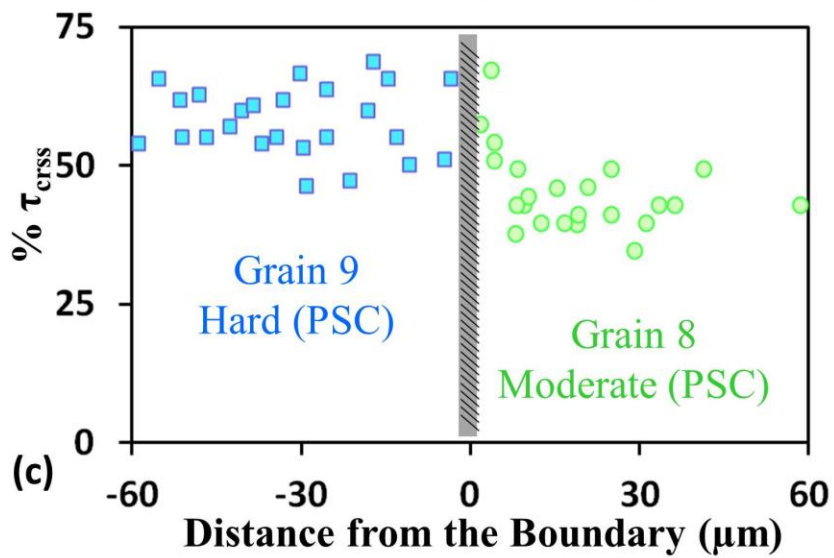
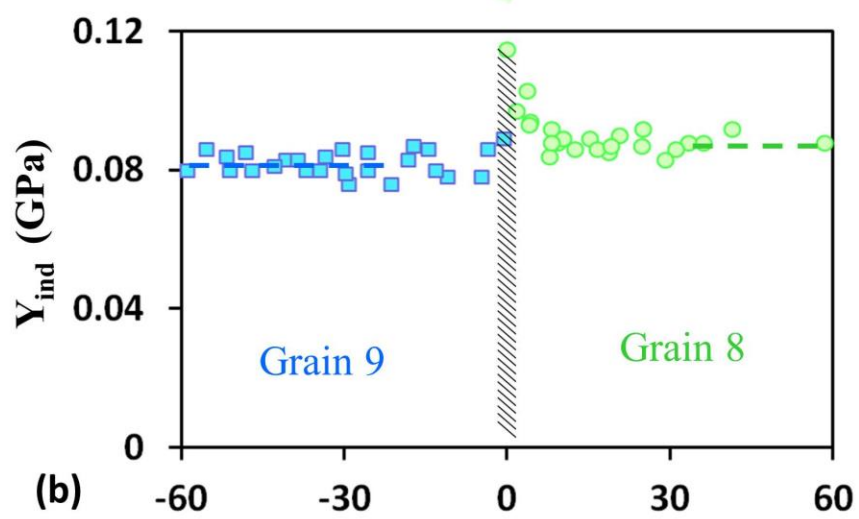
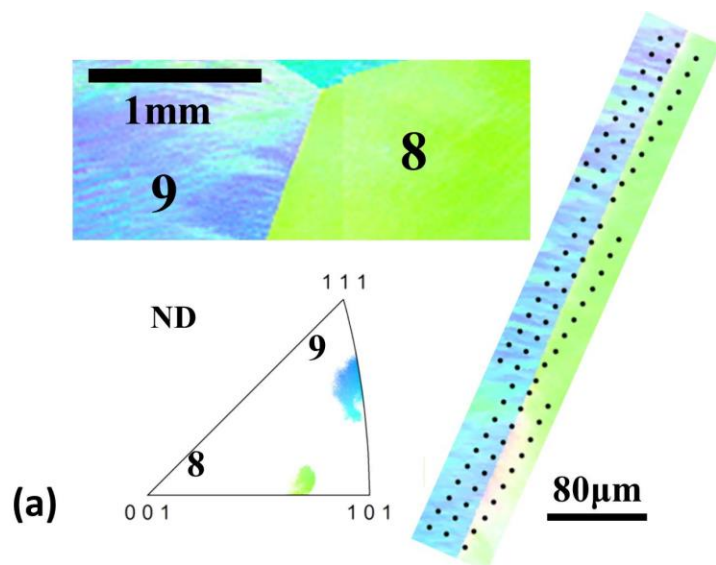


Figure 5: (a) Crystallographic details of the grain boundary 4 (GB-4) and the location of indents across the boundary. (b) The measured Y_{ind} across GB-4 between grain #9 and #8. (c) Percentage change in the Y_{ind} , with respect to the annealed condition.

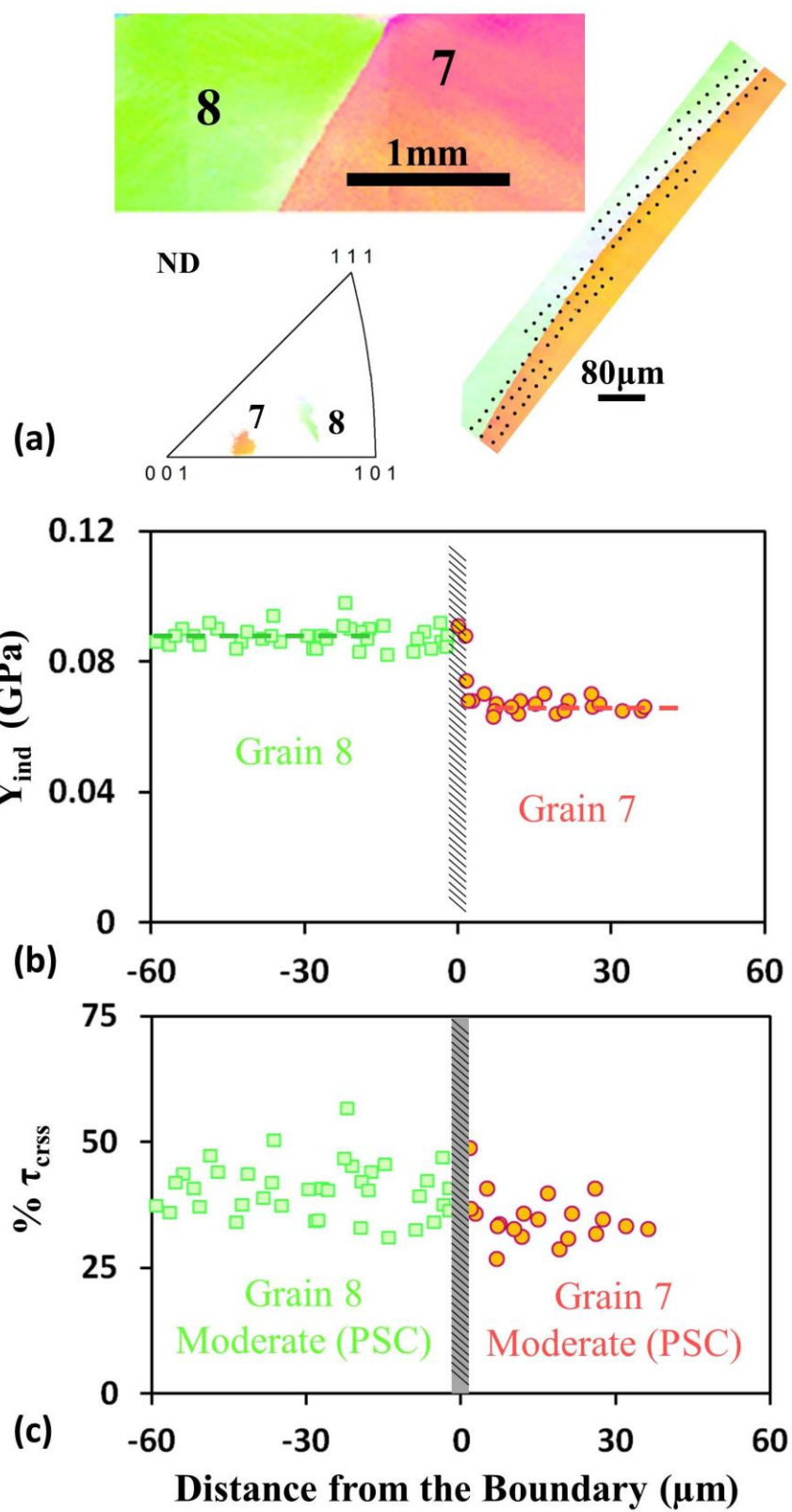


Figure 6: (a) Crystallographic details of the grain boundary 5 (GB-5) and the location of indents across the boundary. (b) The measured Y_{ind} across GB-5 between grain #8 and #7. (c) Percentage change in the Y_{ind} , with respect to the annealed condition.

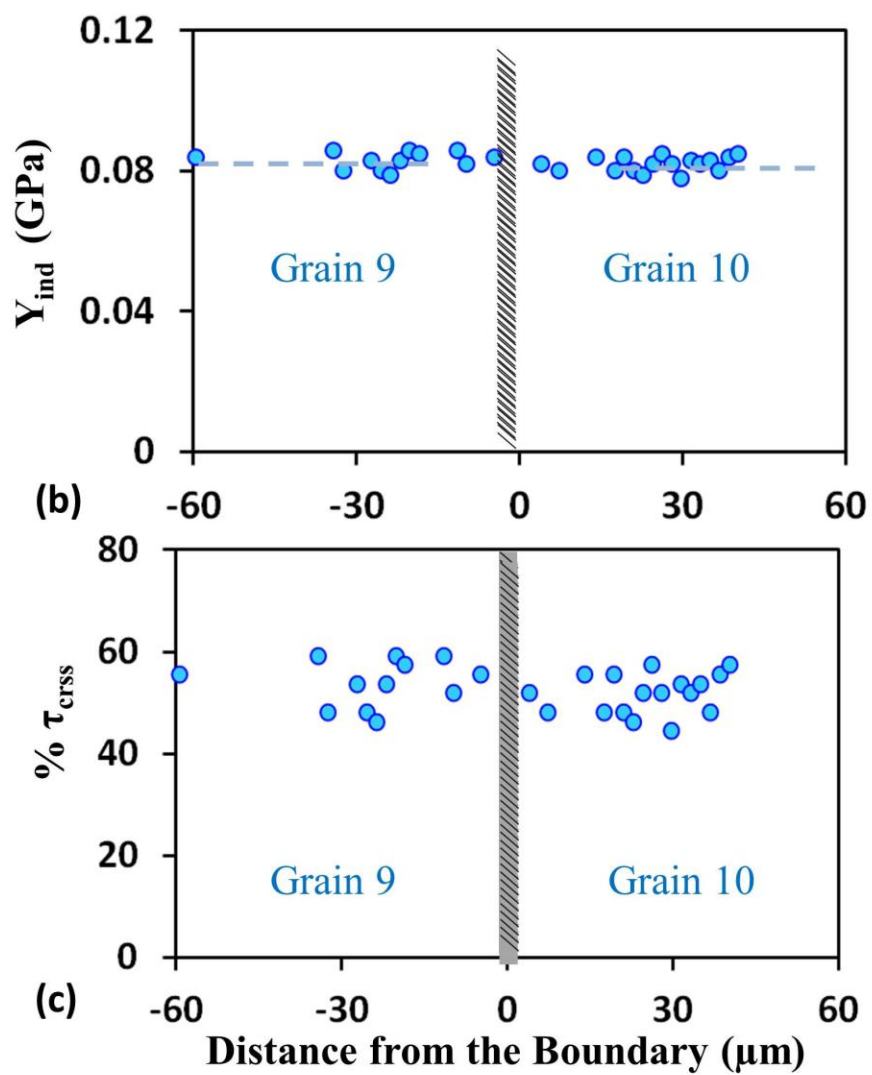
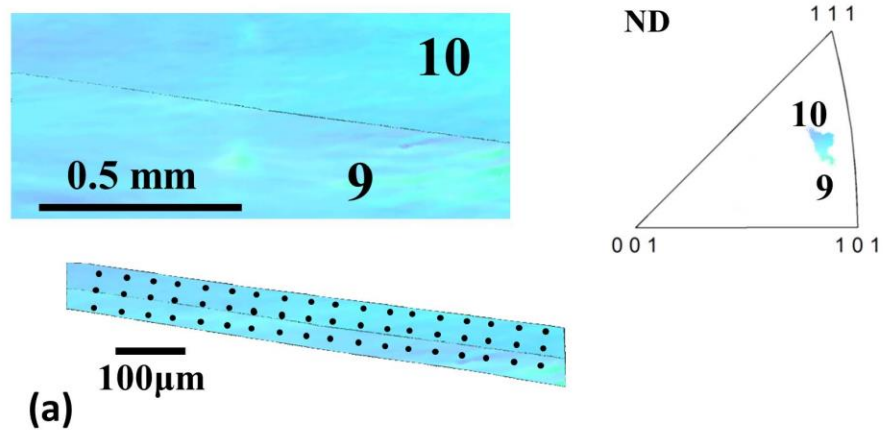


Figure 7: (a) Crystallographic details of the grain boundary 7 (GB-7) and the location of indents across the boundary. (b) The measured γ_{ind} across GB-1 between grain #9 and #10. (c) Percentage change in the γ_{ind} , with respect to the annealed condition. Note that this is a low angle grain boundary (All other boundaries studies are high angle boundaries).

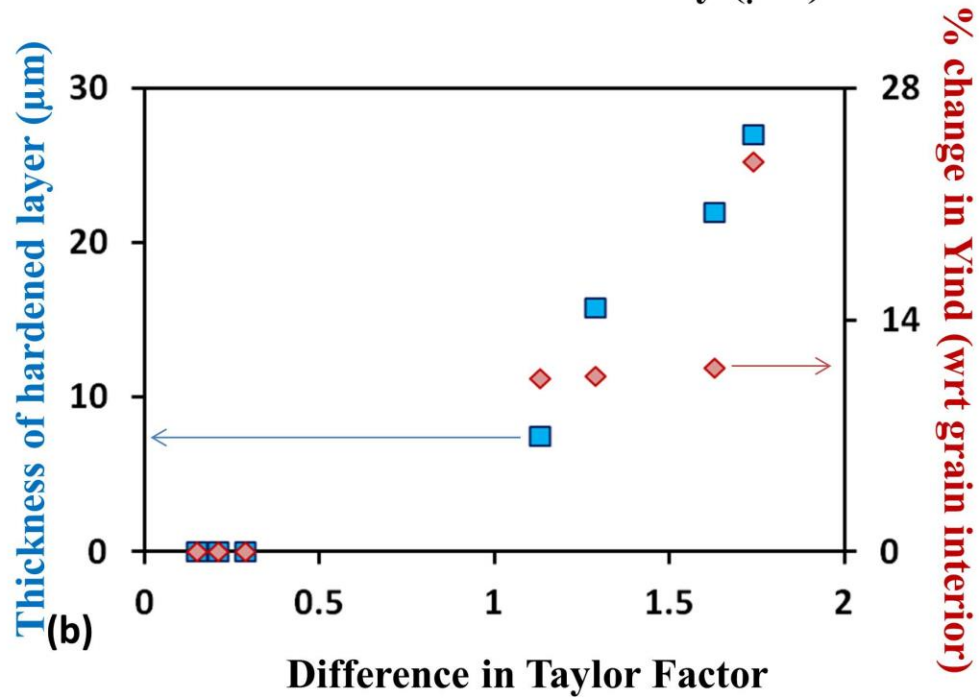
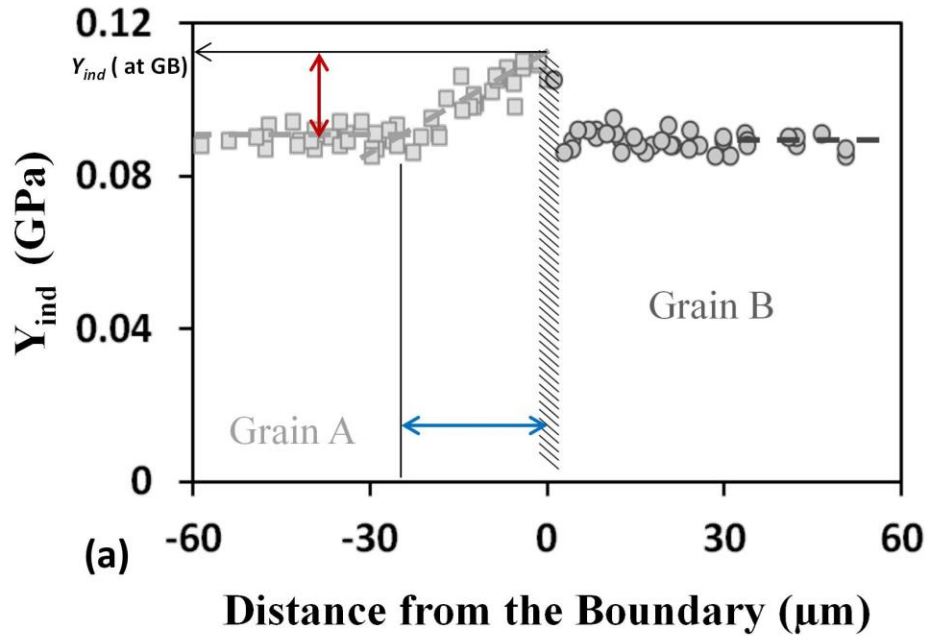


Figure 8: (a) Schematic of Y_{ind} vs. distance from the GB plot, showing the definitions of the hardening parameters used in (b). (b) The variation of the thickness of the hardened layer and the percentage increase in the indentation yield strength (with respect to the grain interior) for the 'soft' grain for 7 grain boundaries (GB-1 to GB-7) as a function of the difference in the Taylor factor for the two grain across the boundary.

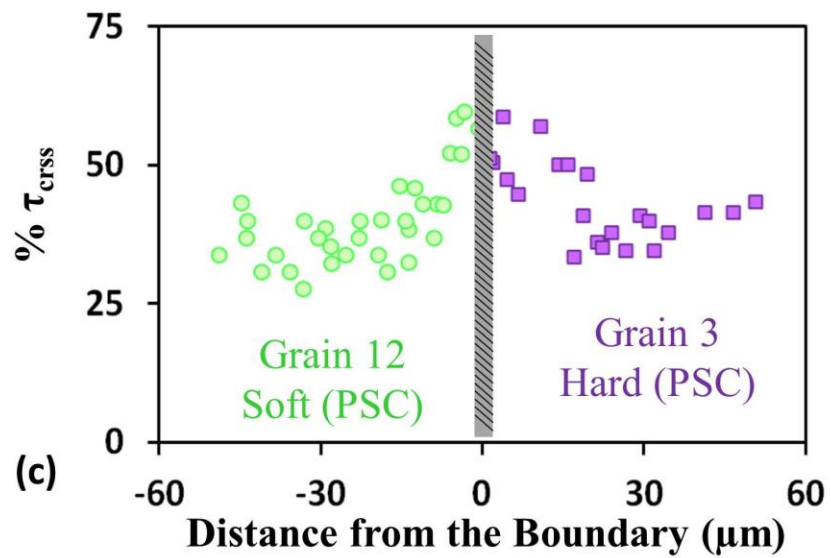
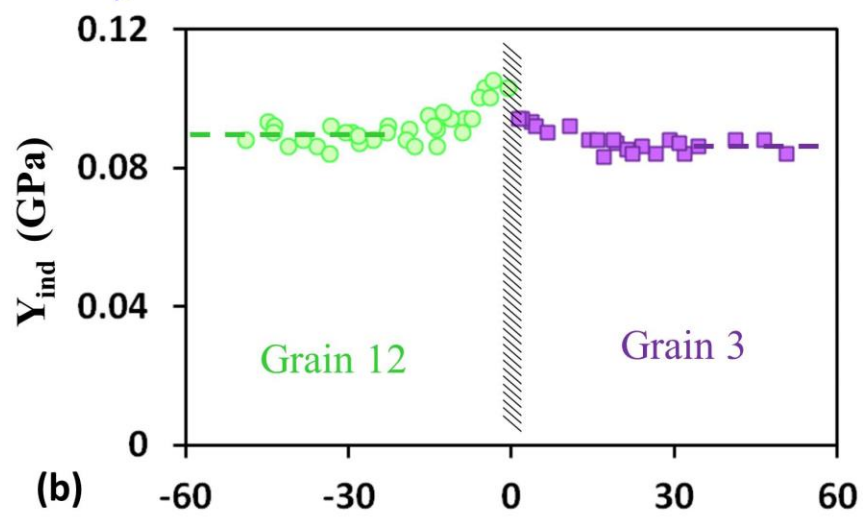
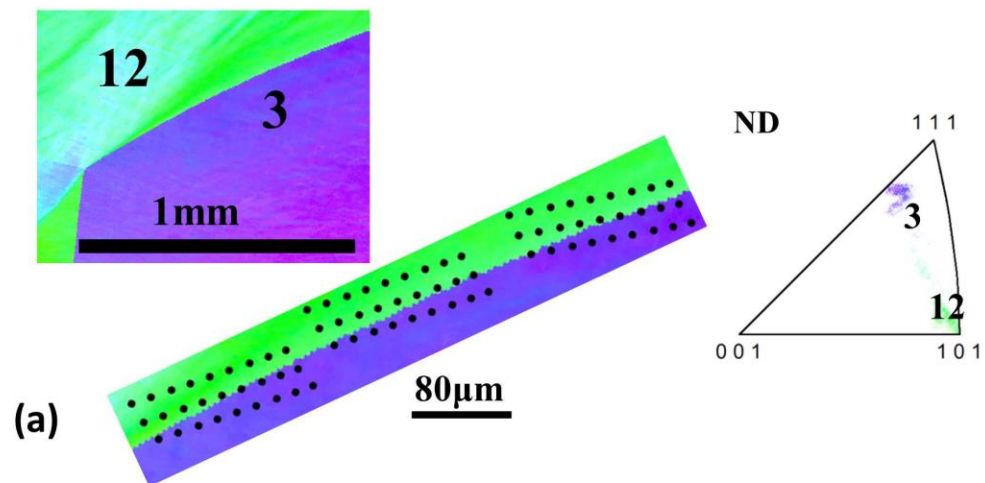


Figure 9: (a) Crystallographic details of the grain boundary 8 (GB-8) and the location of indents across the boundary. (b) The measured Y_{ind} across GB-5 between grain #12 and #3. (c) Percentage change in the Y_{ind} , with respect to the annealed condition.

Tables

Grain Boundary	Δg across GB	Grain No.	Average Orientation			Taylor Factor	GOS	Yind	Predicted Yind (undef)
	(°)		$\phi 1$	Φ	$\phi 2$				
GB-1	46.5	5	116.4	45.3	249.5	4.55	2.39	0.09	0.049
		12	149.1	40.1	176.1	2.80	1.82	0.089	0.066
GB-2	47.3	4	132.9	28.6	260.7	3.02	1.82	0.09	0.064
		5	69	42.7	286.1	4.65	2.37	0.09	0.049
GB-3	33.1	5	269.4	43.3	74.8	4.66	2.11	0.088	0.049
		7	110	25.3	245.8	3.37	1.54	0.066	0.048
GB-4	52	9	64.4	38.5	293.3	4.24	2.47	0.083	0.053
		8	144.4	33.1	255.2	3.11	3.02	0.0887	0.065
GB-5	39.1	7	91.9	17.4	275.5	3.37	1.78	0.067	0.048
		8	144.8	33.4	255.8	3.08	2.39	0.088	0.065
GB-6	29.6	2	143.9	7	184.9	2.34	2.28	0.087	0.063
		12	151.7	36.2	173.3	2.55	1.88	0.089	0.066
GB-7	11.8	8	117.5	41.5	245.7	3.97	0.085	0.082	0.053
		9	268.8	43	114.6	4.12	1.05	0.082	0.054
GB-8	45.6	3	210.3	42.3	138.6	4.03	2.65	0.085	0.056
		12	135.4	48.3	189.5	2.34	7.4	0.088	0.066

Table 1: Summary of OIM and nanoindentation measurements away from the grain boundaries, for the 8 grain boundaries studied in this work: Misorientation across the boundary, average grain orientation (with respect to the macroscopic deformation axes), Taylor factor and grain orientation spread (GOS) of each of the grains, the measured Y_{ind} away from the grain boundary and the predicted Y_{ind} for the orientation in the fully annealed condition

Grain Boundary	Δg across GB	Grain No.	Average Orientation			Taylor Factor	GOS	Δg from center to GB	Yind (undef)	Yind (at GB)	Thickness of Hardened layer
			$\phi 1$	Φ	$\phi 2$						
GB-1	46.5	5	117.6	46.1	249	4.51	2.65	1.2	0.054	0.09	0
		12	155.3	39.8	170.5	2.64	1.35	3.6	0.066	0.11	27
GB-2	47.3	4	132.9	28.6	260.7	3.02	2.14	1.9	0.062	0.1	22
		5	69	42.7	286.1	4.65	2.18	1.3	0.048	0.09	0
GB-3	35.2	5	272.6	42.8	71.5	4.52	1.41	2.4	0.049	0.088	0
		7	111.3	25.5	244.6	3.41	1.47	0.6	0.049	0.073	16
GB-4	52	9	63	39.2	295.4	4.19	2.33	1.2	0.052	0.083	0
		8	144.22	32.2	254.3	3.11	2.45	1.3	0.065	0.098	7.5
GB-5	39.1	7	88.6	17.8	278.1	3.38	1.71	1.2	0.045	0.067	0
		8	148.2	32.3	251.1	3.11	2.11	2.5	0.066	0.088	0
GB-6	29.6	2	157.7	6.6	170.5	2.37	1.88	1.8	0.061	0.087	0
		12	147.2	37	178.5	2.74	1.49	3.1	0.066	0.089	0
GB-7	12.1	8	117.8	41.5	245.4	4.00	0.81	0.2	0.053	0.082	0
		9	268.4	42.6	114.9	4.08	0.88	0.6	0.055	0.082	0
GB-8	45.6	3	212.1	44.1	138.8	3.48	1.55	2.7	0.063	0.095	20
		12	144.1	44.7	180.3	3.09	5.92	7.9	0.066	0.104	17

Table 2: Summary of OIM and nanoindentation measurements near the grain boundary region, for the 8 grain boundaries studied in this work: Misorientation across the boundary, average crystal orientation (with respect to the macroscopic deformation axes), misorientation across the grain boundary, Taylor factor and grain orientation spread (GOS) on either side of the boundary, the predicted Y_{ind} for the orientation in the fully annealed condition, the extrapolated Y_{ind} at grain boundary and the thickness of the hardened layer after which the Y_{ind} is equal to that measured within the grain

Appendix C: Spherical Nanoindentation Stress-Strain Curves

Siddhartha Pathak¹, Surya R. Kalidindi^{2}*

¹ Center for Integrated Nanotechnologies, Los Alamos National Laboratory, Los Alamos, NM, 87545, USA

² George W. Woodruff School of Mechanical Engineering, Georgia Institute of Technology, Atlanta, Georgia, GA, USA

Abstract

Although indentation experiments have long been used to measure the hardness and modulus, the utility of this technique in analyzing the complete elastic-plastic response of materials under contact loading has only been realized in the past few years – mostly due to recent advances in testing equipment and analysis protocols. This paper provides a timely review of the recent progress made in this respect in extracting meaningful indentation stress-strain curves from the raw datasets measured in instrumented spherical nano-indentation experiments. These indentation stress-strain curves have produced highly reliable estimates of the indentation modulus and the indentation yield strength in the sample, as well as certain aspects of their post-yield behavior, and have been critically validated through numerical simulations using finite element models as well as direct *in-situ* scanning electron microscopy (SEM) measurements on

*Contact author: - George W. Woodruff School of Mechanical Engineering, Georgia Institute of Technology, Atlanta, Georgia, GA, USA, Tel: 404.385.2886

E-mail: surya.kalidindi@me.gatech.edu, Website: <http://mined.gatech.edu/>

micro-pillars. Much of this recent progress was made possible through the introduction of a new measure of indentation strain and the development of new protocols to locate the effective zero-point of initial contact between the indenter and the sample in the measured datasets. This has led to an important key advance in this field where it is now possible to reliably identify and analyze the initial loading segment in the indentation experiments.

Major advances have also been made in correlating the local mechanical response measured in nano-indentation with the local measurements of structure at the indentation site using complementary techniques. For example, it has been shown that the combined use of orientation imaging microscopy (OIM) and nanoindentation on polycrystalline metallic samples can yield important information on the orientation dependence of indentation yield stress, which can in turn be used to estimate percentage increase in the local slip resistance in deformed samples. The same methods have been used successfully to probe the intrinsic role of grain boundaries in the overall mechanical deformation of the sample. More recently, these protocols have been extended to characterize local mechanical property changes in the damaged layers in ion-irradiated metals. Similarly, the combined use of Raman spectroscopy and nanoindentation on samples of mouse bone has revealed tissue-level correlations between the mineral content at the indentation site and the associated local mechanical properties. The new protocols have also provided several new insights into the buckling response in dense carbon nanotube (CNT) brushes. These and other recent successful applications of nanoindentation are expected to provide the critically needed information for the maturation of physics-based multiscale models for the mechanical behavior of most advanced materials. In this paper, we review these latest developments and identify the future challenges that lie ahead.

Keywords

Nanoindentation; Orientation Imaging Microscopy (OIM); Polycrystalline metals; Slip resistance; Grain boundaries; Pop-ins; Raman Spectroscopy

Table of Contents

Spherical Nanoindentation Stress-Strain Curves	1
Abstract	1
Keywords	3
Table of Contents	3
1. Introduction.....	5
2. Classical Indentation Theories and Analyses Methods	8
3. Indentation Stress and Strain Measures	12
4. Finite Element Models for Computing Indentation Stress-Strain Curves	15
5. Indentation Stress-Strain curves – Experimental Analysis Techniques	18
5.1 Indentation Stress-Strain Curves using Continuous Stiffness Measurement (CSM) data.....	18
5.2 Indentation Stress-Strain Curves without CSM.....	26
5.3 Effect of Surface Preparation in Indentation Stress-Strain Curves Analysis	31
5.4 Pop-in Events	34
5.5 Effect of the Continuous Stiffness Measurement on Indentation Stress-Strain Curves Analysis	42
6. Applications: Combined OIM - Indentation Studies on Metallic Samples	47
6.1 Quantifying Elastic and Plastic Anisotropy of Single Crystals	50

6.2 Estimating Local Slip Resistance in Deformed Cubic Crystals.....	53
6.3 Investigations of Grain Boundary Regions	56
6.4 Investigations of Surface Modifications	59
6.5 Comparing with Micro-pillar Compression Experiments.....	63
7. Applications: Combined Raman Spectroscopy-Indentation Studies on Bone..	65
8. Applications to Vertically Aligned Carbon Nanotube (VACNT) Brushes	72
9. Summary and Future Trends.....	76
Acknowledgements.....	81
References	81
Figure captions.....	90

1. Introduction

For more than a century, the indentation test has been one of the most commonly employed techniques for characterization of the mechanical properties of a vast range of materials [1, 2]. In a typical test, a hard indenter of known geometry is driven into a softer sample by applying a preset load or displacement. The dimensions of the resultant imprint are then measured and correlated to a hardness index number. With the advent of higher resolution testing equipment, it has now become possible to continuously control and monitor the loads and displacements of the indenter as it is driven into and withdrawn from a sample material. Known as nanoindentation (or instrumented indentation testing, or depth sensing indentation), this significantly expands the capabilities of the traditional hardness testing method [3, 4]. Instrumented indentation has significant advantages over conventional indentation testing, since it can potentially produce very reliable measurements of stress-strain curves from fairly small indentation depths (of the order of a few nanometers).

The popularity of indentation tests stems in part from its versatility, ease of use (see Fig. 1), and its potential for high throughput. This is in contrast to most of the other currently used methods for interrogating the local mechanical properties at micron and sub-micron length scales that rely largely on testing miniaturized samples in nominally homogeneous deformation/stress modes [5]. For example the compression testing of micro-pillars produced by removing material around a selected region of interest using a focused-ion beam (FIB) has attracted the recent attention of many researchers [6]. However these techniques typically require tremendous resources in terms of sample preparation, test conditions and operator time, which make their large scale use uneconomical. On the other hand nanoindentation, when aided with proper analysis methods, is capable of producing the desired information at significantly lower effort

and cost. Moreover, reliable and quantitative measurement of mechanical degradation of surface layers (e.g., ion-irradiated materials in nuclear applications) is currently only possible with indentation techniques. This high throughput methodology when used in conjunction with structure information measured locally at the indentation site has the potential to become a key tool in efforts aimed at the maturation of physics-based multiscale materials models.

A common limitation in a majority of the indentation analysis methods used today is that the estimation of material properties, such as modulus and hardness, are typically made from the measured unloading segments of load-displacement curves (after some amount of elastic-plastic loading) under the assumption that the unloading segments are predominantly elastic [7, 8]. In this approach, the plastic deformation induced during the loading segment is likely to influence strongly the values of the mechanical properties (e.g., hardness) extracted from these experiments. This problem has been recognized since the early 1890s and numerous attempts have been made to measure the ‘absolute hardness’ of a material [9]. However, quantitative estimates of absolute hardness, generally defined as “resistance to permanent deformation” [10] or “the intensity of the maximum pressure which just produces yielding” in indentation [11], have not been feasible before the advent of modern instrumented test methods.

In this review, we focus on a fundamentally different approach to this problem that has enjoyed tremendous success in recent years. This new approach relies heavily on new data analyses procedures for spherical nanoindentation that transform the entire load-displacement dataset, including both the loading and the unloading segments, into much more meaningful indentation stress-strain curves [12, 13]. The use of these indentation stress-strain curves makes it possible to analyze the initial loading segments of spherical indentation, thereby allowing reliable measures of elastic modulus and indentation yield strength of the material prior to the

changes induced by the indentation itself. The ability to produce indentation stress-strain curves has generally been more successful with spherical indenters [14-16], where their relatively smoother stress fields and larger initial elastic segments (compared to sharper indenters) allow one to follow the evolution of the mechanical response in the material, from initial elasticity to the initiation of plasticity to post-yield behavior at finite plastic strains.

This review summarizes the main developments and advances in recent years in the protocols used to generate spherical indentation stress-strain curves. We begin with a description of the recently developed methodology used for extracting indentation stress-strain curves from the corresponding indentation load-displacement data, which include a novel approach for determining the ‘zero-point’ in spherical nanoindentation experiments and a new definition of indentation strain. These concepts are then critically validated through numerical simulations using finite element models as well as direct *in-situ* scanning electron microscopy (SEM) measurements on micro-pillars. Next, we describe a series of applications covering a wide variety of material systems including metallic materials, thin films of dense carbon nanotube (CNT) brushes, and complex hierarchical biological materials (e.g., bone). These applications illustrate the versatility and utility of the indentation stress-strain curves in extracting mechanical information at the micron to sub-micron level. Another salient feature of the case studies described here is that the mechanical information obtained from these tests are correlated to the corresponding local structure information (obtained using complementary characterization techniques such as orientation imaging microscopy (OIM), which images the microstructure using electron backscattered diffraction (EBSD) for crystalline samples, and Raman spectroscopy, which is highly sensitive to both mineral and collagen components of biological tissues such as bone) at similar length scales in the samples.

2. Classical Indentation Theories and Analyses Methods

The most widely used indentation theories are all based on Hertz's model [17] for frictionless contact between two isotropic elastic solids. For spherical indentation, this is usually expressed as

$$P = \frac{4}{3} E_{eff} R_{eff}^{1/2} h_e^{3/2}, \quad a = \sqrt{R_{eff} h_e} \quad (1)$$

where a is the radius of the contact boundary at the indentation load P , and h_e is the elastic indentation depth (see Fig. 2a for definitions of various variables used in Eq. (1)). R_{eff} and E_{eff} denote the effective radius and the effective modulus of the indenter and the specimen system, respectively:

$$\frac{1}{E_{eff}} = \frac{1-\nu_s^2}{E_s} + \frac{1-\nu_i^2}{E_i}, \quad \frac{1}{R_{eff}} = \frac{1}{R_i} + \frac{1}{R_s}. \quad (2)$$

Here, ν and E denote the Poisson's ratio and the Young's modulus, while subscripts s and i refer to the specimen and the indenter, respectively. For elastic loading of a flat sample, R_s approaches infinity, and therefore, $R_{eff} = R_i$.

In practice, the initial elastic loading segments in experimentally measured spherical nanoindentation datasets are very short (typically only a few tens of nanometers of indentation depth). Moreover, the many uncertainties associated with identifying the start and the end of the purely elastic segments in these measurements pose major hurdles in successfully analyzing these segments in the nanoindentation measurements. Consequently, much of the effort in the literature has focused on applying the Hertz's theory (Eqs. (1) and (2)) to the unloading segment (generally presumed to be purely elastic) in the measured load-displacement data. Although the unloading segment is likely to be purely elastic in many materials (confirmed by finite element

models [18]), the main complication in the analyses of the unloading segment stems from lack of knowledge of the residual geometry of the sample surface upon complete unloading since it would have been altered substantially by the inelastic deformation imposed during the loading segment (see Fig. 2b). For the case of sharp indenters, successful analysis of the unloading segment using Hertz's theory has required the use of calibrated area functions and effective indenter shapes [7, 8] to take into account the complex changes in the sample surface geometry caused by the inelastic strains induced during the loading segment.

The analysis of the unloading segment in spherical indentation using Hertz's model leads to the following equations [7, 19]:

$$E_{eff} = \frac{\sqrt{\pi}}{2} \frac{S}{\sqrt{A_c}} = \frac{S}{2a}, \quad A_c = \pi a^2 \quad (3)$$

The value of the contact radius is then generally estimated using the geometry of the spherical indenter as

$$a = \sqrt{2h_c R_i - h_c^2}, \quad h_c = h_t - \frac{3}{4} \frac{P}{S} \quad (4)$$

where S is the slope of the unloading curve (see Fig. 2b) at the peak indentation load (P), A_c is the projected contact area, h_c is the distance from the circle of contact to the maximum penetration depth, and h_t is the total penetration depth at peak load. Note that the two definitions of the contact radius in Eqs. (1) and (4) may not provide consistent results. We shall revisit this in much more detail later. Although Eqs. (2) – (4) have been used extensively to estimate the elastic moduli [3, 7, 8, 20, 21], the real interest in indentation measurements is in estimating the plastic properties of the sample.

Brinell [22-24] and Vickers [25] tests introduced the basic concepts of hardness measurements using spherical and sharp indenters, respectively. A number of hardness measures

were introduced along with these tests that define hardness as the load divided either by the surface area or the projected area of the residual indentation. These hardness measures were found to be extremely valuable in quickly assessing the resistance to plastic deformation in a range of materials, and fine-tuning their thermo-mechanical processing histories to improve their mechanical performance. Furthermore, some of the hardness measures showed a strong correlation to properties measured in standard tension tests such as the ultimate tensile strength. In spite of these advantages, hardness measurements continue to be used mainly as comparative measures because the hardness numbers themselves are quite sensitive to indenter shape, indenter size, and the imposed load level.

As a natural extension of the hardness measurements, Tabor [1] introduced the concept of indentation stress-strain curves. The indentation stress was defined as the mean contact pressure (load divided by projected area of residual indentation; also called Meyer's hardness [26]). The indentation strain was invoked to be $0.2a/R_i$. It is important to note that in Tabor's approach the contact radius was measured directly from the residual indentation in the sample. Therefore, one indentation would produce only one data point on the indentation stress-strain curve. Consequently, a substantial effort is required for extracting a complete indentation stress-strain curve using Tabor's original approach. Tabor [27] demonstrated an excellent correspondence between indentation stress-strain curves (by accumulating data obtained using different indenter radii) and those obtained from standard simple tension tests on mild steel and annealed copper (see Fig 3a).

There have been several efforts in the literature to automate the extraction of multiple data points on the indentation stress-strain curve from a single indentation experiment [15, 28, 29]. Field and Swain [15, 29, 30] developed novel protocols that utilized multiple partial unloads

and estimated the contact radius directly from the measurements of the load and the displacement in each such partial unload (Fig 3b). In their approach, each partial unload is assumed to be purely elastic and is analyzed using Hertz's theory to estimate the contact radius (instead of direct measurement from the residual indentation as performed by Tabor). It should be noted that the estimate of the contact radius based on Hertz's theory corresponds to the value of the contact radius in the loaded geometry, whereas the direct measurement performed by Tabor [1] corresponds to the contact radius estimated from the unloaded geometry. Consequently, there might be a substantial difference in the values of the contact radius obtained using these two approaches. The approach proposed by Field and Swain [15, 29] is attractive because it can be automated with modern instrumentation. Furthermore, extensions have been proposed in literature [29] to these protocols to account for the changes in contact geometry that occur due to the pile-ups and sink-ins associated in the indentation measurements.

A characteristic feature in the indentation stress-strain curves reported in literature (obtained using the methods described above) is the relatively large elastic-plastic transition in these curves [15, 31, 32]. In general, the elastic-plastic transition is observed to occur over the range of values of indentation stress corresponding to $1.1 \sigma_y$ and $3 \sigma_y$, where σ_y is the uniaxial plastic yield strength for the sample material. This large elastic-plastic transition misrepresents a fairly large section of the indentation stress-strain curve as exhibiting high levels of strain hardening (i.e. apparent strain hardening), and makes it very difficult to establish direct connections between the indentation stress-strain curves and those obtained from standard tension or compression curves. The authors believe that this large elastic-plastic segment in the indentation stress-strain curves is directly attributable to the specific protocols used for the estimation of the contact radius. We will present in subsequent sections our recently developed

data analyses protocols for estimation of the contact radius that significantly shrink this undesired transition segment in the indentation stress-strain curves.

3. Indentation Stress and Strain Measures

Hertz's theory (Eq. (1)) can be recast into a linear relationship between indentation stress and indentation strain defined as [15, 29]

$$\sigma_{ind} = \frac{4E^*}{3\pi} \varepsilon_{ind}, \quad \sigma_{ind} = \frac{P}{\pi a^2}, \quad \varepsilon_{ind} = \frac{a}{R_{eff}} \quad (5)$$

Note that the definition of the indentation stress shown is essentially based on the concept of Meyers hardness described earlier. The definition of the elastic indentation strain in Eq. (5) may differ from some of the definitions in current literature by just a constant that can be easily reconciled by re-arranging the coefficients in the equation. The main limitation of the indentation strain measure shown in Eq. (5) is that it does not lend itself to rational extension to the case of elastic-plastic indentation. This is because the ratio a/R_{eff} lacks reasonable physical interpretation as a strain measure. Strain should be fundamentally defined as the ratio of change in length over the initial length on a selected line segment in a region of interest in the sample. a/R_{eff} cannot be interpreted as a strain in any idealization of the sample being indented.

Furthermore, R_{eff} does not even reflect a relevant length scale in characterizing the deformation experienced by the sample (in fact, the contact radius, a , is a better descriptor of the length scale of the indented region; see Fig. 2).

The most common choice of indentation strain measure for elastic-plastic indentations in current literature is a/R_i . A number of recent studies have utilized this measure of indentation strain to derive some physical insights into the material response [33-38]. Although this definition

enjoys some similitude with the definition shown in Eq. (5) for the initial elastic loading of a flat sample (where $R_{eff} = R_i$), there is really no rational justification for its selection for the subsequent elastic-plastic indentation regime.

The authors of this review have recently proposed that the Hertz's theory for elastic indentation be recast as [12]

$$\sigma_{ind} = E^* \varepsilon_{ind}, \quad \sigma_{ind} = \frac{P}{\pi a^2}, \quad \varepsilon_{ind} = \frac{4}{3\pi} \frac{h_e}{a} \approx \frac{h_e}{2.4a} \quad (6)$$

The definition of elastic indentation strain in Eq. (6) can be visualized by idealizing the primary zone of indentation deformation as being equivalent (in an average sense) to compressing by h_e (the elastic indentation depth) a cylindrical region of radius a and height $2.4a$ (see Fig. 2). The cylinder might expand laterally to accommodate this contraction in height. The lateral expansion is, however, not relevant to the definition of the indentation strain. Note that this interpretation allows the visualization of strain in the classical sense as the change in length per unit length. Furthermore, it is easily extendable to elastic-plastic indentations by simply replacing h_e with h_t (the total indentation depth).

This interpretation is much more physical than the definition of indentation strain as a/R_{eff} or a/R_i . The main reason for using a/R_{eff} is its convenient appearance in Eq. (5). In the limit of small spherical indentation depths that are typical of a purely elastic indentation (where $h_t = h_e$)

of the sample, it can be seen that $\frac{h_t}{a} \approx \frac{a}{R_{eff}}$. This implies that the definition of the indentation

strain adopted here is equivalent to the definition used in the literature for the initial elastic loading segment, except for a multiplicative factor. The inclusion of this factor in the definition of the indentation strain conveniently modifies the slope of the elastic indentation stress-strain curve to be equal to the effective modulus, E_{eff} . In other words, Eqs. (5) and (6) are

mathematically equivalent to each other for purely elastic indentation, except that the terms are grouped differently. However, as discussed later, when applied to data sets collected from samples exhibiting both elastic and inelastic deformations, the two approaches result in very different indentation stress-strain curves.

Another source of considerable confusion in the literature stems from the two definitions of contact radius shown in Eq. (1) and Eq. (4). In the case of a fully elastic spherical indentation on a flat surface, it can be shown (both experimentally and theoretically) that the two definitions in Eq. (1) and Eq. (4) provide equivalent values for the contact radius, a . However, in our experimental investigations, we found that the values estimated by these two definitions deviate from each other significantly as the sample experiences a substantial amount of inelastic strain and the contact radius becomes larger. We critically explore the underlying cause of the disagreement using finite element models in the next section.

4. Finite Element Models for Computing Indentation Stress-Strain Curves

Because of the complex and the highly heterogeneous stress and strain fields experienced in elastic-plastic indentation, finite element models are extremely valuable in critically evaluating several of the concepts presented in the preceding sections and to extract meaningful properties from the measured raw data. A majority of the approaches used in the current literature address the extraction of properties from indentation measurements as an inverse problem; the solutions strategies generally demand the use of sophisticated optimization algorithms to minimize the discrepancy between the measured load-displacement data and the corresponding predictions from the finite element simulations [39-43]. However, the fact that the

elastic-plastic transition occurs over a very short regime in the overall load-displacement curve makes it very difficult to directly extract the measures associated with initial plasticity (e.g., yield strength, initial strain hardening rate) using this approach. In fact, in most measured indentation load-displacement datasets, it is very difficult to distinguish the elastic regime from the elastic-plastic regime because of the very smooth transition between these regimes. Consequently, there is tremendous benefit to first recovering the indentation stress-strain curves from the measured indentation load-displacement datasets. In addition to clearly resolving the elastic-plastic transition, the indentation stress-strain curves often provide very useful insights into the material response and provide an opportunity to compare material behavior between different samples even without recovering mechanical properties.

In a recent paper, Donahue et al. [44] utilized a finite element model to gain new insights into three main issues central to recovering reliable indentation stress-strain curves from spherical nano-indentation measurements: (i) What is the accuracy of the different methods used in current literature for estimating the contact radius, a ? (ii) Which definition of indentation strain produces more meaningful indentation stress-strain curves? (iii) How does one reconcile the differences between the indentation stress-strain curves and the conventional uniaxial stress-strain curves from simple tension or simple compression on bulk samples? The use of finite element models for resolving these issues circumvents many of the difficulties and uncertainties faced in experimental investigations (e.g., identification of the point of initial contact, precise geometry of the indenter, assumed isotropy of material response, assumed non-hardening behavior of sample in plastic deformation, friction between indenter and sample surfaces), and offers unique opportunities for critical validation of the main concepts.

More specifically, Donohue et al. [44] assessed critically the precise effect of the different definitions of the contact radius and the different definitions of indentation strain on the resulting indentation stress-strain curves for an elastic-perfectly plastic material response. The table in Fig. 4a lists the four possible ways of generating an indentation stress-strain curve, labeled A through D, from the same simulation dataset. Fig. 4b presents the different indentation stress-strain curves generated using the four different protocols listed in the table in Fig. 4a. It is seen that the initial elastic portions from all four curves (labeled A through D) matched quite well with each other. The curves started to deviate from each other after the initial elastic segments. These authors report that the deviations in the indentation stress-strain curves commenced at about an indentation stress of about $1.2\sigma_y$ and correlated with substantial changes in R_{eff} . It was also noted that only the unloading segment corresponding to curve A showed the expected modulus that matched very well with the modulus from the loading segment.

Indentation stress-strain curves labeled B and C (based on the contact radius definition in Eq. (4)) in Fig. 4a are observed to exhibit a significant post-yield hardening behavior for both materials. In fact these curves indicate that indentation flow stress reaches about $3\sigma_y$ in both materials, consistent with several reports in literature that use the definition of the contact radius in Eq. (4) [14, 15, 29, 38, 45, 46]. Note that the plastic response of both these materials was defined to be non-hardening (i.e. elastic-perfectly plastic with constant yield strength) in the prescription of the material constitutive behavior. Furthermore, the indentation stress-strain curves labeled A and D (based on contact radius definition used in Hertz's theory; Eq. (1)) exhibited very little hardening by comparison. These observations suggest that the apparent hardening reported extensively in indentation stress-strain curves in literature is directly attributable to the definition of the contact radius used in these computations. More importantly,

it is seen that the use of the contact radius definition that is consistent with Hertz's theory provides the best representation of the post-yield behavior in the indentation stress-strain curves.

Donohue et al. [44] also report that the values of the indentation stress and indentation strain computed by protocol A provide the best match with the average stress and strain values in the indentation zone predicted by the finite element model. The predicted indentation strain fields in the finite element model at a depth close to indentation yield are shown in Fig. 5. It is clearly seen that the indentation zone extends approximately to a length of about $2.4a$, justifying the new definition of the indentation strain presented in Eq. (6) (see also Fig. 2a). The authors also report strong correlations between the uniaxial mechanical properties and those extracted from the indentation stress-strain curves obtained using protocol A.

There have also been attempts to extract microscale mechanical properties through inverse solution methodologies that match FE predictions of indentations with the corresponding measurements. Zambaldi et al. have extracted values of the critical resolved shear stresses (CRSS) from spherical nanoindentation measurements conducted on differently oriented grains of alpha-titanium. In their approach, they focused their efforts on matching the FE predictions and the measurements in various aspects of the surface topology at the indentation site (after the indentation was completed). It is not yet clear if a different choice of the parameters selected to quantify the surface topology would significantly affect the extracted values. In a different approach, Patel et al. have recently demonstrated the viability of extracting single crystal elastic stiffness parameters from polycrystalline samples using spherical nanoindentation and orientation measurements combined with finite element simulations. This new approach utilizes compact spectral representations to capture the dependence of the indentation modulus on the crystal lattice orientation at the indentation site as well as the single crystal elastic constants

(defined in the crystal reference frame). Once such a function is established (from running a large array of FE simulations) the unknown single crystal elastic constants for a selected phase in a given sample are estimated through a regression technique that provides the best match between spherical nanoindentation measurements obtained on differently oriented grains of that phase in a polycrystalline sample and the function already established in the first step. The accuracy and viability of this approach were demonstrated for polycrystalline Fe-3%Si.

5. Indentation Stress-Strain curves – Experimental Analysis Techniques

5.1 Indentation Stress-Strain Curves using Continuous Stiffness Measurement (CSM) data

Similar to the results of the finite element model described earlier, indentation stress-strain curves extracted from experimental measurements also show significant sensitivity to the specific data analyses protocols used. Fig. 6 highlights some of the main differences between indentation stress-strain curves plotted using two different sets of protocols: (i) default zero-point identified by the machine (MTS XP[®]) and definitions used in protocol C (see table in Fig. 4a), and (ii) novel protocols for identification of zero-point (discussed later) with definitions used in protocol A (see table in Fig. 4a). Experimentally extracted indentation stress-strain curves using a 13.5 μm radius spherical indenter on individual grains of polycrystalline samples of tungsten and aluminum are shown in this figure. These two metallic samples were chosen due to their low elastic anisotropy (note that Hertz's theory is valid only for isotropic elastic materials) as well as the large variation in their respective mechanical properties (aluminum exhibits a low modulus and a low yield strength while tungsten exhibits a high modulus and a high yield strength).

Two major problems are easily apparent when indentation stress-strain curves are plotted using the protocols used in current literature, i.e. when using protocol C. First, there is a substantial amount of noise, especially in the initial elastic and yield sections of this curve, and second, indentation strain defined as $a/2.4R_i$ does a very poor job of capturing the elastic unloading curves. For example, in case of aluminum, the slope of the unloading stress-strain curve, and hence the unloading modulus, calculated using $a/2.4R_i$ as the indentation strain is actually negative (Fig. 6b). This problem of highly unrealistic unloading slopes in the analyses of spherical indentation data has been noted in numerous other materials, including tungsten, aluminum, silver, gold, steel etc. [12]. In the opinion of the authors, these problems have contributed to the large variance in the reported spherical indentation stress-strain curves and in the values of the properties measured therein. It is also noted that the indentation stress-strain curves for both tungsten and aluminum are much more meaningful when plotted using the novel protocols described in this paper in at least the following two aspects: (i) the unloading segments show the same moduli as the loading segments, and (ii) the indentation stress-strain curve for tungsten exhibits much more strain hardening compared to aluminum.

The substantial scatter in the initial loading portion of the indentation stress-strain curve obtained from the conventional approach stems from an incorrect determination of the zero-point or the point of effective initial contact during nanoindentation, while the unphysical values of the moduli in the unloading segments in this approach arise from the incorrect use of a/R_i as an effective measure of indentation strain.

The problem of identifying a zero-point in nanoindentation analysis has been discussed in detail in recent papers [47] and several methods have already been explored in literature. In one approach [48], the displacement sensor is set to zero upon reaching a pre-set contact force. The

data in the initial segment is then curve-fitted and extrapolated back to zero force. This method, commonly used in other mechanical testing techniques as well, requires a prior knowledge of the sample properties in order to choose an appropriate initial force and often results in an underestimation of the contact area and a corresponding overestimation of the hardness and modulus values [49].

The standard protocol for the MTS machine in the non-CSM mode uses the slope of the load-displacement data for surface detection. In the CSM mode, a small, sinusoidally varying signal is imposed on top of the DC signal that drives the motion of the indenter. This allows constant monitoring of various signals such as the harmonic contact stiffness, the harmonic load, the harmonic displacement and the phase angle, all of which could potentially be used for surface detection. The quantity that shows an immediate and significant change upon initial contact is then generally chosen as the criteria for surface detection. The use of the stiffness signal has been most widely advocated in the literature [8, 48, 49] for this purpose. The accuracy for this method has been reported to be anywhere from ± 2 nm [8] to ± 30 nm [49]. Innovative techniques, such as the use of a video camera for indentation of optically clear materials [50] and photoluminescence of quantum dots due to indentation [51], have also been explored to solve the problem of determining surface contact.

Other than the advancements in instrumentation described above, there has also been multiple efforts on post-processing of the data for zero-point determination. One common approach has been to fit the initial (elastic) response of the indentation data to Hertz theory and back-extrapolate to zero-depth. For example Chudoba et al. [52-55] have proposed fitting the first few nanometers of indentation data to a power-law equation conforming to Hertzian contact: $P = C \cdot (h-h_0)^{1.5}$, where h_0 is the displacement correction and C is a constant. A similar approach

has been used by Ullner [56] and Grau et al. [57] where the fit is to a second-order polynomial. More recently, Kalidindi and Pathak [12] and Moseson et al. [58] proposed new protocols for establishing the effective zero-point that utilizes the CSM signal (stiffness) in addition to the load and displacement signals. While the use of all three measurement signals (load, displacement, and the stiffness, see Eq. 7 below) has a distinct advantage compared to the previous efforts for extracting the zero-point, the details of the methods proposed by these two groups are substantially different from each other. The approach proposed by Moseson et al. [58] is based on Eq. (4) that includes the geometric relationship between contact radius and the indenter radius, whereas the approach proposed by Kalidindi and Pathak [12] is based on Eq. (1). As discussed earlier, the values of contact radii computed from Eqs. (1) and (4) are substantially different from each other (Fig 4), especially after the sample experiences a significant change in the value R_{eff} (after a certain amount plastic strain has been induced in the sample, shown later in Fig 9b). Also, it was pointed out earlier that only Eq. (1) is consistent with Hertz's theory. The procedure outlined in [12] has been very successful in extracting indentation stress-strain curves, as detailed below.

The new data analyses procedures proposed by Kalidindi and Pathak [12] can be summarized as a two-step process. The first step in this process is an accurate estimation of the point of effective initial contact in the given data set, i.e. a clear identification of a zero-point that makes the measurements in the initial elastic loading segment consistent with the predictions of Hertz's theory [17, 59]. For spherical nanoindentation this relationship can be expressed as

$$S = \frac{3P}{2h_e} = \frac{3(\tilde{P} - P^*)}{2(\tilde{h}_e - h^*)}, \quad (7)$$

where \tilde{P} , \tilde{h}_e , and S are the measured load signal, the measured displacement signal, and the continuous stiffness measurement (CSM) signal in the initial elastic loading segment from the

machine, respectively, and P^* and h^* denote the values of the load and displacement signals at the point of effective initial contact. A linear regression analysis can then be used to establish the point of effective initial contact (P^* and h^*) in the indentation experiment. Note that these protocols do not require an estimation of the contact radius a or the effective radius R_{eff} .

Utilization of Eq. (7) is made possible by the use of the CSM signal (in the MTS XP[®] nanoindentation machine and their later generations) which is measured concurrently with the load-displacement values. CSM allows the measurement of the contact stiffness ($S = dP/dh_c$) at every point along the loading curve (and not just at the point of unloading as in the conventional approach). Thus in essence the CSM allows the continuous measurement of S in one single indentation experiment without the need for discrete unloading cycles [60]. A separate procedure for measuring the effective zero point without the use of the CSM signal is described in Section 5.2.

The procedure described above is illustrated in Fig. 7a for a sample of Fe-3%Si steel for a 13.5 μm radius spherical indenter. In this figure, the portion of the initial loading data segment found to be in excellent agreement with Eq. (7) is marked (in blue). The segment before this is probably influenced by various surface artifacts (such as surface roughness, non-ideal indenter shape etc.), while the segment following this segment (not shown in the figure) deviates substantially from the linear relationship shown in the figure, as it is likely influenced by inelastic deformation in the sample. The excellent agreement of this data segment to Hertz's theory is also utilized later in order to calculate the indentation modulus of the sample during loading (using Eq. (1)).

Figure 7b shows the point of initial contact as identified by the default procedure in the MTS software (C_1) and by the procedure described above (C_2). In the default procedure, C_1 is

generally determined as the point at which the S signal first reaches or exceeds 200 N/m. Note that the value for S is generally negative before the indenter is in contact with the specimen. For hard materials such as metals and ceramics, this option almost always underestimates the zero-point. Thus, to arrive at C_2 , the load signal in Fig. 7b needed to be moved by about $P^* = 0.12$ mN and the displacement signal by about $h^* = 6.8$ nm with respect to C_1 .

A major advantage of Eq. (7) is that this approach identifies an “effective” or virtual point of initial contact, and not necessarily the actual point of initial contact. The concept of an effective point of initial contact allows us to de-emphasize any artifacts created at the actual initial contact due to the unavoidable surface conditions (e.g. surface roughness, presence of an oxide layer etc.) and imperfections in indenter shape. For example, the above procedure was found to work even in the case of mechanically polished bone samples (final polishing step 0.05 μm diamond paste) where larger corrections for the displacement signal were needed ($h^* = 10\text{--}15$ nm [61]) than the corresponding ones in well-prepared (i.e. electro-polished where $h^* \sim 5$ nm) metal samples [12, 62-64]. As mentioned above, the effective point of initial contact is not likely to be the point of the actual initial contact. However, the elastic segment of the initial loading beyond h^* is in excellent agreement with Hertz’s theory suggesting that beyond this point, the factors cited above do not appear to have a significant impact on the measurements.

Figure 7c shows the indentation stress-strain curve derived from the load-displacement data in Fig. 7b using the protocol outlined above and compares it to the plot using the machine generated zero point (C_1). Both the initial elastic and yield sections are much better resolved when the zero point is determined using the procedure described above (instead of using the default procedure in the MTS software).

The estimation of the contact radius (a) is the second step in the extraction of indentation stress-strain curves. With the CSM option, the problem is significantly simplified because of Eq. (3) ($a = S / \sqrt{2E_{eff}}$). Once the value of E_{eff} is established from the initial loading curve [12] (or if the Young's modulus of the sample material is already known), the contact radius can be easily computed from Eq. (3) assuming that E_{eff} remains constant during the inelastic deformation caused by the indentation. This assumption is quite reasonable for isotropic metals such as tungsten and aluminum. Although plastic deformation in metals does not itself cause any direct change in the elastic properties, it rotates crystal lattices into new orientations [65], and thereby modifies the texture in the sample. Such changes in the underlying texture caused by plastic deformation usually produce a substantial change in the effective elastic properties of the solid [66-68]. The influence of crystal orientation on the indentation modulus is addressed in detail in Section 6.1. However, in metals such as tungsten and aluminum shown in Fig. 6, the elastic anisotropy at the single crystal level is quite small (in fact tungsten crystals exhibit isotropic elastic response), and therefore it is reasonable to assume that E_{eff} remains constant during the inelastic deformation caused by the indentation. Using Eqs. (3) and (6) the complete indentation stress-strain curves can be computed as shown in Figs. 6 and 7.

After the completion of the two-step process described above, indentation stress-strain curves can be computed using the definitions used in Eq. (6) and protocol A (table in Fig. 4a). An important point to note is that the nanoindentation data analysis approach described in these equations is based on Hertz's theory, which assumes isotropic elastic behavior of the sample. Indeed almost all (macro, micro and nano) indentation studies reported in literature employ the Hertz's theory, even when it is quite clear that the sample material exhibits significant anisotropy in the indentation zone. For example, in most nanoindentation studies of metals and ceramics,

the indentation zones are much smaller than the individual grains in the samples, and therefore the sample is expected to exhibit significant anisotropy in the indentation zone. Surprisingly, a vast majority of such indentation measurements continue to exhibit a linear relationship between P and $h^{3/2}$, as predicted by Hertz's theory. Consequently, the elastic modulus estimated using Hertz's theory on anisotropic solids is often interpreted as the equivalent isotropic value in literature, without explicitly stating this assumption [7, 13, 14, 48, 63, 69, 70].

The main concepts presented so far can be summarized as follows:

1. The new procedures for establishing the effective point of initial contact based on Eq. (7) produces indentation stress-strain curves that exhibit meaningful initial elastic loading segments. This new procedure utilizes the CSM signal provided by modern nano-indentation machines. More specifically, the indentation stress-strain curves generated by this new method do not exhibit the substantial noise and spikes prevalent in the initial loading segments of the indentation stress-strain curves obtained using the zero-point given by the default procedures currently used in the equipment manufacturer's software.
2. A new rational definition of the indentation strain has been formulated (see Eq. (6)). This new definition is highly consistent with Hertz's theory for purely elastic contact. For elastic-plastic contact, it was also found to produce better indentation stress-strain curves that exhibit a clearly identifiable elastic segment, a smooth but relatively short transition to the plastic deformation regime, and an unloading segment where the unloading modulus matched well with the modulus from the loading segment.

5.2 Indentation Stress-Strain Curves without CSM

Both the estimation of the zero-point (Eq. (7)) and the estimation of the contact radius (Eq. (3)) described in Section 5.1 require the use of the continuous stiffness measurement signal

(CSM). However the CSM module is an optional accessory on the MTS/Agilent nanoindenter machine, and hence is available only on some machines. Moreover, other nanoindentation machines (manufactured by companies other than MTS/Agilent) may not even offer the CSM as an option. In this section, an alternate approach is presented for converting the spherical nanoindentation load-displacement data into indentation stress-strain curves, without the need for the CSM.

Extraction of the indentation stress-strain curves without using CSM is described in detail in Ref. [13] and is achieved in a two-step process: (i) establishing the effective zero-point and (ii) estimating the contact radius, a . In [13], the authors have established the zero-load and the zero-displacement point by fitting the recorded initial elastic load (\tilde{P}) and displacement (\tilde{h}_e) signals to the predictions of Hertz's theory. Thus rearranging Eq. (1), the load and displacement during elastic loading in a spherical nanoindentation experiment should be related by

$$\tilde{h}_e - h^* = k(\tilde{P} - P^*)^{2/3} \quad k = \left[\frac{3}{4} \frac{1}{E_{eff}} \frac{1}{\sqrt{R_{eff}}} \right]. \quad (8)$$

Note that k in Eq. (8) is a constant for the entire initial elastic loading segment. The values of P^* and h^* that yield the lowest residual error in the least-squares fit of the initial elastic loading segment to Eq. (8) were chosen to correspond to the effective zero-point. This approach ensures that the corrected data set would be highly consistent with Hertz's theory.

Figure 8 shows an example of a comparison between the zero-points for tungsten as determined by the two methods: (i) Eq. (7) using the CSM, and (ii) Eq. (8) without using the CSM signal. As seen from Fig. 8, both the CSM and the non-CSM data analysis methods for tungsten yield nearly identical values of P^* and h^* . Similar matches were also reported in Ref. [13] over a number of datasets for a range of metallic samples.

It is worth reiterating here that it is possible to analyze the relatively small initial elastic loading segments with remarkable accuracy, because the use of Eq. (7) or Eq. (8) to establish the effective zero-point does not require prior knowledge of the values of R_{eff} and E_{eff} . This is especially beneficial in establishing a reliable value of R_i , i.e. the correct radius of the spherical indenter purchased from the manufacturer (note that in the initial elastic loading segment $R_{eff} = R_i$). For example, in Ref [13] using measurements on samples of known Young's moduli (e.g. Si standards), two indenter radii were estimated to be 1.4 and 20 μm respectively, even though the manufacturer had claimed otherwise. Both these estimates were subsequently confirmed by SEM.

The second step in the extraction of indentation stress-strain curves is an accurate estimation of the contact radius a , which evolves continuously during the indentation experiment. As mentioned in the previous sections, the majority of the methods used for estimation of a in the literature [14, 15, 45, 48] are motivated by the spherical geometry of the indenter, where a is calculated directly from the indentation depth and the radius of the indenter, R_i . However as noted before, although the relationship $R_{eff} = R_i$ holds in the initial elastic loading segment, R_{eff} can no longer be assumed to be equal to R_i after any imposed plastic deformation in the loading segment. As we shall see later, R_{eff} changes quite dramatically with any imposed plastic deformation by the indenter.

Alternatively, one can impose an elastic unloading segment at any point of interest and analyze it using Hertz's theory in order to estimate the contact radius. Indeed, this is exactly what is done in estimating the contact radius using the CSM [7, 8, 60]. Each unloading segment is fit to the expected Hertz's relationship between the total indentation depth, h_t , and indentation load, P , which may be conveniently expressed as (see Fig. 9a)

$$h_e = h_t - h_r = kP^{2/3} \quad (9)$$

Once the value of E_{eff} is established from the initial loading curve (or if the Young's modulus of the sample material is already known), a regression analysis on the unloading segment can determine both h_r and R_{eff} . The value of the contact radius, a , at any point in the unloading segment is then determined from

$$a = \sqrt{R_{eff} h_e} = \sqrt{R_{eff} (h_t - h_r)}. \quad (10)$$

It should be noted that this relationship between R_{eff} and a is implicit in Hertz's theory for the quadratic contacting surfaces. Applying this equation to the data point just before the initiation of the unloading segment provides the value of the contact radius at that point in the original loading segment. This method does however necessitate a large number of loading-unloading segments in order to be able to get a complete description of the indentation stress-strain curve for a given sample, since each unloading curve will produce only one point on the indentation stress-strain curve.

Figure 9b shows the values of R_{eff} estimated at different indentation depths, using the data analysis procedure described earlier, in the measurements obtained using a 20 μ m spherical indenter on samples of electropolished aluminum and tungsten. As seen from this figure, the values for R_{eff} change dramatically with imposed plastic deformation by the indenter. In fact, the changes in the effective radius are most dramatic in the initial stages of plastic deformation under the indenter. It is also seen that R_{eff} takes on much higher values for the softer aluminum samples compared to the harder tungsten samples (at the same depth of indentation). Indeed, it was observed that R_{eff} is not just a function of indentation depth (or load) alone, but varies substantially with the details of the elastic and plastic properties of the sample. This observation raises serious questions regarding the validity of the approaches in literature that establish

calibrated area functions and effective indenter shapes from measurements on a standard material [7, 8], and then use the same on other materials without any other corrections. Note that the values of R_{eff} estimated in Fig. 9b are substantially larger than the indenter radius ($R_i = 20 \mu\text{m}$). These observations are highly consistent with the findings from finite element simulations described earlier in Section 4.

Figures 10a and b show comparisons between the indentation stress-strain curves obtained using both the CSM method described in Section 5.1 and the non-CSM method above on aluminum and tungsten samples for both 1.4 and 20 μm radii indenter sizes. It is seen that the indentation stress-strain curves from the CSM and the non-CSM methods agree well with each other for both indenters. The indentation stress-strain curve produced using the non-CSM method is able to capture all the major features of the stress-strain curves including the linear elastic regime, the plastic yield point, and the post-yield strain-hardening. As expected, the indentation stress-strain curve for tungsten shows more strain hardening compared to the aluminum sample. These results also demonstrate the feasibility of capturing the details of the pop-in phenomenon (discussed later in Section 5.4) occurring in the smaller 1.4 μm indenter with the non-CSM method. These findings indicate that in spite of the non-continuous nature of the non-CSM calculations, this method can be successfully used to characterize the mechanical response of the material during spherical nanoindentation.

5.3 Effect of Surface Preparation in Indentation Stress-Strain Curves Analysis

Since nanoindentation is essentially a surface probe technique, any disturbance to the surface quality is likely to have an impact on the nanoindentation results. In this respect, the data analyses procedures described in the previous sections, with their ability to analyze the initial

loading segments, are highly suited to gauge the quality of surface finish on the indented materials. In this section, we discuss the precise role of surface preparation on the measured nanoindentation data. Here the focus is on three important aspects that commonly affect the initial nanoindentation loading segments of metallic materials, namely i) presence of a highly disturbed surface layer produced by traditional (mechanical) sectioning and polishing methods, (ii) presence of surface irregularities, such as a rough surface finish or a thin oxide film on the surface, and the (iii) occurrence of ‘pop-ins’ or depth excursions at low loads.

One of the most important factors for producing reliable results in nanoindentation experiments is the careful and reproducible preparation of the specimen surfaces to be analyzed. Great care needs to be exercised in sectioning the sample to minimize the disturbed layer produced in the process. Several of the mechanical sectioning methods (e.g. diamond wheels) leave a relatively large disturbed layer. In such situations, it is important to ensure that the disturbed layer is completely removed in the subsequent polishing steps.

The effect of surface finish on nanoindentation results is illustrated in Fig. 11 which shows the indentation stress-strain curves measured on an annealed sample of W prepared with two different surface finishes: (i) a mechanically polished surface (final polishing step 1 μm diamond polish), and (ii) an electro-polished surface; these measurements were obtained using a 13.5 μm radius spherical indenter. It is clearly seen from this figure that the indentation stress-strain curves for the W surface prepared by rough mechanical polishing are consistently higher than that of the electro-polished surfaces (Fig. 11a), whereas those of electro-polished and vibratory-polished (final polishing step 0.02 μm colloidal silica for ~48 hours) surfaces are in excellent agreement with each other (Fig. 11b). Rough mechanical polishing generally leaves a disturbed surface layer with a higher dislocation content than in the original annealed material.

Since the indentation modulus of the material is not altered appreciably by the presence of these dislocations, the main effect of this disturbed surface layer is in the form of an increase in the indentation yield strength and the plastic flow stresses in the material. Furthermore, the indentation yield strengths measured on the mechanically polished samples also result in a large scatter in the measured indentation yield strengths because of the inherent variability in the surface layer produced by this method of surface preparation.

Since the protocols described in this paper aim to isolate and analyze the initial loading segments in the nanoindentation measurements, they place stringent requirements on the preparation of the sample surface. It should be recognized that the indentation zone sizes in the initial loading segment are very small. The contact radius a can be used as a guide in deciding if a good sample surface has been obtained for the measurements. The indentation zone size is typically about $2.4a$, while the location of the highest stress experienced in the indentation zone is about $0.5a$ directly below the indenter. Therefore, it is extremely important to keep the thickness of the disturbed sample surface to be much smaller than the contact radius a . For a 13.5 μm indenter, the contact radius for most metals at the elastic limit is of the order of 300-500 nm. The corresponding numbers for a 1 μm indenter are of the order of 100 nm or less. Consequently, it is substantially more difficult to obtain suitable surfaces and reliable results with smaller indenters compared to the larger indenters.

The above discussion underlines the importance of a high quality surface finish in obtaining reliable data from nanoindentation experiments, especially in the initial elastic loading segments. For metals, having an undisturbed (virgin) sample surface is highly critical in order to get repeatable and reliable results from nanoindentation that correspond to the properties of the original sample and not to the effects of the sample preparation techniques themselves. Both

electro-polishing, where a certain thickness of the metal is removed to generate an undisturbed relatively flat surface, and vibratory-polishing using fine-sized colloidal silica for a significant length of time (~ 24 -48 hours), seem to fulfill these requirements (Fig. 11b). However, as discussed in the next section, electro-polishing may also cause a larger propensity of pop-ins in annealed metallic samples with low dislocation densities.

Surface irregularities are common on most sample surfaces. Common examples include the presence of a thin oxide film on the surface (of metallic samples) and sample-surface roughness, especially in materials where techniques such as electropolishing are not an option (e.g., non-metallic samples such as bone). Our results indicate that the influence of these irregularities, provided they are below a critical threshold, is largely reflected in the very early parts of the measured load-displacement data. Thus, for a metal like tungsten with a ~ 10 nm oxide thickness on the surface, deleting a slightly larger portion of the initial loading segment brings the measured load-displacement data in excellent agreement with the predictions of the Hertz's theory [63]. A similar observation was made earlier for bone samples. This indicates that the method for finding the effective zero-point using Eq. (7) is able to identify the regime in the initial loading segment consistent with Hertz's theory – as long as the thickness of the disturbed layer or irregularities is significantly smaller than the contact radius at the elastic limit of the initial loading segment in the indentation. However, care should be exercised in measurements on surfaces with a larger oxide layer or a very rough polish. In such situations, one needs to either find a way to remove or reduce the surface layer or use an indenter with a bigger tip radius.

5.4 Pop-in Events

Nanoindentation experiments are sometimes affected by the occurrence of the ‘pop-in’ events – when the indenter suddenly experiences an increase in penetration depth without any major increase in the applied indentation load (in a load controlled experiment). These pop-ins, which are generally associated with the onset of significant plastic deformation [71] in the indentation experiment, often generate high stresses that have been estimated to be close to the theoretical limit ($G/2\pi$ [72], where G is the shear modulus) of the material [73-80]. These are attributed to the fact that the indentation zone size in these experiments at the point of plastic yield is comparable or smaller than the dislocation-network length scales in the sample (e.g., spacing of dislocations, dislocation cell size, see the schematic in Figs. 12a and 12c). The occurrence of these pop-ins can therefore be correlated to the difficulty of activating a dislocation source (e.g., Frank-Read source [81]) in the primary indentation zone.

Increasing the indenter radius causes a corresponding increase in the indentation zone size. Hence with the larger indenter, there is a much higher likelihood that the conditions for setting up dislocation sources are more easily attained at lower indentation depths and indentation loads. Consequently, the occurrence of pop-ins during indentation with the larger indenter can be expected to be much more stochastic compared to the indentation with the smaller indenter, as shown for Fe-3%Si steel using a larger 13.5 μm indenter in Fig 12b. With an even larger indenter radius, the pop-ins should disappear completely. Indeed, pop-ins have never been reported with very large (with radii of millimeters and above) indenters.

Pop-ins, which appear as displacement bursts in a load vs. displacement plot, manifest as strain bursts in the indentation stress-strain curves produced using the protocols described earlier. Pop-ins events in vibro-polished samples of Fe-3%Si steel using a 13.5 μm indenter are shown in

Fig. 12b. As seen from this figure, the indentation stress-strain curves after the pop-in event seem to approach the indentation stress-strain curves obtained on the sample without the pop-in. This suggests that the pop-ins observed in these tests are caused by delayed activation of sources for plastic deformation, which essentially extends the initial elastic regime. However, as soon as a good number of sources for plastic deformation are activated, the response is no different than the response obtained in the tests without the pop-in event. In other words, further loading after the pop-in event appears to completely wipe out the memory of the pop-in event; there is no effect on the indentation stress-strain curves at larger indentation strains.

If the pop-ins are indeed caused by delayed activation of dislocation sources, then indentation measurements on cold-worked samples should show a lower propensity for the occurrence of pop-ins. This was verified by conducting spherical indentation on samples of vibro-polished as-cast¹ and 30% deformed samples of Fe-3%Si steel using a 13.5 μm spherical indenter (see Figs. 12b and 12c). It is seen that the occurrence of pop-ins is stochastic in the indentations on the as-cast sample (Fig. 12b), but are completely absent in the indentations on the 30% deformed sample (Fig. 12c). Similarly, rough mechanical polishing – which too increases the dislocation density content in the top disturbed surface layer in the sample – was also found to reduce the occurrence of pop-ins significantly (Fig. 12d).

Figures 12b and 12d also indicate that an indentation stress-strain plot with an initial pop-in often exhibits a large discontinuity. This makes it difficult to accurately estimate the indentation yield strength (Y_{ind}) from such a plot. Particularly, as-cast or annealed samples with very low initial dislocation density prepared using electropolishing are highly susceptible to this

¹ The as-cast state represents a low and uniform dislocation density for the Fe-3%Si sample. However, the same is not true for all metallic systems. For example, FCC metals that contract more on solidification often have a high dislocation density and significant in-grain misorientations due to contraction stresses [82] R.D. Doherty, Scripta Materialia 49 (2003) 1219-1222.. These samples would then need to be annealed to attain a low and uniform dislocation density.

problem. Fortunately vibro-polishing has been found to be an ideal compromise – it introduces only a small number of dislocations into the sample surface, which are enough to suppress the pop-ins for the larger indenter sizes (10 and 13.5 μm radii) but do not appear to influence the measured Y_{ind} on the as-cast samples. This is seen in Fig. 12d, which shows an excellent agreement between the back-extrapolated Y_{ind} obtained on the electro-polished surface (with the pop-in) and the Y_{ind} measured on the vibro-polished surface (without the pop-in).

Following the observations above, both electro-polishing and vibro-polishing of metal surfaces should be explored. Vibro-polishing is particularly advantageous in extracting indentation stress-strain curves from as-cast and annealed samples, as it reduces the propensity for pop-ins. In studies involving grain boundaries, vibro-polishing also reduces the possibility of developing a significant groove at the grain boundary that often results from electropolishing [83, 84]. However, if the aim of the nanoindentation measurements is the study of the pop-ins themselves, then electro-polishing is clearly the preferred procedure.

Indentation stress-strain curves can be highly effective in understanding the physical processes occurring underneath the indenter during and immediately after the occurrence of the pop-in. A close look at the indentation stress-strain curve during pop-ins reveals the following salient features (see Fig. 13 for a pop-in in electropolished W): (i) During the pop-in event, the indentation stress values remain high and stable, while there is a burst in the value of the indentation strain (Fig. 13a). (ii) Subsequent to the pop-in event, the indentation stress decreases only after a finite amount of additional indentation displacement has been applied. (iii) During this additional indentation displacement, the indentation strain actually decreases producing an unloading segment in the indentation stress-strain curve. (iv) The unloading modulus during this additional indentation displacement (subsequent to pop-in) is generally very close to the

indentation modulus measured in the initial loading segment (except when the pop-ins are unusually large [63], as in Figs. 10 and 12). Pop-ins observed in a broad range of materials, including Fe-3%Si (Fig. 12), Al (Fig. 10), Ag, Au, Au, and Cu [13, 62-64], have consistently exhibited the same salient features described above. The above observations are perplexing at first glance as one would intuitively expect a sharp drop in stress during the pop-in event itself.

Given that the load remains constant during the pop-in event (the measurements were conducted in load control), the observation that the indentation stress remains high and almost constant during the pop-in event suggests that the contact radius must also remain more or less constant during the pop-in event (see Fig. 13a). This can be inferred directly from the definition of the indentation stress ($\sigma_{ind} = P/\pi a^2$, see Eq. (6)). However, one would intuitively expect a sudden increase in the contact radius associated with the large excursion in the indentation depth that occurs during the pop-in event. It is interesting that although the excursion in the indentation depth does indeed produce a corresponding increment in the indentation strain, this increment occurs at more or less a constant value of the contact radius. Further evidence for the lack of a sudden increase in the contact radius also comes from a close inspection of the stiffness signal, which showed that the harmonic stiffness remained more or less constant during the pop-in, as shown in Fig. 13b. Since the harmonic stiffness (S) is directly proportional to the contact radius a ($a = S/2E_{eff}$, see Eq. (3)), we can again infer that contact radius did not change much during the pop-in event. Therefore all measured signals during the pop-in are highly consistent with the inference that the contact radius remains more or less constant during the pop-in event.

A second salient feature in the plots shown in Fig. 13b is that there is a short regime of rapid increase in the contact radius a (also seen in the CSM signal) with additional indentation depth immediately following the pop-in. Consequently, there is a rapid decrease in the

indentation stress, which in turn produces the unloading segment seen in Figs. 10, 12, and 13a immediately after the pop-in event. In this unloading segment, the contact radius is increasing much faster than the indentation depth. Hence the overall indentation strain decreases in spite of the fact that the total indentation depth is continuously increasing (note how indentation strain is defined: $\varepsilon_{ind} \approx h_e/2.4a$, see also Eq. (6)). Since the indentation stress is decreasing in this unloading segment, it is reasonable that the unloading modulus in this segment is very close to the modulus measured in the initial loading segment.

The data point at the end of this regime of rapid increase in the contact radius is marked with gold color in Fig 13. By tracking the location of this particular data point in the different plots, it is clearly seen that this regime ends when the indentation stress has fallen to the levels consistent with ISS curves without pop-ins.

It is emphasized here that the trends and insights obtained above regarding pop-ins would not have been possible with the traditional data analyses protocols. For example, the use of protocol C (see table in Fig. 3a) would have suggested that the contact radius increased substantially during the pop-in event because an excursion in the indentation depth would automatically produce an increase in the indentation contact depth (h_c). Not only would this inference be inconsistent with the stiffness measurement, it would also produce an unloading segment with a negative slope. Unloading segments in stress strain curves with negative slopes are completely unphysical as they would imply that while the stress is reducing (which has to be accompanied by a reduction of elastic strain) the total strain is simultaneously increasing by significant amounts.

Figure 14 presents a conceptual model for what might happen during a pop-in that is consistent with the observations made above. As mentioned earlier, the pop-ins are produced by

sudden activation of dislocation sources (upon reaching a certain combination of local stress and size of the indentation zone), which in turn facilitates plastic strain under the indenter by the familiar process of dislocation slip on specific slip systems [74, 78, 85, 86]. The observations described in Fig. 13 suggest that the slip bursts that occur during the pop-in event are actually altering the profile of the sample surface without changing the contact radius significantly. These uncontrolled slip bursts help diffuse the high elastic stresses under the indenter. It is well known from Hertz's model that the stress fields in the indentation zone are such that the highest driving force for plastic deformation occurs at some distance below the indenter tip (not on the sample surface). For an isotropic material, the highest shear stress (needed to initiate plastic strain) is expected to occur at a distance of $0.5a$ below the indenter, where a is the contact radius. Dislocations should therefore be expected to start well below the indenter tip, and travel (in bursts) on specific crystallographic slip systems (e.g., $[110]$ directions on (111) planes in fcc metals [87]). It is also important to recognize that the sample free surface is likely to play an important role in facilitating these slip bursts. For example, the rigid conformation of the indenter and the sample in the contact region would not allow the formation of the step-like features needed to release the dislocations. The sample free surface on the other hand will allow the easy release of the dislocations.

The schematic in Fig 14a gives a possible explanation of how the dislocation burst of a pop-in might significantly alter the profile of the free surface of the sample just outside the indenter contact region, while not changing the contact radius itself. Such a process is expected to be asymmetric, i.e. the profile change is expected to happen only over a limited area for a single pop-in. However, any additional indentation depth immediately following the pop-in would cause a sharp increase in the contact radius (and a corresponding increase in the stiffness

measurement). This expected rapid increase in contact radius and stiffness immediately after the pop-in matches well with the contact radius (CSM) measurements shown in Fig. 13b.

In order to test the above hypothesis the resultant surface profile immediately after a pop-in event (after the load has been taken off) was mapped using an *in-situ* SEM atomic force microscope (AFM). Figure 14b shows the load-displacement curve of the indentation test on a near-(001) surface of aluminum, where the test was stopped after a single large displacement burst of around 180 nm using a 1 μm spherical indenter. As expected, the pop-in produced a large slip burst on one of the potential slip systems – the one that presumably experienced the largest resolved shear stress during the indentation loading. This leads to the appearance of a step-like feature and an associated pile-up along the [110] direction as shown in Figs. 14b (inset) and 14c. The AFM surface profile map shown in Fig. 14c indicates that there are major differences in the residual surface profile of the indent between the direction of the slip burst ([110]) and normal to that direction ($[\bar{1}10]$), and that the major changes in the sample surface profile have occurred outside the contact region. Thus any further loading of the indenter beyond the burst would cause a rapid rise in a and a subsequent decrease in the indentation stress.

The AFM profile shown in Fig. 14b and c also demonstrates the significant anisotropy of the residual imprint. It is easily apparent from these figures that any value of contact radius estimated based on the geometry of the spherical indenter (using Eq. 4 and protocols B and C, see Fig. 4) would be in significant error. Moreover if the indentation is allowed to proceed well beyond the initial burst there would be slip bursts along all of the primary (111) slip planes. Due to the crystallography of the indented (001) surface, the primary slip planes ($\bar{1}\bar{1}1$) and (111) would intersect the indented plane along the [110] and $[\bar{1}10]$ directions. Thus the activation of the above slip systems would produce an excess material pile-up in these directions resulting in a

four-fold pattern of material pile-up around the indent along the [110] directions, as has been noted in literature [87].

5.5 Effect of the Continuous Stiffness Measurement on Indentation Stress-Strain Curves Analysis

The introduction of continuous stiffness measurement (CSM) has been one of the significant recent improvements in nanoindentation testing techniques. CSM is implemented by applying a small, sinusoidally varying load on top of the primary load signal and measuring the amplitude and phase of the displacement oscillation at the same frequency by means of a frequency-specific amplifier [7, 8, 60]. The stiffness (given as the ratio of the load amplitude to the displacement amplitude for elastic contact) can then be measured continuously during the indentation test. The CSM, because of its ability to continuously record the contact stiffness, is central to the extraction of indentation stress-strain curves from the measured raw load-displacement datasets using Eqs. (3-7).

A number of recent reports using sharp tip indenters on both metallic [88-94] and visco-elastic [95, 96] material systems have indicated that the use of CSM can impact directly the values of the measured mechanical properties. These researchers have found that some materials, particularly those with a high modulus to hardness E/H ratio such as Ni single crystal ($E/H \approx 170$) [92], Cu single crystal ($E/H \approx 225$) [89], MgO [94], and Ir ($E/H \approx 210$) [93] show significant softening at low (<100 nm) indentation depths, when using the CSM. Figure 15a describes this effect for hardness (H) values measured on (100) Cu single crystal using a Berkovich indenter [89]. These experiments were performed at various displacement oscillation amplitudes nominally in the range 1–12 nm as characterized by the root-mean-square (rms) displacement amplitude, Δh_{rms} . These researchers used two techniques to measure the hardness –

the first using the Oliver-Pharr method of analysis on the load-displacement data using the stiffness values measured by the CSM along with the calibrated area function (based on measurements on fused silica [7, 8]), and the second by imaging the residual imprints from tests with the CSM turned off ($\Delta h_{rms} = 0$). The following observations can be made from this image: (i) at large depths and small amplitudes, the hardness values measured using CSM agree well with those estimated from SEM images, (ii) at large depths and large amplitudes, the CSM-measured hardness values are significantly lower than the ones estimated from SEM images, and (iii) at small depths, the differences are significant even for small amplitudes.

A part of the discrepancy described above stems from the basic assumption in CSM-related analysis that the amplitude of the oscillation applied is very small, i.e. the effects of such an oscillation on the overall load-displacement behavior can be ignored. This assumption was analyzed critically by Pharr et al. [89], and was found to break down for materials with a high modulus to hardness E/H ratio. The authors identified three main sources of error in the data analyses protocols with the CSM. Firstly, the load and the displacement values are underestimated with the use of CSM. This is due to the fact that the machine does not record the peak values of load and displacement when using the CSM, but rather their mean values during the oscillation cycle. However, the material being tested actually experiences the load and displacement corresponding to the maxima of the superimposed oscillations. Pharr et al. suggest the following simple corrections for this error:

$$P_{act} = P_{app} + \frac{\Delta P}{2} \quad \text{or} \quad P_{act} = P_{app} + \sqrt{2}\Delta P_{rms} \quad (11)$$

$$h_{act} = h_{app} + \frac{\Delta h}{2} \quad \text{or} \quad h_{act} = h_{app} + \sqrt{2}\Delta h_{rms} \quad (12)$$

where P and h refer to the load and displacement signals, respectively, and the subscripts act and app refer to the actual values experienced by the sample and the apparent values recorded by the machine, respectively. ΔP and Δh are the peak-to-peak load and displacement ranges, respectively, associated with the superimposed oscillations when using CSM. The corrections are easy to apply since the machine provides the rms values of the oscillating signal.

The second source of error results from an underestimation of the contact stiffness (S). The apparent stiffness ($S_{app} = \Delta P / \Delta h$) reported by the machine is essentially the ratio of the peak-to-peak amplitudes of the load and displacement signal. However, from Hertz theory [97, 98], it is known that the relationship between load and displacement is not linear in the elastic regime (Eq. 1), and therefore this measurement underestimates the stiffness at peak load. By modeling the unloading curve in nanoindentation, the actual stiffness S_{act} can be computed from the apparent stiffness S_{app} as follows:

$$S_{act} = \frac{1}{\sqrt{2\pi}} \frac{P_{max}}{\Delta h_{rms}} \left(\frac{1}{K} \right)^{1/m} \left[1 - \left(1 - \frac{2\sqrt{2}\Delta h_{rms}S_{app}}{P_{max}} \right)^{1/m} \right] \quad (13)$$

where S_{act} is the corrected stiffness signal, K and m are constants ($K = 0.757$ and $m = 1.38$ for Berkovich indenters [89] and $K = 0.6524$ and $m = 3/2$ for spherical indenters [99]).

The third source of error identified in Ref. [89] arises from the loss of contact between the indenter tip and the sample at low loads during the dynamic oscillations. This is specially true for materials with a high modulus to hardness E/H ratio, where the amount of dynamic unloading during the displacement oscillation may become larger than the total applied force (at small total depths of penetration). When this happens the indenter behaves as the tapping mode operation of an atomic force microscope, where it lifts from the surface and loses contact during part of the oscillation cycle. Note that while this process has been successfully modeled in Ref.

[89] including estimations of the depth below which tapping occurs, no corrections were suggested for this error. The authors of Ref. [89] recommend that the measurements be performed at smaller displacement oscillation amplitudes in order to reduce this error.

The hardness data for Cu (100), with corrections to P , h , and S (Eqs. 11-13), is shown in Fig 15b. It is apparent that as compared to the uncorrected data in Fig. 15a, the corrected CSM-hardness curves are higher. The CSM-hardness values after corrections also match well with the hardness values measured directly in the SEM for large indentation depths. However at small depths, the tapping problems prevail, and the measured hardness values, even after correction, continue to underestimate the true values.

The effects of the CSM corrections (Eqs. 11-13) on the extraction of indentation stress-strain curves from spherical indenters and on the estimations of the contact radius have been studied in detail by Vachhani et al. [99] and is summarized in Figs. 15c-16f. Note that the data shown in these figures have already been corrected for the effective zero-point (using Eq. 7) which also indirectly corrects for the tapping problem mentioned earlier. Figures 15c and 15e show the original harmonic stiffness-displacement ($S-h_t$) and indentation stress-strain responses for high purity 20% deformed aluminum measured using a 100 μm radius spherical tip over a range of frequencies and Δh_{rms} values, while Figs. 15d and 15f show the same after using the corrections mentioned above in Eqs. 11-13 respectively. The values for the harmonic contact stiffness are seen to be progressively lower for the tests carried out with CSM at 10 Hz–2 nm and 10 Hz–1 nm oscillations respectively particularly at higher indentation depths, compared with the tests carried out at 45 Hz frequency (Figs. 15c, 15d). On the other hand, the 45 Hz–1 nm oscillations showed higher levels of inherent noise in the stiffness signal. The authors also

observed that the corrections from Eqs. 11-13 failed to bring the curves for the displacement–harmonic stiffness data with the different CSM conditions closer (compare Figs. 15c and 15d).

Similar trends were also seen in the indentation stress-strain data (Figs. 15e, 15f). Thus the data is noisiest for the tests carried out at the 45 Hz–1 nm test condition, and the tests carried out using the 10 Hz–2 nm and 10 Hz–1 nm CSM conditions show pronounced post-elastic hardening, with the effect being most severe for the latter. Since both stress and strain are inversely related to the contact radius and hence inversely related to the stiffness as well (see Eqs. 3-7), these trends can be directly related to the lower stiffness values recorded for these test conditions. The authors in Ref. [99] have hypothesized that the decrease in the stiffness values at higher indentation depths is a likely artifact of the machine dynamic control system, while the higher noise levels for the stiffness signal obtained for the 45 Hz–1 nm CSM condition could be due to the fact that this test condition presents the most difficult case for the feedback control to accurately maintain low-amplitude–high-frequency oscillations.

The corrections in Eqs. 11-13 appear to have a much smaller effect on the spherical indentation stress-strain curves as compared to their effect on the raw data (compare Figs. 15a, 15b to Figs. 15c-15f). The results in Ref. [99] suggest that the corrections to individual signals appear to negate each other to some extent in the indentation stress-strain computations. In some cases the corrections can also be detrimental to the indentation stress-strain calculations; for example most of the initial elastic segment for the 45 Hz–2 nm CSM condition was lost while correcting for the stiffness signal using Eq. 13 (Fig. 15f).

Thus, for accurate estimation of the indentation stress-strain curves, the authors in Ref. [99] suggest that the CSM corrections (Eqs. 11-13) be skipped altogether; the CSM signal at 45

Hz–2 nm oscillations was also deemed to be the most reasonable choice for indentation stress-strain calculations.

6. Applications: Combined OIM - Indentation Studies on Metallic Samples

Since the length scales in nanoindentation are smaller than the typical crystallite (also called grain) sizes in polycrystalline samples, this technique is an ideal tool for detailed characterization of the microscale heterogeneities present in these materials and their evolution during various metal shaping/working operations. The local mechanical properties measured at these length scales using indentation are expected to be strongly dependent on the local material structure at the indentation site. For example, one should expect the local lattice orientation(s) at the indentation site to influence strongly the elastic-plastic properties extracted from the indentation datasets obtained on polycrystalline samples. However, in most currently used experimental protocols, the differences in properties extracted from different locations on a given polycrystalline sample are often treated as “experimental scatter” and just averaged in reporting the measured properties. It is argued here that these differences arise because of the inherent differences in the local material structure at the indentation site. For example, it is fully expected that the indentation yield strength (Y_{ind}) will vary significantly from one crystal orientation to another, even in fully annealed samples where there are no major differences in the dislocation content of the differently oriented grains (see the illustration in Fig. 16a). This is because the plastic deformation imposed by the indenter needs to be accommodated locally at the indentation site by slip activity on the available slip systems, whose orientation and activation are strongly dependent on the local crystal lattice orientation with respect to the indentation direction. It is

now possible to measure the local lattice orientation in polycrystalline samples using a technique called Orientation Imaging Microscopy (OIM) [100, 101]. This method is based on automated indexing of back-scattered electron diffraction patterns (obtained using a scanning electron microscope) and has a spatial resolution of less than a micron, with certain new enhancements promising to improve the spatial resolution to below 10 nm [102]. Therefore, coupling the structure information obtained from OIM with the mechanical data obtained from nanoindentation should produce vastly enriched datasets that are potentially capable of providing new insights into the local elastic-plastic properties of interest.

Additionally, when subjected to plastic strain (especially when deformed at low homologous temperatures; also called cold-working) metallic samples are known to harden significantly. However, as a result of the grain-scale heterogeneity in their microstructures, the individual grains do not harden equally. This is demonstrated schematically in Fig. 16 for as-cast and 30% deformed polycrystalline samples of Fe-3%Si steel. Fig. 16c shows the indentation stress-strain curves obtained from the raw displacement datasets shown in Fig. 16b respectively. Of main interest here are the differences seen in the elastic indentation moduli, the indentation yield strengths, and the post-yield characteristics in the measurements at different locations in the as-cast samples and in the deformed samples. Indeed these differences are more easily seen in the indentation stress-strain plots compared to the raw load-displacement plots. We note again that it is only possible to extract reliably the estimates of the indentation moduli and the indentation yield strength from the initial elastic portion of the indentation stress-strain curve, because the indentation itself will alter the local microstructure and its properties once it imposes additional local plastic deformation.

In this section, we illustrate how the data obtained from the initial loading segments of spherical nanoindentation, when combined with the complementary structure information measured locally at the indentation site, can be utilized to provide new physical insights into the local elastic-plastic properties of interest. Using a series of examples, we demonstrate that it is possible to extract information on the local elastic-plastic properties of constituent single crystals in a polycrystalline sample. We also demonstrate the potential of this new approach to interrogating the mechanical response of interfaces (e.g., grain boundaries) in the samples. New physical insights into all of the phenomena mentioned above at these lower length scales are crucial for the further development of physics-based multiscale material models for polycrystalline material systems.

6.1 Quantifying Elastic and Plastic Anisotropy of Single Crystals

As discussed above, the changes in the yield strength of individual grains in a polycrystalline metallic sample are a combination of both the local crystal lattice orientation at the indentation site as well as the macroscale plastic deformation imposed on the sample. Therefore, a rigorous methodology is needed to decouple these two effects – once we can successfully account for the effect of the crystal lattice orientation on the indentation yield strength it should then be possible to estimate the local increase in the average slip resistance (and hence indirectly estimate the dislocation content) at the indentation site [103].

One major challenge in using indentation stress-strain curves for this task arises from the fact that the mechanical response of individual grains is inherently anisotropic, whereas the nanoindentation data analyses methods shown in Eqs. (6) and (7) are built on Hertz's theory [17] that assumes an isotropic elastic material behavior. The problem of elastic indentation of anisotropic samples has been studied in detail by Vlassak and Nix [104, 105], who propose a

modified form of Hertz's analysis designed for cubic materials. These authors demonstrate that Eqs. (2) and (3) can be used for elastic indentation of cubic crystals, provided an anisotropy parameter, β , is appropriately introduced into the definition of the effective indentation modulus. In particular, they show that Eq. (2) can be modified as

$$\frac{1}{E_{eff}} = \frac{1}{\beta} \left(\frac{1 - \nu_s^2}{E_s} \right) + \left(\frac{1 - \nu_i^2}{E_i} \right) \quad (14)$$

In Eq. (14), E_s and ν_s denote the effective values of Young's modulus and Poisson's ratio, respectively, for a randomly textured polycrystalline aggregate of crystals with the same elastic properties as the single crystal being studied [104, 106]. For cubic crystals, the value of β depends strongly on the crystal lattice orientation and the degree of cubic elastic anisotropy. The elastic anisotropy (A) of a cubic crystal is usually defined by $A = 2C_{44}/(C_{11} - C_{12})$, where C_{11} , C_{12} , and C_{44} denote the cubic elastic constants used to define the crystal elastic stiffness in its own reference frame.

The modified form of Hertz's theory shown in Eq. (14) is highly amenable to the analyses protocols described earlier for obtaining nanoindentation stress-strain curves. This has been demonstrated in Ref. [64] using measurements on as-cast polycrystalline samples of Fe-3%Si steel with very large (~mm) sized grains. The OIM scan of the sample used in Ref. [64] is shown in Fig. 17a. The OIM scans are color-coded to reflect the positions of the orientations in the inverse pole figure map in Fig. 17b using the standard convention (i.e. grains colored red, green, and blue have (001), (101), and (111) crystallographic planes parallel to the sample surface respectively). As seen from Fig. 17a, the selected region of the sample has a range of grain orientations that provide a good coverage of the corners of the fundamental triangle in the inverse pole figure map shown in Fig. 17b. Because of the very large grains in the sample, the

indentation measurements in any one grain are also unlikely to be influenced by the neighboring grain orientations or grain boundaries.

For the as-cast sample shown in Fig. 17a, the anisotropic elasticity parameter β , and the back-extrapolated indentation yield strengths Y_{ind} , were calculated [64] for a total of 11 different grain orientations. The values of β were computed using Eq. (14), by assigning the values of E_s and ν_s to be 207.9 GPa and 0.3 following the approach described in [104, 106], while Y_{ind} was calculated using the back-extrapolation method shown in Fig. 16c. The grain orientation, measured by OIM, is in general described by a set of three angles called Bunge-Euler angles [107], usually denoted as $(\varphi_1, \Phi, \varphi_2)$. Since the rotation of the sample about the normal to the indentation surface (i.e. the ND direction) does not influence the measurements presented here, the indentation modulus and the indentation yield strengths measured using a spherical indenter are functions of only two of the Bunge-Euler angles, namely (Φ, φ_2) .

By interpolating the values β and Y_{ind} in the 11 grains studied, contoured surface plots of the dependence of β and Y_{ind} on the grain orientation were obtained, and are shown in Figs. 17c and 17d, respectively. As seen from Fig. 17c, the measured differences in the indentation moduli range from a minimum of $\beta = 0.92$ to a maximum of $\beta = 1.12$. These measurements are highly consistent with the values predicted by Vlassak and Nix [104], who predicted values of 0.90 for (001) oriented grains, 1.04 for (101) oriented grains, and 1.10 for (111) oriented grains based on an anisotropy factor of $A=2.84$ for Fe-3%Si. Another important observation from Fig. 17d is that the differences in the measured Y_{ind} values of different grain orientations are as high as 30%. Since there are no expected differences in the dislocation content of the differently oriented grains in the as-cast sample studied here, all of the observed differences in the indentation yield

strengths are attributable to differences in the activities of the different slip systems in the different grains and their orientation with respect to the indentation direction (see the illustration in Fig. 16). Note also the similarity between the two plots in Figs. 17c and 17d, indicating a high degree of correlation between the measured indentation moduli and the indentation yield strengths for the differently oriented grains. Similar results have also been obtained for fcc metals, attesting to the broad applicability of the protocols described above. For the fcc metal studied, it was shown that the influence of the crystal lattice orientation on the measured indentation yield strength could be as large as 40%, with the lowest values corresponding to the [100] (cube) orientation and highest values corresponding to the [111] orientation. The value of these plots (especially the plot for Y_{ind}) will become clear as the data analysis methods for deformed samples are discussed in the next section.

6.2 Estimating Local Slip Resistance in Deformed Cubic Crystals

In order to track and estimate the changes in the local slip resistance in deformed samples we first need to account for the effect of the crystal lattice orientation at the indentation site. It is suggested that the plots shown in [64] and in Figs. 17c and 17d capture this effect quite accurately for Fe-3%Si, and could be used in studies on the deformed samples of this material.

As a specific example, one of the as-cast Fe-3%Si samples was subjected to 30% reduction in simple compression, and another as-cast sample to 80% reduction in plane strain compression (see Fig. 18). These reduction levels were selected to produce one moderately deformed sample and one heavily deformed sample. Indentations were performed in selected regions within individual grains in each of the deformed samples. The indentation measurements on the deformed samples are summarized in the table in Fig. 18c. For each of the grains studied in the deformed sample, the indentation yield point was estimated in the fully annealed condition

using the grain orientation and the contoured plot presented in Fig. 17d. In other words, this would have been the indentation yield point if the same grain was in the as-cast sample. As discussed in the previous section, it is important to establish this value because it can vary by as much as 30% from the near-(001) “soft” orientations to the near-(111) “hard” orientations. The difference between the measured indentation yield point in the deformed sample and the estimated indentation point in the as-cast condition then provides a reliable estimate of the increment in the indentation yield point at the indentation site in the deformed sample. This increment can be attributed to the changes in the dislocation content at the indentation site from its initial state in the as-cast sample (see the illustration in Fig. 16).

The simplest relationship one can establish between the increment in the indentation yield point and the local dislocation content is through the increment in the critical resolved shear strength of the slip system. In a highly simplified approach, this relationship has been expressed in [64] as

$$Y_{ind} = M(\Phi, \varphi_2) \tau_{CRSS}, \quad \Delta \tau_{CRSS} \propto \sqrt{\rho} \quad (15)$$

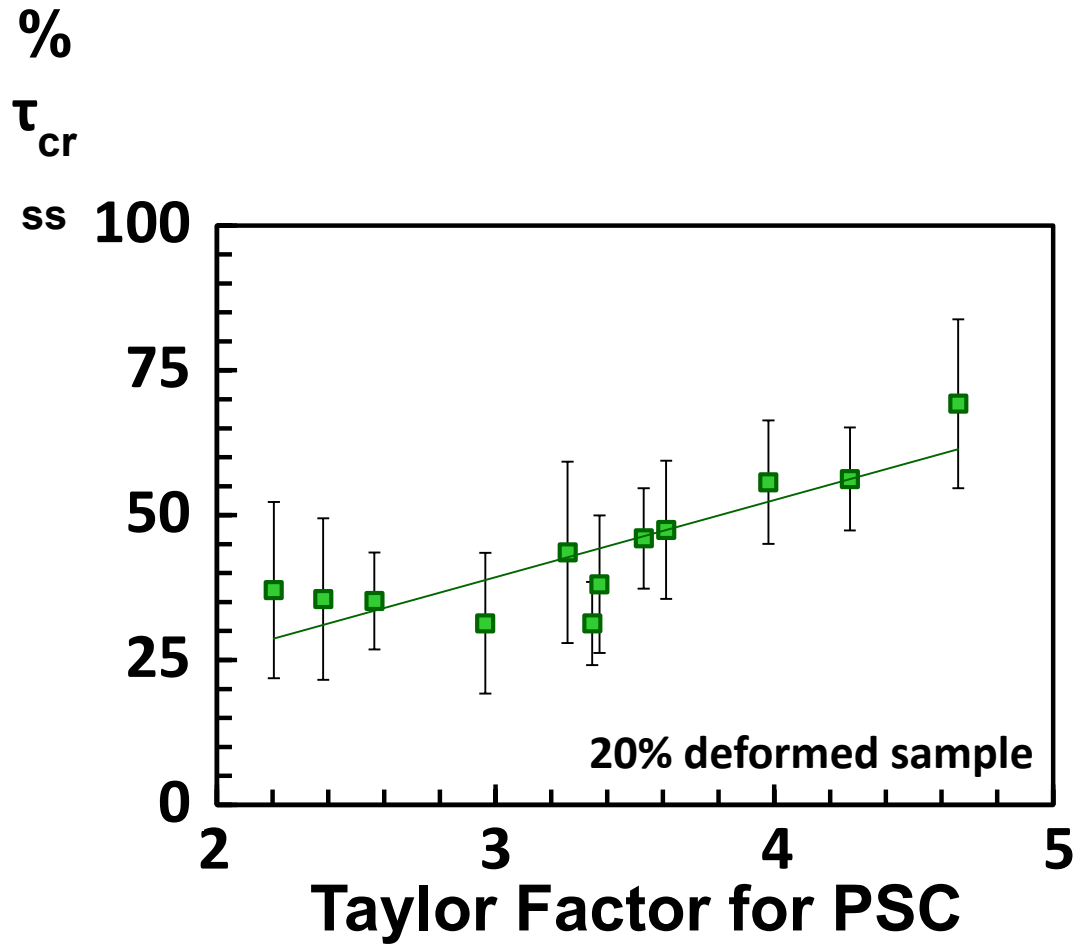
where M is a Taylor-like factor that depends only on the grain orientation, τ_{CRSS} is the averaged critical resolved shear stress in the crystal, $\Delta \tau_{CRSS}$ is the increment in the local averaged critical resolved shear strength between the as-cast and cold-worked conditions, and ρ is the local dislocation density. Since the factor M is the only orientation dependent variable, it is easy to see that percentage increase in the indentation yield point should be equal to the percentage increase in τ_{CRSS} . These are reported in the table in Fig. 18c for all the measurements obtained on the deformed sample [64]. The percentage increases in τ_{CRSS} provide an indirect measure of the local dislocation content or the local stored energy in the deformed sample. As seen from the table in

Fig. 18c, the changes in τ_{CRSS} vary significantly from one deformation step to another and also from one region to another in the same deformed sample resulting in a heterogeneous microstructure in the deformed polycrystalline samples. It is also clear from Fig. 18c that any conclusions drawn regarding the local slip resistance or the local dislocation content directly from the measured indentation yield points without accounting for the effect of the crystal lattice orientation at the indentation site would be highly erroneous.

The protocols described above have the potential for opening completely new avenues of research by facilitating the measurement of both local structure (using OIM) and its associated mechanical properties (using spherical indentation). For example, numerous studies have been reported in literature [108-111], where the microstructure evolution during finite plastic strains in polycrystalline samples has been carefully documented using OIM. While the goal of these studies was to derive a better understanding of the microscale deformation mechanisms in these materials, they were significantly limited by the inability to document the corresponding evolution of the local mechanical properties (at the grain-scale). The combined OIM-spherical indentation approach was utilized by Stojakovic [112] in his investigations on the effects of thermo-mechanical processing on polycrystalline Fe-3%Si samples with columnar grains. This is shown in Fig. 19 which illustrates the deformation of the columnar Fe-3%Si sample to a true strain of 1.21 in plane strain compression. In this sample, the compression was interrupted at selected strain levels and the microstructure was documented using OIM and the evolution of the local mechanical (plastic yield) properties were tracked using the spherical nanoindentation protocols described above. Only minor changes are visible in Fig. 19a as the strain is increased first to 0.34 and then to 0.81, apart from a slight increase in grain misorientation and a steady grain elongation in the rolling direction. However at the highest strain of 1.21 the sample

develops significant heterogeneity at the grain-scale (both between grains as well as within the original grains) in both structure as well as mechanical properties (see the table in Fig. 19b). It is seen that the B regions of the split grains have rotated away from their initial orientations, and they also show a large difference in indentation yield behavior from their A counterparts (see grains 5A, 5B, 6A and 6B in particular). It is therefore now possible to acquire a very large amount of information using this approach, which when carefully analyzed will provide new insights into the microscale mechanisms of plastic deformation in polycrystalline metals.

In this a more recent study, the approaches described above have been successfully demonstrated on deformed polycrystalline samples of Al (an fcc metal). Of particular note was the fact that the a clear positive correlation was observed between the percentage increase in the local slip resistance and the value of the Taylor factor computed for the local crystal orientation at the indentation site subjected to the macroscale imposed deformation (see Figure x). This important observation suggests that orientations with a lower Taylor factor (soft grains) harden at a lower rate compared to grains with a higher Taylor factor (hard grains). In fact, the authors go on to explain the observed linear relationship in Figure x with a highly simplified physical model for the hardening rate in each grain.



The above examples demonstrate a meaningful approach for extracting correlations between local crystal lattice orientation measurements obtained from OIM and the estimates of local elastic and yield properties from nanoindentation measurements.

6.3 Investigations of Grain Boundary Regions

Indentation stress-strain curves – due to their ability for obtaining meaningful mechanical information from indentation depths of as small as a few nanometers – have great potential in interrogating the mechanical role of interfaces (e.g. grain boundaries) in a polycrystalline sample. Since this technique can be applied across individual grain boundaries in a polycrystalline sample, they can be efficiently used to probe the physical origins of a number of

interface-related strengthening mechanisms (e.g., the well-known Hall-Petch effect [113, 114]) in these materials.

As described in the earlier sections, the use of these indentation stress-strain curves makes it possible to analyze the initial loading segments of spherical indentation, thereby allowing us to obtain measures of elastic modulus and indentation yield strength of the material prior to the damage induced by the indentation itself. This approach is fundamentally different to other indentation studies involving grain boundaries reported in literature which have primarily focused on measuring the resistance offered by grain boundaries (i.e. the hardness) to dislocation transmission across them using sharp (Vickers, Berkovich, cube corner) indenters [83, 84, 115-123]. In these studies, the sharp indenters introduced substantial amount of plastic deformation in the sample before the dislocations were pushed to the grain boundaries and impeded by them. Therefore, the plastic deformation introduced by indentation in those experiments is likely to strongly influence the mechanical property being measured.

The effect of plastic deformation caused by the indentation itself was systematically studied by Eliash *et al.* [83] in their study of indentation hardness across grain boundaries in molybdenum, and is shown in Fig. 20. The grain boundary affected zone in the figure can be seen to become progressively less pronounced with increasing maximum indentation load (and hence increasing plastic deformation due to indentation). For indentation loads exceeding 10 mN (for a Berkovich tip) the indentation induced hardening masks the effect completely and the trend vanishes. Indeed the subtle changes of hardness across the grain boundaries have only been reported for low load indentations [84, 115, 118, 120-122]; indentations at high loads have been a poor indicator for measuring grain boundary strengthening effects [119, 124]. Moreover, under such high loads, significant indentation strain imposed by the indenter can also cause the local

crystal orientation under the indenter to change [64]. These studies point to the importance of calculating the contact stresses at or close to yield in indentation experiments.

The application of spherical nanoindentation stress-strain curves as an effective tool for this purpose was demonstrated in [62] where the authors measured the differences in indentation modulus and yield stresses across grain boundaries both as a function of the grain boundary character (high vs. low angle grain boundary measured using OIM), and imposed cold work on the sample. The main results are presented in Fig. 21. In this figure, the grains are labeled as ‘soft’ and ‘hard’ in a relative sense based on their indentation yield strengths. Figure 21a shows the results for the as-cast Fe-3%Si samples. Since the as-cast samples are not expected to have any excess dislocation storage at the grain boundaries, both E_{eff} and Y_{ind} are fairly uniform in each grain and there is almost a step transition at the grain boundary.

However the response changes markedly once the samples are deformed to 30% (Fig. 21b). Here although the values of E_{eff} are fairly uniform in each grain and show a step like transition at the grain boundary (as in the as-cast sample), the variation of Y_{ind} indicates a substantial transition zone on one side of the grain boundary. Further insights are obtained when these values are normalized to account for the orientation dependence of the indentation measurements (following the procedure discussed earlier in Section 6.2). Since the percentage increase in the Y_{ind} can now be interpreted as the percentage increase in the local slip resistance (and hence as an indicator of the local dislocation density) at the indentation site, it appears that the grain boundary region on the side of Grain D5 accumulated much less dislocation density in the immediate vicinity of the grain boundary than far away from the boundary. Furthermore, the dislocation density very near the grain boundary on the side of Grain D5 is also seen to be somewhat lower than the dislocation density in the grain boundary region on the side of Grain

D4. These observations suggest that the nature of the grain boundary or the grain boundary character on both sides of a grain boundary can be substantially different from each other. In other words the grain boundary on the side of Grain D5 is thought to be acting as an efficient dislocation sink by absorbing the dislocations from the grain boundary region on the side of Grain D5. The above example demonstrates how monitoring the changes in Y_{ind} can offer indications about the roles of certain grain boundaries in mechanical deformation. Similar trends were also reported more recently for polycrystalline deformed samples of Al [125].

6.4 Investigations of Surface Modifications

The indentation stress-strain protocols described here in the review paper are particularly attractive for systematic studies of surface modifications (e.g., coatings, irradiated layers, shot-peened surfaces) because of the extremely small indentation volumes (with length scales as small as 50 nms). An example of the versatility of this approach has been shown in the work of Wheeler et al. [126] in their study of electrolytic coatings which are routinely used to modify the surface of a 5052 aluminum alloy (AA5052) up to a depth of 50-100 μm . Figure 22 compares the main results of their work across the cross-sections of two leading electrolytic coating methods – hard anodizing and plasma electrolytic oxidation (PEO) on AA5052. Note the significant differences in the indentation stress-strain responses of the modified surfaces as compared to the original AA5052 substrate. The PEO coatings also show higher yield stresses and post-yield hardening as compared to the anodized coatings, with the highest values coming from the tests located closest to the substrate-coating interface. These effects have been correlated in [126] to the differences in the microstructure of the modified surfaces (crystalline vs. amorphous for PEO and anodized respectively), as well as changes in porosity and crystallinity with distance from the substrate-coating interface.

Other surface modification techniques, such as the study of mechanical degradation of irradiated materials [127-129], are more challenging because of extremely small thickness of the damaged layer (typically less than a micron, Fig. 23a). Most commonly used nano-mechanical test techniques, such as ones requiring the use of focused ion beams (FIB) to fabricate micro-pillars or any other such small scale test geometries [130-134], are not likely to be able to address this challenge. Nanoindentation, with its high resolution load and depth sensing capabilities, shows the greatest promise due to its non-destructive nature, ease of experimentation (only a polished surface prior to ion irradiation is needed) and versatility [3, 130, 135-137].

One of the main advantages of nanoindentation techniques is that it allows a systematic study of the local mechanical responses at different length scales, accomplished by simply varying the indenter tip radii. As an example the table in Fig 23d shows the approximate indentation depth (h_i) and the corresponding contact radius (a) and the depth of the indentation zone (which scales as $2.4a$, see Eq. 6) at yield in annealed tungsten for 4 different indenter radii. A proper choice of indenter size can thus match the volume probed by nanoindentation (Figs. 23a and 23b [44]) to the depth of radiation-damaged (or any other surface-modified) region of interest (Fig. 23c). Furthermore, the ability to make a large number of measurements on a given sample surface also has the potential to provide quantitative information on the variance of properties in the irradiated layer.

Figures 24a-24c show spherical nanoindentation measurements reported recently [138] on annealed (not irradiated) and He ion-irradiated samples of electro-polished tungsten using indenters tips of different radii. All of the measurements reported in these figures were for grains whose surface normals were very close to [100] directions. These grains were purposely

selected to avoid the need to correct for the effect of the lattice orientation at the indentation site in comparing the different measurements presented in these plots (see Section 5.1).

The indentation stress-strain curves from the irradiated samples revealed several interesting features. Strikingly, none of the measurements (including the measurement with the smallest indenter tip $R_i = 1 \mu\text{m}$, Fig 24a) revealed any pop-ins (cf. the measurements on the annealed samples which clearly show pop-ins for the measurements with the smaller indenters). This is consistent with the expectation that the ion-irradiation introduces a large density of defects in top surface of the material (e.g., radiation induced defects such as dislocation loops [139], He bubbles, etc.) that can help set up highly potent dislocation sources without any need for pop-ins [140]. Another obvious consequence of these new defects introduced by irradiation is that the Y_{ind} values in the irradiated samples are higher than the corresponding values in the annealed samples. It is also observed that in addition to the higher yield values, the irradiated samples are exhibiting higher hardening rates compared to the annealed samples.

As mentioned earlier, upon ion-irradiation the metal surface is modified by a thin radiation-damaged layer (see Fig. 23a), and investigations with different indenter radii can help ascertain the depth and severity of this damage. The post-yield measurements on the He-irradiated near (001) grain with the $1 \mu\text{m}$ radius indenter tip (see Fig 24a) indicate a zone of very high strain hardening (within a short range 0.03-0.1 of indentation strains) followed by a regime of near stress saturation [139, 141, 142] with a slight softening in stress from 11.6 to 10.5 GPa. The contact radius in this test was estimated to range from $\sim 32 \text{ nm}$ at Y_{ind} to $\sim 200 \text{ nm}$ at an indentation strain of 0.1 (end of hardening zone) to $\sim 500 \text{ nm}$ at the end of the test (indentation strain of 0.2). The indentation stresses at $a \sim 500 \text{ nm}$ were still significantly higher (10.5 GPa) in the irradiated sample as compared to the annealed material (6.2 GPa) tested with the same indenter. These

observations indicate that the damage layer due to irradiation extends to depths of the order of 500 nm (assuming that the active indentation zone size is at least of the order of the contact radius a , see Figs 23a-c). On the other hand, the corresponding measurements with the $R_i = 10\ \mu\text{m}$ indenter tip (Fig. 24b) show an initial post-elastic zone of a high strain hardening (from an indentation strain of 0.02 to 0.045) followed by a regime of marked softening. Intriguingly, the softening regime brings the indentation stress values in agreement with the values measured with the same indenter on the annealed samples. These measurements suggest that the initial hardening regime for the $R_i = 10\ \mu\text{m}$ indenter is attributable to the plastic deformation induced by the indenter in the irradiated top layer, while the later softening regime is attributable to the expansion of the plastic zone to the undamaged annealed region below the irradiated top layer. Support for this hypothesis comes from the estimated values of the contact radius in this measurement (using Eq. 3). The contact radius for the $R_i = 10\ \mu\text{m}$ indenter after irradiation is estimated to be $\sim 260\ \text{nm}$ at Y_{ind} , $\sim 500\ \text{nm}$ at the peak indentation stress level, and $a \sim 1.5\ \mu\text{m}$ at the end of the test (Fig. 24b). These measurements suggest that the irradiated layer in this sample is of the order of 500 nm.

As expected, in the measurement with the larger $R_i = 100\ \mu\text{m}$ indenter tip (Fig 24c) the differences between the measurements from the annealed and the irradiated samples are very small. This is not surprising since the contact radii at Y_{ind} for both the annealed and irradiated cases are around $a \sim 1\ \mu\text{m}$ for the $100\ \mu\text{m}$ radius indenter tip, i.e. at yield the indentation zone extends well beyond the radiation damaged region.

The measurements shown in Figs 23-24 demonstrate the viability and tremendous potential of the spherical indentation stress-strain curves in investigating the changes in the mechanical response of nuclear materials with radiation-damage. A similar approach can also be used for

other materials with modified surfaces – which can form either as a consequence of a graded or layered [143] microstructure, or when such changes are caused unintentionally, such as in wear applications [144], or due to an intentional alteration of the surface such that its physical, chemical or biological characteristics are different than the bulk of the material– all of which are of increasing interest for a variety of applications ranging from enhanced wear and corrosion resistance, superior thermal and biomedical properties, higher fracture toughness, and reduced stress intensity factors etc. [145, 146].

6.5 Comparing with Micro-pillar Compression Experiments

A major advantage of using indentation stress-strain curves in the case studies described above is in their ability to reliably measure the material properties (such as indentation modulus and indentation yield strength) from the initial loading segment of the tests. This is in contrast to traditional hardness measurements which utilize the unloading segments of the indentation experiments and are thus influenced by the imposed additional local plastic deformation which can alter the local microstructure and its properties. Since the properties measured by the indentation stress-strain curves are thus representative of the pristine undamaged material, it should be possible to develop a one-to-one correlation between these values and those measured using traditional uniaxial testing techniques.

Figure 25 displays an example of the comparative stress-strain responses between indentation and compression on as-cast and 30% deformed Fe-3%Si samples. Both the indentation and compression experiments shown in this figure were done inside individual grains of near (100) orientation (grains #1 and #D4, see Fig. 21). The large (~mm) size of the grains in this sample help insure that these results are free from the influence of neighboring grain orientations and/or grain boundaries. For the compression tests, micro-pillars of ~3 μm diameter

and $\sim 6 \mu\text{m}$ height were fabricated using a focused-ion beam (FIB), which were then tested using a custom-built instrumented in-situ flat punch indenter inside a Zeiss DSM 962 SEM chamber [147, 148].

It is reassuring to note that both the indentation and micro-compression experiments demonstrate very similar trends. Thus while there is a 46% increase in the indentation yield strength (Y_{ind} see Fig. 18c) of the Fe-3%Si sample after 30% deformation, a very similar (around 43%) increase is also noted in the yield strength (calculated as the flow stress at 2% offset strain) of the uniaxial micro-compression experiments. Since the orientations of both the grains #1 and #D4 are very close to near-(100) orientations, these increments are directly related to the changes in the dislocation content between the two samples. Figure 25 suggests that stress-strain responses from both indentation and micro-compression experiments are capable of quantifying these differences. Indentation stress-strain curves, with its potential for high throughput, has a distinct advantage in this respect, since it requires far less resources and operator time as compared to FIB-fabricated micro-pillars.

Another important observation from Fig. 25 is the difference in the post-yield behavior between the two test methods. These are of course influenced by the specific strain paths involved in these tests and need to be studied in more detail. In particular, the tests on deformed samples constitute a strain-path change, and deserve careful consideration in extracting useful post-yield plastic deformation parameters from both these test methods.

7. Applications: Combined Raman Spectroscopy-Indentation Studies on Bone

Beyond structural metals, indentation stress-strain curves have also enjoyed a fair degree of success in elucidating structure-property relationships in other materials systems, including the study of micrometer and sub-micrometer sized domains in biological materials such as bone [21]. Bone has highly complex hierarchical internal structure that gives it the capability to perform diverse mechanical, biological and chemical functions. The relevant components span several hierarchical length scales from the material level (including its basic building blocks of collagen fibrils and mineral crystals, and their organization and composition), to tissue level organization and distribution, to the size and geometry of whole bone organs and their macroscale internal components [149-151]. Due to the complex details of this internal hierarchical structure [152], bone is a particularly challenging material to characterize mechanically, especially at the micron length scales where the mineral and collagen components are closely intertwined and the available testing methods are limited. Multiple studies involving nanoindentation have tried to correlate tissue level variation in mechanical properties of bone relative to animal age [153], tissue age and composition [154-156], genetic background [157-159] or even to assess the effects of specific diseases [160] or treatment conditions [161]. These studies have shown mixed results, with some showing support for relationships between local properties and variables affecting tissue composition (e.g. [153, 162]), and others not [156]. To a large extent the inability of these studies to elucidate such structure-property relationships in bone can be attributed to the specific data analyses protocols used in these studies. Since most of these studies involve estimations of modulus and hardness from the unloading segments of load-displacement curves (after some amount of elastic-plastic loading), these property estimates

often reflect values which have been changed by the experiment itself. Moreover the sharp indenter tip geometries (such as Berkovich and cube corner) used in these studies generally have a very small initial elastic regime, which makes it difficult to follow the elastic-plastic transition in these materials.

On the other hand, the use of spherical nanoindentation stress strain curves allows one to reliably follow the changes in the mechanical response in the biological material. More importantly, the use of these indentation stress-strain curves makes it possible to analyze the initial loading segments of spherical indentation, thereby allowing the elastic modulus and indentation yield strength of the material to be estimated prior to the damage induced by the indentation itself.

The use of indentation stress-strain curves on biomaterials (enamel and dentin) was initially demonstrated by Angker and Swain [16]. Recently, the use of this technique on bone samples has also been validated by Pathak et al. [61]. In their work, Pathak et al. [61] have utilized samples from two different strains of inbred mouse, A/J and C57BL/6J (B6), which are known to significantly differ in their matrix mineralization and whole bone brittleness [163-166]. Because of the pre-existing detailed knowledge of the growth patterns in the selected mouse strains [165], these samples form the ideal validation tool to demonstrate correlations between the mechanical properties measured using nanoindentation to the corresponding structural information measured using Raman spectroscopy at similar micron (lamellar) length scales.

Figure 26 shows the experimental procedure for generating spherical indentation and Raman spectroscopy maps on the dehydrated and embedded ‘dry’ mouse femora followed in [61]. Detailed investigations were carried out on the endosteal surface of the antero-medial (AM) cortex of the mouse femora. This region was chosen due to the particular pattern of cortical drift

in these mice at 16 weeks of age [165, 167] in which they tend to add new bone endosteally along their AM cortex (as illustrated in Fig. 26). Owing to this growth pattern, the chemical composition, and hence the mechanical properties, are expected to differ between regions of newly formed bone at the surface relative to the older bone matrix intracortically in this region. Thus, in the right panel of Fig. 26 the newest bone is present closest to the endosteal edge, while the bone is more mature as we proceed away from this surface.

However bone in its ‘dry’ dehydrated/embedded state is far removed from its naturally hydrated *in-vivo* environment, and the preservation and processing steps involved in Ref. [61] can adversely affect the physical and mechanical properties of mineralized tissues. In order to avoid these sample preparation issues a (different) set of mouse femur samples of the same two strains were also tested in their ‘wet’ hydrated state by the same authors [168]. For the wet samples the femora were kept moist with phosphate-buffered saline (PBS) solution (pH 7.4) mixed with CaCl_2 (210 mg of CaCl_2 per liter of PBS) at all times during their preparation and testing. The viscoelastic properties of the wet samples were investigated using nanoindentation following a very similar test pattern as shown in Fig. 26 (with the exception of the spectroscopy study which is applicable only on dry samples). While providing complimentary information about the dynamic mechanical behavior of the hydrated bone samples, these tests also serve as a validation tool for the tests on the dry samples.

Representative results on both the ‘dry’ [61] and ‘wet’ [168] bone samples are shown in Fig. 27. Figure 27a shows the representative backscattered electron microscopy (BSEM) images of the A/J and B6 femur sections at 14 weeks of age. Figure 27b shows the 2D surface maps of the mineral-to-matrix ratio close to the AM cortex of the dry mouse femora. These maps were generated using Raman spectroscopy in which the different mineral and collagen components in

bone can be correlated to different Raman peaks in the measured spectra [169]. The mineral-to-matrix ratio, which relates to bone mineralization [170], was determined using the phosphate to CH₂ wag peak intensity ratio. Similarly Fig. 27c illustrates the variations in the viscoelastic response (on a different sample set) of the femora in their ‘wet’ condition across a 2D surface area close to the endosteal edge of the AM cortex. Here the viscoelastic response is measured in terms of the $\tan \delta$ values at a representative frequency of 101 Hz using the nano-DMA[®] (Dynamic Mechanical Analysis) software in the Hysitron Triboscope, where the linear viscoelastic frequency dependent dynamic response of the material can be ascertained as

$$\tan \delta = \frac{E''}{E'} = \frac{\omega C_s}{k_s} , \quad (16)$$

Here E' and E'' denote the storage and loss moduli, ω is the frequency of the applied force and k_s and C_s are the sample stiffness and damping coefficients, respectively. The 2D surface maps in Figs. 27b and c are color coded to reflect the values of the mineral-to-matrix ratio and the $\tan \delta$ values, respectively, where a deeper shade represents a higher response.

Figures 27b and c show that the trends from both the dry and wet sample sets are highly complementary to each other. For example, both mouse strains in Fig. 27b show smaller values of the mineral-to-matrix ratio close to the endosteal edge, with the values increasing progressively away from the edge. Correspondingly in Fig. 27c, the highest $\tan \delta$ values across both strains are also found close to the endosteal surface, with the values decreasing as the indenter moves away from the endosteal edge. Since hydrated bone owes its remarkable viscoelasticity to the collagen fibrils in the bone matrix [164, 171], the above trend supports a direct relationship between larger viscoelastic response and lower mineral-to-matrix ratio (a

higher collagen content). Thus the decrease in the values of $\tan \delta$ away from the endosteal edge is indicative of the higher degree of maturity of the bone in this region.

Figure 27 also highlights some important differences in the degree of mineralization between the two mouse strains: not only do the A/J mice appear to reach a higher mineral-to-matrix ratio (and correspondingly lower values of $\tan \delta$) than B6, this increase happens over a much shorter distance from the endosteal edge in A/J than it does in B6. This trend suggests a larger degree of mineralization in the A/J femur than in the B6 at a similar distance into the cortex.

The above results indicate that the differences in the growth patterns between the two mouse strains have not been substantially altered by the dehydration/embedding procedures employed in [61], and thus these structural differences are ideally suited for correlation studies with their local mechanical properties using indentation stress-strain curves. Spherical indents were conducted on the same regions as the Raman spectroscopy measurements on the ‘dry’ samples as shown schematically in Fig. 27b. The results from the indentation stress-strain curves, namely the indentation modulus from the initial loading segment (E_s) and the indentation yield strength, Y_{ind} (calculated as the indentation stress at 0.2% offset strain) are shown along with their associated Raman measurements in Fig. 28. Note the strong, approximately linear, correlations of both E_s and Y_{ind} with the mineral-to-matrix ratios in Figs. 28a and c. These data suggest that both the local chemical composition (in terms of the mineral-to-matrix ratio) and the local mechanical behavior (E_s and Y_{ind}) of bone follow a similar pattern in the AM cortices of these mouse femora. Thus a lower mineral-to-matrix ratio close to the edge results in a lower indentation modulus and yield behavior at similar locations, and the higher mineralization of the A/J samples are reflected as higher values of both E_s and Y_{ind} in Figs. 28a and c. The authors

also note that these correlations are much weaker when the modulus and hardness values are calculated from the unloading segments of the curve using the calibrated area functions [7, 8] (Figs. 28b and d).

The combined indentation-Raman spectroscopy study also helps us to understand the inter-strain differences between the two mouse strains. It is known that while the A/J femora have a smaller diameter and correspondingly a smaller moment of inertia compared to B6 (see the BSEM images in Fig. 27a), they do not differ in their cortical areas [163, 164]. However, instead of a less structurally efficient structure as one would expect (if the bone compositions were identical across the two mouse strains), the A/J femora are found to possess similar overall stiffness and strength values [164]. This would indicate that the A/J bones have biologically coupled a change in bone quality in order to satisfy the imposed mechanical demands [163].

The results from the indentation and Raman spectroscopy studies described above help validate this hypothesis. These results indicate that the A/J mice appear to have obtained a higher degree of mineralization in their femora as compared to B6, since they consistently show the highest local values of the mineral-to-matrix ratios in the intracortical regions, and correspondingly the highest local values of E_s and Y_{ind} , and lower values of $\tan \delta$. Thus by biologically coupling a change in their bone quality, in terms of a higher mineral-to-matrix ratio, the A/J mouse strain appears to have satisfied the increased mechanical demands imposed by their particular bone morphology. Interestingly, this trade-off between the reduced diameter and an increased mineral content in the A/J mice is not without consequences – at the whole bone level the A/J femora were also found to have reduced toughness and they fracture in a more brittle manner than the B6 in whole bone bending tests [163, 164]. So while the increased

mineral content in A/J femura makes them mechanically robust in terms of stiffness (in that they are similar to B6), they are still weaker with regard to their post-yield behavior.

8. Applications to Vertically Aligned Carbon Nanotube (VACNT) Brushes

Other than bone, indentation stress-strain curves have also been successfully applied to other hierarchical structures. In this section, we discuss the use of these new protocols on a novel hierarchical material system consisting of dense layers of vertically aligned carbon nanotube (VACNT) brushes.

Considerable efforts have been dedicated to exploring the deformation mechanisms of VACNT brushes, in part motivated by their wide range of potential applications in areas such as energy dissipation devices, electrical interconnects, thermal interface materials, micro-electro-mechanical-systems (MEMS) and microelectronics [172-174]. While individual CNTs have been announced as the strongest material known [175] and have shown extremely high strength and Young's modulus in tensile tests on individual tubes [176], much less is known about the VACNT brushes in terms of their mechanical behavior. The hierarchical architecture of the VACNT brushes renders their mechanical response as a complex phenomena occurring across multiple length scales. The collective behavior of these materials thus relies heavily on the properties of the individual CNTs, as well as on the variations in the collective inter-tube interactions and inherent property gradients of the microstructure, which in turn are dictated by their synthesis techniques [177-179].

Instrumented indentation, although being a common method for studying mechanical properties of films and coatings, has not been used widely for VACNT brushes [180, 181]. This

is primarily due to the extremely low density of VACNT brushes (>90% porosity) produced so far, which often result in the CNTs bending away from the indenter under contact loading, making analysis difficult [182]. Additionally while VACNT brushes/films may have micrometer-to-millimeter-sized lateral and vertical dimensions, they are comprised of individual nanotubes with diameters in the nanometer range, which drives their mechanical response to be distinct from monolithic materials. Hence, the accurate estimation of the contact area between the VACNT film and the commonly used sharp pyramidal indenter tip geometries [180, 183, 184], necessary for indentation data analysis, poses a significant challenge. Similarly maintaining parallel contact between the indenter and the sample is a major concern when using flat punch indenters on VANCTs, which tends to obscure their initial buckling response [180, 185-187]. Another complicating factor is the extremely high aspect ratio of the CNTs, which makes them highly susceptible to buckling at very low compressive loads under the indenter tip [188].

In order to mitigate some of these problems, highly dense VACNT brushes made of small-diameter (1-3 nm outer diameter, 1-4 walled) CNTs, produced by high temperature vacuum decomposition of SiC single crystals [189], have been used for analysis using indentation stress-strain curves in Ref. [190]. These novel carbide-derived carbon (CDC) VACNT brushes have been shown to have a density close to 0.95 g/cm^3 [189], which is significantly (10 times or more) higher than in catalytic growth of any kind of nanotubes [172, 173, 191] – making them highly amenable to contact loading experiments.

Figure 29a shows a SEM micrograph of the 200nm thick VACNT brush and the VACNT brush – graphite interface. The higher density of these brushes, which makes them ideal for indentation testing, is evident in this image where no apparent porosity is visible. Figures 29b and c show the indentation load-displacement and stress-strain responses respectively for a $1 \mu\text{m}$

spherical indenter into this VACNT brush. Note in particular how the indentation stress-strain curves enables one to follow the entire evolution of the mechanical response in the VACNT array, from initial elasticity to the initiation of buckling to post-buckling behavior at finite plastic strains. This is visible as three distinct stages during indentation of these VACNT brushes in Fig. 29c: there is an initial linear portion where the indenter elastically compresses the CNT array (see the schematic in the figure), followed by the initiation of buckling at a critical load, and finally a sharp increase in the slope of the curve signaling the influence of the SiC substrate. In addition, the indentation stress-strain curves also allow one to calculate the elastic modulus and the stress at buckling in the indentation experiment. From this figure, the modulus of these 200 nm thick VACNT brushes can be estimated to be ~ 17 GPa and the critical buckling stress was estimated as ~ 0.3 GPa at a load of 0.02 mN.

The authors in Ref. [190] also describe how indentation stress-strain curves from different indenter radii can be used on these VACNT brushes to explore the effects of indentation zone sizes and the material defect density on the VACNT buckling stress. This is shown in Fig. 30 where the indentation response on a much thicker VACNT brush (thickness 1.2-1.4 μm , see Fig. 30a inset) is shown as a function of 3 different indenter radii. In general all three indenter sizes show a similar trend in the VACNT response: an initial elastic behavior (modulus ~ 18 GPa), followed by a sharp drop at a critical stress corresponding to CNT buckling. Note however that the values of buckling stresses vary significantly between the three different indenters, where indentation with the smaller 1 μm indenter shows the highest buckling stress, followed by the 5 μm indenter, while buckling with the largest 13.5 μm indenter occurs at a significantly lower indentation stress. This point is further illustrated in the table in Fig. 30b, where the average and standard deviation values (of ≥ 5 tests) of the indentation buckling stress,

and the average values of contact radius (a) and indentation zone size ($\sim 2.4a$; see Eq. (6)) at buckling from these tests for the 3 different indenters are presented.

As seen from the above table, the indentation zone sizes at buckling for the larger 13.5 μm indenter ($\sim 3.58 \mu\text{m}$) extends well beyond the VACNT brush thickness (1.2-1.4 μm), while only a limited thickness of the VACNT brush ($\sim 0.39 \mu\text{m}$) is exposed to indentation stress for the smaller 1 μm indenter (see schematic in Fig. 29c inset). The corresponding differences in buckling stress are thus largely a consequence of the effective buckling length available in each case; with smaller indenters there is only a smaller buckling length and the material is able to withstand higher buckling stresses.

The table in Fig. 30b also shows larger variations in the values of the buckling stress for the small 1 μm radii indenter compared to the larger indenters. These values seem to indicate that defect density varies from one location to another in one VACNT brush. As seen from the above table, the smaller volume sampled by the 1 μm indenter is more sensitive to the variation in defect density when different regions of the sample are probed, as indicated by the large spread of the buckling stress values when using this indenter. The larger indenters, on the other hand, encounter a bigger volume, and hence they mostly register a combined VACNT-defect response leading to a lower buckling stress and a smaller spread in the buckling stress.

The above results have been validated by conducting compression tests on VACNT micro-pillars machined using a focused ion beam (FIB) on the same sample. This is shown in Fig. 31 which shows the uniaxial compression data for a $\sim 600 \text{ nm}$ diameter VACNT pillar. As seen from this figure, the values measured from indentation and compression tests are highly complementary to one another. The slight increase in the modulus values in the micro-pillar compression tests ($\sim 30 \text{ GPa}$ as compared to $\sim 17\text{-}18 \text{ GPa}$ in indentation) is due to ion-beam

irradiation during the micro-machining process using FIB. This modifies the structure of the outer rim of CNTs in the VACNT pillar, which potentially results in intertube bridging between the densely packed CNTs and hence an increase in their modulus [192].

These numbers suggest that these VACNT brushes have a respectable level of the mechanical properties with the modulus of elasticity 1-2 orders of magnitude higher [193], and buckling strengths several orders of magnitude higher [180, 188] compared to a CVD VACNT turf – a difference which is explained by the much higher density of the tubes per unit area in the CDC-VACNT resulting in considerably higher mechanical properties. These higher properties are of extreme importance for making selective CNT membranes for gas or liquid filtration/separation or CNT coatings for tribological applications.

9. Summary and Future Trends

The new protocols described in this review for producing meaningful indentation stress-strain curves have demonstrated tremendous potential for reliably extracting microscale structure-property correlations in a broad range of material systems, especially when combined with appropriate structure characterization techniques (e.g., orientation image mapping (OIM, Raman spectroscopy)). It is also seen that these methods can be applied to study mechanical responses of local constituents as well as interfaces. These new experimental tools open up numerous avenues of potential future research. In particular, it is expected that the new protocols and tools described in this review are critical to identifying and understanding the physical origin of the superior properties of certain high-performance composites that exhibit effective properties that exceed by orders of magnitude the properties of their constituents [194]. It is generally believed that the ‘mechanical property amplification’ is intricately linked to the multi-level hierarchical composite structure present in these material systems [195, 196]. As a specific

example, α - β Ti alloys exhibit a very rich class of microstructures (and superior properties compared to either pure α or pure β titanium), although the level of hierarchy in the microstructure and the mechanical property amplification is significantly lower compared to that in the biological polymer-ceramic composites mentioned earlier. But even for these simpler α - β Ti alloys, the establishment of robust physics-based composite theories is at a primitive and premature stage. One of the main hurdles has been the lack of validated fundamental data on the anisotropic elastic-plastic behavior (including strain hardening) of the α and β phases at the lower length scales (single crystal level and below), and more importantly on the role of the α - β interfaces. The novel protocols described in this review are expected to play a critical role in gaining a better understanding of the local mechanical behavior of the individual microscale constituents and interfaces (both phase boundaries and grain boundaries) present in the material, and in developing high fidelity, multi-scale, physics-based models for new material systems of interest in emerging advanced technologies.

Similarly in biomaterials such as bone, the use of indentation stress-strain curves also have the potential to build a new rigorous framework for study of structure-property linkages, and lead to development of new methods for diagnosis and treatment of a number of bone-related health conditions. In osteoporosis, for example, there is reduced mechanical strength and an increased susceptibility to fracture, particularly in anatomical areas such as the spine and the hip. With over 10 million Americans affected by osteoporosis, there are heavy costs associated with this disease in terms of medical expenditures, reduced quality of life and increased mortality risk [197]. Existing techniques for screening patients for fracture risk, such as Dual-Energy X-Ray Absorptiometry (DXA) measures of bone mineral density (BMD), largely reflect bone quantity and are only able to account for 60-70% of the variation in bone strength [198]. Clearly

there are additional details of bone quality (tissue and matrix level composition) and geometry (tissue quantity and distribution) that contribute significantly to bone's mechanical competency [150, 199] that BMD cannot measure. New techniques using indentation are currently being developed that can test the mechanical properties of living tissue like cartilage [200-203], bone and surgical implants [204] with and without [205] arthroscopic surgical control. Similarly, a range of novel techniques also exist for measuring the structural information of bone in its *in-vivo* state such as transcutaneous Raman spectroscopy [206, 207], high-resolution peripheral quantitative computed tomography (HR-pQCT [208]), and micro-magnetic resonance imaging (microMRI [209, 210]). The utility of such methodologies in a clinical environment will be limited unless the precise linkages between the details of bone's internal structure and its effective mechanical response are known. Thus the physical insights into the structure-property relationships in bone obtained using indentation stress-strain curves shown in this review are truly translational, since it would allow us to appropriately interpret the results on a set of controlled samples before venturing into the more complex *in vivo* body environment. Future studies of this nature are expected to help formulate robust metrics of bone quality that can be used by medical practitioners to more effectively assess bone health in their patients and recommend appropriate treatment.

The biggest potential of the indentation techniques described here might actually be in the reliable assessment of the mechanical behavior of modified surfaces (e.g., coatings, irradiated, shot-peened, oxidized, and corroded). Instrumented indentation offers the most practical and cost-effective approach available today for these investigations. Furthermore, as demonstrated in this review, indentation with different indenter sizes can allow estimation of the thickness of the surface modified layers without actually sectioning the samples and studying

them in electron microscopes. Future studies are expected to further develop this methodology and demonstrate a much broader range of applications.

It should also be recognized that the methods described here need significant further development and validation. Extending the methods to rigorously account for anisotropic behavior of the sample material (at the indentation length scales) is particularly important for future studies. In a similar vein, it is also important to extend the data analyses protocols to take into account rate effects of deformation (e.g., visco-elasticity, visco-plasticity). It is expected that finite element models of spherical indentation will play an important role in developing these enhancements and modifications to the data analyses procedures described in this work. Additionally, there have been several new developments in the indenters themselves to allow for testing at different temperatures, which can pave the way to extending the protocols described here to study thermo-mechanical response of local constituents and interfaces. Finally, extension of these methods to other indenter shapes can greatly enhance the space of stress fields experienced in the indentation zone, and provide additional insights into the local anisotropy of mechanical response.

The development and utilization of the finite element models of indentation are also key to the successful estimates of properties of constituents and interfaces from the indentation stress-strain curves described in this review. This was evident from the brief discussion presented in this review based on Ref. [44], where a simple isotropic elastic-plastic material constitutive description was employed. However, keeping in mind, the length scales involved in the indentation measurements, it is imperative to develop and validate finite element models of indentation that employ more physics-based constitutive descriptions. It is very likely that the more sophisticated constitutive descriptions will require three-dimensional (3-D) finite element

models of the indentation experiment. However, these are critically needed to successfully estimate reliable and meaningful properties from the indentation stress-strain curves. In a very recent paper [211], this problem was posed as an inverse problem, and a specific strategy was outlined that made extensive use of Fourier representations. This new approach was demonstrated for estimating the single crystal elastic properties from a multitude of indentation and OIM measurements on a polycrystalline sample. Future studies are expected to extend this approach to a number of elastic-plastic properties of interest in the microscale constituents and interfaces prevalent in most advanced hierarchical material systems.

Acknowledgements

Authors acknowledge funding from ARO grant W911NF-10-1-0409. SP gratefully acknowledges funding from the Los Alamos National Laboratory Director's Postdoctoral Fellowship for part of this work and during the writing of this manuscript. This work was performed, in part, at the Center for Integrated Nanotechnologies, an Office of Science User Facility operated for the U.S. Department of Energy (DOE) Office of Science. Los Alamos National Laboratory, an affirmative action equal opportunity employer, is operated by Los Alamos National Security, LLC, for the National Nuclear Security Administration of the U.S. Department of Energy under contract DE-AC52-06NA25396.

References

- [1] D. Tabor, The Hardness of Metals, Oxford University Press, 1951.
- [2] S.M. Walley, Materials Science and Technology (2012) DOI 10.1179/1743284711Y.0000000127.
- [3] A.C. Fischer-Cripps, Nanoindentation, Springer, 2004.
- [4] R.W. Armstrong, W.L. Elban, Materials Science and Technology (2012 - focused issue).

- [5] K.J. Hemker, W.N. Sharpe Jr, K.H.J. Buschow, W.C. Robert, C.F. Merton, I. Bernard, J.K. Edward, M. Subhash, V. Patrick, Mechanical Testing of Very Small Samples, in: Encyclopedia of Materials: Science and Technology, Elsevier, Oxford, 2006, pp. 1-6.
- [6] J.R. Greer, J.T.M. De Hosson, Progress in Materials Science 56 (2011) 654-724.
- [7] W.C. Oliver, G.M. Pharr, Journal of Materials Research 7 (1992) 1564-1580.
- [8] W.C. Oliver, G.M. Pharr, Journal of Materials Research 19 (2004) 3-20.
- [9] E.G. Mahin, J.G.J. Foss, American Society for Metals -- Transactions 27 (1939) 337-354.
- [10] Z. Jeffries, R.S. Archer, The science of metals, McGraw-Hill, 1924.
- [11] K. Honda, Science Reports of the Tohoku Imperial University 6 (1917) 95-99.
- [12] S.R. Kalidindi, S. Pathak, Acta Materialia 56 (2008) 3523-3532.
- [13] S. Pathak, J. Shaffer, S.R. Kalidindi, Scripta Materialia 60 (2009) 439-442.
- [14] S. Basu, A. Moseson, M.W. Barsoum, Journal of Materials Research 21 (2006) 2628-2637.
- [15] J.S. Field, M.V. Swain, Journal of Materials Research 8 (1993) 297-306.
- [16] L. Angker, M.V. Swain, Journal of Materials Research 21 (2006) 1893-1905.
- [17] H. Hertz, Miscellaneous Papers, MacMillan and Co. Ltd., New York, 1896.
- [18] G.M. Pharr, A. Bolshakov, Journal of Materials Research 17 (Oct 2002) 2260-2671.
- [19] M.F. Doerner, W.D. Nix, Journal of Materials Research 1 (1986) 601-609.
- [20] A.C. Fischer-Cripps, Vacuum 58 (2000) 569-585.
- [21] D.M. Ebenstein, L.A. Pruitt, Nano Today 1 (2006) 26-33.
- [22] J.A. Brinell, Teknisk Tidskrift 5 (1900) 69.
- [23] A. Wahlberg, Iron and Coal Trades Review (1901).
- [24] J.A. Brinell, Baumaterialienkunde 5 (1900) 276-280, 294-297, 317-320, 364-367, 392-394, 412-416.
- [25] R.L. Smith, G.E. Sandland, Institution of Mechanical Engineers -- Proceedings 1 (1922) 623-641.
- [26] E. Meyer, Zeitschrift des Vereines Deutscher Ingenieure 52 (1908) 645-654.
- [27] D. Tabor, Proceedings of the Royal Society of London. Series A, Mathematical and Physical Sciences 192 (1948) 247-274.
- [28] B.L. Hammond, R.W. Armstrong, Philosophical Magazine Letters 57 (1988) 41-47.
- [29] J.S. Field, M.V. Swain, Journal of Materials Research 10 (1995) 101-112.
- [30] J.S. Fielda, M.V. Swain, Carbon 34 (1996) 1357-1366.
- [31] K.L. Johnson, Contact Mechanics, Cambridge University Press, Cambridge, 1987.
- [32] H.A. Francis, Transactions of the ASME. Series H, Journal of Engineering Materials and Technology 98 (1976) 272-281.
- [33] S. Basu, M.W. Barsoum, S.R. Kalidindi, Journal of Applied Physics 99 (2006).
- [34] A.G. Zhou, M.W. Barsoum, S. Basu, S.R. Kalidindi, T. El-Raghy, Acta Materialia 54 (2006) 1631-1639.
- [35] M.W. Barsoum, A. Murugaiah, S.R. Kalidindi, T. Zhen, Physical Review Letters 92 (2004).
- [36] A. Murugaiah, M.W. Barsoum, S.R. Kalidindi, T. Zhen, Journal of Materials Research 19 (2004) 1139-1148.
- [37] M.W. Barsoum, A. Murugaiah, S.R. Kalidindi, T. Zhen, Y. Gogotsi, Carbon 42 (2004) 1435-1445.
- [38] M.V. Swain, Materials Science & Engineering A: Structural Materials: Properties, Microstructure and Processing 253 (1998) 160-166.
- [39] S. Stauss, P. Schwaller, J.L. Bucaille, R. Rabe, L. Rohr, J. Michler, E. Blank, Determining the stress-strain behaviour of small devices by nanoindentation in combination with inverse

- methods, in: Proceedings of the 28th International Conference on MNE, vol 67-68, Elsevier, Lugano, Switzerland, 2003, pp. 818-825.
- [40] J. Michler, S. Stauss, P. Schwaller, J.-L. Bucaille, E. Felder, EMPA (Swiss Federal Laboratories for Materials Testing and Research) Publication (2002) 6-7.
- [41] B. Taljat, T. Zacharia, F. Kosel, International Journal of Solids and Structures 35 (1998) 4411-4426.
- [42] M. Beghini, L. Bertini, V. Fontanari, International Journal of Solids and Structures 43 (2006) 2441-2459.
- [43] H. Pelletier, Tribology International 39 (2006) 593-606.
- [44] B.R. Donohue, A. Ambrus, S.R. Kalidindi, Acta Materialia 60 (2012) 3943-3952.
- [45] E.G. Herbert, G.M. Pharr, W.C. Oliver, B.N. Lucas, J.L. Hay, Thin Solid Films 398-399 (2001) 331-335.
- [46] A.C. Fischer-Cripps, B.R. Lawn, Acta Materialia 44 (1996) 519-527.
- [47] J. Mencik, M.V. Swain, Journal of Materials Research 10 (1995) 1491-1501.
- [48] A.C. Fischer-Cripps, Surface and Coatings Technology 200 (2006) 4153-4165.
- [49] J. Deuschle, S. Enders, E. Arzt, Journal of Materials Research 22 (2007) 3107-3119.
- [50] Y.Y. Lim, M.M. Chaudhri, Mechanics of Materials 38 (2006) 1213-1228.
- [51] Y. Arai, Y.H. Liang, K. Ozasa, M. Ohashi, E. Tsuchida, Physica E 36 (2007) 1-11.
- [52] T. Chudoba, M. Griepentrog, A. Duck, D. Schneider, F. Richter, Journal of Materials Research 19 (2004) 301-314.
- [53] T. Chudoba, N. Schwarzer, F. Richter, Surface and Coatings Technology 127 (2000) 9-17.
- [54] V. Linss, N. Schwarzer, T. Chudoba, M. Karniychuk, F. Richter, Surface and Coatings Technology 195 (2004) 287-297.
- [55] F. Richter, M. Herrmann, F. Molnar, T. Chudoba, N. Schwarzer, M. Keunecke, K. Bewilogua, X.W. Zhang, H.-G. Boyen, P. Ziemann, Surface and Coatings Technology 201 (2006) 3577-3587.
- [56] C. Ullner, Measurement 27 (2000) 43-51.
- [57] P. Grau, G. Berg, W. Fraenzel, H. Meinhard, Physica Status Solidi (A) Applied Research 146 (1994) 537-548.
- [58] A.J. Moseson, S. Basu, M.W. Barsoum, Journal of Materials Research 23 (2008) 204-209.
- [59] A.E.H. Love, J. Math 10 (1939) 161-175.
- [60] X. Li, B. Bhushan, Materials Characterization 48 (2002) 11-36.
- [61] S. Pathak, S.J. Vachhani, K.J. Jepsen, H.M. Goldman, S.R. Kalidindi, Journal of the Mechanical Behavior of Biomedical Materials (2012) DOI: 10.1016/j.jmbbm.2012.1003.1018.
- [62] S. Pathak, J. Michler, K. Wasmer, S.R. Kalidindi, Journal of Materials Science 47 (2012) 815-823.
- [63] S. Pathak, D. Stojakovic, R. Doherty, S.R. Kalidindi, Journal of Materials Research - Focus Issue on Indentation Methods in Advanced Materials Research 24 (2009) 1142-1155.
- [64] S. Pathak, D. Stojakovic, S.R. Kalidindi, Acta Materialia 57 (2009) 3020-3028.
- [65] S.R. Kalidindi, C.A. Bronkhorst, L. Anand, Journal of the Mechanics and Physics of Solids 40 (1992) 537-569.
- [66] M. Knezevic, S.R. Kalidindi, Computational Materials Science 39 (2007) 643-648.
- [67] D.T. Fullwood, S.R. Niezgoda, B.L. Adams, S.R. Kalidindi, Progress in Materials Science 55 (2010) 477-562.
- [68] G. Proust, S.R. Kalidindi, Journal of the Mechanics and Physics of Solids 54 (2006) 1744-1762.

- [69] S. Enders, N. Barbakadse, S.N. Gorb, E. Arzt, *Journal of Materials Research* 19 (2004) 880-887.
- [70] J.Y. Rho, P. Zioupos, J.D. Currey, G.M. Pharr, *Journal of Biomechanics* 35 (2002) 189-198.
- [71] C.A. Schuh, *Materials Today* 9 (2006) 32-40.
- [72] T.H. Courtney, *Mechanical Behavior of Materials* McGraw-Hill Science/Engineering/Math, 1999.
- [73] N. Gane, F.P. Bowden, *Journal of Applied Physics* 39 (1968) 1432-1435.
- [74] W.W. Gerberich, J.C. Nelson, E.T. Lilleodden, P. Anderson, J.T. Wyrobek, *Acta Materialia* 44 (1996) 3585-3598.
- [75] W.W. Gerberich, S. Venkataraman, J. Nelson, H. Huang, E. Lilleodden, W. Bonin, Yield point phenomena and dislocation velocities underneath indentations into BCC crystals, in: *Mater. Res. Soc.*, Boston, MA, USA, 1995, pp. 629-644.
- [76] W.W. Gerberich, S.K. Venkataraman, H. Huang, S.E. Harvey, D.L. Kohlstedt, *Acta Metallurgica et Materialia* 43 (1995) 1569.
- [77] A.E. Giannakopoulos, S. Suresh, *Scripta Materialia* 40 (1999) 1191-1198.
- [78] A. Gouldstone, H.J. Koh, K.Y. Zeng, A.E. Giannakopoulos, S. Suresh, *Acta Materialia* 48 (2000) 2277-2295.
- [79] S. Suresh, T.G. Nieh, B.W. Choi, *Scripta Materialia* 41 (1999) 951-957.
- [80] R.C. Thomas, J.E. Houston, T.A. Michalske, R.M. Crooks, *Science* 259 (1993) 1883.
- [81] S.A. Syed Asif, J.B. Pethica, *Philosophical Magazine A (Physics of Condensed Matter: Structure, Defects and Mechanical Properties)* 76 (1997) 1105-1118.
- [82] R.D. Doherty, *Scripta Materialia* 49 (2003) 1219-1222.
- [83] T. Eliash, M. Kazakevich, V.N. Semenov, E. Rabkin, *Acta Materialia* 56 (2008) 5640-5652.
- [84] T. Ohmura, K. Tsuzaki, *Journal of Physics D: Applied Physics* 41 (2008) 074015 (074016 pp.).
- [85] N. Gane, F.P. Bowden, *Journal of Applied Physics* 39 (1968) 432-435.
- [86] A. Gouldstone, K.J. Van Vliet, S. Suresh, *Nature* 411 (2001) 656-656.
- [87] Y. Wang, D. Raabe, C. Kluber, F. Roters, *Acta Materialia* 52 (2004) 2229-2238.
- [88] M.J. Cordill, N.R. Moody, W.W. Gerberich, *Journal of Materials Research* 23 (2008) 1604-1613.
- [89] G.M. Pharr, J.H. Strader, W.C. Oliver, *Journal of Materials Research* 24 (2009) 653-666.
- [90] M.J. Cordill, M.S. Lund, J. Parker, C. Leighton, A.K. Nair, D. Farkas, N.R. Moody, W.W. Gerberich, *International Journal of Plasticity* 25 (2009) 2045-2058.
- [91] M.J. Cordill, N.R. Moody, W.W. Gerberich, *International Journal of Plasticity* 25 (2009) 281-301.
- [92] K. Durst, O. Franke, A. Boehner, M. Goeken, *Acta Materialia* 55 (2007) 6825-6833.
- [93] J.G. Swadener, E.P. George, G.M. Pharr, *Journal of the Mechanics and Physics of Solids* 50 (2002) 681-694.
- [94] G. Feng, W.D. Nix, *Scripta Materialia* 51 (2004) 599-603.
- [95] M.R. VanLandingham, N.K. Chang, P.L. Drzal, C.C. White, S.H. Chang, *Journal of Polymer Science Part B-Polymer Physics* 43 (2005) 1794-1811.
- [96] J. Mencik, G. Rauchs, J. Bardon, A. Riche, *Journal of Materials Research* 20 (2005) 2660-2669.
- [97] H. Hertz, New York: MacMillan and Co., Ltd (1896).
- [98] K.L. Johnson, *Indentation Contact Mechanics*, Cambridge University Press, Cambridge, 1985.

- [99] S.J. Vachhani, R.D. Doherty, S.R. Kalidindi, *Acta Materialia* 61 (2013) 3744-3751.
- [100] B.L. Adams, *Ultramicroscopy* 67 (1997) 11-17.
- [101] B.L. Adams, S.I. Wright, K. Kunze, *Metallurgical Transactions A* 24A (1993) 819-831.
- [102] D. Dingley, *Journal of Microscopy* 213 (2004) 214-224.
- [103] G. Proust, S.R. Kalidindi, *TMS Letters (The Minerals, Metals and Materials Society)* 7 (2004) 151.
- [104] J.J. Vlassak, W.D. Nix, *Philosophical Magazine A (Physics of Condensed Matter, Defects and Mechanical Properties)* 67 (1993) 1045-1056.
- [105] J.J. Vlassak, W.D. Nix, *Journal of the Mechanics and Physics of Solids* 42 (1994) 1223-1245.
- [106] Z. Hashin, S. Shtrikman, *Journal of the Mechanics and Physics of Solids* 10 (1962) 343-352.
- [107] H. Bunge, *Texture Analysis in Materials Science*, London, 1982.
- [108] S. Panchanadeeswaran, R.D. Doherty, R. Becker, *Acta Materialia* 44 (1996) 1233-1262.
- [109] S.R. Kalidindi, A. Bhattacharya, R. Doherty, *Proceedings of the Royal Society of London: Mathematical, Physical and Engineering Sciences*. 460 (2004) 1935 - 1956
- [110] A. Bhattacharyya, E. El-Danaf, S.R. Kalidindi, R.D. Doherty, *International Journal of Plasticity* 17 (2001) 861-883.
- [111] S.R. Kalidindi, A. Bhattacharyya, R.D. Doherty, *Advanced Materials* 15 (2003) 1345-+.
- [112] D. Stojakovic, *Microstructure Evolution in Deformed and Recrystallized Electrical Steel*, in: *Department of Materials Science and Engineering*, vol Doctor of Philosophy, Drexel University, Philadelphia, PA, 2008.
- [113] E.O. Hall, *Proceedings of the Physical Society. Section B* 64 (1951) 747-753.
- [114] N.J. Petch, *Iron and Steel Institute -- Journal* 174 (1953) 25-28.
- [115] M. Goken, M. Kempf, M. Bordenet, H. Vehoff, *Surface and Interface Analysis* 27 (1999) 302-306.
- [116] Y.-H. Lee, D. Kwon, *Scripta Materialia* 49 (2003) 459-465.
- [117] T. Ohmura, A.M. Minor, E.A. Stach, J.W. Morris, Jr., *Journal of Materials Research* 19 (2004) 3626-3632.
- [118] T. Ohmura, K. Tsuzaki, *Journal of Materials Science* 42 (2007) 1728-1732.
- [119] T. Ohmura, K. Tsuzaki, Y. Fuxing, *Materials Transactions* 46 (2005) 2026-2029.
- [120] W.A. Soer, K.E. Aifantis, J.T.M. De Hosson, *Acta Materialia* 53 (2005) 4665-4676.
- [121] W.A. Soer, J.T.M. De Hosson, *Materials Letters* 59 (2005) 3192-3195.
- [122] Y.M. Soifer, A. Verdyan, M. Kazakevich, E. Rabkin, *Scripta Materialia* 47 (2002) 799-804.
- [123] P.C. Wo, A.H.W. Ngan, *Journal of Materials Research* 19 (2004) 189-201.
- [124] M.G. Wang, A.H.W. Ngan, *Journal of Materials Research* 19 (2004) 2478-2486.
- [125] S.R. Kalidindi, S.J. Vachhani, *Current Opinion in Solid State and Materials Science* 18 (2014) 196-204.
- [126] J. Wheeler, J. Curran, S. Shrestha, *Surface and Coatings Technology* 207 (2012) 480-488.
- [127] R.S. Nelson, D.J. Mazey, J.A. Hudson, *Journal of Nuclear Materials* 37 (1970) 1-12.
- [128] G.S. Was, J.T. Busby, T. Allen, E.A. Kenik, A. Jensson, S.M. Bruemmer, J. Gan, A.D. Edwards, P.M. Scott, P.L. Andreson, *Journal of Nuclear Materials* 300 (2002) 198-216.
- [129] S.J. Zinkle, A. Möslang, *Fusion Engineering and Design* 88 (2013) 472-482.
- [130] P. Hosemann, J.G. Swadener, D. Kiener, G.S. Was, S.A. Maloy, N. Li, *Journal of Nuclear Materials* 375 (2008) 135-143.

- [131] D. Kiener, P. Hosemann, S.A. Maloy, A.M. Minor, *Nature Materials* 10 (2011) 608-613.
- [132] P. Landau, Q. Guo, K. Hattar, J.R. Greer, *Advanced Functional Materials* 23 (2013) 1281-1288.
- [133] N. Li, N.A. Mara, Y.Q. Wang, M. Nastasi, A. Misra, *Scripta Materialia* 64 (2011) 974-977.
- [134] Q.M. Wei, N. Li, N. Mara, M. Nastasi, A. Misra, *Acta Materialia* 59 (2011) 6331-6340.
- [135] P. Hosemann, D. Kiener, Y. Wang, S.A. Maloy, *Journal of Nuclear Materials* 425 (2012) 136-139.
- [136] P. Hosemann, C. Vieh, R.R. Greco, S. Kabra, J.A. Valdez, M.J. Cappiello, S.A. Maloy, *Journal of Nuclear Materials* 389 (2009) 239-247.
- [137] J.T. Busby, M.C. Hash, G.S. Was, *Journal of Nuclear Materials* 336 (2005) 267-278.
- [138] S. Pathak, S.R. Kalidindi, Y. Wang, R. Doerner, N. Mara, submitted (2014).
- [139] M. Victoria, N. Baluc, C. Bailat, Y. Dai, M.I. Luppó, R. Schaublin, B.N. Singh, *Journal of Nuclear Materials* 276 (2000) 114-122.
- [140] M. Miyamoto, D. Nishijima, M.J. Baldwin, R.P. Doerner, Y. Ueda, K. Yasunaga, N. Yoshida, K. Ono, *Journal of Nuclear Materials* 415 (2011) S657-S660.
- [141] B.N. Singh, A.J.E. Foreman, H. Trinkaus, *Journal of Nuclear Materials* 249 (1997) 103-115.
- [142] A. Patra, D.L. McDowell, *Journal of the Mechanics and Physics of Solids* (2014 (in review)).
- [143] X.Y. Liu, R.G. Hoagland, M.J. Demkowicz, J. Wang, M. Nastasi, A. Misra, J.P. Hirth, UNDERSTANDING OF INTERFACE STRUCTURES, DEFECTS, AND MECHANICAL PROPERTIES AT GENERAL FCC-BCC INTERFACES USING "TUNABLE" POTENTIALS, 2011, p. 326-327.
- [144] D.A. Rigney, X.Y. Fu, J.E. Hammerberg, B.L. Holian, M.L. Falk, *Scripta Materialia* 49 (2003) 977-983.
- [145] S. Suresh, *Science* 292 (2001) 2447-2451.
- [146] A.J. Markworth, K.S. Ramesh, W.P. Parks, *Journal of Materials Science* 30 (1995) 2183-2193.
- [147] R. Rabe, J.M. Breguet, P. Schwaller, S. Stauss, F.J. Haug, J. Patscheider, J. Michler, *Thin Solid Films* 469-470 (2004) 206-213
- [148] S. Pathak, S.R. Kalidindi, B. Moser, C. Klemenz, N. Orlovskaya, *Journal of the European Ceramic Society* 28 (2008) 2039-2047.
- [149] C.J. Hernandez, T.M. Keaveny, *Bone* (2006).
- [150] C.H. Turner, *J Musculoskelet Neuronal Interact* 2 (2002) 527-528.
- [151] S. Weiner, W. Traub, *Faseb J* 6 (1992) 879-885.
- [152] J.D. Currey, *Journal of Biomechanics* 36 (2003) 1487-1495.
- [153] J. Burket, S. Gourion-Arsiquaud, L.M. Havill, S.P. Baker, A.L. Boskey, M.C.H. van der Meulen, *J Biomech* 44 (2011) 277-284.
- [154] E. Donnelly, A.L. Boskey, S.P. Baker, M.C.H. van der Meulen, *Journal of Biomedical Materials Research - Part A* 92 (2010) 1048-1056.
- [155] P. Roschger, E.P. Paschalis, P. Fratzl, K. Klaushofer, *Bone* 42 (2008) 456-466.
- [156] R.M.D. Zebaze, A.C. Jones, M.G. Pandy, M.A. Knackstedt, E. Seeman, *Bone* 48 (2011) 1246-1251.
- [157] X. Bi, C.A. Patil, C.C. Lynch, G.M. Pharr, A. Mahadevan-Jansen, J.S. Nyman, *J Biomech* 44 (2011) 297-303.

- [158] Y. Jiao, H. Chiu, Z. Fan, F. Jiao, E.C. Eckstein, W.G. Beamer, W. Gu, *Calcif Tissue Int* 80 (2007) 383-390.
- [159] L.M. Miller, W. Little, A. Schirmer, F. Sheik, B. Busa, S. Judex, *J Bone Miner Res* 22 (2007) 1037-1045.
- [160] Z. Fan, P.A. Smith, G.F. Harris, F. Rauch, R. Bajorunaite, *Connect Tissue Res* 48 (2007) 70-75.
- [161] Y. Bala, B. Depalle, D. Farlay, T. Douillard, S. Meille, H. Follet, R. Chapurlat, J. Chevalier, G. Boivin, *J Bone Miner Res* (2011) doi: 10.1002/jbmr.1501.
- [162] S. Gourion-Arsiquaud, J.C. Burket, L.M. Havill, E. DiCarlo, S.B. Doty, R. Mendelsohn, M.C.H. van der Meulen, A.L. Boskey, *J Bone Miner Res* 24 (2009) 1271-1281.
- [163] K.J. Jepsen, O.J. Akkus, R.J. Majeska, J.H. Nadeau, *Mamm Genome* 14 (2003) 97-104.
- [164] K.J. Jepsen, D.E. Pennington, Y.L. Lee, M. Warman, J. Nadeau, *Journal of bone and mineral research* 16 (2001) 1854-1862.
- [165] C. Price, B.C. Herman, T. Lufkin, H.M. Goldman, K.J. Jepsen, *J Bone Miner Res* 20 (2005) 1983-1991.
- [166] S.M. Tommasini, T.G. Morgan, M. van der Meulen, K.J. Jepsen, *J Bone Miner Res* 20 (2005) 817-827.
- [167] W.G. Beamer, L.R. Donahue, C.J. Rosen, D.J. Baylink, *Bone* 18 (1996) 397-403.
- [168] S. Pathak, J. Gregory Swadener, S.R. Kalidindi, H.-W. Courtland, K.J. Jepsen, H.M. Goldman, *Journal of the Mechanical Behavior of Biomedical Materials* 4 (2011) 34-43.
- [169] J.A. Timlin, A. Carden, M.D. Morris, *Applied Spectroscopy* 53 (1999) 1429-1435.
- [170] A.L. Boskey, N. Pleshko, S.B. Doty, R. Mendelsohn, *Cells and Materials* 2 (1992) 209-220.
- [171] M. Fois, A. Lamure, M.J. Fauran, C. Lacabanne, *Journal of Applied Polymer Science* 79 (2001) 2527-2533.
- [172] A.Y. Cao, P.L. Dickrell, W.G. Sawyer, M.N. Ghasemi-Nejhad, P.M. Ajayan, *Science* 310 (2005) 1307-1310.
- [173] S. Pathak, E.J. Lim, P. Pour Shahid Saeed Abadi, S. Graham, B.A. Cola, J.R. Greer, *ACS Nano* 6 (2012) 2189-2197.
- [174] J. Suhr, L. Ci, P. Victor, P.M. Ajayan, Fatigue characteristics of carbon nanotube blocks under compression, in: *Behavior and Mechanics of Multifunctional and Composite Materials 2008*, March 10, 2008 - March 13, 2008, vol 6929, SPIE, San Diego, CA, United states, 2008, p. The International Society for Optical Engineering (SPIE); American Society of Mechanical Engineers.
- [175] M.M.J. Treacy, T.W. Ebbesen, J.M. Gibson, *Nature* 381 (1996) 678-680.
- [176] Y. Min-Feng, O. Lourie, M.J. Dyer, K. Moloni, T.F. Kelly, R.S. Ruoff, *Science* 287 (2000) 637-640.
- [177] M. Kumar, Y. Ando, *Journal of Nanoscience and Nanotechnology* 10 (2010) 3739-3758.
- [178] S.B. Hutchens, L.J. Hall, J.R. Greer, *Advanced Functional Materials* 20 (2010) 2338-2346.
- [179] S.B. Hutchens, A. Needleman, J.R. Greer, *Journal of the Mechanics and Physics of Solids* 59 (2011) 2227-2237.
- [180] J.F. Waters, P.R. Guduru, M. Jouzi, J.M. Xu, T. Hanlon, S. Suresh, *Appl. Phys. Lett.* 87 (2005) 103109-103103.
- [181] C.P. Deck, J. Flowers, G.S.B. McKee, K. Vecchio, *Journal of Applied Physics* 101 (2007) 23512-23511-23519.

- [182] H.J. Qi, K.B.K. Teo, K.K.S. Lau, M.C. Boyce, W.I. Milne, J. Robertson, K.K. Gleason, *Journal of the Mechanics and Physics of Solids* 51 (2003) 2213-2237.
- [183] A. Qiu, D.F. Bahr, A.A. Zbib, A. Bellou, S.D. Mesarovic, D. McClain, W. Hudson, J. Jiao, D. Kiener, M.J. Cordill, *Carbon* 49 (2011) 1430-1438.
- [184] S.D. Mesarovic, C.M. McCarter, D.F. Bahr, H. Radhakrishnan, R.F. Richards, C.D. Richards, D. McClain, J. Jiao, *Scripta Materialia* 56 (2007) 157-160.
- [185] M.R. Maschmann, Z. Qiu, D. Feng, D. Liming, J. Baur, *Carbon* 49 (2011) 386-397.
- [186] P.D. Bradford, X. Wang, H. Zhao, Y.T. Zhu, *Carbon* 49 (2011) 2834-2841.
- [187] P. Pour Shahid Saeed Abadi, S. Hutchens, J.H. Taphouse, J.R. Greer, B.A. Cola, S. Graham, *Nanoscale* (2012) (accepted).
- [188] J.F. Waters, L. Riestler, M. Jouzi, P.R. Guduru, J.M. Xu, *Appl. Phys. Lett.* 85 (2004) 1787-1789.
- [189] Z.G. Cambaz, G. Yushin, S. Osswald, V. Mochalin, Y. Gogotsi, *Carbon* 46 (2008) 841-849.
- [190] S. Pathak, Z.G. Cambaz, S.R. Kalidindi, J.G. Swadener, Y. Gogotsi, *Carbon* 47 (2009) 1969-1976.
- [191] J. Suhr, P. Victor, L.C.S. Sreekala, X. Zhang, O. Nalamasu, P.M. Ajayan, *Nature Nanotechnology* 2 (2007) 417-421.
- [192] A. Kis, G. Csanyi, J.P. Salvetat, T.-N. Lee, E. Couteau, A.J. Kulik, W. Benoit, J. Brugger, L. Forro, *Nature Materials* 3 (2004) 153-157.
- [193] S.D. Mesarovic, C.M. McCarter, D.F. Bahr, H. Radhakrishnan, R.F. Richards, S.D. Richards, D. McClain, J. Jiao, *Scripta Materialia* 56 (2007) 157-160.
- [194] U.G.K. Wegst, M.F. Ashby, *Philosophical Magazine* 84 (2004) 2167-2181.
- [195] H.M. Yao, H.J. Gao, *Int. J. Solids Struct.* 44 (2007) 8177-8193.
- [196] C. Ortiz, M.C. Boyce, *Science* 319 (2008) 1053-1054.
- [197] America's bone health: The state of osteoporosis and low bone mass in our nation, in: National Osteoporosis Foundation, Washington (DC), 2002.
- [198] P. Ammann, R. Rizzoli, *Osteoporos Int* 14 Suppl 3 (2003) S13-18.
- [199] D.B. Burr, *J Musculoskelet Neuronal Interact* 2 (2002) 525-526.
- [200] T. Lyyra, J. Jurvelin, P. Pitkanen, U. Vaatainen, I. Kiviranta, *Med Eng Phys* 17 (1995) 395-399.
- [201] J. Toyra, T. Lyyra-Laitinen, M. Niinimäki, R. Lindgren, M.T. Nieminen, I. Kiviranta, J.S. Jurvelin, *J Biomech* 34 (2001) 251-256.
- [202] P.A. Brama, A. Barneveld, D. Karssen, G.P. Van Kampen, P.R. van Weeren, *J Vet Med A Physiol Pathol Clin Med* 48 (2001) 213-221.
- [203] A.I. Vasara, J.S. Jurvelin, L. Peterson, I. Kiviranta, *Am J Sports Med* 33 (2005) 408-414.
- [204] I. Hvid, F. Linde, Penetration testing of bone using an osteopenetrometer, in: Y.H. An, R.A. Draughn (Eds.), *Mechanical Testing of Bone and Bone-Implant Interface*, 1999.
- [205] P.K. Hansma, P.J. Turner, G.E. Fantner, *Review of Scientific Instruments* 77 (2006) 075105-075106.
- [206] P. Matousek, E.R. Draper, A.E. Goodship, I.P. Clark, K.L. Ronayne, A.W. Parker, *Appl Spectrosc* 60 (2006) 758-763.
- [207] E.R. Draper, M.D. Morris, N.P. Camacho, P. Matousek, M. Towrie, A.W. Parker, A.E. Goodship, *J Bone Miner Res* 20 (2005) 1968-1972.
- [208] S. Boutroy, M.L. Bouxsein, F. Munoz, P.D. Delmas, *J Clin Endocrinol Metab* 90 (2005) 6508-6515.

- [209] F.W. Wehrli, L. Hilaire, M. Fernandez-Seara, B.R. Gomberg, H.K. Song, B. Zemel, L. Loh, P.J. Snyder, *J Bone Miner Res* 17 (2002) 2265-2273.
- [210] F.W. Wehrli, P.K. Saha, B.R. Gomberg, H.K. Song, P.J. Snyder, M. Benito, A. Wright, R. Weening, *Top Magn Reson Imaging* 13 (2002) 335-355.
- [211] D.K. Patel, H.F. Al-Harbi, S.R. Kalidindi, *Acta Materialia* 79 (2014) 108-116.
- [212] L.H. He, N. Fujisawa, M.V. Swain, *Biomaterials* 27 (2006) 4388-4398.
- [213] S. Pathak, J. Riesterer, S.R. Kalidindi, J. Michler, submitted (2014).

Figures

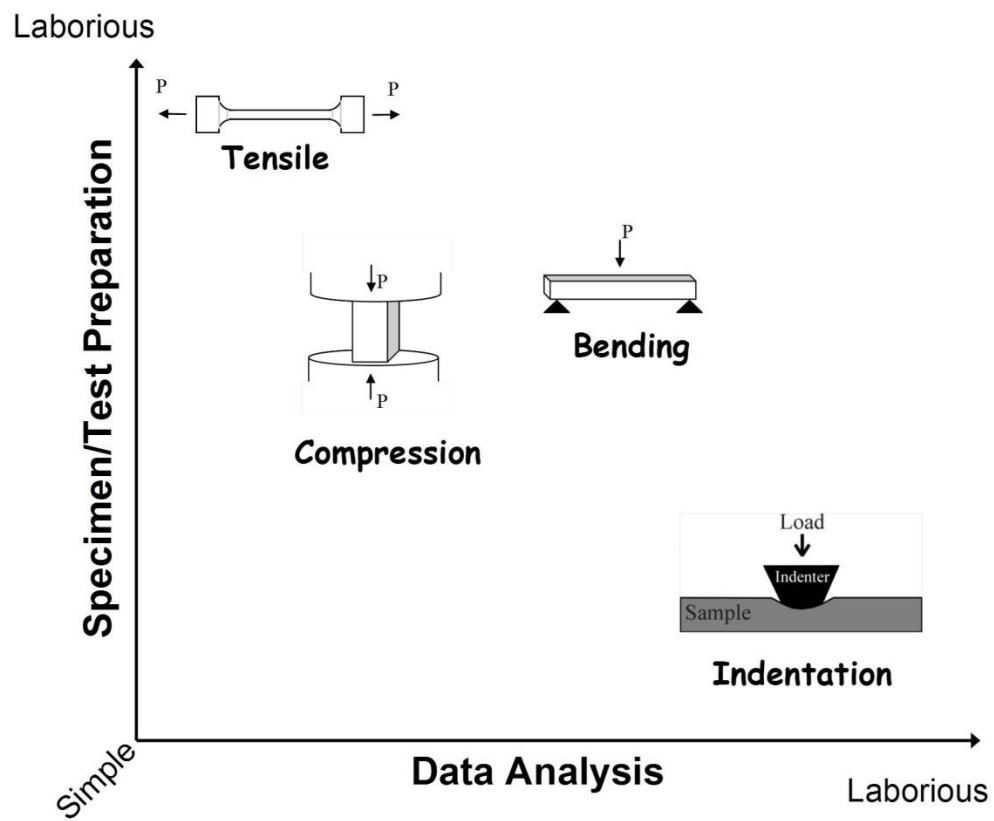


Figure 1. Various mechanical testing methods for micron to sub-micron length samples

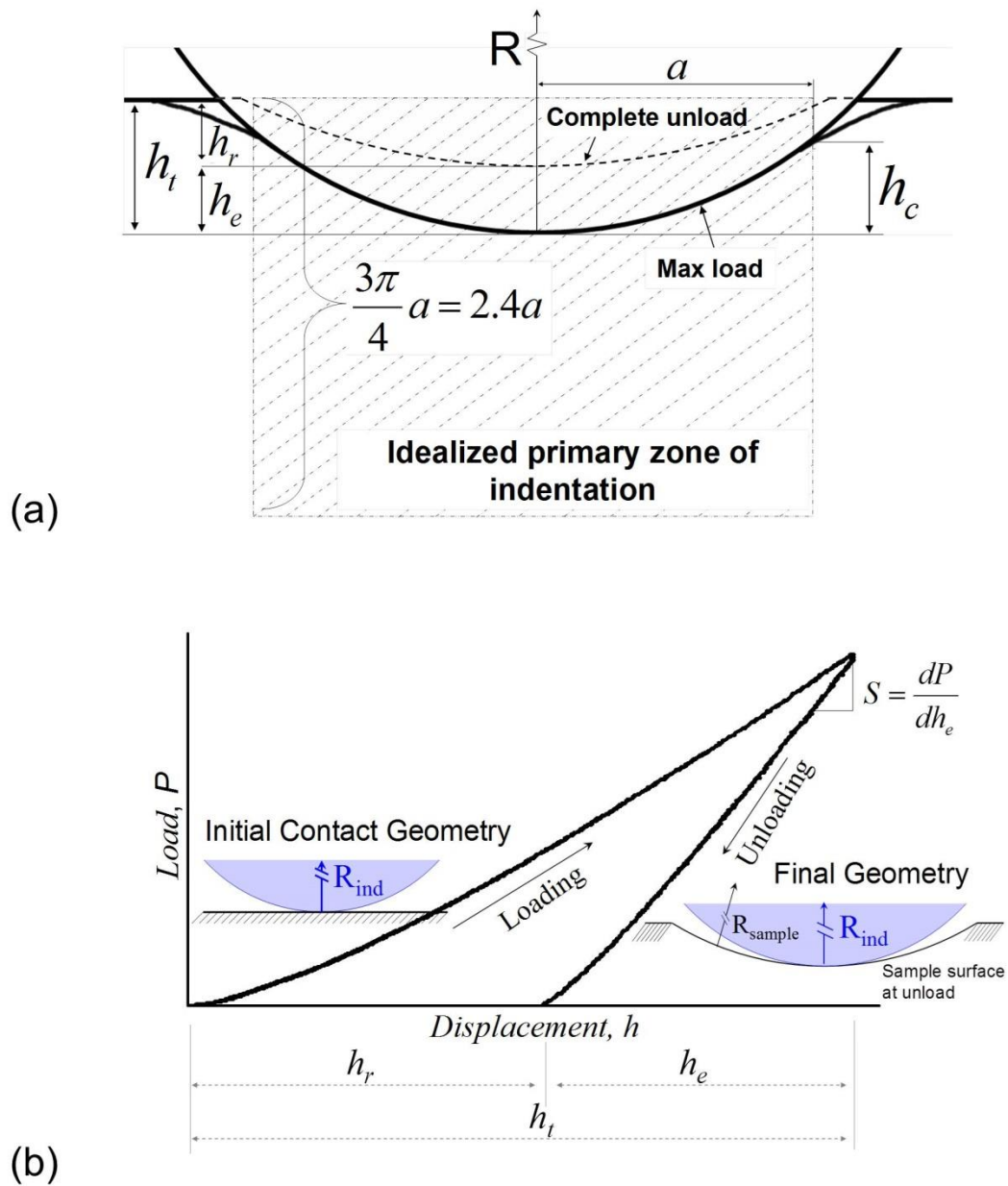


Figure 2. (a) Schematic of the indentation zone in spherical indentation. **(b)** Schematic of a typical measured spherical indentation load-displacement curve with the initial and final contact geometries.

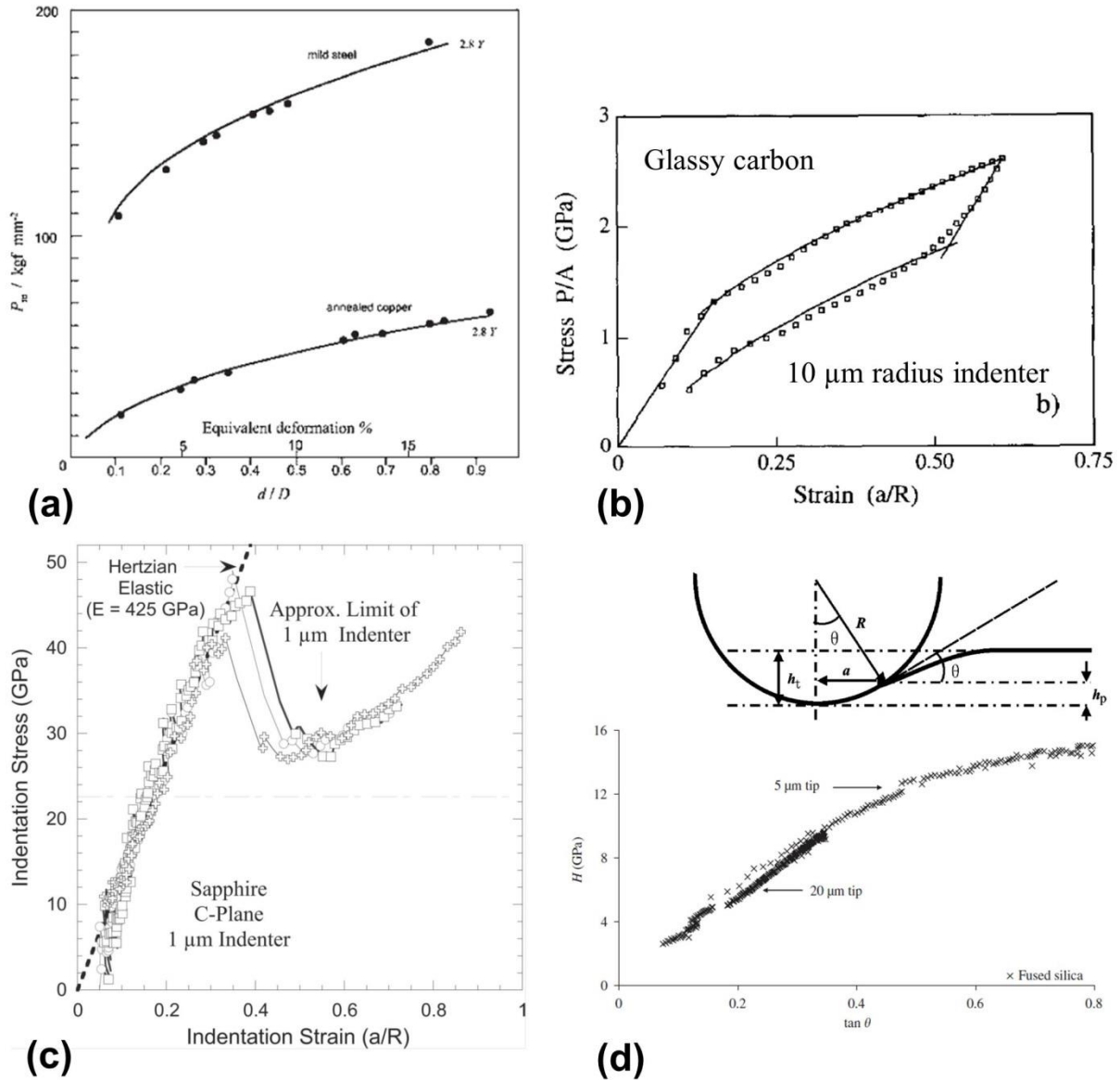


Figure 3. History of indentation stress-strain curves. (a) The concept of indentation stress-strain curves was first introduced by Tabor [1]. His models provided a direct correlation between hardness measurements and uniaxial tests, as shown here for ball indentation of mild steel and annealed copper compared with uniaxial compression (solid curves). Here indentation strain is measured as a/R_i or d/D where a , d and R_i , D are the radii and diameters of the residual imprint and the ball indenters respectively. (b) This process was automated by Field and Swain using multiple partial unloads and the indenter geometry to estimate a [30], and further extended in the work from (c) Barsoum's research group [14]. Most research groups have used a/R_i as a measure of indentation strain or some variations of the same such as (d) the use of $\tan \theta$ as indentation strain where $\sin \theta = a/R_i$ [212].

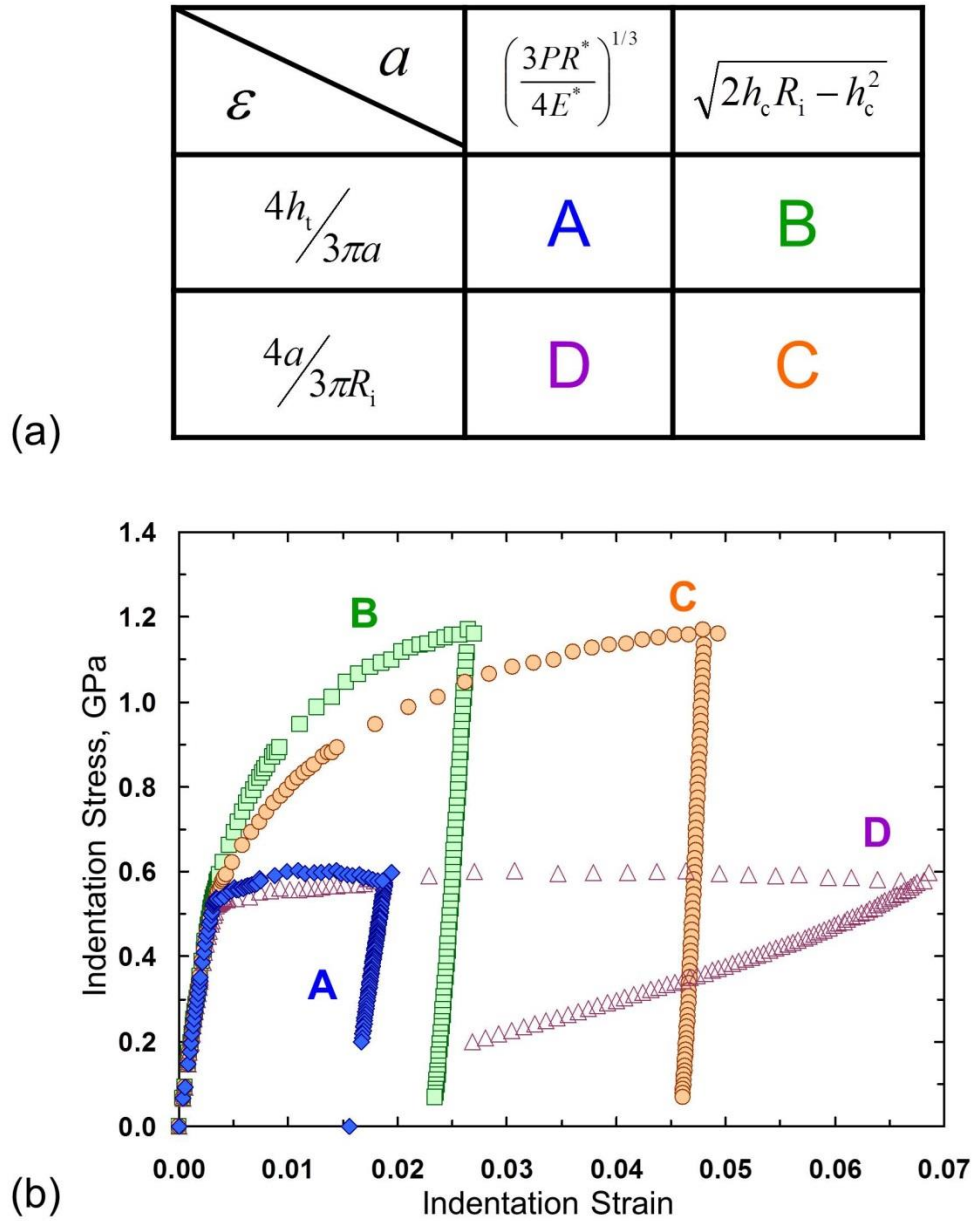


Figure 4. (a) Strain and contact radius definitions used to label curves in Figs. 4b, 5, and 6. (b) Indentation stress-strain curves based on different definitions of contact radius and indentation strain, generated from load-displacement data predicted by finite element models [44].

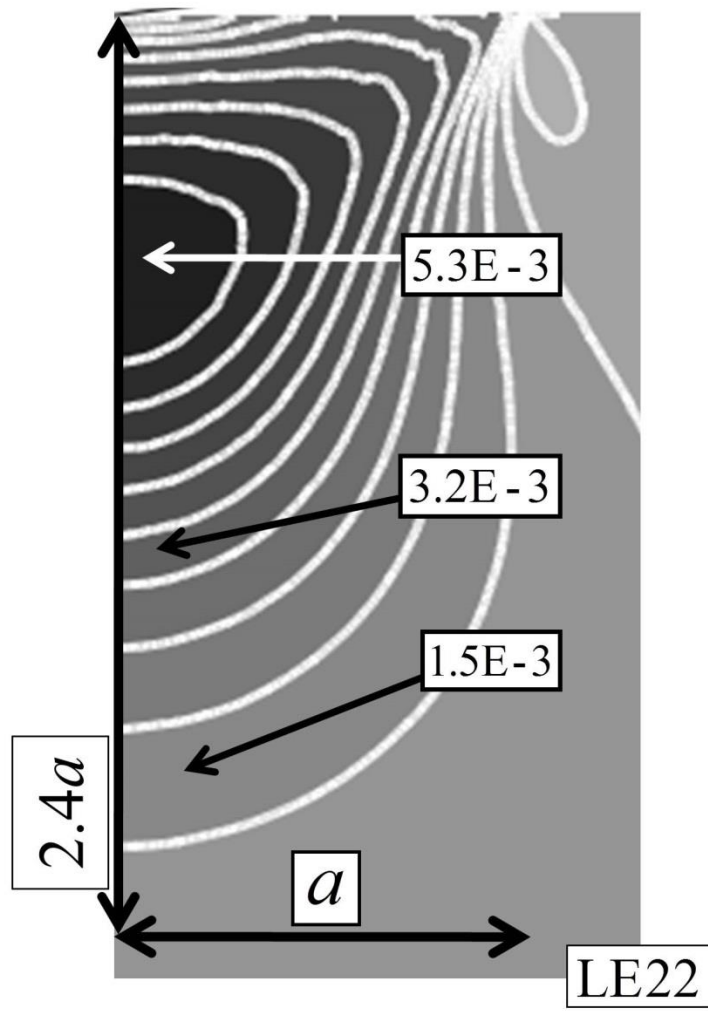


Figure 5. Logarithmic strain field (along the indentation direction) in the indentation zone close to the indentation yield. The model axis of symmetry is the left edge of the figure [44].

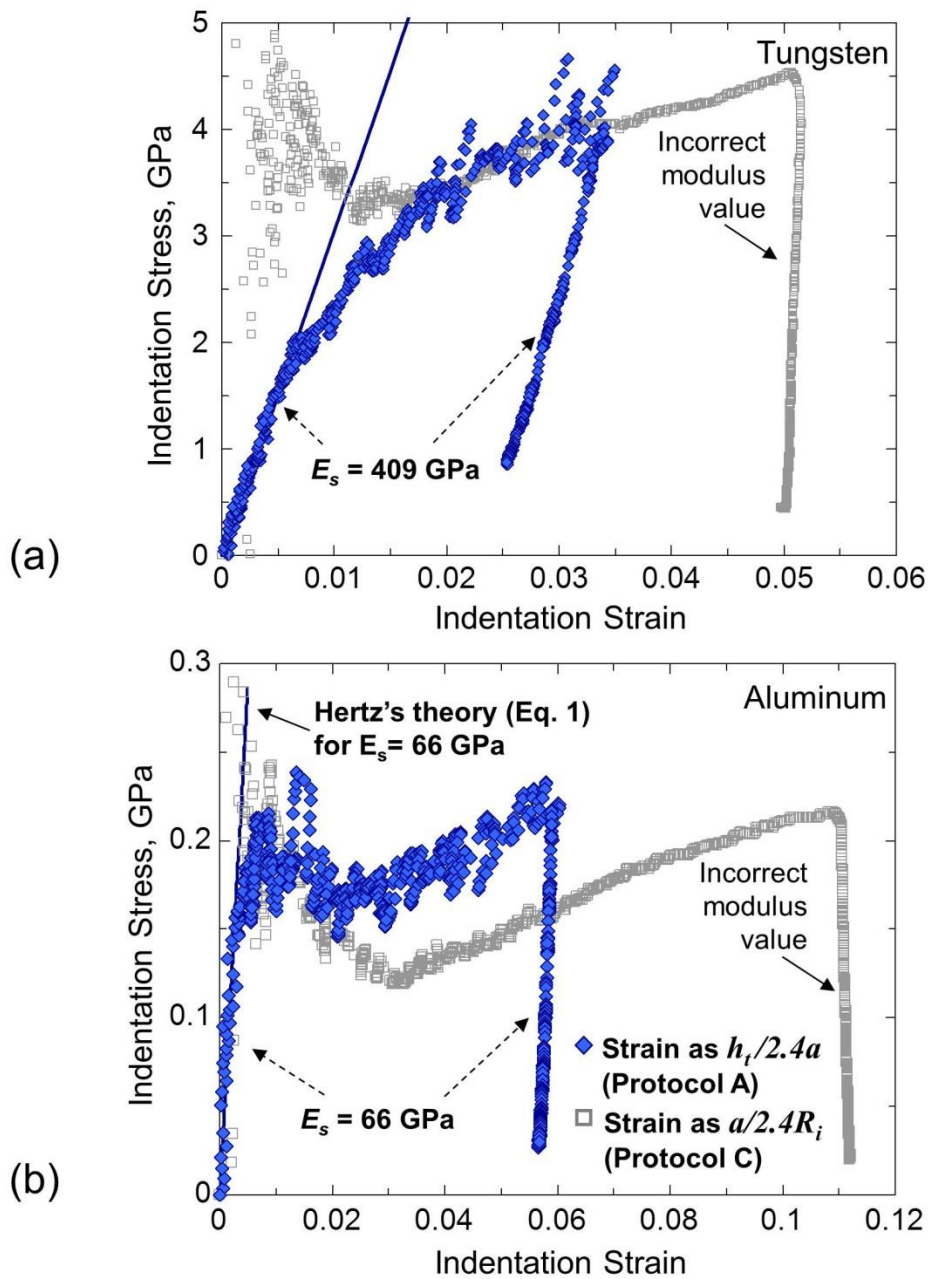


Figure 6. A comparison of the extracted indentation stress-strain curves for (a) tungsten and (b) aluminum, using the two different definitions of indentation strain. The definition of the indentation strain ($= h_t/2.4a$, Protocol A in Fig. 4) produces significantly better indentation stress-strain curves with correct values of modulus during both loading and unloading.

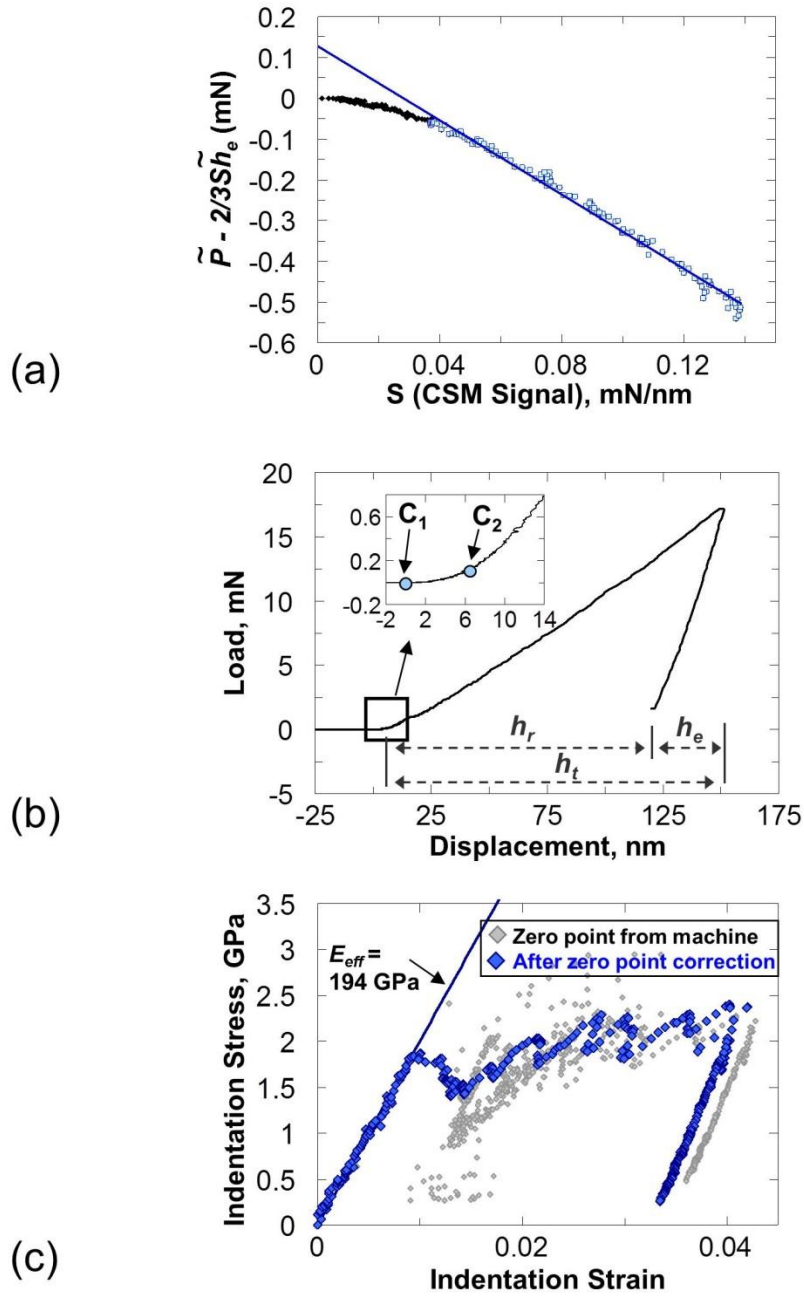


Figure 7. (a) The identification of the effective zero-point in the dataset measured on a vibro-polished Fe-3%Si steel sample indented with a 13.5 μm radius spherical indenter [12]. The measured (b) load-displacement curve and the extracted (c) indentation stress-strain curves for Fe-3%Si steel using two different estimates of the zero-point. The inset in (b) shows the two different estimates of the zero-point: C_1 - zero point given by the machine and C_2 - effective zero point determined using [12].

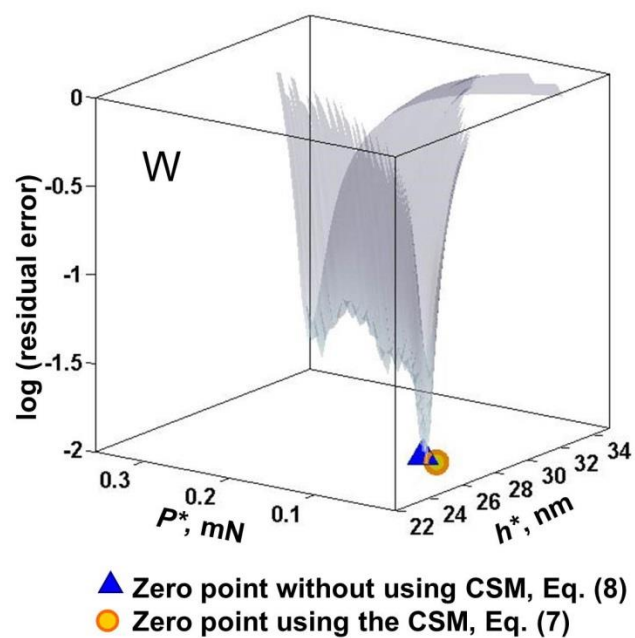


Figure 8. Comparison between the effective zero-points identified by the CSM technique (Eq. 7) and the non-CSM technique (Eq. 8) for tungsten using a 1.4 μm spherical indenter. The residual error is obtained from regression analyses as measure of the degree of fit to Eq. 8.

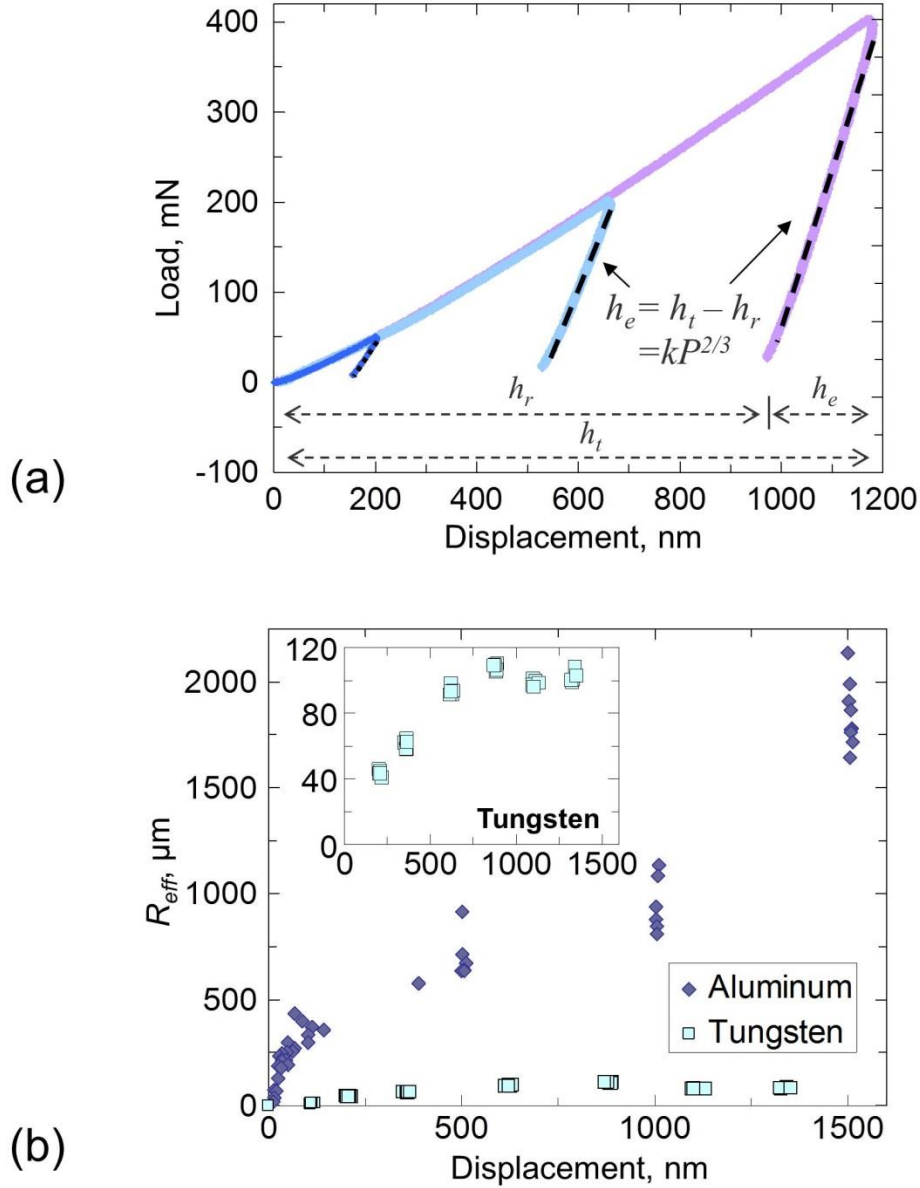


Figure 9.

- (a) Schematic of the procedure involved in establishing the contact radius, a , at different load levels. The unloading segment at each of these load levels is fitted to Eq. 9 to estimate h_r and k . R_{eff} and a can then be calculated using Eqs. 8 and 10.
- (b) Values of R_{eff} computed at different indentation depths which differ significantly between the softer aluminum and the harder tungsten sample. The values for R_{eff} are also significantly larger than $R_i (= 20\mu\text{m})$ for both samples. Inset: Expanded view for the tungsten sample.

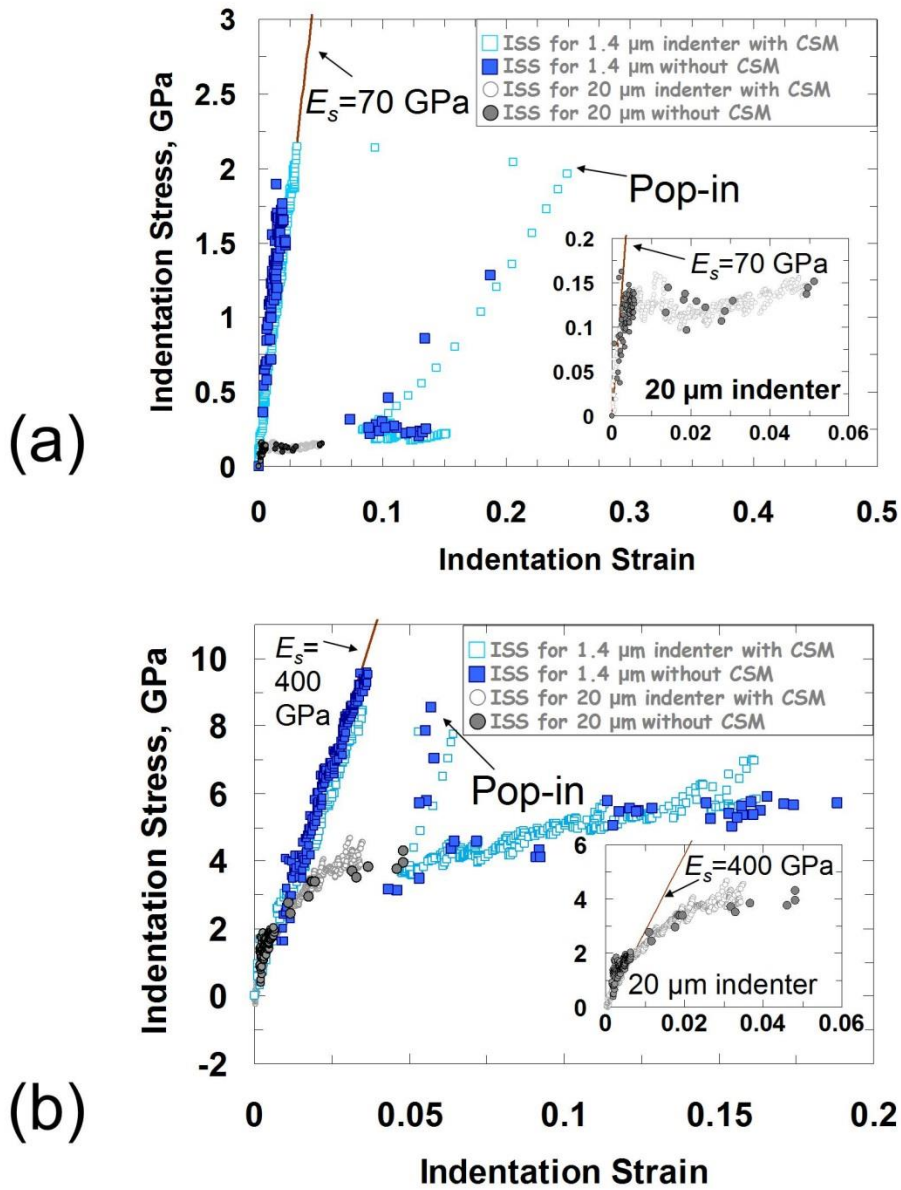


Figure 10. Comparison between the indentation stress-strain curves obtained using the CSM method (Section 5.1) and the non-CSM method (Section 5.2) on (a) aluminum and (b) tungsten samples with the 1.4 and 20 μm radii indenters. The insets show expanded views of the indentation stress-strain curves for the larger 20 μm indenter.

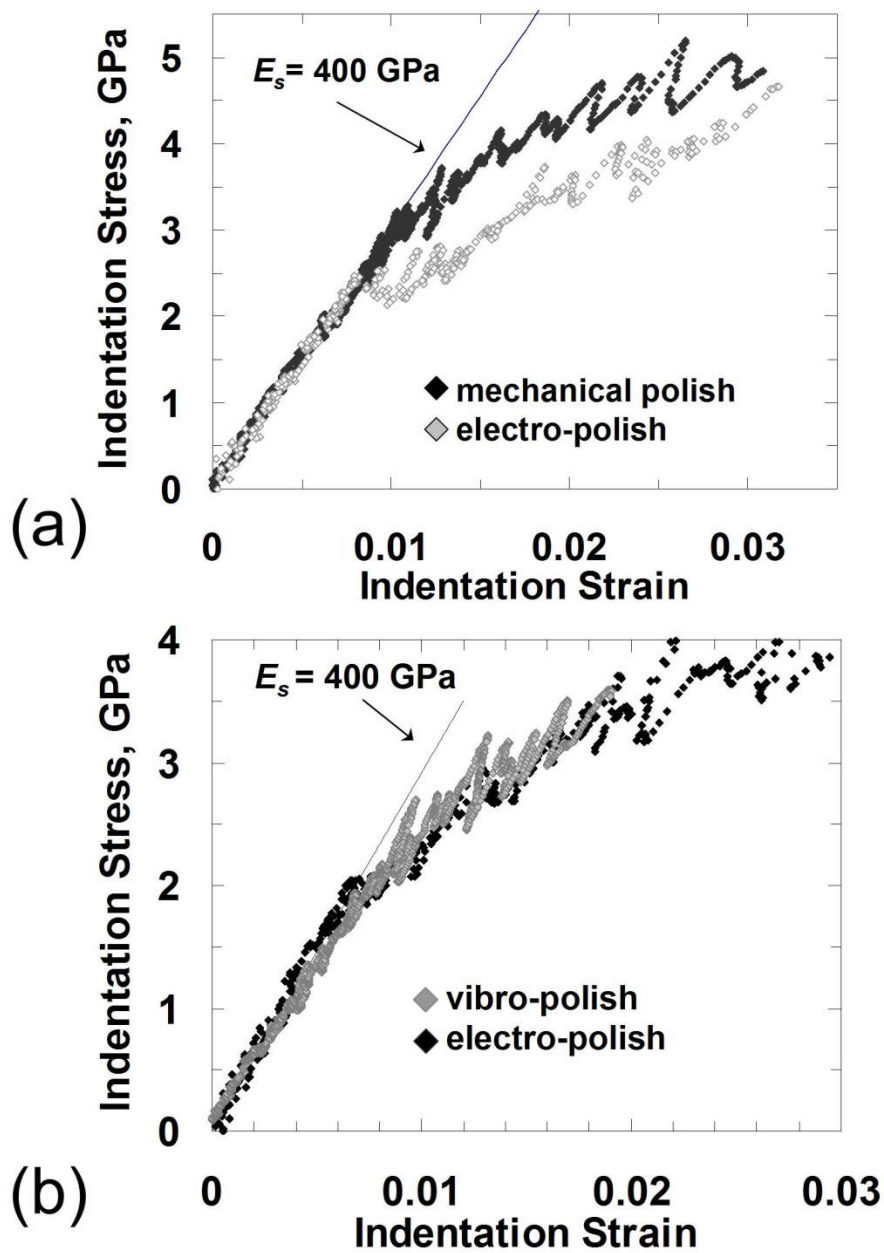


Figure 11. Comparison between the indentation stress-strain responses in (a) mechanically polished and electro-polished surfaces and (b) electro-polished and vibro-polished surfaces of annealed W. These tests were carried out using a 13.5 μm spherical indenter [63].

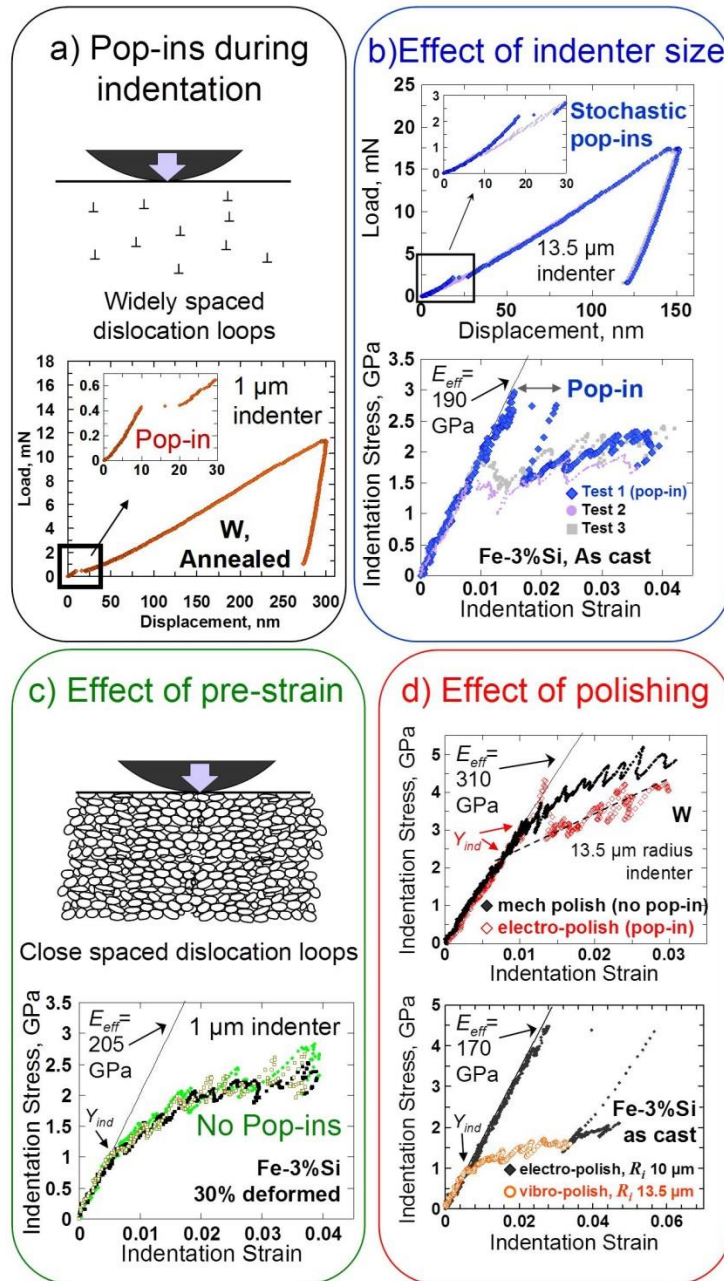


Figure 12. (a) Pop-ins in nanoindentation are generally revealed as sudden excursions in depth and strain (in a load controlled experiment) and occur most readily in indentation experiments on annealed samples with very small indenter tip radii, such as during indentation on annealed W with a 1 μm radius indenter [63]. (b) Their occurrence is more stochastic when using a larger indenter (such as during indentation on as-cast Fe-3%Si with a 13.5 μm radius indenter [63]) and (c) pop-ins are almost always absent in tests on cold-worked samples with high dislocation densities. Thus tests on 30% deformed Fe-3%Si steel do not show any pop-in even with a small sized indenter of 1 μm radius [63]. (d) Rough mechanical polishing can cause the near-surface dislocation density to increase, thus reducing pop-ins but artificially increasing the yield stress (Y_{ind}) in annealed W [63]. Vibro-polished samples show the ideal combination for measuring Y_{ind} : suppressing pop-ins in as-cast Fe-3%Si but not adversely affecting the Y_{ind} value [62].

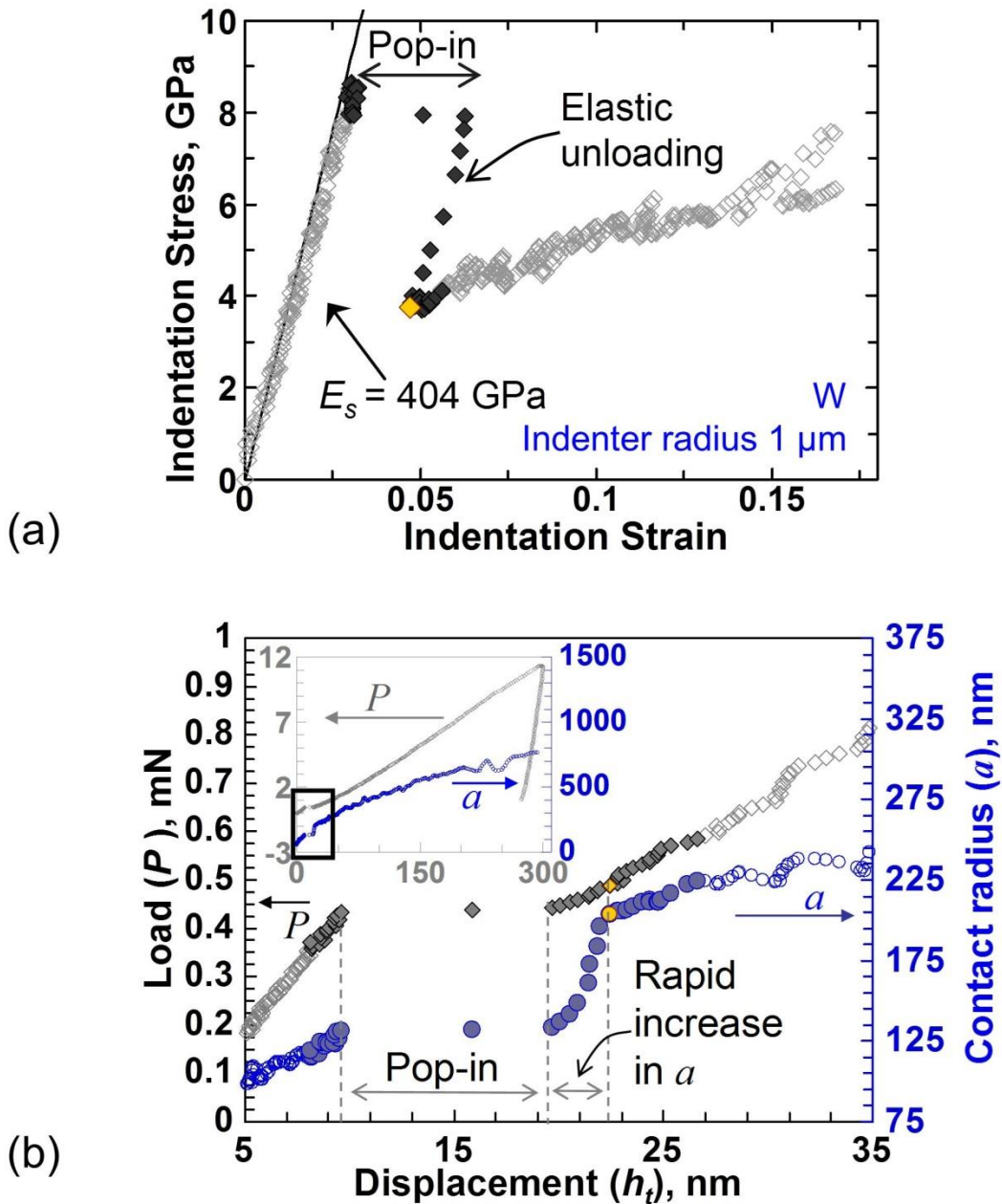


Figure 13. (a) Indentation stress-strain response of a pop-in event in an electropolished tungsten sample using a spherical indenter of $1 \mu\text{m}$ radius. The pop-in is manifested as a strain burst at constant stress, which is immediately followed by an unloading segment after the pop-in. **(b)** Corresponding measurements of the indentation load, displacement and contact radius (CSM signal) show that the contact radius remains constant during the pop-in but increases rapidly immediately afterwards. Note the data point marked in gold color, which signifies the end of the regime of rapid increase in the contact radius, and its corresponding location in the indentation stress-strain curve.

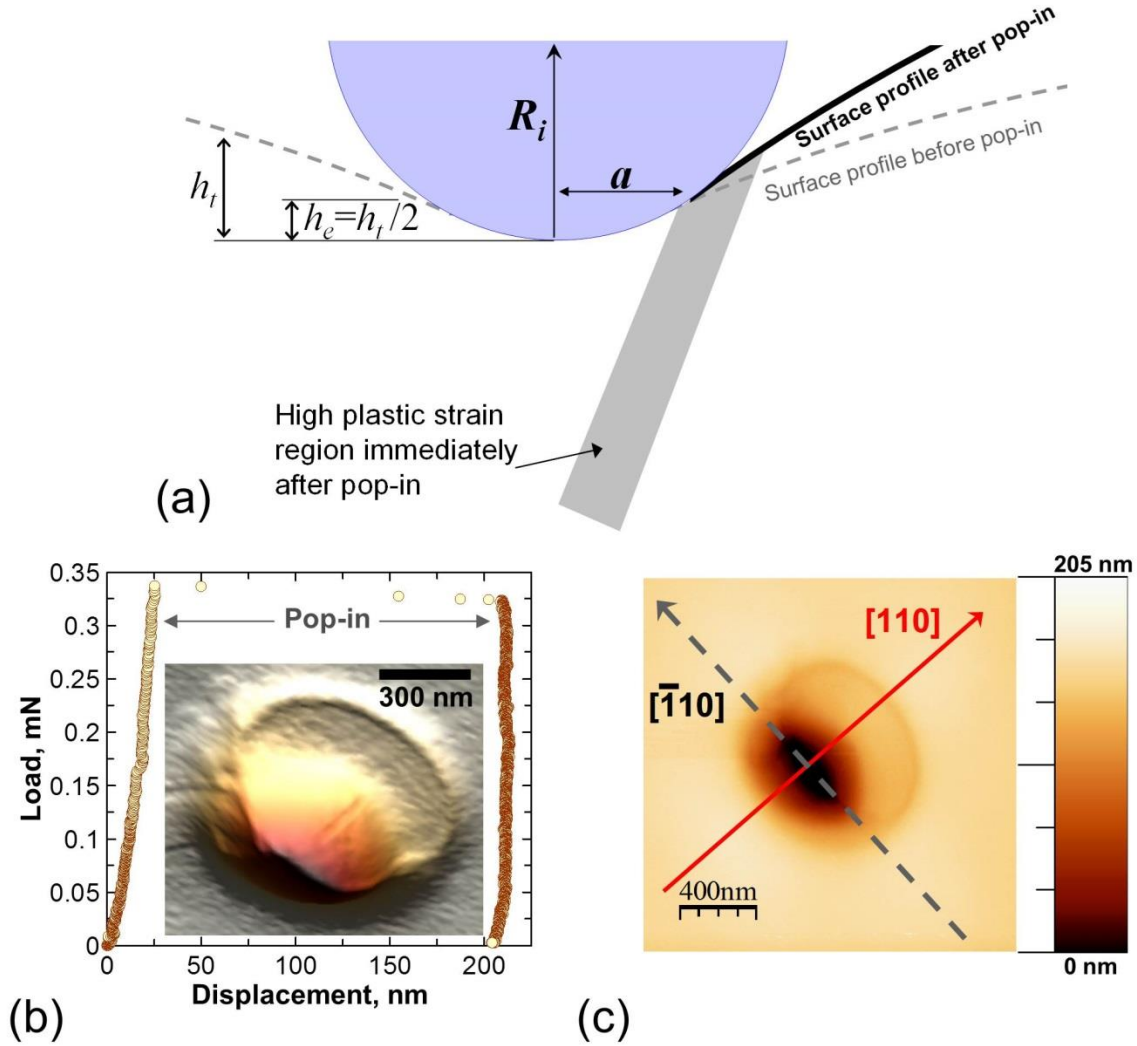


Figure 14. (a) Schematic of the sequence of events immediately following a pop-in in spherical nanoindentation. Before pop-in (the curve in gray) both the indenter and the sample surface are highly conforming up to a contact radius of a . Upon pop-in, there is a sudden increase in the indentation depth, but no immediate increase in a . Rather dislocations traveling (in bursts) along specific crystallographic planes get released along the free surface adjacent to the indenter. This brings the sample surface in closer proximity to the indenter. Thus any further loading causes a large increase in a .

(b) Load-displacement response on a near-(001) aluminum surface using a 1 μm indenter showing a test stopped after a single large pop-in event. **(b inset)** 3D and **(c)** surface profiles of the above indent measured using a hybrid AFM-SEM system showing a large step formation along the $[110]$ direction of the indent surface. Note the significant anisotropy of the residual indent imprint, no such pile-up is visible in the perpendicular $[\bar{1}10]$ direction $[213]$.

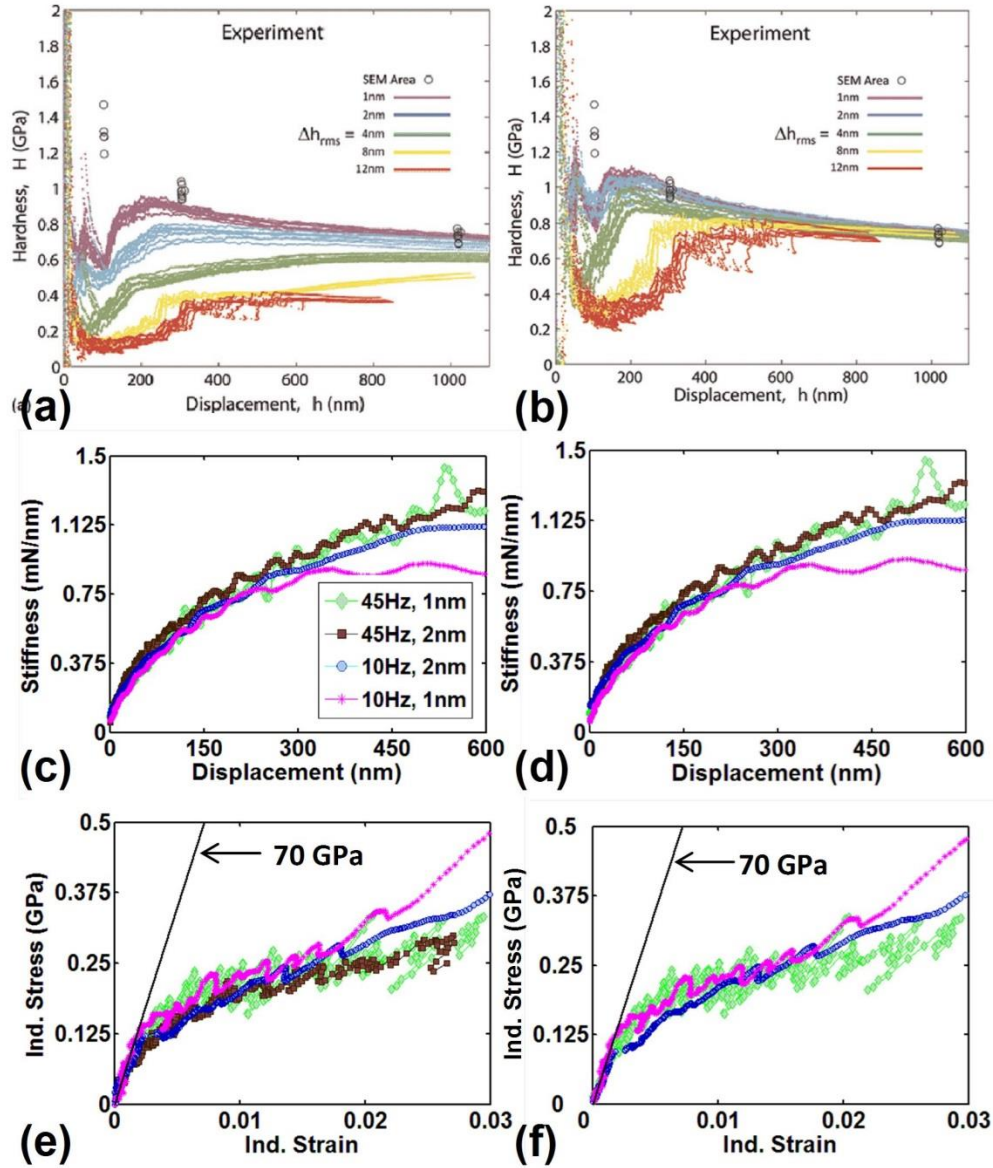


Figure 15. (a) Influence of the displacement oscillation on hardness, H , measured on Cu (100) using a Berkovich tip. (b) Hardnesses derived from corrected $P-h-S$ data. Reprinted with permission from [89].

(c) Influence of CSM on the indentation stiffness-displacement response: Raw stiffness-displacement data corresponding to measurements conducted using a 100 μm spherical tip on 20% deformed ultra-high purity aluminum; (d) Corresponding corrected data [99].

(e) Influence of CSM on the Indentation stress-strain curves for tests on 20% deformed ultra-high purity aluminum using a 100 μm spherical tip; (d) the corresponding corrected data (Note that for tests with 45Hz – 2nm oscillations, most of the initial elastic segment is lost while correcting for the stiffness signal, and hence the indentation stress-strain curve could not be extracted) [99].

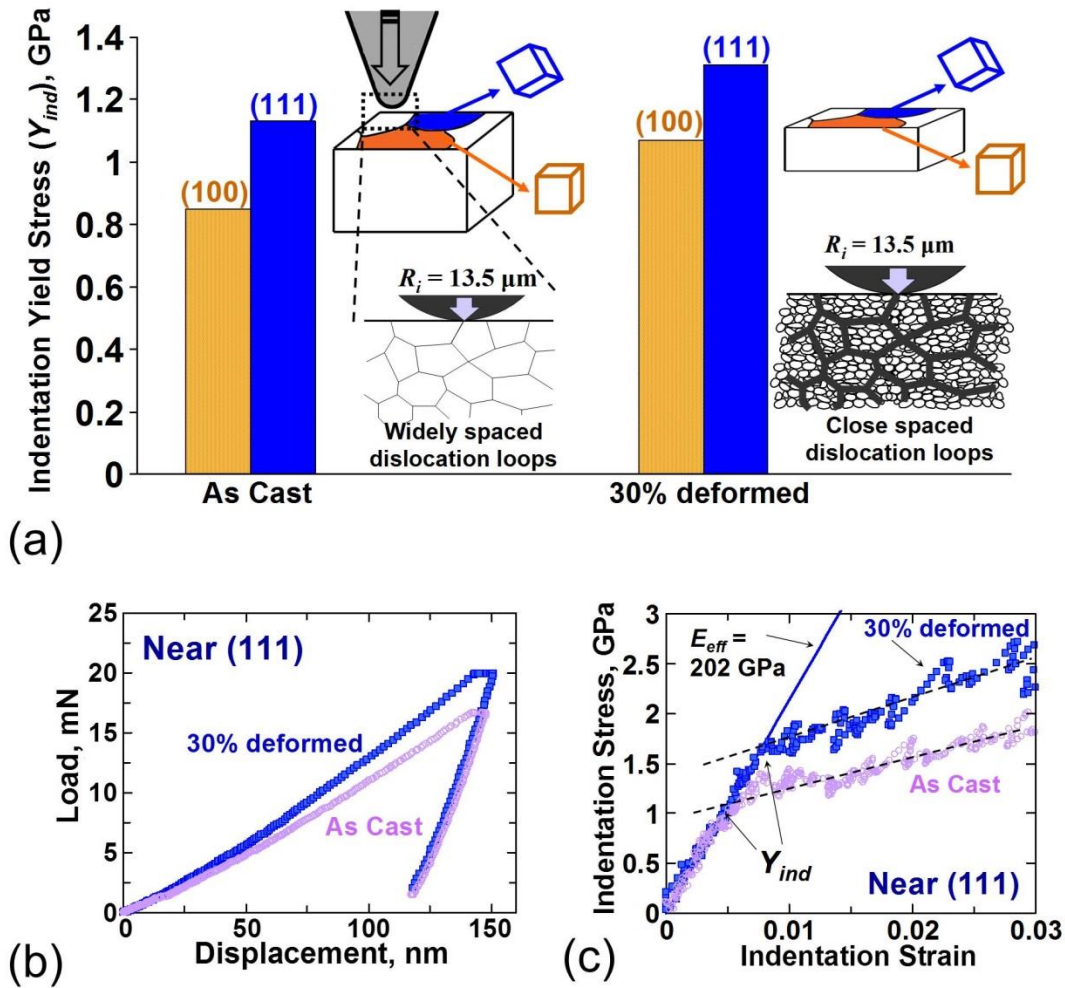


Figure 16. (a) Causes for the change in Y_{ind} . In an as-cast sample of Fe-3%Si steel, the dislocation content is fairly uniform across all the grains. Here Y_{ind} varies from one grain to another mainly due to the differences in the activities of the different slip systems in the different grains and their orientation with the indentation direction. When the metal is 30% deformed, its dislocation content increases and varies both within individual grains and between grains. The Y_{ind} in deformed samples therefore depends on both the grain orientation and the dislocation content at the indentation site.

(b) and **(c)** show the typical load-displacement and their corresponding indentation stress-strain responses respectively for spherical indentations performed on near (111) grains in as-cast and 30% deformed Fe-3%Si steel. The E_{eff} , Y_{ind} and the post-yield characteristics are much better discerned in (c). Only the loading sections are shown for the indentation stress-strain plots. A 13.5 μm radius spherical indenter was used for the tests.

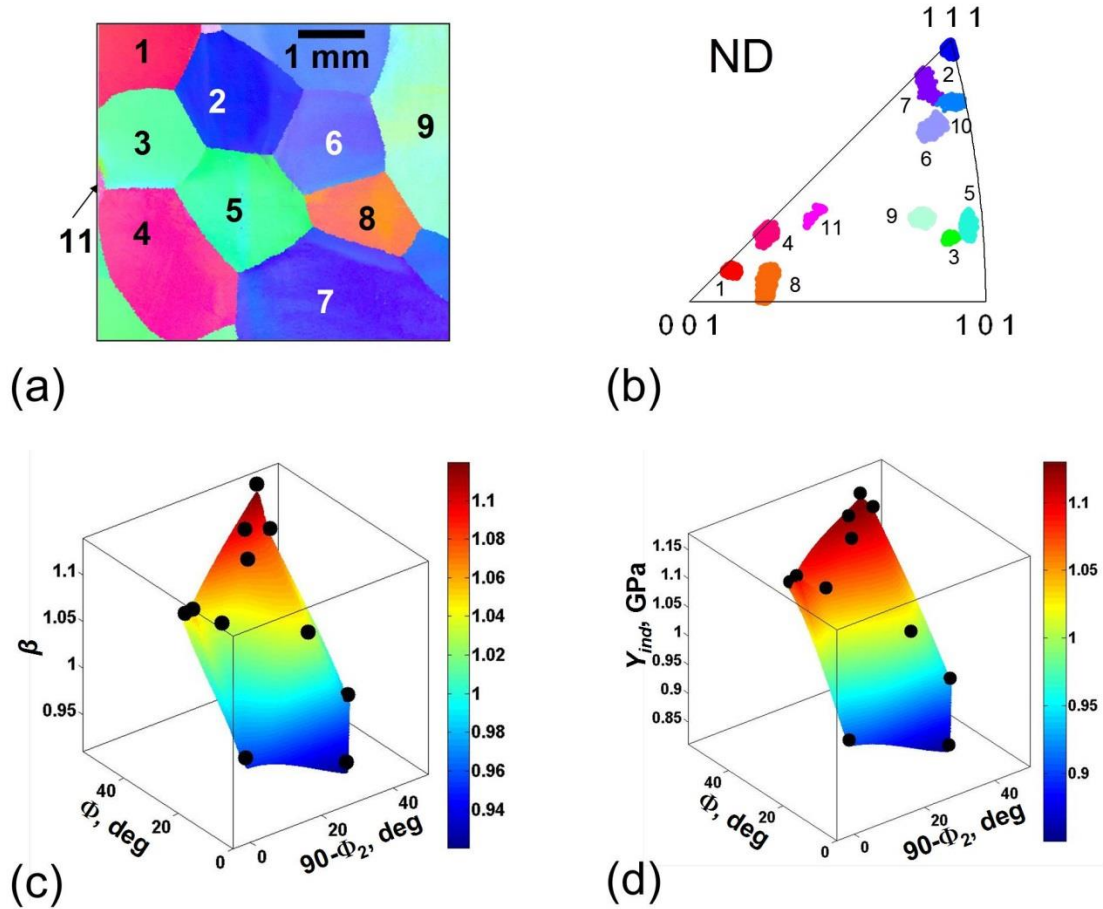
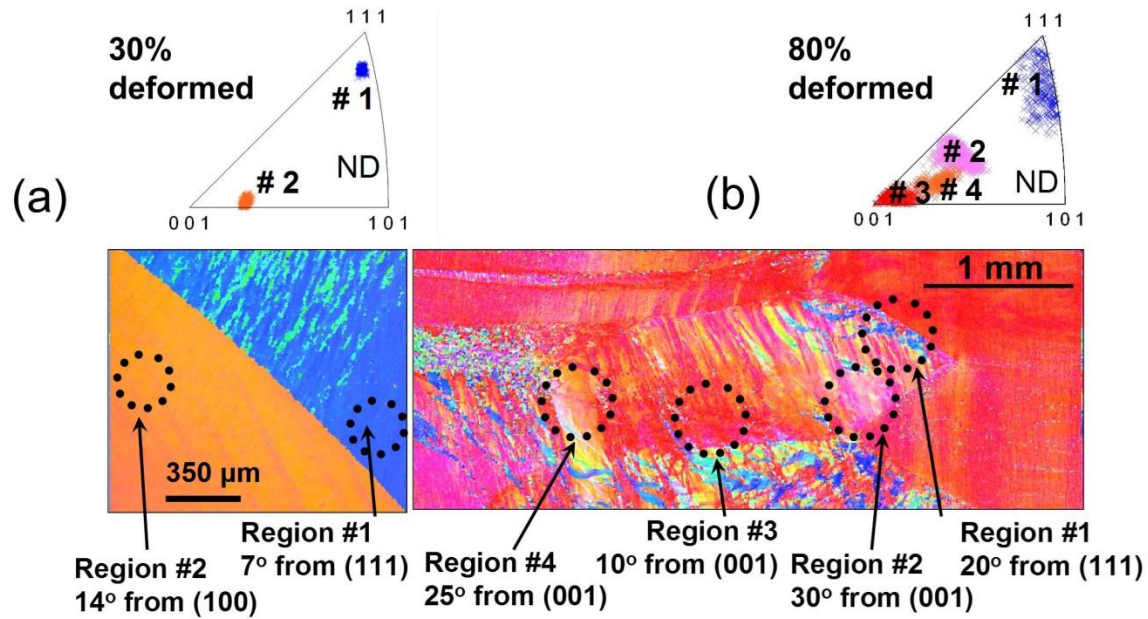


Figure 17. (a) OIM scan and (b) inverse pole figure map obtained on a sample of as-cast and polished Fe-3%Si showing a wide range of grain orientations. Surface contour plots for (c) β and (d) Y_{ind} . The full circles indicate values extracted directly from the measurements [64].

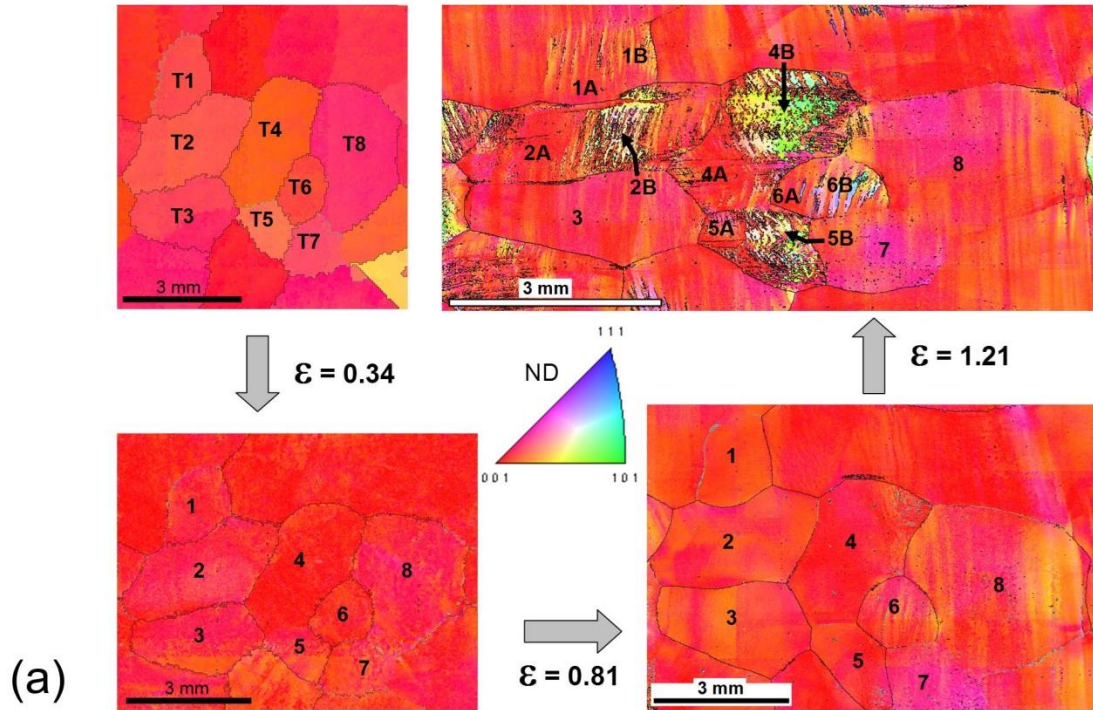


30% deformed Fe-3%Si							
Region #	Orientation ($\varphi_1, \Phi, \varphi_2$)	Misorientation	E_{eff} , GPa	β	Measured Y_{ind} in the deformed condition, GPa	Estimated Y_{ind} in the annealed condition, GPa	% change in τ_{CRSS}
1	148.3, 49.8, 50.7	7° from (111)	198.0±3.9	1.09	1.31±0.13	1.12	16.9%
2	294.2, 13.5, 83.8	14° from (001)	174.2±1.59	0.93	1.07±0.05	0.90	18.9%
80% deformed Fe-3%Si							
Region #	Orientation ($\varphi_1, \Phi, \varphi_2$)	Misorientation	E_{eff} , GPa	β	Measured Y_{ind} in the deformed condition, GPa	Estimated Y_{ind} in the annealed condition, GPa	% change in τ_{CRSS}
1	111.6, 49.4, 54.2	20° from (111)	198.1±1.26	1.09	1.69±0.06	1.12	50.9%
2	326.3, 23.2, 58	30° from (001)	191.1±1.42	1.04	1.46±0.07	1.00	46.0%
4	263, 16.2, 73.7	25° from (001)	185.9±0.75	1.00	1.37±0.07	0.92	48.9%
3	259, 3.9, 84.4	10° from (001)	174.3±0.19	0.93	1.27±0.08	0.85	49.4%

(c)

Figure 18. (a) and (b) show the inverse pole figure maps and the OIM scans for 30% and 80% deformed Fe-3%Si samples respectively. Indentations were performed in the regions marked by the dotted circles in each of these samples [64].

The table in (c) summarizes the values from indentations on the 30% and 80% deformed Fe-3%Si samples. The estimated Y_{ind} values in the annealed condition were calculated from the surface contour plot in Fig. 17d. The measured values of E_{eff} and Y_{ind} in the deformed condition were calculated from the indentation stress-strain curves, as shown in Fig. 16. The values for β were calculated from Eq. (14).



(b)

$\epsilon = 1.21$				
Grain #	Orientation (ϕ_1, Φ, ϕ_2)	Measured Y_{ind} in the deformed condition, GPa	Estimated Y_{ind} in the annealed condition, GPa	% change in τ_{CRSS}
1A	339, 5.6, 56.2	1.23 ± 0.06	0.85	44.4
1B	246, 15.2, 82	1.24 ± 0.09	0.91	36.6
2A	339, 2, 39.2	1.15 ± 0.07	0.85	35.2
2B	266, 25.9, 81	1.29 ± 0.14	0.99	30.7
3	342, 5.8, 56.5	1.14 ± 0.17	0.86	33.1
4A	324, 1.4, 30	1.11 ± 0.16	0.85	30.9
4B	272, 37.1, 84	1.24 ± 0.07	1.03	20.1
5A	99.4, 6.3, 90	1.07 ± 0.09	0.86	24.6
5B	288, 27.3, 70	1.58 ± 0.13	1	58.0
6A	331, 7.2, 66.5	0.96 ± 0.13	0.87	10.6
6B	122, 58, 71.6	1.95 ± 0.38	1.08	80.6
7	346, 12.2, 57	1.05 ± 0.09	0.89	18.3
8	167, 9.5, 53.1	1.16 ± 0.18	0.87	32.9

Figure 19. (a) OIM scans of the top surface showing the as-cast microstructure of the columnar Fe-3%Si sample, and microstructure after plane strain compression to true strains of 0.34, 0.81 and 1.21. **(b)** Extracted values of indentation yield strength and changes in critical resolved shear stress after the third deformation stage [112].

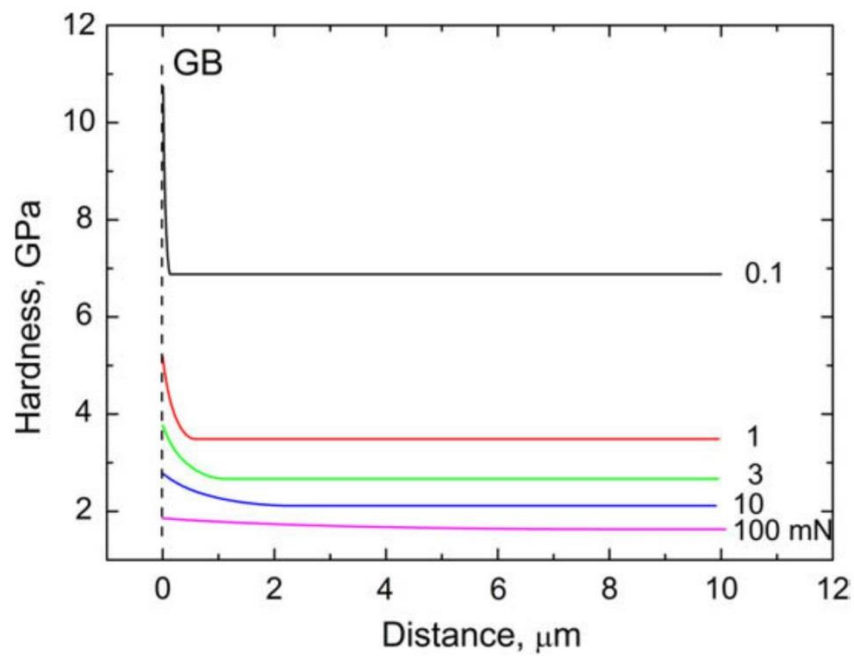
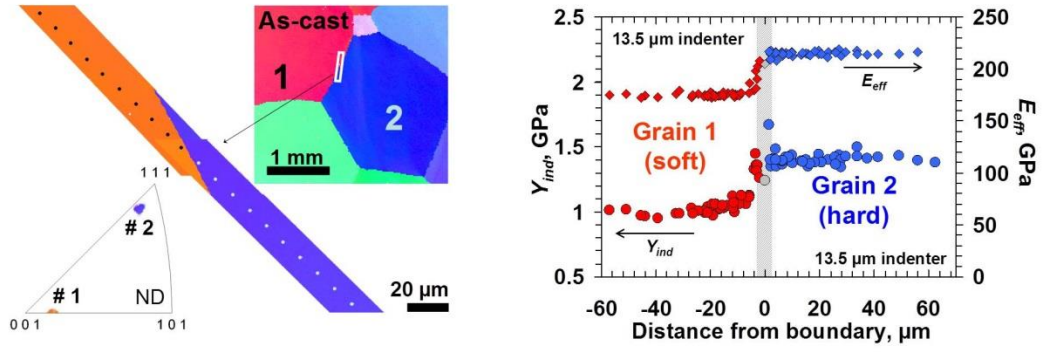
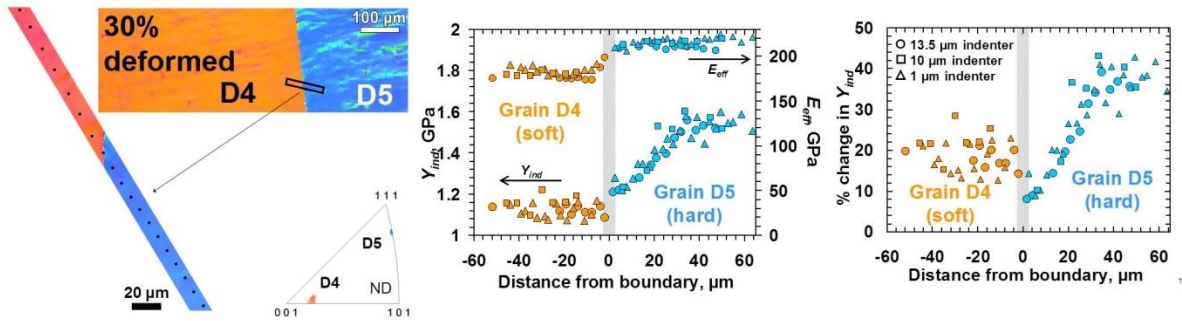


Figure 20. Indentation-induced deformation in Mo showing the dependence of hardness on the distance from grain boundary for different maximum indentation loads. At loads >10 mN the hardened zone near the grain boundary is masked by the additional local plastic deformation caused by indentation itself. Reprinted with permission from [83].



(a)



(b)

Figure 21. Measure of E_{eff} and Y_{ind} across a high angle grain boundary between **(a)** Grains 1 and 2 in as-cast Fe-3%Si steel and **(b)** Grains D4 and D5 in 30% deformed Fe-3%Si steel [62].

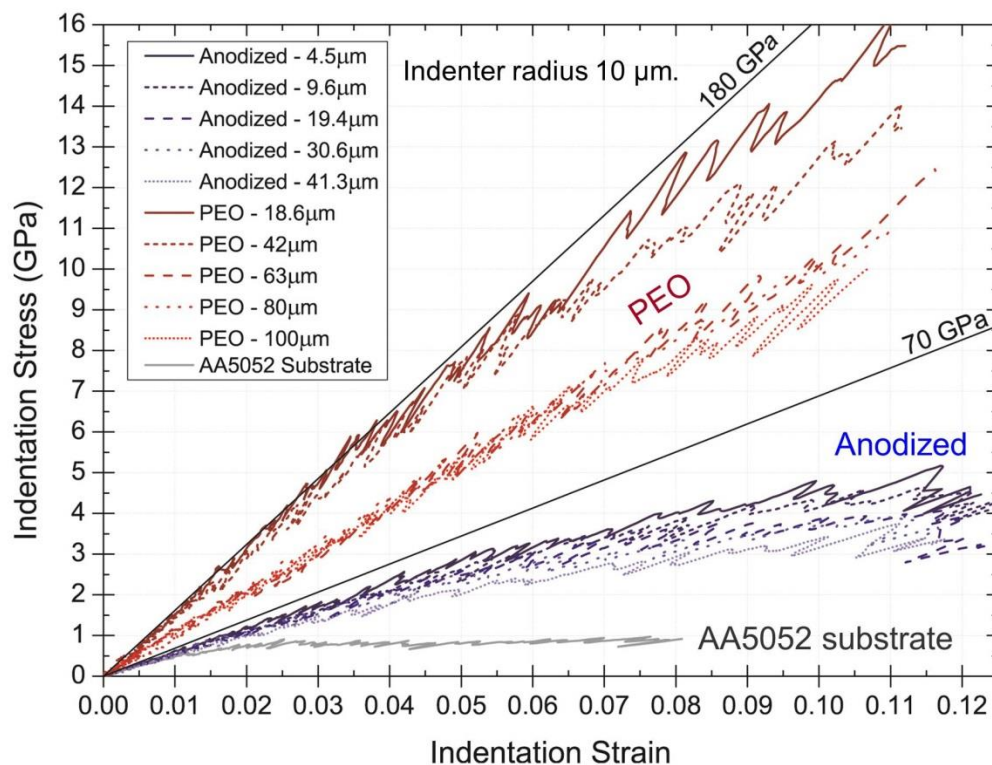


Figure 22. Comparing the indentation stress-strain responses across the cross-sections of two common electrolytic coating methods - hard anodizing and plasma electrolytic oxidation (PEO) – on a 5052 aluminum alloy at various distances from the substrate interface and within the aluminum substrate [126].

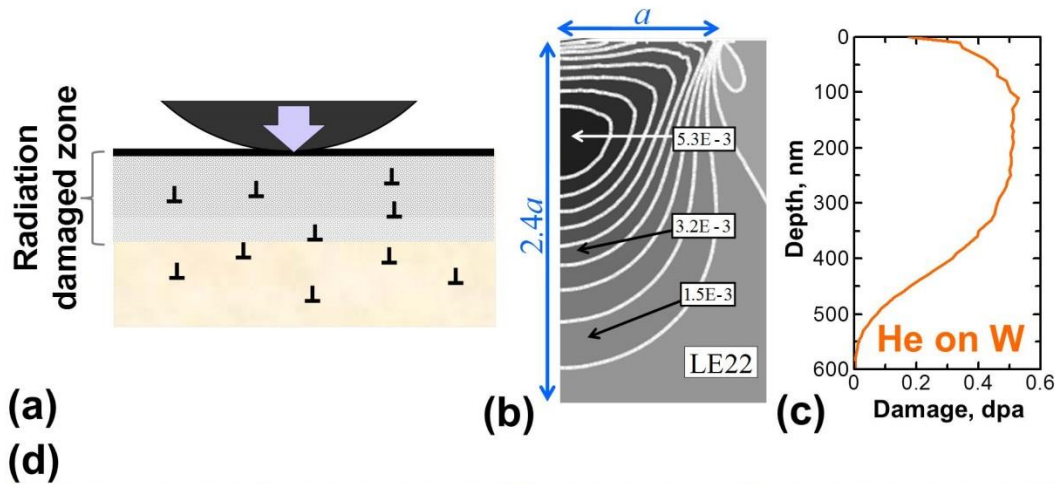
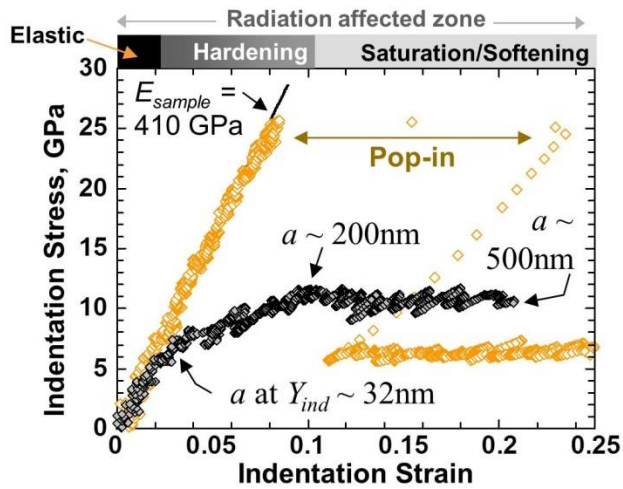


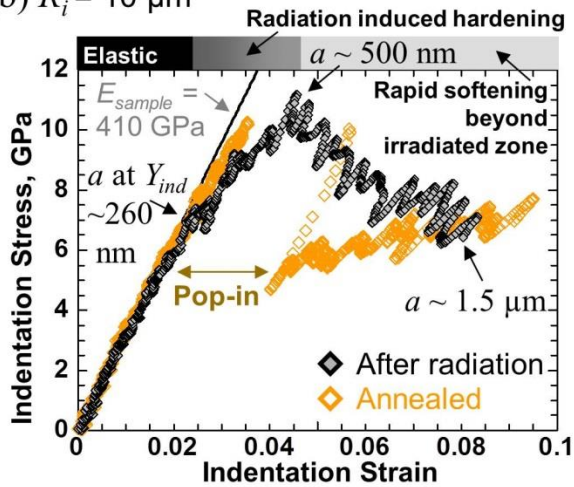
Figure 23. (a) Upon ion-irradiation, the metal surface is modified by a damaged layer, which causes a change in its mechanical response as compared to the bulk of the sample. (b) Logarithmic strain field (along the indentation direction) for a spherical indenter in the indentation zone ($\sim 2.4a$, where a is the contact radius) close to the indentation yield [44]. Both the contact radius a , and hence the volume probed by indentation, can be controlled with a proper choice of indenter radii. This approach is thus ideally suited for measuring any mechanical changes in the material surface layers, such as probing the (c) damage caused by He irradiation on a tungsten sample. (d) Table showing indentation depth (h_t), contact radius (a) and indentation zone size ($\sim 2.4a$) at yield for W using 4 different indenter radii.

* For the 1000 μm radius indenter, the response was all elastic up to $h \sim 200$ nm (instrument limit).

(a) $R_i = 1 \mu\text{m}$



(b) $R_i = 10 \mu\text{m}$



(c) $R_i = 100 \mu\text{m}$

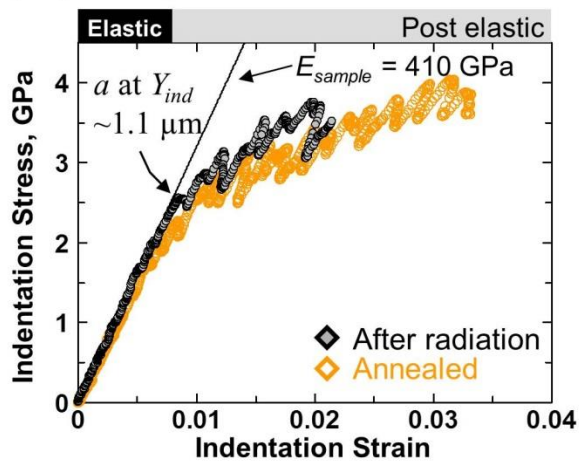


Figure 24. Comparing the indentation stress-strain responses between annealed (orange curve) and irradiated (black curve) W grains of near (001) orientation for three different indenter tip radii (a) 1 μm , (b) 10 μm and (c) 100 μm .

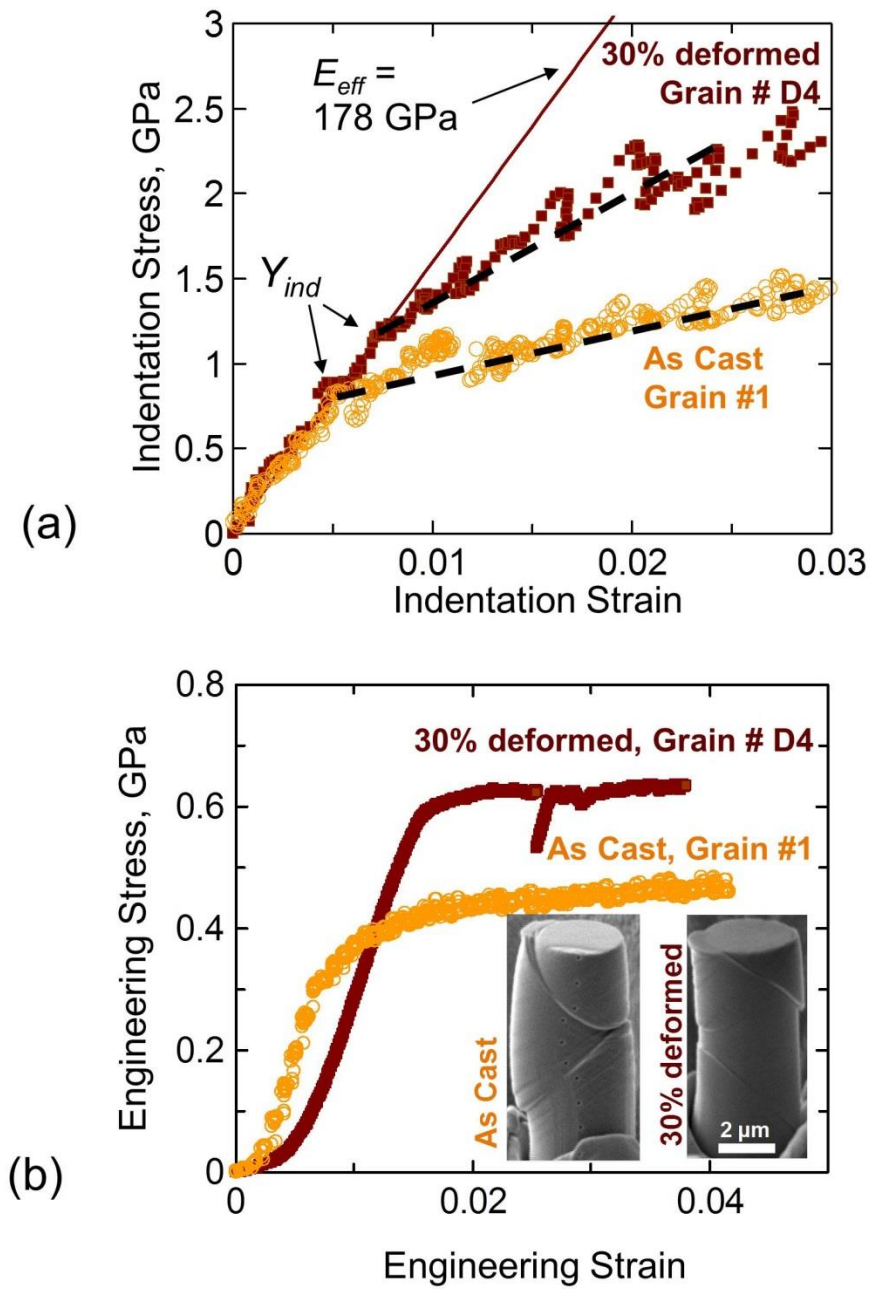


Figure 25. Comparison of (a) indentation vs. (b) compression stress-strain curves between as-cast and 30% deformed Fe-3%Si samples. Both grains #1 and #D4 have a near (100) orientation as shown in Fig. 21. SEM images of the pillars were taken at 70 deg tilt angle after a nominal strain of around 20%.

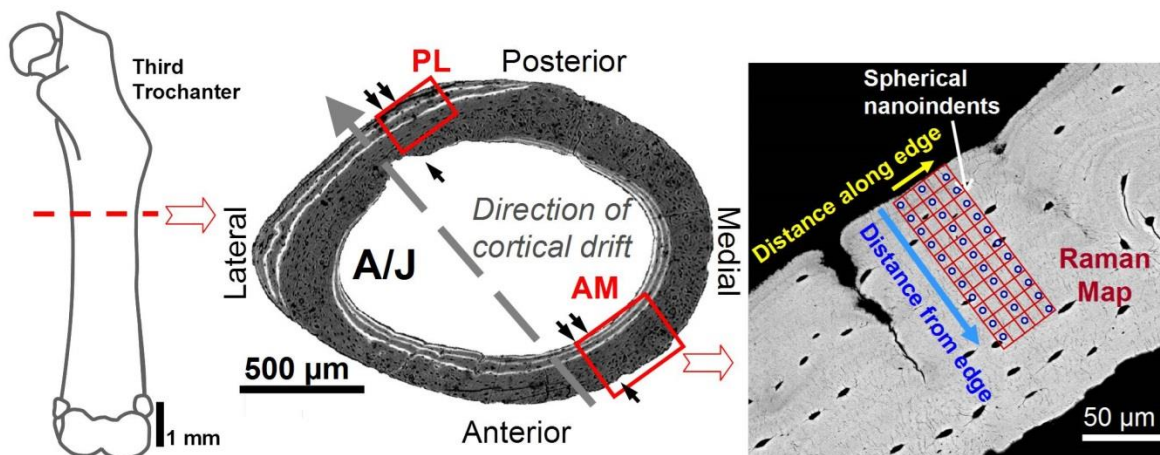


Figure 26. For indentation testing both the ‘dry’ and ‘wet’ mouse femora were sectioned transversely, distal to the third trochanter. During post-natal growth, bone is deposited (double arrows) and resorbed (single arrows) at different sites around these regions of the femoral cortex resulting in a net cortical drift (large arrow). Spherical nanoindentations (shown as blue dots in the SEM image) at the antero-medial (AM) cortex thus probe newer bone closer to the endosteal edge (double arrows) while the bone is more mature away from this surface. Three rows of indentations were performed on each sample. For the ‘dry’ bone samples the region surrounding the indents was then mapped by Raman Spectroscopy (shown by the red grid around the indented region) [61].

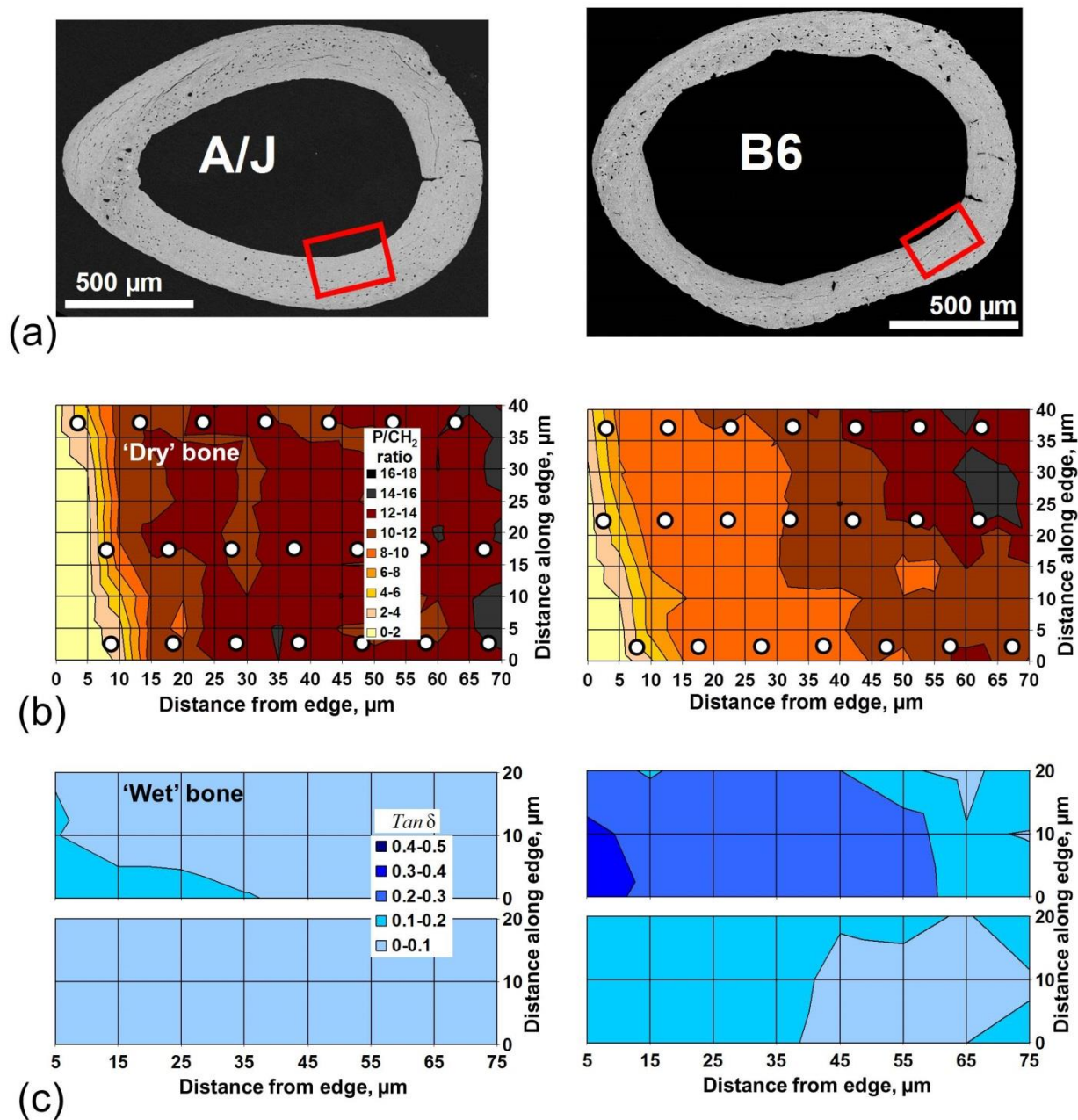


Figure 27. (a) Representative BSEM images of A/J and B6 mouse femora. **(b)** 'Dry' samples: representative 2D surface maps of the mineral-to-matrix ratios (defined as the phosphate to CH₂ wag peak intensity ratio from Raman spectroscopy measurements) in the 'dry' dehydrated/embedded bone samples across a 40 μm x 70 μm region close to the endosteal edge of the AM cortex. The white circles denote the approximate size and location of the indentation tests in relation to the Raman maps [59]. **(c)** 'Wet' samples: 2D surface maps of tan δ values at a representative mid-range frequency of 101 Hz across a 20 × 70 μm region close to the endosteal edge of the AM cortex in two A/J and B6 samples in the 'wet' hydrated condition [168].

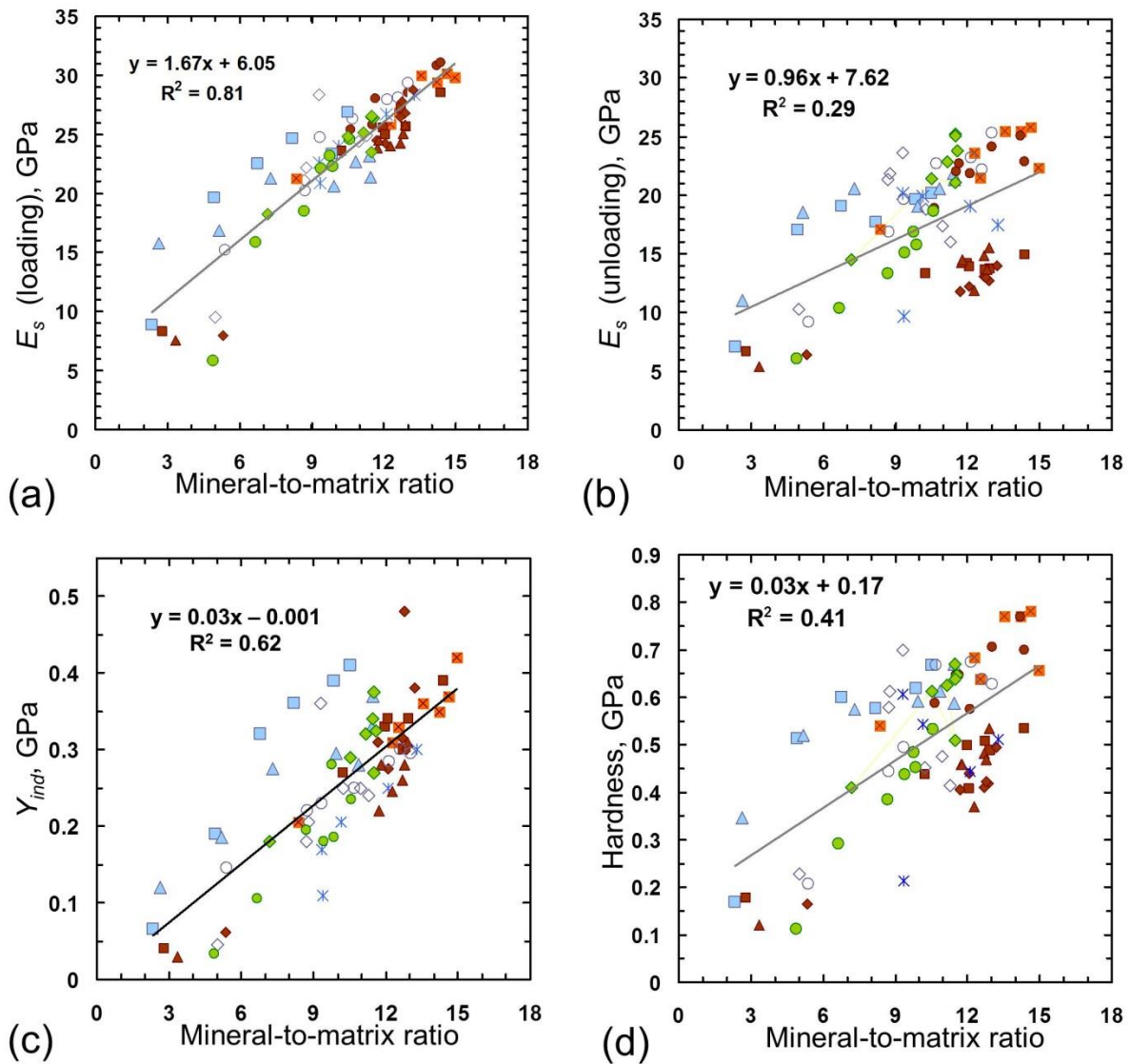
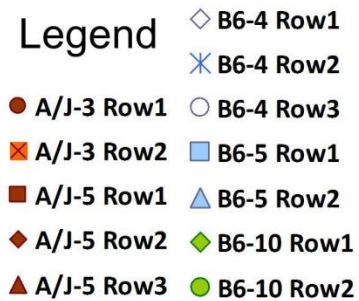


Figure 28. Scatter plots of (a) the elastic modulus E_s measured from the initial loading segment of the indentation stress-strain curves, (b) E_s calculated from the unloading portion of the load-displacement data, (c) indentation yield strength (Y_{ind}) and (d) indentation hardness at max load, all as functions of the mineral-to-matrix ratio measured by Raman spectroscopy across two A/J and three B6 samples [61].



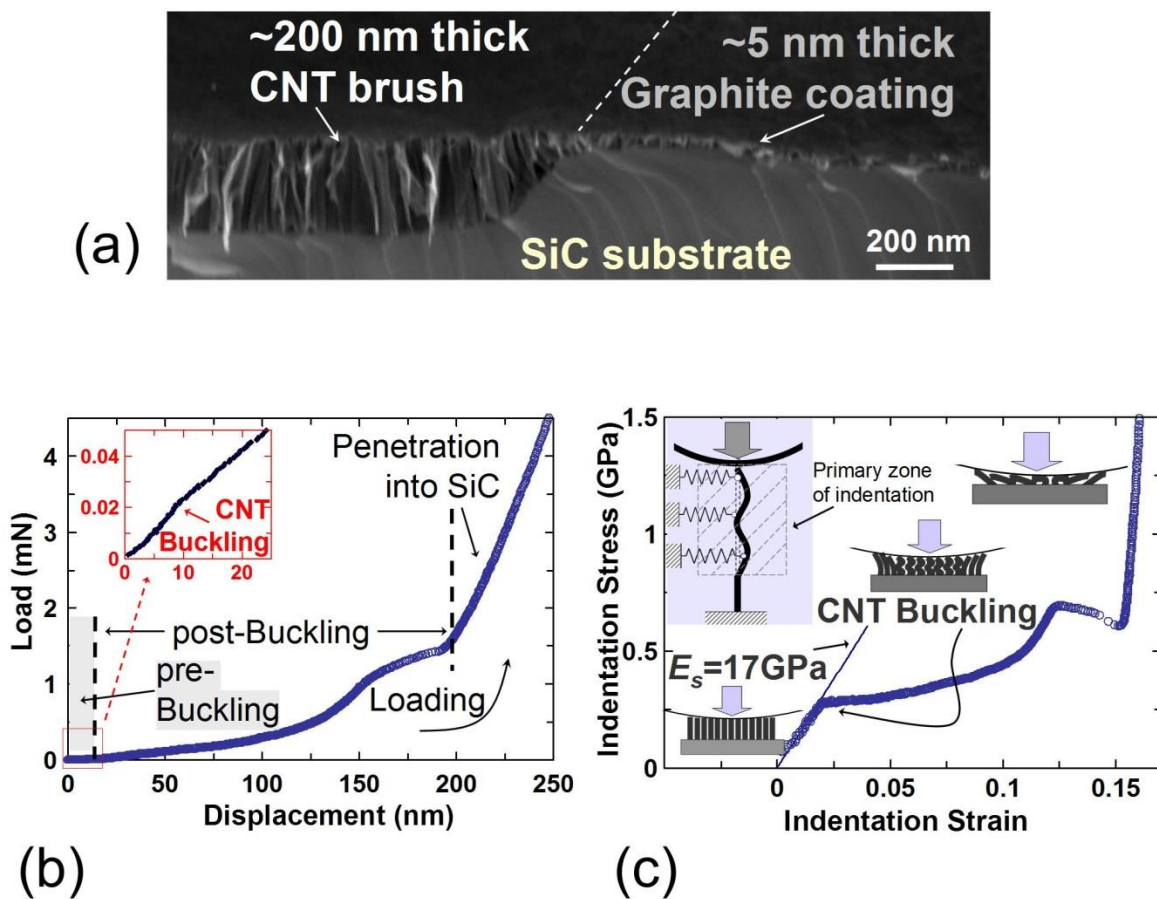
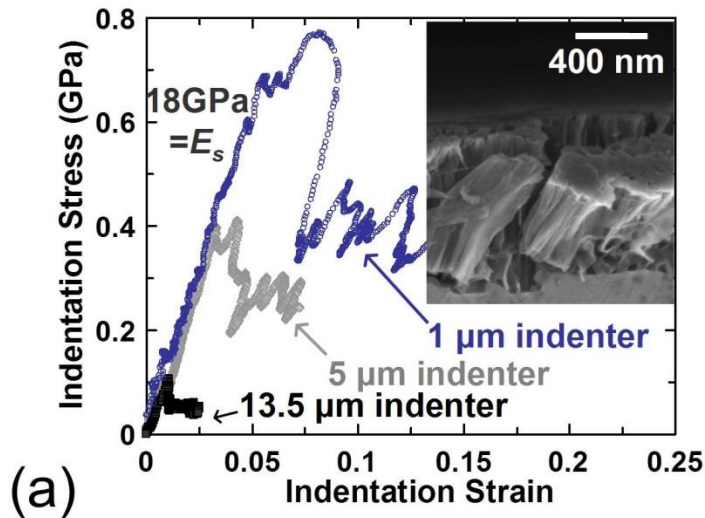


Figure 29. (a) SEM micrograph showing the VACNT brush – graphite interface [190]. (b) Indentation load-displacement and (c) indentation stress-strain response of a 1 μm spherical indenter on the ~200 nm thick CNT brush showing three distinct stages of VACNT indentation. (c inset) Schematic illustration of buckling of the CNTs in a dense CNT brush in the indentation zone.



	1 μm radius indenter	5 μm radius indenter	13.5 μm radius indenter
Indentation buckling stress	0.59 ± 0.41 GPa	0.40 ± 0.11 GPa	0.09 ± 0.02 GPa
Contact radius at buckling (a)	$0.16 \mu\text{m}$	$0.36 \mu\text{m}$	$1.49 \mu\text{m}$
Indentation zone size at buckling ($\approx 2.4a$)	$0.39 \mu\text{m}$	$1.01 \mu\text{m}$	$3.58 \mu\text{m}$

(b)

Figure 30. (a) Indentation stress-strain response on 1.3 μm thick VACNT brush as a function of indenter size (radius) showing an initial elastic behavior followed by the buckling instability. The table in **(b)** shows summarized average and standard deviation (of ≥ 5 tests) values of indentation buckling stress, contact radius and indentation zone size at buckling for the 3 different indenters used [190].

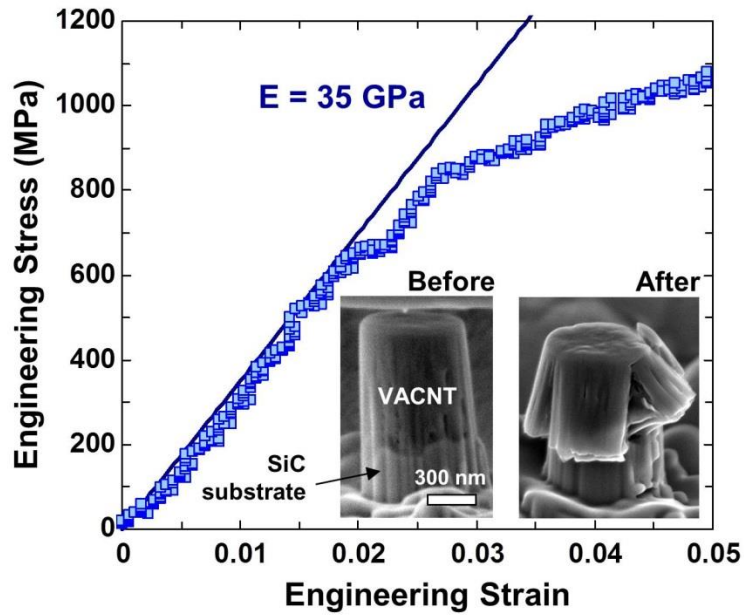


Figure 31. Uniaxial compression of a CDC-VACNT micro-pillar of diameter $\sim 600 \text{ nm}$. Both the loading modulus and buckling strength in compression show good agreement with the indentation results showed earlier. The inset images show the VACNT micro-pillar before and after compression.

Appendix D: Nanoindentation Stress-Strain Curves for Titanium

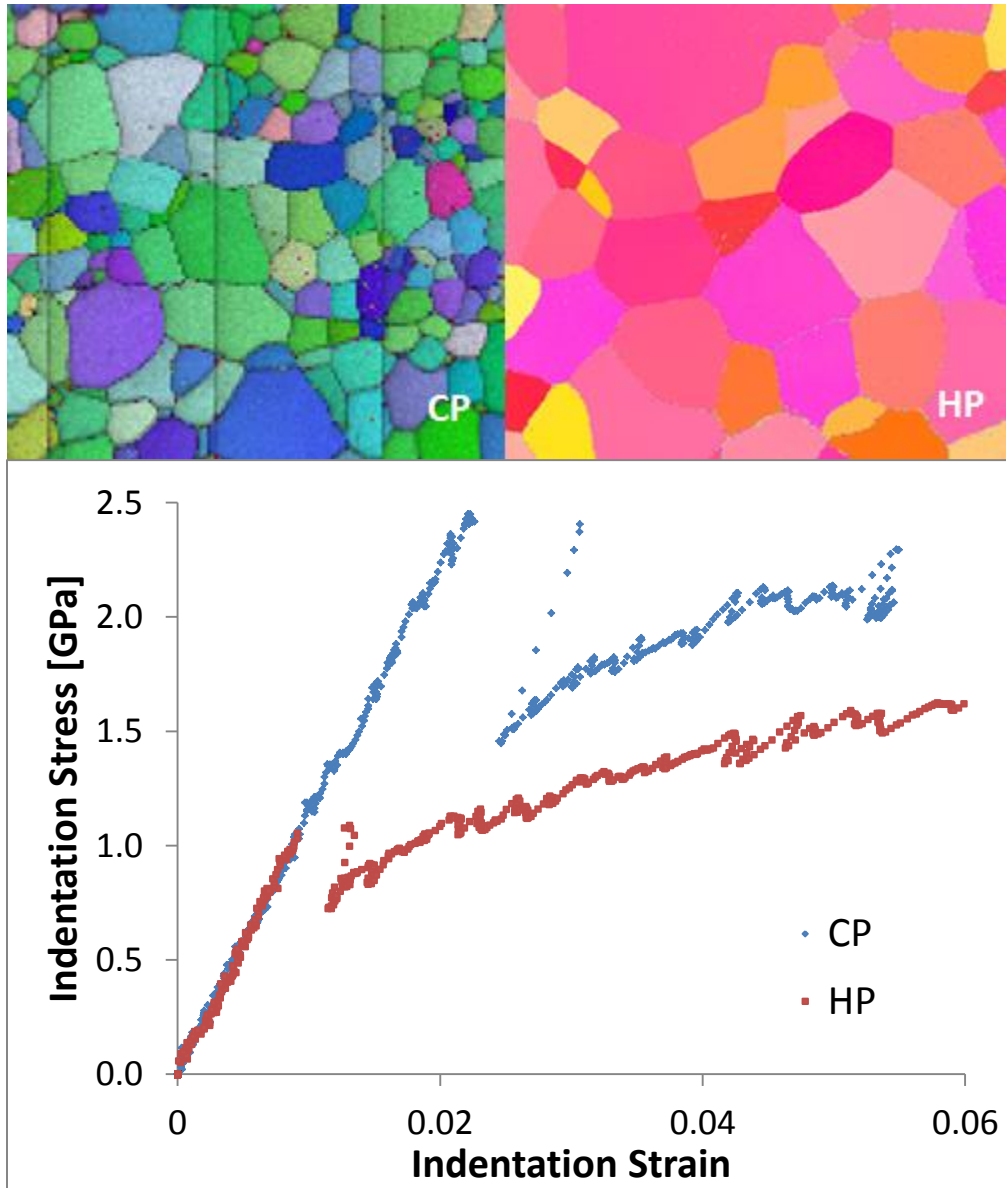


Figure 1: Representative electron backscatter diffraction maps and indentation stress-strain curves of commercial (CP) and high purity (HP) titanium.

Appendix E: Structure-Processing Correlations and Mechanical Properties in Freeze-Cast Ti-6Al-4V with Highly Aligned Porosity

*By Jordan S. Weaver, Surya R. Kalidindi and Ulrike G.K. Wegst**

[*] Prof. Ulrike G.K. Wegst. Corresponding Author.

Thayer School of Engineering, Dartmouth College,

14 Engineering Drive, Hanover, NH 03755 (USA)

E-mail: ulrike.wegst@dartmouth.edu

Jordan S. Weaver, Prof. Surya R. Kalidindi

George W. Woodruff School of Mechanical Engineering, Georgia Institute of Technology,

801 Ferst Drive, Atlanta, GA 30344 (USA)

Keywords: Directional Solidification, Honeycombs, Porous metals, Sintering, Toughness

In contrast to freeze-cast ceramics and polymers, which have been studied in considerable detail, few freeze-cast metal scaffolds have been described, to date. Our systematic study on structure-processing correlations in freeze-cast Ti-6Al-4V scaffolds reports, how processing parameters determine the scaffold architecture formed during the directional solidification of water-based metal slurries and the final architecture after sintering. In addition to the carefully controlled freeze-casting conditions, sedimentation in the slurry during freezing and volume shrinkage during burnout and sintering were found to significantly affect both structure and properties of the Ti-6Al-4V scaffolds. Using two freezing rates, $1^{\circ}\text{C min}^{-1}$ and $10^{\circ}\text{C min}^{-1}$, two water-based polymer solutions as binders (chitosan and carboxymethyl cellulose) and two different metal volume fractions in the metal slurry, 20 and 30 vol.%, Ti-6Al-4V scaffolds could be prepared with pore length, width, and porosity ranging from 41 μm to 523 μm , 14.5 μm to 76.5 μm , and 65% to 34%, respectively. Their compressive strength, stiffness, and toughness (work to 20% strain) fall in the range of 83-412 MPa, 7-29 GPa, and 14-122 MJ m^{-3} , respectively.

1. Introduction

Titanium is greatly valued for its excellent mechanical properties, low density, and both high temperature and chemical resistance ^[1]. These traits make titanium and its alloys highly desirable, particularly in the form of foams, which offer high mechanical efficiency at high porosity for applications that are structural, such as in tissue scaffolds for bone substitution, chemical, in the case of substrates for catalysis, and thermal, as in heat exchangers ^[2, 3]. Methods for the manufacture of titanium foams and scaffolds primarily rely on powder metallurgy. Porosity can be introduced before, during, or after sintering of the titanium particles. Various methods to fabricate porous titanium and to tailor the pore structure for a specific application exist; they include powder sintering with and without placeholders, pressured pore expansion, freeze casting, gel-casting, electron beam melting, and electrochemical dissolution, to list but a few ^[2, 4, 5-10].

One particularly promising method for the production of directionally porous metals, which has to date primarily been studied for the manufacture of highly porous, ceramic-based bone substitute materials and lightweight composites with high toughness is freeze casting ^[11, 12, 13]. This method produces directional porosity through the directional solidification of slurries. Challenging in the case of metals is the fact that slurries have to be made from particles, which, with a diameter of 3-9 μm , are an order of magnitude larger than those of the ceramic powders typically used in freeze casting. This means that key slurry and processing parameters have to be adapted for the freeze casting of larger metal particles. Additionally, structure-processing correlations need to be established, so that the mechanical properties of the metal scaffolds can be carefully controlled and tailored for a given application.

While a handful of groups have used ice-templating methods to produce porous metals, thus far, only three studies have successfully produced titanium scaffolds with highly aligned,

unidirectional porosity using freeze casting; [5-10, 14, 15]. In these three studies, the titanium powders used were composed of relatively small (10-45 μm) atomized and hydride-dehydride (HDH) particles; both water and camphene-based slurries were used [5, 6, 10]. Camphene was chosen as an alternative liquid carrier because the morphology of the dendrites that form during solidification and phase separation in camphene-based systems greatly differs from those in water-based slurries. An advantage of camphene-based slurries is that their freezing temperatures are close to room temperature (33-45°C) and that larger pore sizes (>100 μm) can be produced due to fast diffusion; a disadvantage is an inherent difficulty to grow highly-aligned camphene dendrites of greater length [7, 10]. Finally, also the literature on directional, freeze-cast titanium scaffolds is limited, to date: effects of compositional and processing variables such as particle loading, the viscosity of the liquid carrier, and freezing rates on the material properties have yet to be studied [5, 6, 10].

In this study, we explore, how changes in particle loading from 20-30 volume percent (vol.%), freezing rates of 1°C min⁻¹ and 10°C min⁻¹, and binder viscosity affect the structure and mechanical performance of freeze-cast Ti-6Al-4V (Ti64) scaffolds.

2. Structure of freeze-cast Ti-6Al-4V scaffolds

Structure and properties are highly correlated in porous or cellular materials [16]. In fact, two of the three most important factors that influence their properties are the overall porosity of the material and the pore morphology; the third is the material, from which the cellular materials are made. Both overall porosity and pore morphology of the freeze-cast Ti-6Al-4V scaffolds of this study were, before and after sintering, carefully analyzed using density measurements, microscopy, and X-ray tomography.

The optical and SEM micrographs of **Figure 1** illustrate the structure and architecture of the freeze-cast Ti-6Al-4V. An entire wine-cork sized scaffold before sintering is shown in **Figure 1a**. The SEM micrograph of **Figure 1b** reveals how, in the green body, the metal particles are bound by the chitosan binder, and **Figure 1c**, an optical micrograph of a cross-section transverse to the freezing direction, shows the lamellar structure of Ti-6Al-4V scaffolds. Cross sections parallel and perpendicular to the freezing direction obtained by wire electrical discharge machining (EDM) after sintering are shown in **Figure 2** and reveal the final pore structure after the cell walls have densified.

3. Structure-processing correlations

The slurry properties, which include the particle loading, the metal particle size, the viscosity of the liquid carrier, and the use of additives, as well as the processing conditions, such as the applied cooling rate, determine the structure of the final freeze-cast scaffolds. For freeze-cast ceramic scaffolds, the effect of slurry composition and freezing parameters on the scaffold architecture has been documented for a number of systems ^[12, 13, 17-19, 20]. The solvent fraction in the slurry roughly equals the green body porosity after sublimation. Thus, scaffolds with a range of porosities can be produced by varying the particle loading. The size of the pores and the lamellar spacing, which is the sum of the pore size and the wall thickness and often referred to as “structural wavelength”, is inversely proportional to the freezing front velocity, which is largely controlled by the applied freezing rate. This relationship is given by **Equation 1** where w is the structural wavelength and v is the freezing-front velocity with typical values of n ranging from 0.5 to 2 ^[20]. **Equation 2** gives an expression for estimating the critical freezing-front velocity at which the titanium particles will be entrapped by the growing ice based on a balance of repulsive

and attractive forces where $\Delta\sigma_0$ is the thermodynamic free energy of the system, a_0 is the mean distance between the molecules in the liquid layer, η is the viscosity of the liquid, μ is the ratio of the thermal conductivity of the particle over that of the liquid, r is the particle radius^[20, 21]. The structural wavelength is also limited by the fact that achieving wavelengths smaller than the average particle size is not possible. Lastly, additives have been shown to change the freezing behavior of slurries and result in changes in pore morphology^[17, 22, 23]. The change in morphology can be correlated to changes in the slurry properties, changes in the ice crystal growth, and changes in particle solvent interactions; however, the effect of new additives on ice crystal growth and morphology is not yet very predictable^[18].

3.1 The effect of binder viscosity and freezing rate on sedimentation and critical freezing front velocity

Sedimentation during the freezing process leads to a density gradient in the structure along the height of the scaffold. Particle aggregation, the clustering of particles, causes undesired heterogeneity in the structure. Powder depleted regions towards the top of the samples were observed in aqueous agar solutions with freezing front velocities of 2-12 $\mu\text{m/s}$ ^[5, 6]. Advantage was taken of sedimentation in a method called reverse freeze casting, in which an initial camphene structure was partially solidified followed by the addition of a camphene-particle mixture^[10]. In one case, a small amount of surfactant was added to the slurry to improve dispersion^[5]. No systematic study exists in the literature, to date, on sedimentation during the freeze casting of metals. In the research presented here, the viscosity of the binder and the freezing rate were adjusted to the particle properties to reduce sedimentation. **Equation 3** describes the relationship between particle size, solution viscosity, and particle velocity derived

from Stokes' Law and a balance of forces for the simple case of spherical particles, assuming laminar flow and the absence of particle-particle interactions ^[20] where ρ_p and ρ_L are the densities of the particle and liquid, respectively, g is the gravitational acceleration constant, η is the dynamic viscosity of the liquid carrier, and r is the particle radius.

Because the sedimentation speed varies quadratically with the particle radius, selecting the smallest particle size available for a desired material has the greatest effect. Increasing the liquid carrier's density and viscosity can further reduce sedimentation. There are two time dependencies: one, the distance travelled by a particle will increase with time; two, the system will eventually solidify. Therefore, increasing the freezing rate (reducing the time to solidification) and/or using a solvent, which is sensitive to temperature change (increasing viscosity with decreasing temperature), will again reduce sedimentation. Such changes will conversely produce changes in the freeze-cast structure, of course. Most desirable is a liquid carrier, which already has a high viscosity at room temperature to reduce sedimentation at the most critical time of the freeze-casting process, when most of the sample is still liquid.

To quantify sedimentation effects in the freeze-cast scaffolds, the local scaffold density was measured on 5 mm cubes cut at decreasing heights of the same sample. **Figure 3** shows how the local density changes with along the height, measured from the bottom to the top, of the scaffold at cube center positions. Freezing rates of 1, 6, and 10°C min⁻¹ were explored for different particle loadings using two different binders, aqueous solutions of chitosan and CMC. The first observation is that of increasing sedimentation with decreasing freezing rate measured via a linear best fit slope. The second is a decrease in sedimentation with an increase in liquid carrier viscosity at 10°C min⁻¹; the use of CMC reduces sedimentation in comparison to chitosan.

Particle entrapment was observed by Chino and Dunand, when the freezing front velocity of their system was near and above a critical freezing-front velocity^[5]. The equation that Chino and Dunand used was derived from similar principles as **Equation 2**, but accounts for the buoyancy force and neglects thermal gradients^[5]. Because the buoyancy and drag forces approach the same order of magnitude only when the particle size approaches millimeter size^[24], the buoyancy force can be ignored for the particle sizes used in this study.

The critical freezing front velocities for the systems in this paper were calculated using both **Equation 2** and **Equation 4** which relates the Hamaker constant, A , to the free energy of the system and the smallest distance between the ice front and particle, d ^[25]. The physical constants used in the calculations are listed in **Table 2**. The freezing front velocity for a particle loading of 5 vol.% of Ti-6Al-4V, the chitosan binder, and an applied freezing rate of 10 °C min⁻¹ was measured to be constant at 25.5 µm s⁻¹ up to 27 mm height. The freezing front velocity for an applied freezing rate of 1 °C min⁻¹ was estimated to be constant at 5 µm s⁻¹ based on trends observed by Hunger et al. using the same freeze-casting system and a comparable material system^[12]; their ceramic and our metal systems are, because of the low particle volume fraction, dominated by the liquid carrier in their freezing behavior.

If the room temperature viscosities of the chitosan (84.0 ± 2.18 cP) and CMC (604 ± 22.8 cP) polymer solutions, which are 1-2 orders of magnitude greater than that of water, are inserted into **Equation 2**, particle entrapment is predicted for both freezing velocities 1 and 10 °C min⁻¹. However, entrapment was not observed in our experiments. This illustrates that the particle-freezing front interaction is much more complex, and that higher viscosity solutions and liquid carriers can successfully be used at typical freezing-front velocities.

3.2 The effect of ethanol on the green body pore aspect ratio

Two studies have reported the addition of ethanol to aqueous freeze-cast solutions ^[17, 23]. In this study, we observe a similar trend for freeze-cast titanium. The change in cross-sectional pore shape is shown in **Figure 4**. The pore cross-section transverse to the ice-crystal growth direction can be described as an elongated oval with a long and a short axis. A summary of pore dimensions for a particle loading of 10 vol.% with varying amounts of ethanol is given in **Table 1**. It should also be noted that at higher volume percentages of ethanol (15 vol.%), large singular pores appeared in addition to the smaller regular pore structure, as reported in the literature ^[17, 23]. The decrease in aspect ratio of the pores and the introduction of large singular pores is not fully understood, at this time, and a proper explanation is beyond the scope of this paper. However, the addition of 5 vol.% ethanol to the metal slurry produced a desirable and uniform change, decreasing the in-plane aspect ratio by more than 50% from 5.4 to 2.2. We will see later that the addition of ethanol also resulted in changes in the sintering behavior, final overall porosities, and resulting mechanical properties.

3.3 Effect of slurry composition and freezing rates on shrinkage and scaffold densification

In most powder metallurgy processes, green body porosity is low and final porosities near zero are desired. However in freeze-cast green bodies, porosities are typically very high (70-95%) and a final porosity close to the green body porosity is desired, the goal being to preserve the templated structure, while creating structural integrity through fully dense cell walls. The shrinkage, typically defined as the change in length between the green and sintered body divided by the green body length, can be rather significant ^[26]. In this paper, we calculate the shrinkage by the change in volume between the green body and sintered scaffold. The scale of volume

change for two compositions is illustrated by before and after photos shown in **Figure 6**. The shrinkage of 10 vol.% Ti-6Al-4V loading, approximately 80%, is so significant that the green-body structure is scarcely preserved. A trend of decreasing shrinkage with increasing particle loading is observed for both binders and freezing rates. This can be explained by closer particle packing in the walls as seen in **Figure 7**. Increasing the particle loading also reduces the dry polymer to metal ratio thus reducing the volume lost by regions of polymer burned out in the sintering process; however, the volume the polymer occupies in the scaffold is not significant. Scaffolds with CMC overall shrank less than scaffolds with chitosan. It is believed that this is because of both reduced sedimentation and a reduced dry polymer to metal volume ratio. The difference of dry polymer to metal ratio between chitosan and CMC scaffolds for the same metal content is significant (CMC scaffolds have a ratio 99% less than chitosan scaffolds). This difference arose because CMC has lower solubility in water than chitosan has in 1% acetic acid. Comparing CMC to chitosan at $10^{\circ}\text{C min}^{-1}$, the reduced sedimentation can be expected to allow for a wider particle size distribution in the cell walls. Packing density increases with multi-modal particle distributions, particularly, when there is greater than a sevenfold difference between modes ^[26-28]. A higher packing density will lead to less shrinkage ^[26]. Scaffolds with CMC freeze-cast at $1^{\circ}\text{C min}^{-1}$ had the least amount of shrinkage. In this case, the effect of wall thickness must be considered to explain the further reduction in shrinkage. McGeary has shown for the case of a monodisperse spherical particles in different sizes cylinders that the packing density decreases when the container to particle diameter ratio drops below ten ^[27]. This was also studied as a wall effect, where the porosity near the container wall increases in comparison to the rest of the container within a distance of five particle diameters from the wall ^[29]. In our system, the ice lamellae represent the container walls, thus for small interlamellar gaps of less than 10

times the average particle size, which in the case of the titanium particles corresponds to 100 microns, this effect becomes significant, the packing density is reduced and increased shrinkage during sintering is observed. The difference in the titanium cell wall thickness between freezing rates of $10^{\circ}\text{C min}^{-1}$ and $1^{\circ}\text{C min}^{-1}$ is shown in **Figure 8**.

Scaffolds manufacture with a particle loading of 40 vol. % in CMC freeze cast at a rate of $1^{\circ}\text{C min}^{-1}$ were unsuccessful, because the green body lacked the necessary strength for further processing. However, 20 vol. % and 30 vol. % particle loadings in CMC and chitosan freeze cast at $1^{\circ}\text{C min}^{-1}$ could successfully be prepared with. In these cases the scaffold porosities (measured on whole scaffolds which includes depleted and dense regions at the top and bottom respectively) ranged from 57% (20 vol.% Ti-6Al-4V, CMC, $1^{\circ}\text{C min}^{-1}$) to 30% (30 vol.% Ti-6Al-4V, chitosan, $10^{\circ}\text{C min}^{-1}$). Local porosity measurements are detailed in Section 4.

4. Sintered porosity and pore size

Scaffolds of select compositions and processing parameters were identified for sectioning and property analysis for different well-defined heights within each sample. An average increase in porosity of 0.4% per millimeter increase in height measured from the sample bottom is primarily caused by sedimentation that occurs during the freezing process (**Figure 9**). X-ray tomography and compression tests were completed on specimens of 4mm cubes whose centers were positioned at heights between 8 and 24 mm from the bottom. **Figure 10** shows the final cross-sectional pore structure obtained by X-ray tomography; **Table 3** lists their positions and respective average pore sizes. For chitosan scaffolds at a loading of 20vol.% Ti-6Al-4V frozen at $10^{\circ}\text{C min}^{-1}$, the addition of 5vol.% ethanol increased the final porosity by 10%. Changes in particle packing in the walls could not be observed. Rather, it is reasoned that the result can be

attributed to the structural change that occurs in the green body scaffolds frozen with ethanol, where the decrease in pore aspect ratio produced a more stable homogenous structure, thus preserving the templated porosity better. This can be seen in X-ray tomography scans in **Figure 10a** and **Figure 10b**. The porosity is further increased for the composition of 20vol% Ti-6Al-4V, CMC, frozen at $1^{\circ}\text{C min}^{-1}$ due to the thicker walls which reduced the overall shrinkage of the templated structure. This shows that the final porosity for the same particle loading, particle size distribution, and sintering can significantly be altered and custom-designed by binder selection, additives, and freezing rates.

4. Mechanical Performance

Figure 11 shows the typical compression stress-strain behavior of the selected freeze-cast Ti-6Al-4V scaffolds. Beyond the sample's yield point, all scaffolds show a plateau region followed by typical crushing behavior of porous materials. The large drops in stress in the plateau region are most likely micro-failure events for which further investigations would be required to determine the type of failure events. The properties span a range of 7 to 29 GPa in modulus, 83 to 412 MPa in compressive strength, and 14 to 122 MJ/m³ of work to 0.2 strain, the latter a measure chosen to be able to compare our values with those reported in the freeze-cast titanium literature.

The effective Ti-6Al-4V scaffold properties fall well below the model for an axial dominated out-of-plane honeycomb and lie much closer to those of a bending dominated equiaxed foam as shown in **Figure 12** ^[16]. To estimate scaffold properties from the solid from which it is made using **Equation 5** and **6**, an empirical correlation constant of $C=0.3$ determined for equiaxed aluminum foams was used for the bending dominated equation ^[16]. A cell wall solid

modulus and strength of 114 GPa and 970 MPa was assumed based on reported values of Ti-6Al-4V ^[30]. Reasons for the mechanical properties of our scaffolds falling below these values for a perfectly aligned strut network with cell walls of constant cross-sections are that our scaffolds have a somewhat imperfect honeycomb-like structure. Because of the cell-wall misalignment with the loading direction and small variations in thickness, they will never be loaded perfectly along their length, but instantly be loaded in bending and buckle.

Table 4 and **Figure 12** show literature values for freeze-cast titanium scaffolds. When specific values were not listed in text or tables, image analysis software was used to extract values and perform area under the curve measurements from graphs. A plot of strength versus modulus reveals that the camphene and water based scaffolds separate into two groups. This is believed to be caused by the difference in solidification and dendritic growth which results in different structures, also in comparison to materials freeze-cast from water-based solutions. Despite the better yield strength of Ti-6Al-4V over pure titanium, the Ti-6Al-4V freeze-cast scaffolds do not perform better than to those made with pure titanium. Explanations for this observation could be that on the one hand, when the higher oxygen content in the unalloyed titanium scaffolds is taken into account, the strength difference of the two solid materials is not that significant and, on the other hand, the strength of the porous material is more sensitive to the pore morphology than small changes in solid material properties. However, we would still expect to see a benefit in toughness since the high oxygen content in the unalloyed titanium strengthens but reduces ductility ^[31]. In fact, a plot for water based freeze-cast scaffolds of specific energy measured to 50% strain versus the stress level at 25% strain reveals that the Ti-6Al-4V scaffolds have a higher work to 50% strain (Figure 14). Additionally, one would expect improved fatigue and fracture toughness over the unalloyed titanium scaffolds for the same scaffold structure.

5. Conclusions

Ti-6Al-4V with a honeycomb-like aligned pore structure and porosities in the range of 34-65% were freeze cast using chitosan and carboxymethylcellulose as binders. This systematic study of effects of composition and processing parameters on scaffold structure and properties revealed that both the solution viscosity and additives which increase the template scaffold pore size are of critical importance. Viscosities of 84 and 604 cP, which are higher than those predicted to cause particle entrapment during freezing, could successfully be used and were found to be highly advantageous for the freeze casting of slurries composed of larger metal particles (10 micron diameter) for which sedimentation is otherwise significant. Small amounts of the additive ethanol (5-10 vol.%) were found to result in larger pore sizes, which lead to significantly reduced scaffold shrinkage during binder burnout and sintering, and thus significantly increasing overall porosities.

The structural analysis by optical and scanning electron microscopy and X-ray microtomography, and the mechanical characterization of the sintered scaffolds in compression revealed the imperfections of the freeze-cast scaffolds such as cell wall misalignment and their non-uniform cross-sections, which reduce particularly the scaffolds' modulus but also their yield strength well below the assumed stretch dominated Gibson-Ashby model for materials with a honeycomb-like structure. Comparing our results with those reported in the literature, we discovered that scaffolds made from camphene and water-based suspensions fall into two separate areas of the property space. This is due to the inherently different nature of camphene and ice-crystal growth and the scaffold architecture, which the two substances template. The property differences are attractive, because each scaffold type is likely both in structure and

mechanical performance better suited for a particular final application. A comparison of freeze-cast scaffolds made from the alloy Ti-6Al-4V with unalloyed titanium revealed that the latter has a higher specific toughness, which means that it absorbs more energy per unit weight, when loaded to 50% strain.

The conclusion we can draw from these collated results is that, because of the excellent control over material structure and properties and the high overall porosities, which can be achieved, freeze-cast titanium scaffolds are attractive candidates for applications as diverse as tissue scaffolds for bone substitution and lightweight armor for energy absorption. They also offer additional potential in the form of composite materials, which are formed, when the pore space is infiltrated by a second material phase. These composite material systems will be discussed in a companion paper.

6. Experimental Section

6.1 Choice of scaffold materials and solution preparation

The titanium alloy Ti-6Al-4V was chosen for this study. Thanks to its high modulus and strength, and outstanding corrosion resistance, as well as good machinability, it is favored in aerospace and automotive applications; because of its excellent biocompatibility it is the material of choice for many biomedical applications. There are competing requirements when choosing a particle size. Small particles are desired to minimize sedimentation during freezing and allow for fast freezing rates which provide small lamellae spacing; however, because titanium is highly reactive in particle form and embrittled by high oxygen contents, larger particle sizes are more practical. The Ti-6Al-4V powder used in this study was manufactured by TLS Technik (Bitterfeld, Germany) using an Electrode Induction-melting Gas Atomization (EIGA) process.

The particles are spherical with an average diameter of 10 μ m; the size distribution is shown in **Figure 15**; the oxygen content no higher than 0.13 wt.% as specified by the manufacturer.

Low molecular weight chitosan (75-85% deacetylated) from Sigma-Aldrich (St. Louis Missouri) and AQUALON 7HF PH Sodium Carboxymethyl cellulose (CMC) were chosen as binders because water-based solutions of high viscosity can be prepared with these and because both are readily available at low cost. The stock chitosan solution was prepared by mixing chitosan (2.4 g) in de-ionized water (99ml) and glacial acetic acid (1ml) on a Wheaton benchtop roller for a minimum of 24 hours. The stock CMC solution was prepared by mixing CMC (1ml) in de-ionized water (50 ml) on a stir plate for 24 hours. The viscosity of the binders, which determines the speed of particle sedimentation, was measured three times at room temperature using a Brookfield rheometer (Middleboro, MA); their respective values are listed in **Table 2**.

6.2 Freeze casting of Ti-6Al-4V scaffolds

Suspensions of varying volume percentages of Ti-6Al-4V (5-40 vol.%) in either a chitosan or a CMC solution, to which varying amounts of ethanol (0, 5, 10, and 15 vol.%) had been added were shear mixed on a DAC 150 FVZ-K SpeedMixer at 1800-2000 rpms in three 60 seconds steps. Approximately 12 ml of the metal slurry was pipetted into a cylindrical polytetrafluoroethylene (PTFE) mold, which was sealed with a copper bottom plate. The mold was placed on a copper coldfinger held at 5°C and immediately frozen at a cooling rate of 1, 6, or 10°C min⁻¹ to a final temperature of -150°C using liquid nitrogen as the cooling agent for the cold finger. Frozen samples were removed from the mold using an arbor press and lyophilized on a FreeZone 4.5Liter bench top freeze dry system (Labconco Kansas City, MO) under vacuum for 48-72 hours.

This process of directional solidification of water-based suspensions which contain dissolved and/or suspended particles is also known as freeze casting. In this process, the ice crystals grow pure and in a lamellar fashion aligned parallel to the thermal gradient and their [11-20] crystal direction. During solidification, the materials dissolved and suspended in the slurry are concentrated in the interlamellar spaces, the volumetric expansion of the ice phase causes a shear flow in the increasingly more viscous slurry and metal particles self-assemble into neatly packed cell walls ^[12]. Once the entire sample is frozen, the ice phase is removed by sublimation during lyophilisation. The resulting metal scaffold has a highly aligned porosity templated by the ice phase; the metal particles that form the cell walls are bound by either chitosan or CMC. The velocity with which the freezing front travels through the slurry during sample solidification was measured using a modified insulated mold, which is equipped with thermocouples that are located equidistant in 6.5 mm intervals along the height of the mold. The position of the freezing front was assumed to follow the 0°C isotherm and determined from three measurements.

Pure metal scaffolds were produced from the green bodies by sintering. First, the binders were burned out under vacuum (10^{-5} Torr) at 400°C for approximately 2 hours. A slow ramp rate of 2°C min⁻¹ was used to raise the scaffolds to 400°C. After burnout, a ramp rate of 10°C min⁻¹ was used to reach a soak temperature of 1300°C at which it was held for 1 hour. Finally, the samples were cooled to room temperature at 10°C min⁻¹. Four to eight scaffolds were sintered per run on either Ti-6Al-4V powder or wire in alumina crucibles. All sintering experiments were conducted at Lawrence Berkeley National Laboratory (LBNL) in a modified Abar 90 High Temperature Vacuum Furnace (Bensalem, PA).

6.3 Sectioning and microscopy of scaffolds

Un-sintered (green body) scaffolds were sectioned using a custom-built Well Diamond Wire Saw (Norcross, GA). Sintered samples were sectioned using an HS-3100 Wire EDM (Brother International Corporation, Bridgewater, NJ). Optical micrographs were taken using a Leica M205C microscope (Leica Microsystems Inc., Buffalo Grove, IL). Scanning Electron micrographs were taken on an XL30 Environmental Scanning Electron Microscope (FEI, Hillsboro, Oregon). Micro-computed tomography was conducted on samples using a Skyscan 1172 (Kontich, Belgium) with a 1 mm aluminum filter applied at a pixel resolution of 2.1 μm .

Pore sizes in green bodies were measured on one sample per composition (15 pores manually measured for each micrograph) using optical microscopy and ImageJ (v.1.46r) on micrographs with dimensions of 1260 x 940 μm . The sections were taken at a consistent height of 25mm from the bottom of the sample. Pore sizes on sintered samples were measured on single tomography slices at the heights listed in **Table 3** using ImageJ (v.1.46r) (12 pores manually measured for each slice) approximating the shape as an oval with long and short axes.

6.4 Mechanical testing of sintered scaffolds

All samples were tested on an MTS 793 (MTS Systems Corp., Eden Prairie, MN) single axis servo-hydraulic testing frame with a 100 kN load cell. Compression samples were 4 mm cubes cut using the wire EDM. Teflon tape was used to reduce friction during testing. One sample per composition, three cubes from the middle layer of each sample, was tested. See **Table 3** for layer positions. Strain was measured using the crosshead displacement and subtracting the measured compliance up to 0.25 mm at 12.5 kN. Tests were displacement controlled and run at a constant strain rate of 10^{-3} s^{-1} with full unloading segments at 0.1, 0.35, and 0.5 mm displacements. The modulus was calculated using a linear fit to the initial linear stress-strain curve. The yield point was calculated using the 0.2% strain offset method.

Acknowledgments

The authors would like to thank Dr. Antoni P. Tomsia and Mr. James K. Wu, Lawrence Berkeley National Laboratory, for their expert advice and sintering of our samples. The authors also wish to acknowledge the Central Research Facilities at Drexel University, where much of the microscopy and tomography work was completed. This research was supported by the following grants and fellowships: The Army Research Office under grant number W911NF-10-1-0409, NSF IGERT Program under grant DGE-0654313, and U.S Department of Education under grant P200A100145.

- [1] M. J. Donachie, *Titanium : a technical guide*, ASM International, Materials Park, OH 2000.
- [2] D. C. Dunand, *Advanced Engineering Materials* 2004, 6, 369.
- [3] M. F. Ashby, *Philosophical Transactions of the Royal Society a-Mathematical Physical and Engineering Sciences* 2006, 364, 15.
- [4] I. H. Oh, N. Nomura, N. Masahashi, S. Hanada, *Scripta Materialia* 2003, 49, 1197; D. C. Dunand, S. Oppenheimer, *Acta Materialia* 2010, 58, 4387; K. A. Erk, D. C. Dunand, K. R. Shull, *Acta Materialia* 2008, 56, 5147; L. E. Murr, S. M. Gaytan, F. Medina, E. Martinez, J. L. Martinez, D. H. Hernandez, B. I. Machado, D. A. Ramirez, R. B. Wicker, *Materials Science and Engineering a-Structural Materials Properties Microstructure and Processing* 2010, 527, 1861; J. Parthasarathy, B. Starly, S. Raman, A. Christensen, *Journal of the Mechanical Behavior of Biomedical Materials* 2010, 3, 249; D. J. Jorgensen, D. C. Dunand, *Materials Science and Engineering a-Structural Materials Properties Microstructure and Processing* 2010, 527, 849.
- [5] Y. Chino, D. C. Dunand, *Acta Materialia* 2008, 56, 105.
- [6] D. C. Dunand, J. C. Li, *Acta Materialia* 2011, 59, 146.
- [7] H. E. Kim, S. W. Yook, B. H. Yoon, Y. H. Koh, Y. S. Kim, *Materials Letters* 2008, 62, 4506.
- [8] Y. H. Koh, H. D. Jung, S. W. Yook, H. E. Kim, *Materials Letters* 2009, 63, 1545.
- [9] Y. H. Koh, S. W. Yook, H. E. Kim, *Materials Letters* 2009, 63, 1502.
- [10] S. W. Yook, H. D. Jung, C. H. Park, K. H. Shin, Y. H. Koh, Y. Estrin, H. E. Kim, *Acta Biomaterialia* 2012, 8, 2401.
- [11] S. Deville, E. Saiz, R. K. Nalla, A. P. Tomsia, *Science* 2006, 311, 515; M. E. Launey, Etienne Munch, Daan Hein Alsem, Eduardo Saiz, Antoni P. Tomsia, and Robert O. Ritchie, *Journal of the Royal Society Interface* 2009; E. Munch, M.E. Launey, D.H. Alsem, E. Saiz, A.P. Tomsia, and R.O. Ritchie, *Science* 2008, 322; M. E. Launey, E. Munch, D. H. Alsem, H. B. Barth, E. Saiz, A. P. Tomsia, R. O. Ritchie, *Acta Materialia* 2009, 57, 2919.
- [12] P. M. Hunger, A. E. Donius, U. G. K. Wegst, *Acta Biomaterialia* 2013, 9, 6338.
- [13] P. M. Hunger, A. E. Donius, U. G. K. Wegst, *Journal of the Mechanical Behavior of Biomedical Materials* 2013, 19, 87.
- [14] D. Driscoll, A. J. Weisenstein, S. W. Sofie, *Materials Letters* 2011, 65, 3433; T. V. Le, in *Materials Science and Engineering*, Vol. Master of Science, Drexel University, Philadelphia, PA. 2010.
- [15] H. D. Jung, S. W. Yook, T. S. Jang, Y. Li, H. E. Kim, Y. H. Koh, *Mat Sci Eng C-Mater* 2013, 33, 59.
- [16] L. J. Gibson, M. F. Ashby, *Cellular solids : structure and properties*, Cambridge University Press, Cambridge ; New York 1997.
- [17] S. Deville, E. Munch, E. Saiz, A. P. Tomsia, *Journal of the American Ceramic Society* 2009, 92, 1534.
- [18] S. Deville, *Advanced Engineering Materials* 2008, 10, 155.
- [19] T. Waschkes, R. Oberacker, M. J. Hoffmann, *Acta Materialia* 2011, 59, 5135; E. Saiz, S. Deville, A. P. Tomsia, *Acta Materialia* 2007, 55, 1965; S. Deville, *Materials* 2010, 3, 1913; B. W. Riblett, N. L. Francis, M. A. Wheatley, U. G. K. Wegst, *Advanced Functional Materials* 2012, 22, 4920.

- [20] U. G. K. Wegst, M. Schechter, A. E. Donius, P. M. Hunger, *Philosophical Transactions of the Royal Society a-Mathematical Physical and Engineering Sciences* 2010, 368, 2099.
- [21] G. Lipp, C. Körber, *J Cryst Growth* 1993, 130, 475.
- [22] S. W. Sofie, F. Dogan, *Journal of the American Ceramic Society* 2001, 84, 1459; Y. H. Koh, E. J. Lee, B. H. Yoon, J. H. Song, H. E. Kim, H. W. Kim, *Journal of the American Ceramic Society* 2006, 89, 3646; S. Deville, C. Viazzi, J. Leloup, A. Lasalle, C. Guizard, E. Maire, J. Adrien, L. Gremillard, *Plos One* 2011, 6, e26474.
- [23] P. M. Hunger, in *Materials Science and Engineering*, Vol. Doctor of Philosophy, Drexel University, Philadelphia, PA 2011.
- [24] P. Casses, M. A. Azouniaidi, *Advances in Colloid and Interface Science* 1994, 50, 103.
- [25] G. Lipp, C. Korber, *J Cryst Growth* 1993, 130, 475.
- [26] R. M. German, *Powder metallurgy science*, Metal Powder Industries Federation, Princeton, N.J. 1994.
- [27] R. K. McGeary, *Journal of the American Ceramic Society* 1961, 44, 513.
- [28] R. M. German, *Particle packing characteristics*, Metal Powder Industries Federation, Princeton, N.J. 1989.
- [29] W. van Antwerpen, C. G. du Toit, P. G. Rousseau, *Nuclear Engineering and Design* 2010, 240, 1803.
- [30] W. D. Callister, *Materials science and engineering : an introduction*, John Wiley & Sons, New York 1997.
- [31] J. M. Oh, B. G. Lee, S. W. Cho, S. W. Lee, G. S. Choi, J. W. Lim, *Metals and Materials International* 2011, 17, 733.

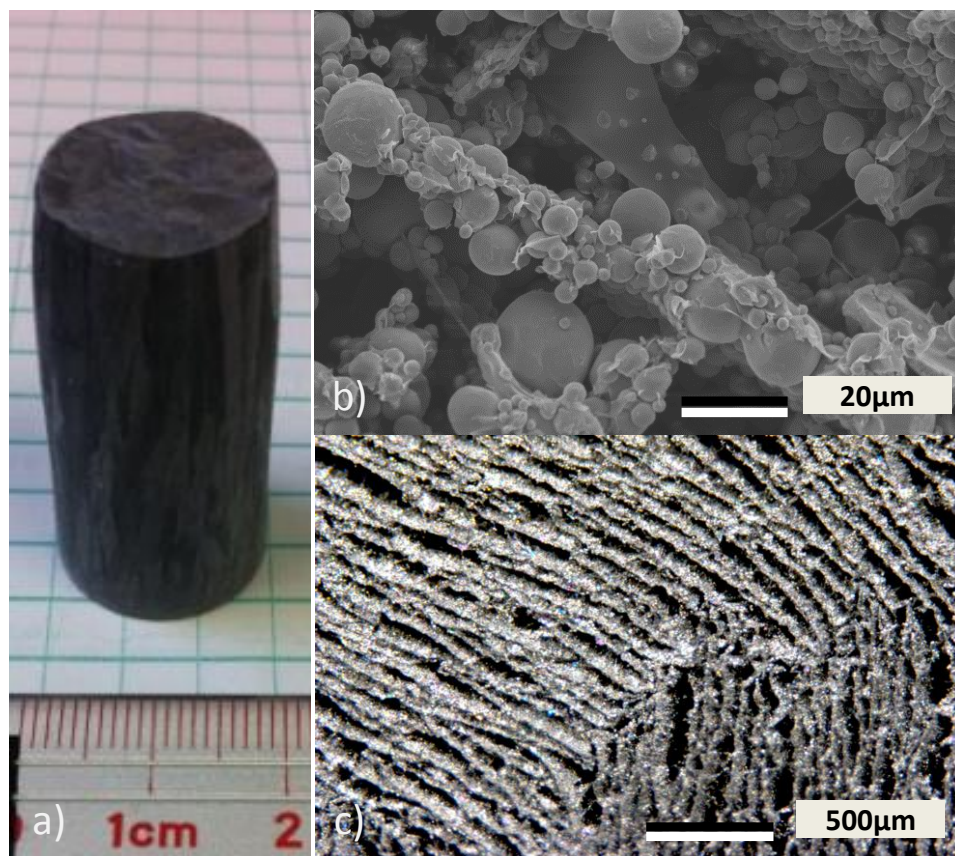


Figure 1. Optical and SEM micrographs of Ti-6Al-4V scaffolds: a) typical wine-cork sized freeze-cast scaffold before sintering; b) SEM micrograph of the scaffold wall before sintering; c) optical micrograph of a cross-section transverse to the freezing direction.

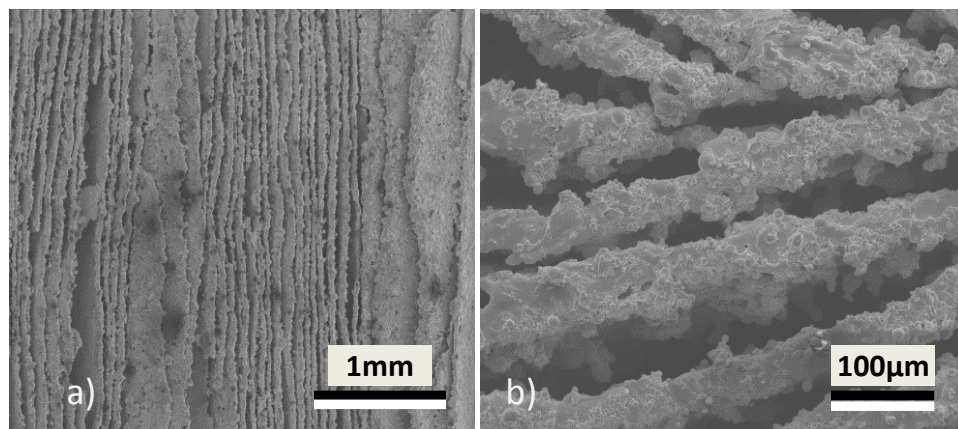


Figure 2. SEM images of sintered Ti-6Al-4V scaffold: a) SEM longitudinal wire-EDM section; b) SEM wire-EDM cross-section.

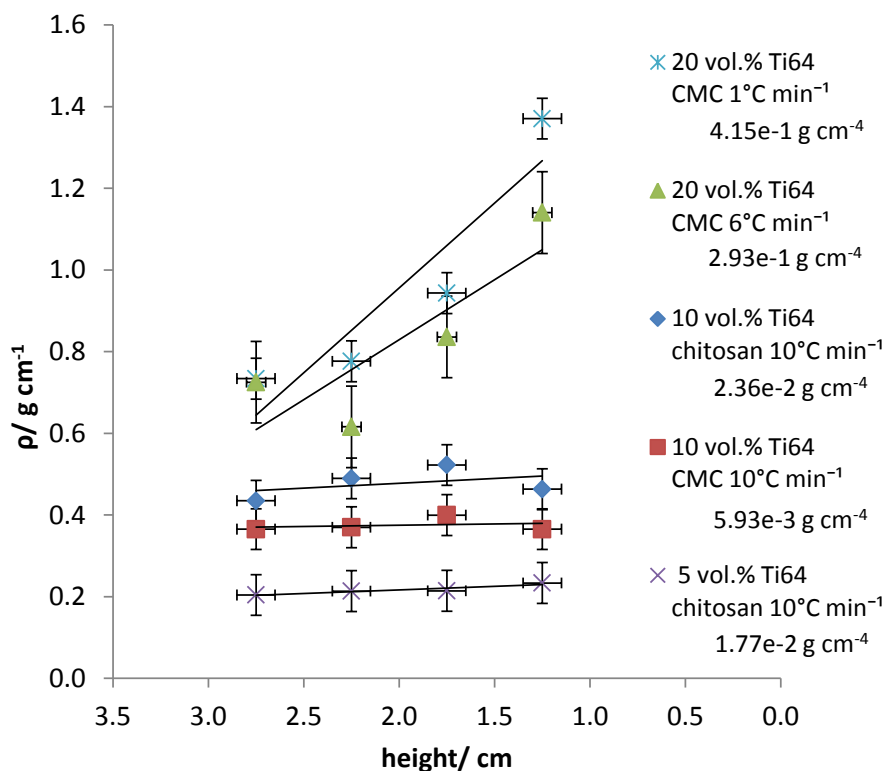


Figure 3. Density gradients in Ti-6Al-4V scaffolds with different particle loading, binders, and freezing rates. The linear approximation slopes are given in the legend. Each point is a single measurement. Density error bars are a fixed at 0.05 g cm^{-1} . Height error bars are fixed at 0.1 cm .

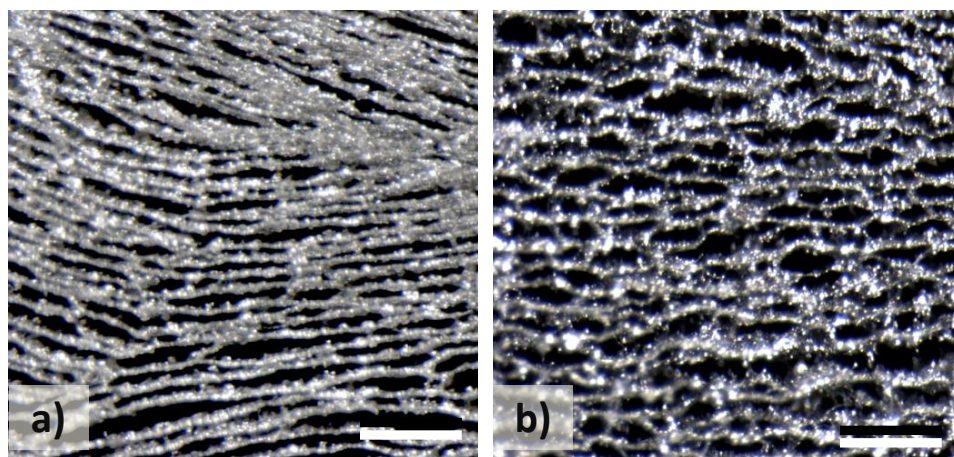


Figure 4. Optical micrographs showing the effect of ethanol on cross-section pore dimensions: a) 0 vol.%; b) 5 vol.%, scale bar $200 \mu\text{m}$

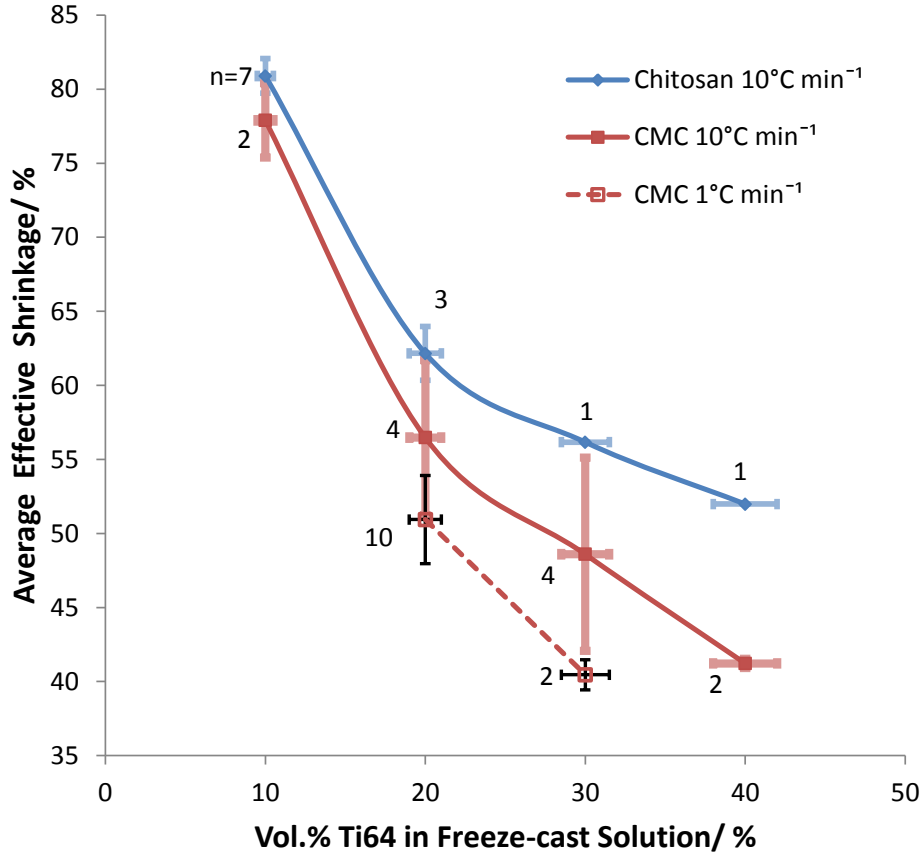


Figure 5. The volume shrinkage for different slurry compositions, all containing either 5 or 10 vol.% ethanol. Error bars in the y-axis are one standard deviation. Error bars in the x-axis are estimated as 5%. n is the number of samples.

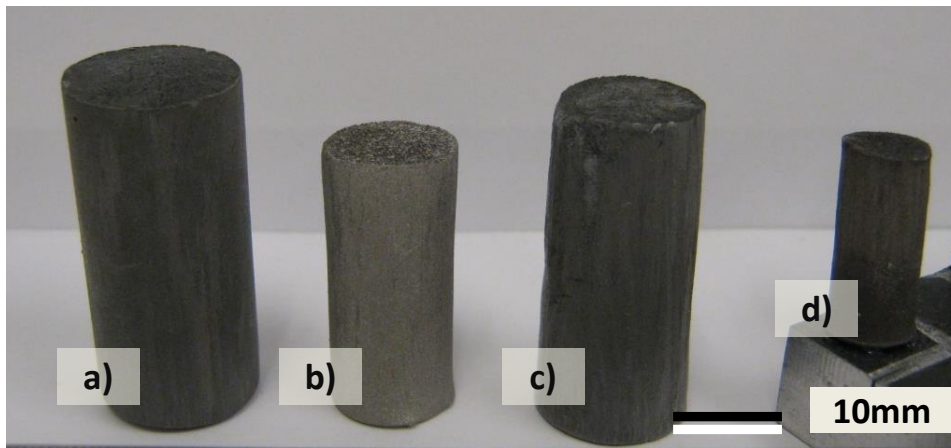


Figure 6. Green body and sintered scaffold comparison: a) 40 vol.% Ti-6Al-4V, CMC, 10°C min⁻¹ green body; b) sintered; c) 10 vol.% Ti-6Al-4V, chitosan, 10°C min⁻¹ green body; d) sintered.

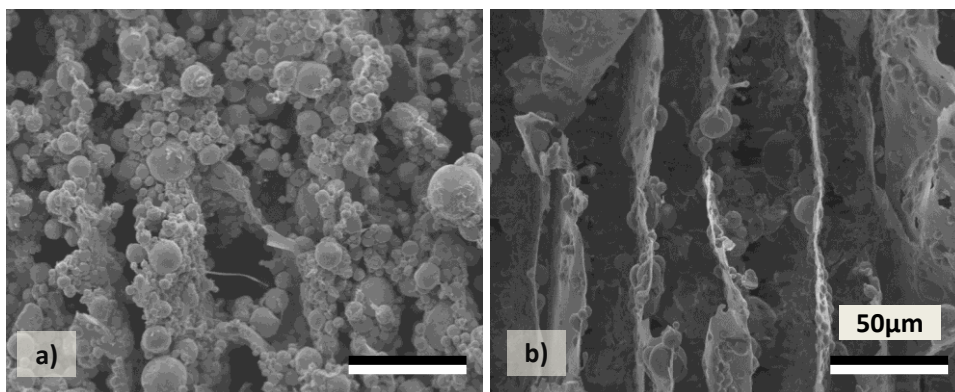


Figure 7. SEM images showing the packing of particles in the green body walls for two different particle loading: a) 20 vol.% Ti-6Al-4V, chitosan, $10^{\circ}\text{C min}^{-1}$; b) 5 vol.% Ti-6Al-4V, chitosan.

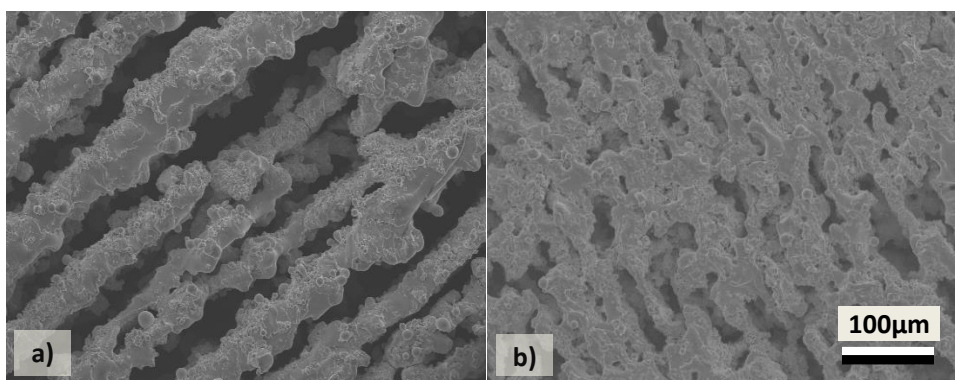


Figure 8. SEM images showing the difference in wall thickness between freezing rates: a) $1^{\circ}\text{C min}^{-1}$; b) $10^{\circ}\text{C min}^{-1}$ for particle loadings of 20 vol.%

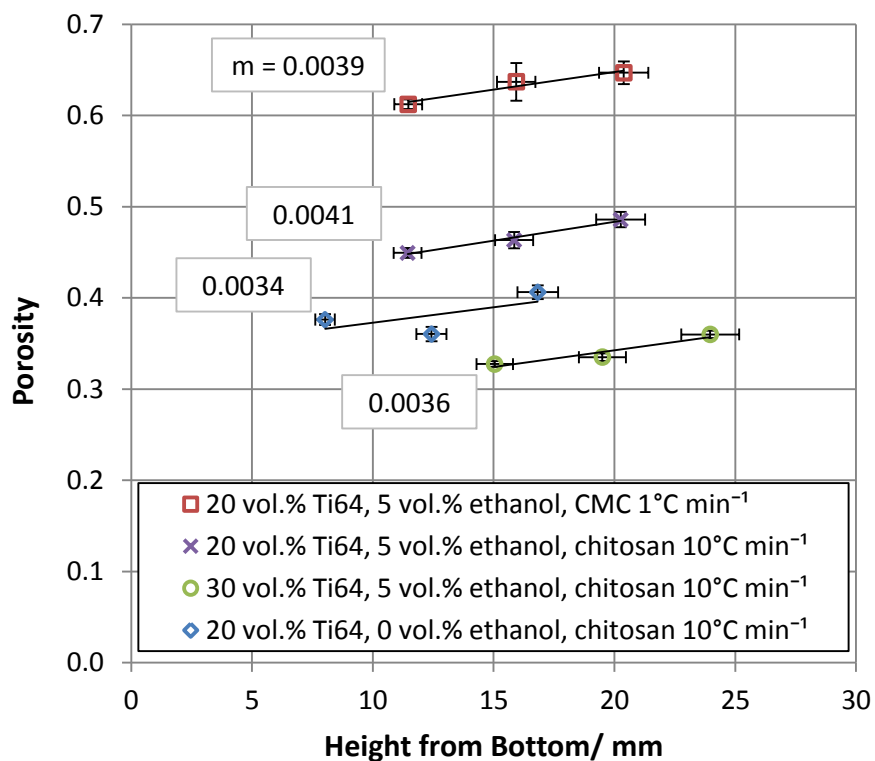


Figure 9. Local porosity measurements of sintered scaffolds. Specimens are 4mm cubes. Each point is four cubes. Porosity error bars are one standard deviation. Height errors bars are 5%. m is the slope of the linear trendline with units of porosity per millimeter.

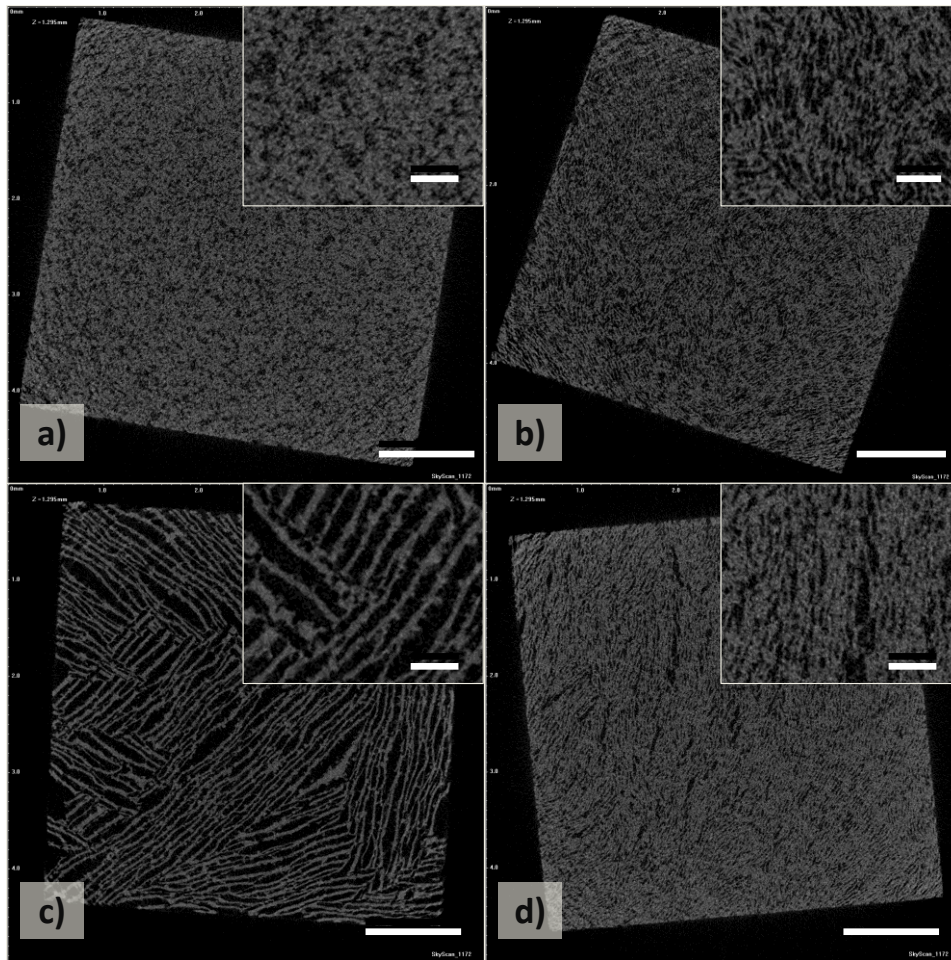


Figure 10. X-ray tomography of mechanical test specimens from which average pore size measurements were made. Scale bars on full cross-sections are 1mm. Scale bars on close ups are 200μm.

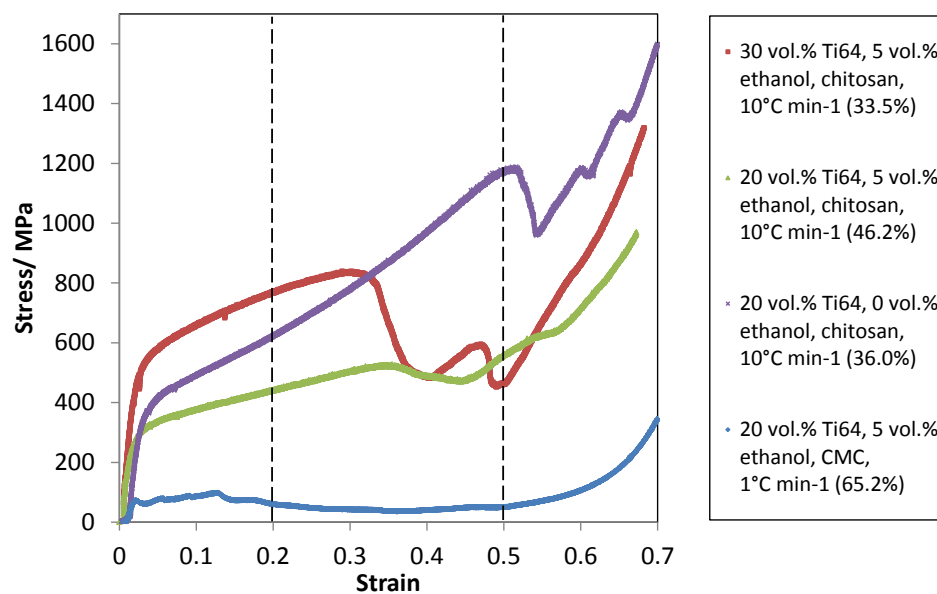


Figure 11. Typical compression stress-strain curves. Toughness or work was measured as the area under the stress-strain curve to 20 and 50% strain for comparing to literature values.

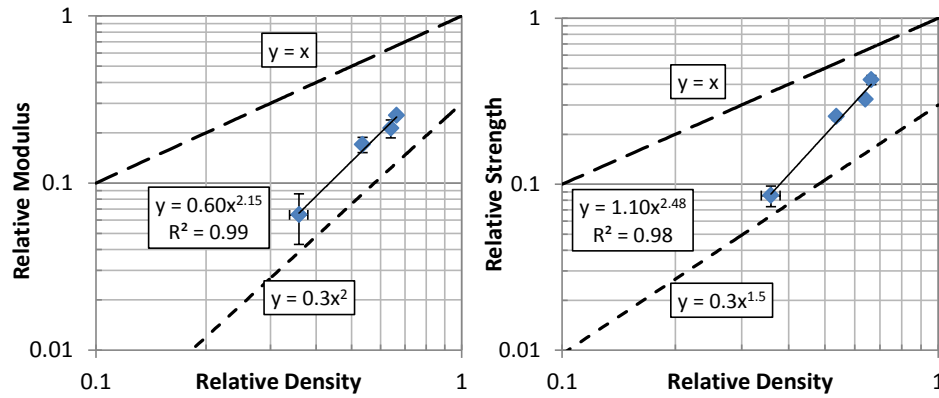
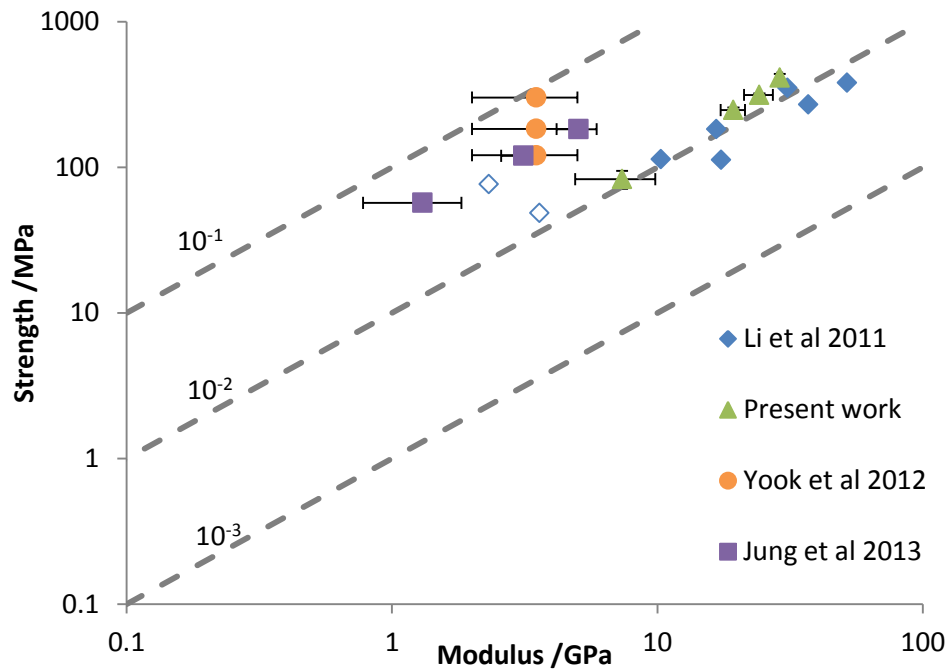


Figure 12. Relative modulus and strength versus relative density with stretch and bending dominated structure predictions. The upper line represents the expected stretch dominated honeycomb, and the bottom line represents the expected equiaxed foam bending dominated structure. Error bars are one standard deviation.



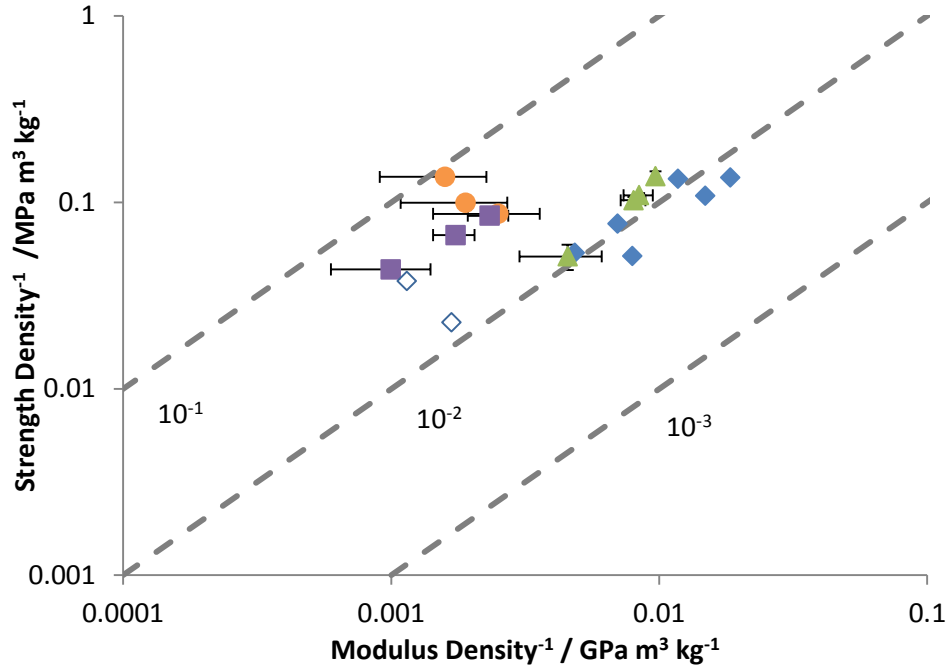


Figure 13. Strength versus Young's Modulus and specific strength versus Young's Modulus for all freeze-cast titanium and titanium alloys samples. Hollow shapes indicated orientations tested perpendicular to the freezing direction. Error bars represent one standard deviation of modulus, strength, and relative density.

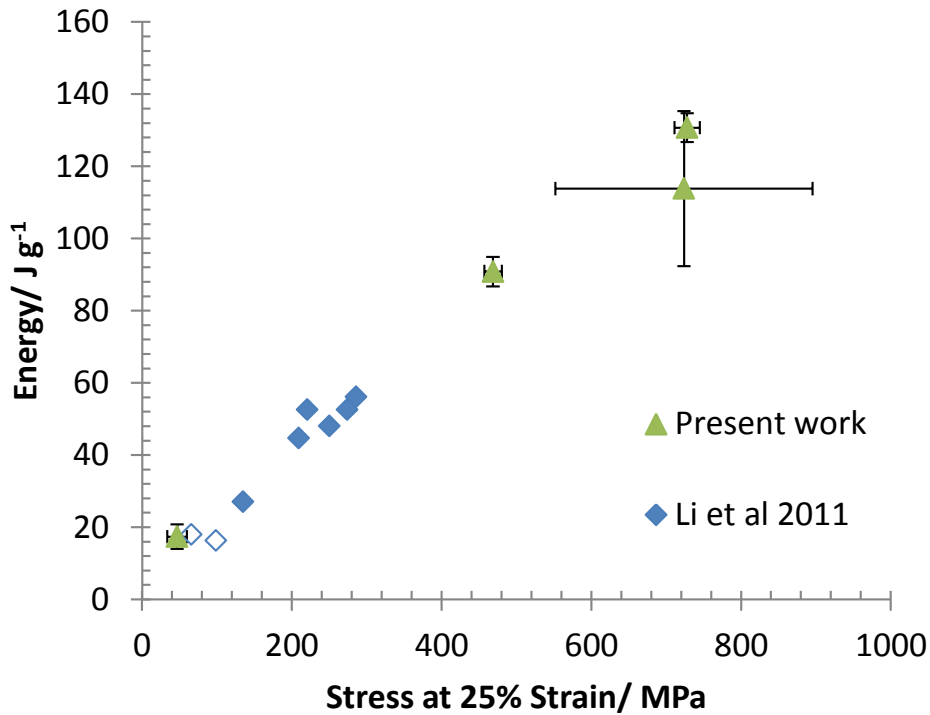


Figure 14: Toughness (area under the stress-strain curves up to 50% strain) versus the stress at 25% strain. Error bars pertain to one standard deviation for all variables.

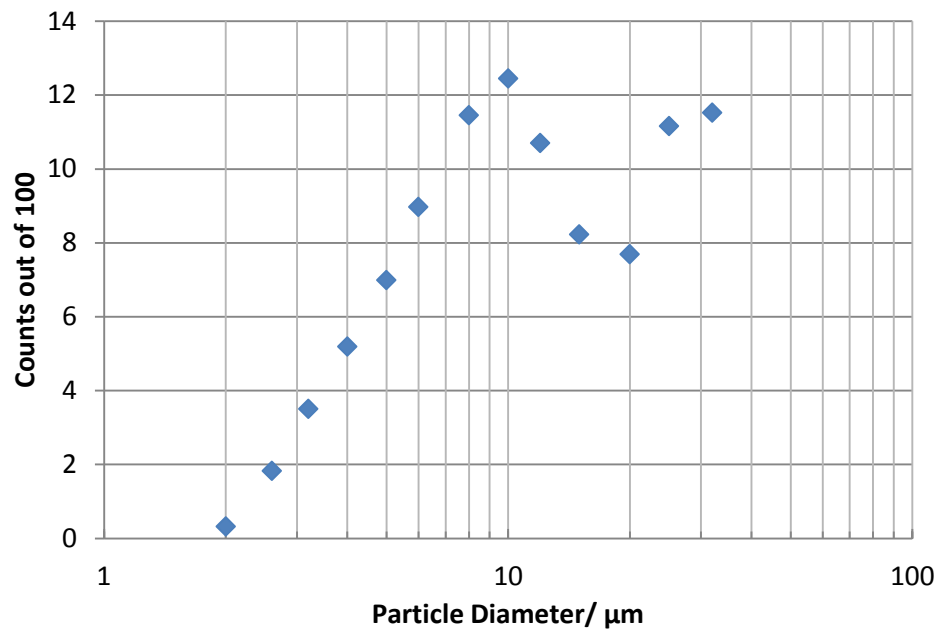


Figure 15. Particle size distribution provided by the manufacturer in the form of a frequency plot.

Table 1. Average pore size measurements for 10 vol.% Ti-6Al-4V and different volume percentages of ethanol measured on optical images of razor cut cross-sections.

Slurry Composition	Long Axis [μm]	Short Axis [μm]	Aspect Ratio
10v%Ti 0v%Ethanol	98 ± 35	18 ± 5.7	5.4
10v%Ti 5v%Ethanol	80 ± 21	37 ± 13	2.2
10v%Ti 10v%Ethanol	89 ± 20	30 ± 15	3.0

Table 2. Physical properties of freeze-cast solutions for Equations 2-4.

η Chitosan [cP]	η CMC [cP]	η water [cP]
84.0 ± 2.18	604 ± 22.8	1.8
d [nm]	A [J]	a_0 [nm]
1	$-7\text{e-}20$	10
ρ water/ice [kg m^{-3}]	ρ Ti [kg m^{-3}]	μ
1000 / 920	4500	11.7

Table 3. Final average pore size for different Ti-6Al-4V and ethanol vol.%, freezing rate, and binders measured from tomography images on 4mm cubes.

Slurry Composition and Freezing Rate	Long Axis [μm]	Short Axis [μm]	Position [mm]
a) 20vol.%Ti-6Al-4V, 0vol.%ethanol, Chitosan, $10^\circ\text{C min}^{-1}$	41.2 ± 24.2	16.4 ± 6.83	12
b) 20vol.%Ti-6Al-4V, 5vol.%ethanol, Chitosan, $10^\circ\text{C min}^{-1}$	56.8 ± 12.8	14.5 ± 4.60	16
c) 20vol.%Ti-6Al-4V, 5vol.%ethanol, CMC, 1°C min^{-1}	523 ± 225	76.5 ± 30.0	16
d) 30vol.%Ti-6Al-4V, 5vol.%ethanol, Chitosan, $10^\circ\text{C min}^{-1}$	103 ± 36.8	27.8 ± 12.4	20

Table 4. Tabulated literature values of porosities, pore sizes, and mechanical properties for freeze-cast titanium. Specific Energy was calculated from work to 20% strain.

Raw Powder Material	Ti	TiH ₂	TiH ₂	Ti	Ti	Ti	Ti-6Al-4V
Powder Size [μm]	<45	Ball milled	Ball milled	<20,-325 mesh (20),-500 mesh(10)	10-30	Ball milled	<32 (10)
Particle Loading [Vol. %]	22	15, 20, 25	10	22	20	15, 20, 25	20,30
Freezing Vehicle	water	camphene	camphene	water	camphene	camphene	water
Porosity [%]	60	49-63	64	37-55	51-69	52-71	34-64
Pore Size (Cross-section) [μm]	150-180	Up to 100	143-271	50-70	250-500	95-362	41-523
Stiffness [GPa]	-	-	-	10-52	2-5	7-31	7-29
Strength [MPa]	40-60	81-253	48-110	110-380	121-302	84-423	82-414
Specific Energy [J g ⁻¹]	2.45	-	-	13.6-13.7	11.2-20.1	8.05-15.3	8.89-41.1
Source	[5]	[7]	[9]	[6]	[10]	[15]	Present work

$$\text{Equation 1} \quad \boldsymbol{w} \propto \frac{1}{v^n}$$

$$\text{Equation 2} \quad v_{cr} = \frac{\Delta\sigma_0 a_0}{12\eta\mu r}$$

$$\text{Equation 3} \quad v_p = \frac{2(\rho_p - \rho_L)g}{9} \frac{r^2}{\eta}$$

$$\text{Equation 4} \quad \boldsymbol{A} = -\mathbf{12} \boldsymbol{d}^2 \Delta \boldsymbol{\sigma}_0$$

$$\text{Equation 5} \quad \boldsymbol{E}_f = \boldsymbol{C} * \boldsymbol{E}_s \left(\frac{\rho_f}{\rho_s} \right)^2$$

$$\text{Equation 6} \quad \boldsymbol{\sigma}_f = \boldsymbol{C} * \boldsymbol{\sigma}_s \left(\frac{\rho_f}{\rho_s} \right)^{\frac{3}{2}}$$

Appendix F: Nacre-Like Hybrid Films: Structure, Properties, and the Effect of Relative Humidity

*Mohammed T. Abba, Philipp M. Hunger, Surya R. Kalidindi, Ulrike G.K. Wegst**

M. T. Abba, Prof. S. R. Kalidindi
The George W. Woodruff School of Mechanical Engineering
Georgia Institute of Technology, Atlanta, GA 30332-0405, USA
Dr. P. M. Hunger, Prof. U. G. K. Wegst
Thayer School of Engineering, Dartmouth College, Hanover, NH 03755, USA
E-mail: ulrike.wegst@dartmouth.edu

Keywords: nacre, biomimetics, tensile tests, thin films, chitosan

Functional materials often are hybrids composed of biopolymers and mineral constituents. The arrangement and interactions of the constituents frequently lead to hierarchical structures with exceptional mechanical properties and multifunctionality. In this study, hybrid thin films with a nacre-like microstructure were fabricated in a straightforward and reproducible manner through manual shear casting using the biopolymer chitosan as the matrix material and alumina platelets as the reinforcing particles. The ratio of inorganic to organic content was varied from 0% to 15% and the relative humidities from 36% to 75% to determine their effects on the mechanical properties. It was found that increasing the volume fraction of alumina from 0% to 15% results in a twofold increase in the modulus of the film, but decreases the tensile strength by up to 30%, when the volume fraction of alumina is higher than 5%. Additionally, this study quantifies and illustrates the critical role of the relative humidity on the mechanical properties of the hybrid film. Increasing the relative humidity from 36% to 75% decreases the modulus and strength by about 45% and triples the strain at failure.

1. Introduction

A considerable research effort is currently focused on the synthesis of stronger, tougher, and “greener” materials based on the principles of function and optimization found in natural materials.^[1-4] This is because natural materials often exhibit a superior mechanical performance in comparison to their synthetic, monolithic counterparts due to their hierarchical structural arrangements.^[5-7] One example of such a natural material, that has attracted particular interest in recent years, is nacre. Also termed ‘mother of pearl’, it forms the inner layer of the shells of a large number of mollusks (e.g., abalone), and has demonstrated impressive performance under tensile loading.^[8] Nacre is essentially a two-phase composite material with an intricate, interlocked brick-and-mortar structure comprised of about 95 vol.%, of hexagonal aragonite platelets ‘glued’ together by a thin polymer film (~10–50 nm thick) composed of proteins and polysaccharides.^[9-11] The tensile strength of nacre is about 78-130 MPa (wet) and 90-167 MPa (dry), and the Young’s modulus is about 58-70 GPa (wet) and 68-90 GPa (dry).^[9] With a high volume fraction of ceramic, one would expect the material to be brittle. However, nacre has a work of fracture as high as 1240 J m^{-2} , in a three-point bending test, which is about 3000 times greater than that of monolithic CaCO_3 .^[10, 12] The work of fracture, in this case, is defined as the critical strain energy release rate or the energy necessary to drive a crack through a sample. This intriguing observation and the relative simplicity of the structure of nacre was the motivation for this study of fundamental structure-property relationships, including the often neglected effect of moisture, in a nacre-like model material system.^[11]

The bio-inspired research presented here aims to identify the principles of function and optimization in biological materials and to mimic the same in engineered material systems. Numerous studies have described materials that match or even exceed the properties of nacre.^{[2, 3,}

^{13-16]} For example, using a layer-by-layer (LBL) assembly yields nanocomposites that can have tensile strengths up to 400 MPa.^[2, 3, 13, 15] Freeze casting yields, when infiltrated by a second phase, layered structures that are up to 300 times tougher than its constituents.^[1, 14, 16] Toughness, in this case, is defined as the plane-strain fracture toughness, K_{Ic} . Casting methods, such as slip-casting,^[4] evaporation,^[17] and combined gel-casting and hot-pressing,^[18, 19] all yielding a brick and mortar structure, have been reported to produce materials with tensile strengths up to 250 MPa, thus exceeding that of nacre. Samples with a nacre-like structure that can be produced using some of the techniques described in prior literature are usually extremely small in volume and require time-consuming processes and specialized equipment. The scaling-up both of sample volumes and production rates for real-life applications continues to pose considerable difficulties and usually leads to a considerable loss in mechanical properties.

The use of self-assembly mechanisms is increasingly being explored to overcome these problems. Taking advantage of particle self-assembly that occurs during freeze casting, for example, the manufacture of large sample sizes with a nacre-like structure could recently be demonstrated.^[20] The resulting cellular materials, composed of alumina platelets in a chitosan-gelatin matrix, had a honeycomb-like structure, whose cell walls exhibited nacre-like structures and resulted in considerably improved mechanical properties both parallel and perpendicular to the long pore axis.^[20, 21] In an effort to better understand the mechanisms that determine the mechanical properties of the wall material of the freeze-cast scaffolds and to mimic the structure of biological materials in a well-controlled model system, we fabricated alumina-platelet reinforced chitosan films. Alumina platelets were chosen as the inorganic ceramic phase because of their close resemblance, in shape and aspect ratio, to the aragonite platelets in nacre.^[22]

Chitosan, a linear biopolymer derived by N-deacetylation of chitin was chosen for the matrix material, because it is ideally suited for a study of property dependence on relative humidity.^[23]

One critical factor that is frequently not addressed and reported is the effect of moisture content on the mechanical properties of the films produced. Since chitosan readily absorbs water, its mechanical properties will greatly vary depending on the relative humidity of the environment at the time of the test.^[24] Chitosan films have been reported to have as much as a 99% loss in Young's modulus and 88% loss in stress at break when immersed in deionized water for one night and an 80% loss in tensile strength when the conditioning relative humidity was increased from 15.6% to 93%.^[24, 25] To investigate the effect of moisture content, this study focused on controlled relative humidities of 35%, 55%, and 75%.

A relatively simple and reproducible processing method to fabricate thin hybrid films is utilized in this study. The goals are to show that the films produced using this technique result in highly aligned microstructures, to investigate the mechanical properties of these films in tension, and to show that relative humidity of the environment can have a significant effect on the measured mechanical properties.

2. Mechanical Properties

Prompted by investigations into the toughness of nacre (and bone), the mechanics of polymer composites reinforced with anisotropic particles have been pursued in depth in recent years. Models have been developed that describe, how the aspect ratio of the platelets, the properties of the different phases as well as that of the interfaces determine the failure mode of the whole composite.^[11, 26, 27] Two simple rule of mixture models are commonly used to describe the mechanical behavior of two-component composites with continuous and aligned phases: the Voigt model and the Reuss model.^[28, 29] The Voigt model, mostly applicable in the case of a

composite with fibers running parallel to the loading direction, as shown in **Figure 1a**, assumes that the whole composite experiences the same strain. This case is dominated by the stiffer and stronger phase and describes the upper bound of the achievable mechanical properties. The Reuss model, applicable in the case of a composite with fibers running perpendicular to the loading direction, as shown in Figure 1b, assumes that the whole composite experiences the same stress. This case is dominated by the softer phase and describes the lower bound of the achievable mechanical properties. Since our composites do not have continuous phases, these models are only used to define the upper and lower bounds of the composite's stiffness.

Jaeger and Fratzl showed that the microstructure of biocomposites can be described by staggered mineral bricks in a protein matrix as shown in Figure 1c.^[30] In tension, the mechanical behavior of the Jaeger-Fratzl model can be represented using the shear lag model, in which the mineral platelets are loaded in tension and the protein matrix transfers the load between platelets via shear stresses as shown in **Figure 2**. Models that describe the mechanical behavior of particulate reinforced composites, such as nacre and the alumina-reinforced chitosan films studied here, include the Padawer-Beecher model for composite modulus and the Glavincevski model for the composite strength.^[31, 32] The Padawer-Beecher model is based on a force balance on an individual platelet assuming the composite material follows the shear lag model. The Padadwer-Beecher model estimates the composite modulus as:

$$E_c = V_f E_f \left[1 - \frac{\tan u}{u} \right] + (1 - V_f) E_m \quad (1)$$

$$u = s \sqrt{\frac{G_m V_f}{E_f (1 - V_f)}} \quad (2)$$

where s is the aspect ratio of the platelets, E is the elastic modulus, V is the volume fraction, G is the shear modulus of the matrix phase, and the subscripts c , m , and f denote the composite, matrix, and filler phase, respectively.

The ultimate tensile strength of the composite can be modeled using the Glavinchevski model as:

$$\sigma_c = \alpha V_f \sigma_f + (1 - V_f) \sigma_m \quad (3)$$

where σ is the tensile strength. The factor α is a function of the platelet aspect ratio, the matrix yield shear strength, and the tensile strength of the platelets.^[31] The failure mode of the composite is determined by the aspect ratio of the platelet.^[26] The critical aspect ratio of the platelet can be determined by the length at which the stress build-up in the platelets is equal to its tensile strength as shown in **Figure 3**. The critical aspect ratio can also be estimated by the ratio of the platelet strength to the lower value among the shear strength of the matrix, τ_y , and the shear strength of the polymer-platelet interface, τ_i . For the case where the aspect ratio of the platelet is greater than the critical value, the platelets fracture, leading to a brittle failure of the composite and the factor α can be defined as:

$$\alpha = 1 - \frac{\sigma_f}{2\tau_{min}s} \quad (4)$$

where τ_{min} is either the shear strength of the matrix or the shear strength of the polymer-platelet interface whichever is lower.^[2] For the case where the aspect ratio of the platelet is lower than the critical value, the matrix will yield before the platelet, leading to platelet pull-out and plastic yielding of the matrix before the composite completely fails.^[7, 33] The factor α is then defined as:

$$\alpha = \frac{\tau_{min}s}{2\sigma_f} \quad (5)$$

In the models discussed, the following assumptions were made to simplify the calculations: the matrix adheres perfectly to the platelets; the platelets don't interact with each other; all the platelets have the same dimensions; the platelets are arranged parallel to and equidistant from each other; the moduli of all the platelets are the same; and the matrix is linearly elastic. The first assumption is dependent on the surface chemistry between the platelet and the matrix and that there are no pores generated during processing of the matrix. As the volume fraction of the platelets is increased, the likelihood of particle clustering, interactions, and disorder increases, leading to the second and fourth assumptions not being satisfied. For smaller dimensions, manufacturing limitations may cause a larger variation in the dimensions of individual platelets, which may not satisfy the second assumption. If using crystalline platelets, changes in crystal orientation between individual platelets may lead to differences in their modulus; however, they would probably cancel out with a large volume of platelets. The matrix, being a polymer, is most likely viscoelastic. For higher accuracy of the models, it is important to include the time and temperature dependence of the matrix mechanical properties into the models, which in the case of biopolymers are significantly affected by relative humidity.

3. Results and Discussion

3.1. Fabrication of Hybrid Composites

A method to fabricate ceramic-reinforced polymer hybrid films with highly aligned microstructures in larger sample volumes and faster processing times is introduced. The films have been successfully fabricated with volume fractions of ceramic platelets ranging from 5 vol.% to 15 vol.% by first making a slurry of alumina platelets in a chitosan solution and then using a slip casting method. For best results, it is important to use surface-treated tissue culture dishes, which allow for better wettability between the dish and the chitosan-alumina slurry. The

films can be produced with thicknesses ranging from 15 μm to 75 μm and can easily be peeled off, once dry. We found that volume fractions of alumina greater than 15% rendered the dry films too brittle to be removed intact from the petri dish.

3.2. Structural Analysis

Analysis by scanning electron microscopy, shown in **Figure 4**, revealed that the platelets are very uniformly distributed in the matrix and aligned parallel to the film's free surfaces. The cross-sections show that the platelets form a brick and mortar like structure similar to that found in nacre and the freeze-cast scaffolds. **Figure 4** further shows, how the structure changes with an increasing platelet volume fraction and that there appears to be very little increase in misalignment with increasing ceramic volume fraction. The misalignment appears primarily to be due to the freeze-fracturing process before imaging. There also appears to be increased clustering at higher volume fractions, which may result in films with lower composite strengths as discussed in the next section.

3.3. Mechanical Characterization

Alumina reinforced free-standing chitosan films with different volume fractions of alumina were mechanically tested in tension, at three relative humidities of 35%, 55%, and 75%. Typical true stress – true strain plots, shown in **Figure 5**, illustrate that the Young's modulus increases and the strain at failure decreases with increasing platelet volume fraction.

3.3.1. Elastic Modulus

The elastic modulus was calculated from the slope of the initial linear region of the stress-strain curves. The Padawer-Beecher model described by Equation (1) was used to estimate the elastic modulus of the chitosan-alumina films. The platelets had an average thickness and diameter of 400 ± 100 nm and 7.5 ± 2.5 μm respectively, giving them an aspect ratio of about

19.^[20] The elastic modulus of the alumina platelets was assumed to be 375 GPa,^[34] and the shear modulus of the chitosan film was calculated, using the model assumption of a linear elastic material, by the relationship:

$$G_m = \frac{E_m}{2(1 + \nu)} \quad (6)$$

where ν is the Poisson ratio of chitosan, $\nu = 0.272$.^[35] Since the elastic modulus of chitosan can vary depending on the relative humidity of the environment at the time of testing, the elastic modulus of the pure chitosan films as the matrix in the Padawer-Beecher model was determined experimentally for the three different relative humidities.

We also compared our results with average values found in the literature for materials reinforced with nano-size platelets at volume fractions similar to the ones studied here. Bonderer et al. fabricated freestanding chitosan-alumina hybrid thin films using a layer-by-layer method.^[31] The alumina platelets were surface modified with 3-aminopropyltriethoxysilane (APS) to improve the platelets' adhesion to the matrix. Bonderer et al. also fabricated polypropylene-alumina and polyurethane-alumina hybrid thin films using a gel-casting and hot-pressing method.^[18, 19] Shukla et al. fabricated epoxy-alumina hybrid thin films using a curing method.^[36] The study reported here was performed with uncoated platelets and platelets surface modified with 3-glycidoxypopyltrimethoxysilane (GPS) to improve platelet adhesion to the matrix.

The elastic modulus results for our study, predictions from the Padawer-Beecher model, and the literature values are plotted in **Figure 6a**. Our results show that increasing the platelet fraction increases the tensile modulus and increasing the relative humidity decreases the tensile modulus of the composite. Our results also show a good experimental correlation to the model prediction. The same trend is observed in composites characterized by other researchers with property values dependent on the matrix material used. Since no mention is made of the relative

humidities at which the literature values were obtained, it is not possible to provide a meaningful direct comparison with these.

3.3.2 Tensile Strength

Tensile strength was calculated from the maximum stress reached during the tests. The Glavinchevski model described by Equation (3) is used to estimate the tensile strength of the chitosan-alumina composite. Since we are assuming that the matrix adheres perfectly to the platelets, the matrix will yield before the polymer-platelet interface, and the shear strength of the polymer will be used to estimate the critical aspect ratio and the mode of failure of the composite. The tensile strength of the alumina platelets is taken to be $\sigma_p = 2$ GPa and the shear strength of the polymer is estimated, using the von Mises criterion, to be $\tau_y = 0.577\sigma_m$ at the three different relative humidities.^[2, 37] The critical aspect ratio is then 53.4, 55.5, and 87.4 for the 35%, 55%, and 75% relative humidities, respectively. The platelet aspect ratio is 19, which is lower than the critical aspect ratios, so Equation (5) is used to estimate the α factor meaning that the matrix should ideally yield before the platelet. In this case α is 0.18, 0.17, and 0.11 for the 35%, 55%, and 75% relative humidities, respectively.

The tensile strength results of our study, predictions from the Glavinchevski model, and the literature values are plotted in **Figure 6b**. We notice an initial increase in tensile strength but the strength decreases as the volume fraction of the platelets is increased beyond 5%. The reduction in strength, we suggest, is due to the introduction of flaws, such as porosity formed when the particles are added to the matrix, or insufficient bonding of the platelets to the chitosan matrix, so that full debonding is initiated early and occurs well before the matrix fails. Porosities are further increased in the material once debonding has occurred and the strain increases. Additionally, we also notice increased clustering of the platelets with increasing volume fraction

(Figure 4), which causes an increase in the stress concentrations around those areas leading to cracks being formed. Composites in the literature, in which the surfaces of the alumina platelets were not modified to enhance adhesion, show a decrease in strength with increasing platelet volume fraction. For the composites whose particles surfaces were modified, the strength increases with increasing platelet volume fraction especially in the case of Bonderer et al.,^[3] with a 500% increase in tensile strength at a 15% volume fraction of platelets. This suggests that enhancing the bond between the matrix and platelets can significantly improve the tensile strength of the composite.

3.3.3 Effect of Relative Humidity

Table 1 shows that a decrease in relative humidity results in an increase in elastic modulus and tensile strength and a decrease in the strain at failure. The three stress–strain curves shown in **Figure 7** for a film with 10 % volume fraction alumina show this even more clearly. The tensile modulus and strength decrease by about 45% with an increase of relative humidity of 20%, whereas the strain at failure is almost tripled; as the humidity increases, the films absorb more of the plasticizer water, rendering the polymer phase more ductile. This dramatic effect of the moisture content on the mechanical properties shows that it is very important to take into account the environmental conditions, when mechanical tests are performed on samples containing significant amounts of biopolymers such as chitosan. Humidity can further play a crucial role in determining the material’s performance and effectiveness for a given application.

4. Conclusion

Nacre-inspired composite films were successfully prepared with alumina-platelets in a chitosan solution. They emulate the brick-and-mortar structure of the natural material and could

be made with film thicknesses and volumes significantly higher than those of similar composition reported in the literature.^[2, 3] While the modulus increased and the strain decreased with an increase in particle content, the strength did not increase with volume fractions greater than 5%. Voids, insufficient particle-matrix bonding, and platelet clustering are thought to introduce flaws, which result in decreased tensile strength. This can be investigated in the future by functionalizing the alumina surface to facilitate a chemical bond between the alumina and chitosan, thus increasing the interfacial strength of the composite. Also at higher volume fractions, processing methods would have to be improved to reduce the clustering that occurs. We have shown that an organized structure can be maintained at higher volume fractions and the fabrication method has a potential to be used for larger scale applications. Particularly noteworthy is the effect of relative humidity, a frequently neglected factor, on the mechanical performance. An increase in the relative humidity from 35% to 75% results in a 48.1% decrease in modulus and up to fourfold increase in strain at failure for the chitosan-alumina films. These results are steps towards a better understanding of the mechanisms that drive biological systems as well as towards improved processes to emulate them in the laboratory. With improvements in the materials and processing techniques, it will become possible to manufacture complex hybrid materials whose mechanical properties can be custom-designed for specific applications and environmental conditions.

5. Experimental Section

Materials: Low molecular weight chitosan (75-85% deacetylated) was purchased from Sigma Aldrich, St. Louis, MO, USA. Glacial acetic acid, deionized water, and tissue culture dishes were purchased from VWR International, Radnor, PA, USA. Alumina platelets with a diameter and a thickness of 5-10 μm and 300-500 nm, respectively, were obtained from

AlusionTM, Antaria Limited, Bentley, Western Australia. Deionized water was used for all experiments and all chemicals were used without further modifications.

Film Preparation: To prepare the nacre-inspired alumina-chitosan hybrid films, first 3.6% (w/v) of low molecular weight chitosan was dissolved in 1% (v/v) glacial acetic acid in de-ionized water. The chitosan solution was homogenized on a bottle roller for 48 hours at room temperature (25°C). To prepare the ceramic slurry, alumina platelets were added to the chitosan solution to achieve the required volume fraction of alumina in the dry film once the solution was cast. For example, to prepare a 5% volume fraction thin film, we took 10 mL of the chitosan solution, which contains 0.36 g or 0.295 cm³ of chitosan (density of chitosan is 1.22 g/cm³), and added 0.0155 cm³ or 0.0621 g of alumina (density of alumina is 4 g/cm³). Similarly, for 10% and 15% volume fraction, 0.1312 g and 0.2082 g of alumina is added. The ceramic slurry was then shear-mixed (SpeedMixer DAC 150 FVZ-K, FlackTek Inc., Landrum, SC, USA) at 2700 rpm for two minutes before film preparation. The hybrid films were slip cast in a 150mm diameter petri dish using the method depicted in **Figure 8**. Electrical tape was placed at the edges as shown in Figure 8 such that the final width of the film was 90 mm and final thickness was 10–40 μm. The petri dish was then placed in a fume hood and allowed to dry at room temperature for at least 24 hours. Once dry, the films were then slowly peeled from the petri dishes by hand. The thickness of the dry film can be controlled by increasing the thickness of the electrical tape.

Scanning Electron Microscopy: For observation by scanning electron microscopy (SEM), the films were first freeze-fractured in liquid nitrogen, to reduce disturbance to the cross-section, and then sputter-coated (Cressington 108 Auto Sputter Coater, Cressington Scientific Instruments Inc., Watford, England, UK) with a 2–5 nm thick platinum-paladium layer. Cross-

sections of the films were observed in a scanning electron microscope (Zeiss Supra 50VP, Carl Zeiss SMT Inc., Peabody, MA, USA).

Mechanical Testing: For mechanical testing in tension, the films were cut into a dumbbell shape (ASTM D1708-06), with a narrow section 17 mm long and 5 mm wide, with a microtensile die (Pioneer-Dietecs, Weymouth, MA, USA).^[38] The strips were taped with double-sided tape into custom made paper-frames to stabilize them before the test and gripping in the vices with a gauge length of 22 mm for testing (**Figure 9**). To condition the films at $36\pm0.1\%$, $56\pm0.1\%$ and $75\pm0.1\%$ relative humidity, saturated solutions of Sodium Chloride (ACS grade, EMD Chemicals, Gibbstown, NJ, USA), Magnesium Nitrate (ACS grade, Alfa Aesar, Ward Hill, MA, USA), and Magnesium Chloride (ACS grade, Alfa Aesar) were prepared. The solutions were then poured into the bottom of a desiccator with the framed films placed on a ceramic plate and allowed to condition for at least 48 hours as specified by ASTM D618-13.^[39, 40] At least 5 strips were tested for all four compositions at three different relative humidities. Mechanical testing was carried out in tension on an Instron 5948 (Instron, Norwood, MA, USA) with a 50 N load cell and a crosshead speed of 1 mm/min, corresponding to a strain rate of 0.045/s. For testing, a climate chamber was built around the Instron, which ensured that the samples could be tested at a well-defined humidity identical to that, at which the films had been conditioned prior to testing. The climate chamber consisted of a BioPuls (Instron, Norwood, MA, USA) bath chamber around the testing system sealed by elastic bellows (TheRubberStore.com, Dayton, Ohio, USA) as shown in **Figure 10**. Tests were performed after the relative humidity in the chamber had reached and stabilized at each respective relative humidity. The true stress–true strain curves were plotted using the measured force and displacement and the dimensions of the film. Young’s modulus was calculated from the slope of the initial linear region, the tensile

strength was taken to be the highest stress of the true stress-strain curve, and the strain at failure was taken when the stress started decreasing before it fully failed.

Humidity control: The saturated salt solutions mentioned above were prepared by adding the salts in boiling deionized water until no more salt could be dissolved. Magnesium Chloride was used to achieve an average relative humidity of $35.7\pm0.1\%$, Magnesium Nitrate was used to achieve an average relative humidity of $56\pm0.1\%$, and Sodium Chloride was used to achieve an average relative humidity of $75.4\pm0.1\%$. Before the start of each tensile test, salt solutions were placed in separate containers at the bottom of the biobath and a small fan was used to circulate the air over salt solutions and to ensure a uniform relative humidity in the climate chamber. The required humidity was usually reached within a few minutes and stayed within 0.1% relative humidity for the duration of the test. The fan was turned off for the duration of each test directly before each test was performed.

Acknowledgements

The authors would like to acknowledge the Central Research Facilities at Drexel University, where the scanning electron microscopy work was performed. This research was supported by The Army Research Office under grant number W911NF-10-1-0409.

- [1] E. Munch, M. E. Launey, D. H. Alsem, E. Saiz, A. P. Tomsia, R. O. Ritchie, *Science* 2008, 322, 1516.
- [2] L. J. Bonderer, A. R. Studart, L. J. Gauckler, *Science* 2008, 319, 1069.
- [3] L. J. Bonderer, A. R. Studart, J. Woltersdorf, E. Pippel, L. J. Gauckler, *Journal of Materials Research* 2009, 24, 2741.
- [4] A. Walther, I. Bjurhager, J. M. Malho, J. Pere, J. Ruokolainen, L. A. Berglund, O. Ikkala, *Nano Lett* 2010, 10, 2742.
- [5] J. W. C. Dunlop, P. Fratzl, in *Annual Review of Materials Research, Vol 40*, Vol. 40 (Eds: D. R. Clarke, M. Ruhle, F. Zok), Annual Reviews, Palo Alto 2010, 1.
- [6] Z. Zhang, Y. W. Zhang, H. Gao, *Proceedings. Biological sciences / The Royal Society* 2011, 278, 519.
- [7] M. E. Launey, R. O. Ritchie, *Advanced Materials* 2009, 21, 2103.
- [8] A. R. Studart, *Advanced Materials* 2012, 24, 5024.
- [9] H. Kakisawa, T. Sumitomo, *Science and Technology of Advanced Materials* 2011, 12, 064710.

- [10] A. P. Jackson, J. F. V. Vincent, R. M. Turner, *Proceedings of the Royal Society of London. Series B. Biological Sciences* 1988, 234, 415.
- [11] F. Barthelat, *Bioinspir. Biomim.* 2010, 5.
- [12] M. A. Meyers, P.-Y. Chen, A. Y.-M. Lin, Y. Seki, *Progress in Materials Science* 2008, 53, 1.
- [13] P. Podsiadlo, A. K. Kaushik, E. M. Arruda, A. M. Waas, B. S. Shim, J. Xu, H. Nandivada, B. G. Pumplin, J. Lahann, A. Ramamoorthy, N. A. Kotov, *Science* 2007, 318, 80.
- [14] U. G. K. Wegst, M. Schecter, A. E. Donius, P. M. Hunger, *Philosophical Transactions of the Royal Society a-Mathematical Physical and Engineering Sciences* 2010, 368, 2099.
- [15] M. M. Malwitz, A. Dundigalla, V. Ferreira, P. D. Butler, M. C. Henk, G. Schmidt, *Physical Chemistry Chemical Physics* 2004, 6, 2977.
- [16] S. Deville, E. Saiz, R. K. Nalla, A. P. Tomsia, *Science* 2006, 311, 515.
- [17] H. B. Yao, Z. H. Tan, H. Y. Fang, S. H. Yu, *Angewandte Chemie International Edition* 2010, 49, 10127.
- [18] L. J. Bonderer, K. Feldman, L. J. Gauckler, *Composites Science and Technology* 2010, 70, 1958.
- [19] L. J. Bonderer, K. Feldman, L. J. Gauckler, *Composites Science and Technology* 2010, 70, 1966.
- [20] P. M. Hunger, A. E. Donius, U. G. K. Wegst, *Journal of the Mechanical Behavior of Biomedical Materials* 2013, 19, 87.
- [21] P. M. Hunger, A. E. Donius, U. G. K. Wegst, *Acta Biomaterialia* 2013, 9, 6338.
- [22] H. J. Gao, B. H. Ji, I. L. Jager, E. Arzt, P. Fratzl, *Proc. Natl. Acad. Sci. U. S. A.* 2003, 100, 5597.
- [23] P. K. Dutta, J. Dutta, V. Tripathi, *Journal of Scientific and industrial research* 2004, 63, 20.
- [24] A. Domard, M. Domard, in *Polymeric Biomaterials*, (Ed: S. Dumitriu), Marcel Dekker, New York 2002, 187
- [25] P. Rachtanapun, P. Wongchaiya, *Chiang Mai Journal of Science* 2012, 39, 133.
- [26] M. Richardson, *Polymer engineering composites*, Elsevier Science & Technology, 1977.
- [27] F. Barthelat, M. Mirkhalaf, *Journal of The Royal Society Interface* 2013, 10.
- [28] K. K. Chawla, *Composite materials: science and engineering*, Springer, 2012.
- [29] M. A. Meyers, K. K. Chawla, *Mechanical Behavior of Materials*, Cambridge University Press, 2009.
- [30] I. Jäger, P. Fratzl, *Biophysical Journal* 2000, 79, 1737.
- [31] B. Glavinchevski, M. Piggott, *Journal of Materials Science* 1973, 8, 1373.
- [32] G. E. Padawer, N. Beecher, *Polymer Engineering & Science* 1970, 10, 185.
- [33] B. Ji, H. Gao, *Annual Review of Materials Research* 2010, 40, 77.
- [34] D. Shukla, V. Parameswaran, *Journal of Materials Science* 2007, 42, 5964.
- [35] M. Nurul Hazwani, M. Halimah, K. Kaida, W. Daud, M. Zaki, *Journal of Solid State Science and Technology* 2011, 19, 120
- [36] D. K. Shukla, S. V. Kasisomayajula, V. Parameswaran, *Composites Science and Technology* 2008, 68, 3055.
- [37] K. Liu, M. R. Piggott, *Composites* 1995, 26, 829.

- [38] D1608, ASTM International 2006.
- [39] D618, ASTM International 2013.
- [40] E104, ASTM International 2002.

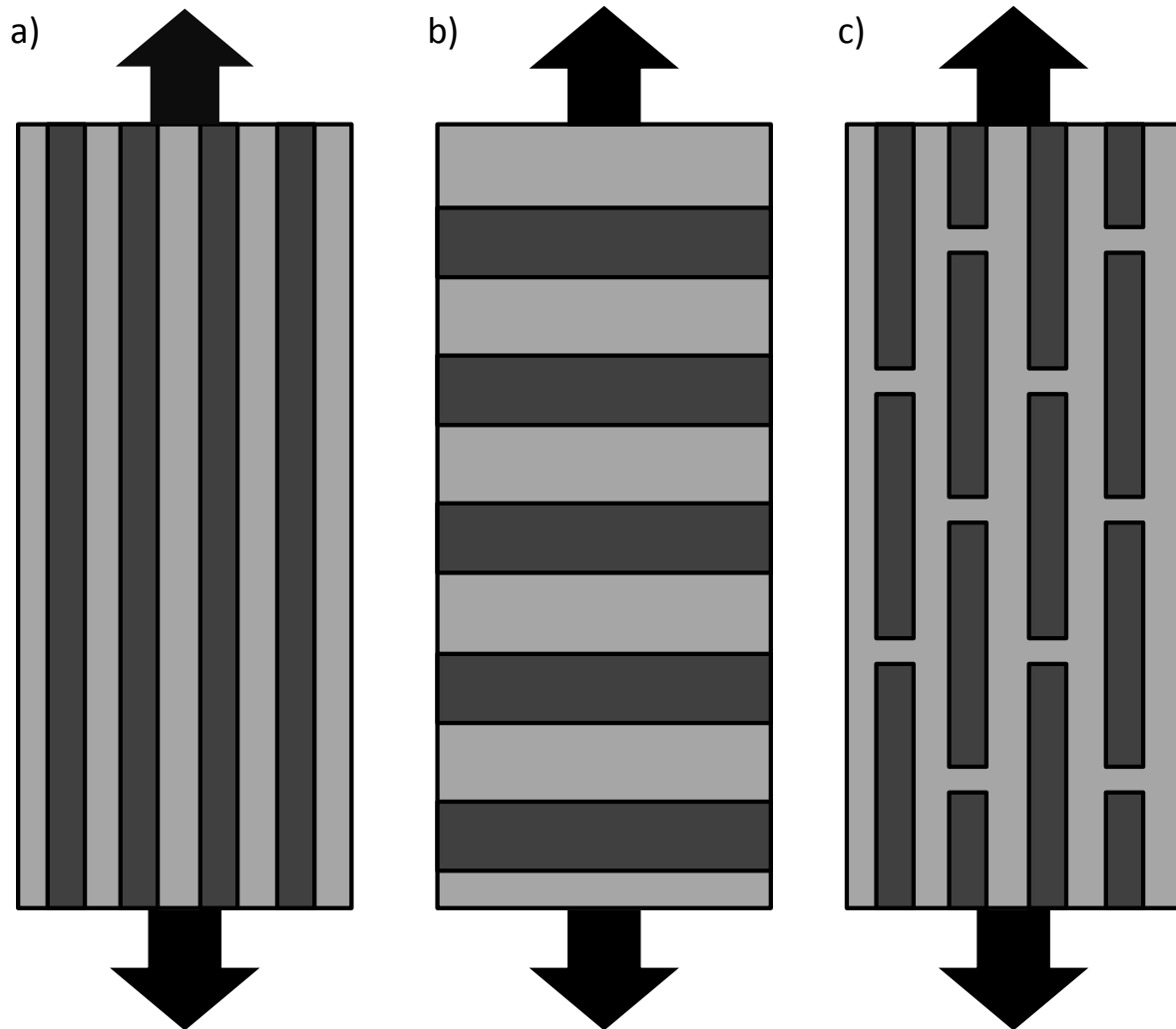


Figure 1 - Models to describe mechanical behavior of composites: a) Voigt model, b) Russ model, and c) Jaeger-Fratzl model.

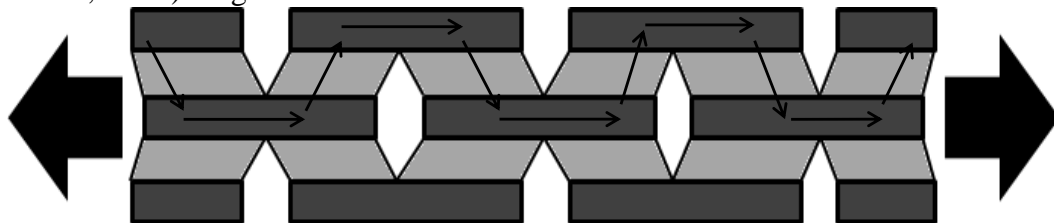


Figure 2 - The shear lag model transfers load between the mineral platelets, where most of the load is carried, via interfacial shear stresses.

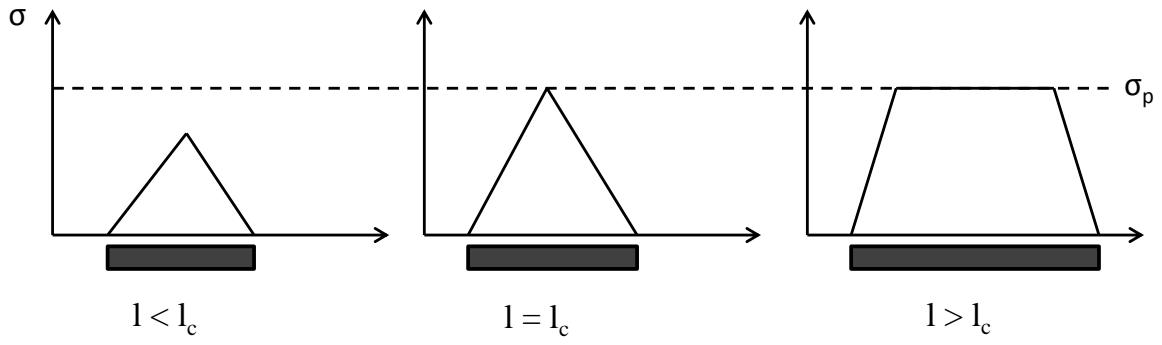


Figure 3 - Variation of tensile stress in the platelet as a function of its length. σ_p is the platelet fracture strength.

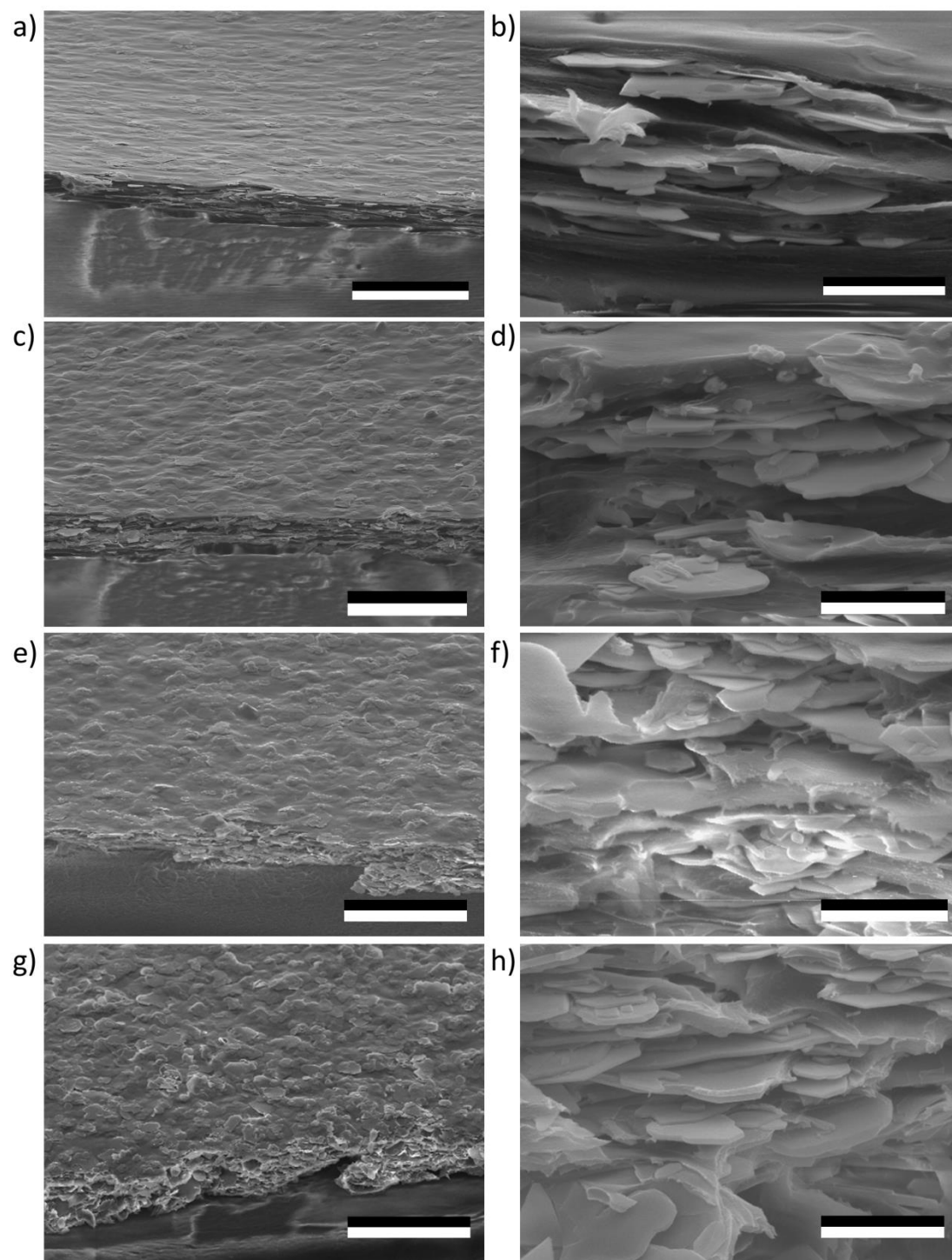


Figure 4 - Films with 5% a,b), 10% c,d), 15% e,f), and 20% g,h) volume fraction of alumina platelets (scale bars are $50\mu\text{m}$ for a,c,e,g) and $5\mu\text{m}$ for b,d,f,h)).

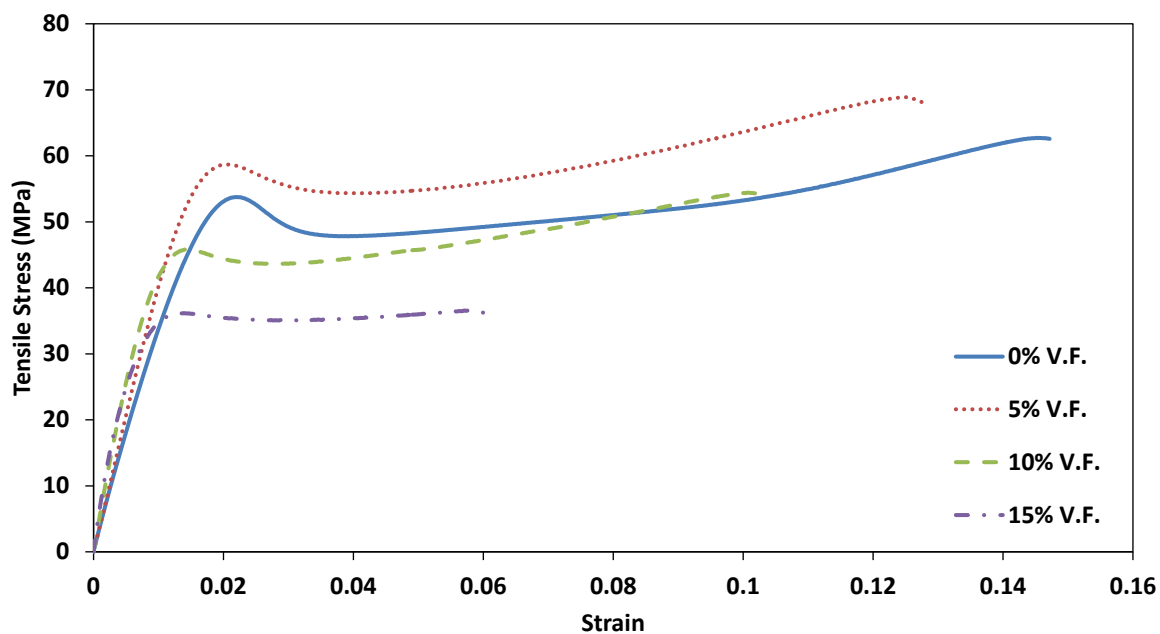


Figure 5 - Typical tensile stress versus strain curves of chitosan-alumina films with increasing volume fractions (V.F.) of alumina platelets (displacement rate is 1 mm s^{-1} , relative humidity is 55%).

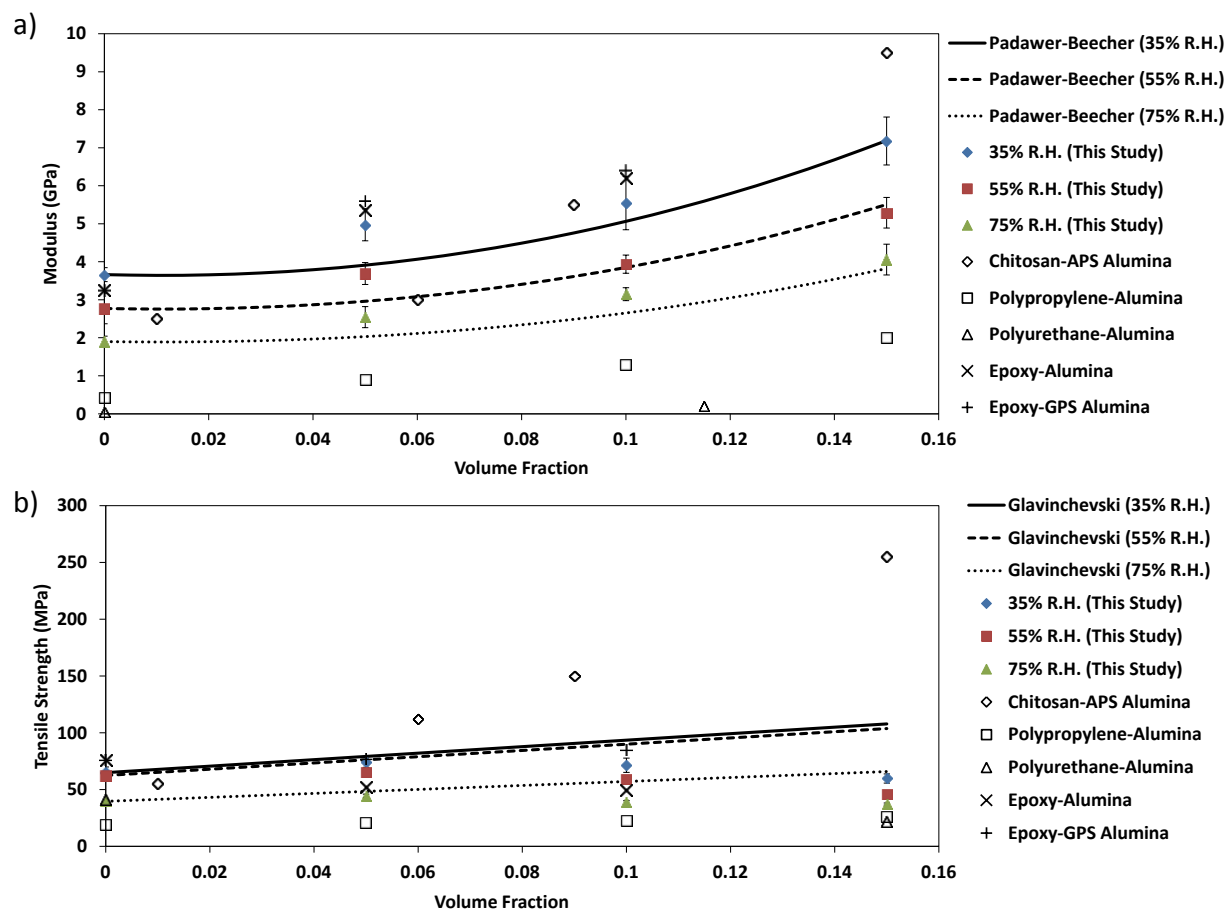


Figure 6 - a) Tensile modulus and b) tensile strength as a function of platelet volume fraction at three different relative humidities. Included are predictions of the composite a) tensile modulus based on the Padawer-Beecher model, b) tensile strength based on the Glavinchevski model, and literature values for chitosan-APS alumina^[3], polypropylene-alumina^[18], thermoplastic polyurethane^[19], epoxy-alumina^[36], and epoxy-GPS alumina^[36] hybrid composites.

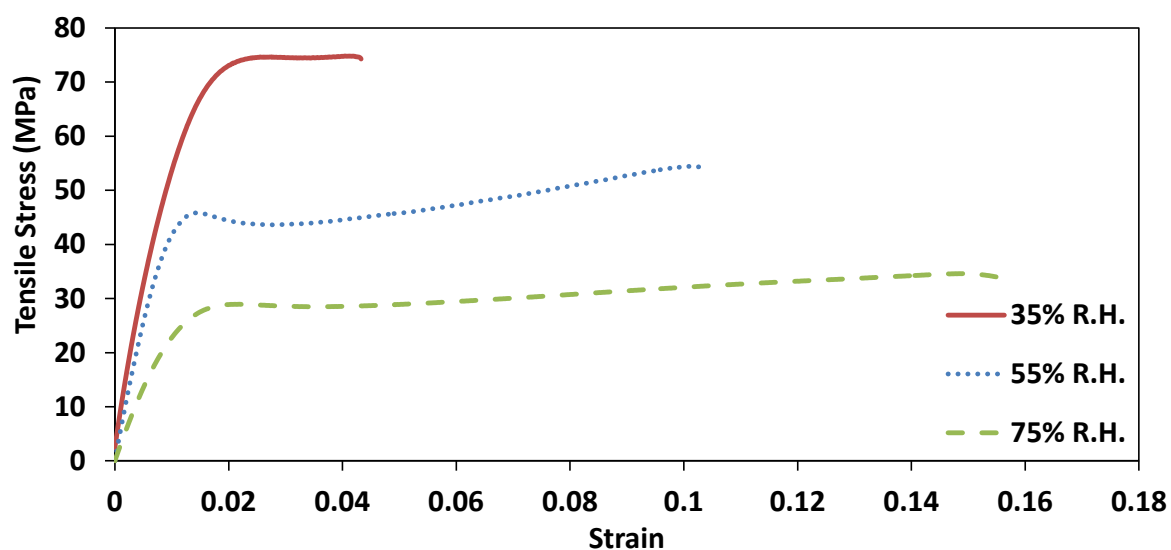


Figure 7 - Tensile stress versus strain of 10% V.F. alumina-chitosan films conditioned and tested at three different relative humidities.

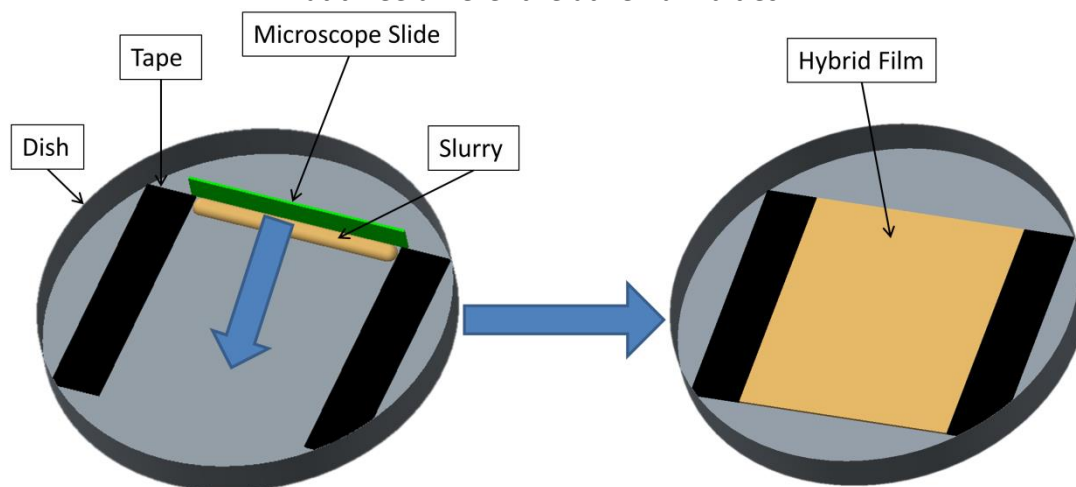


Figure 8 - Preparation of hybrid thin films using a slip casting method.

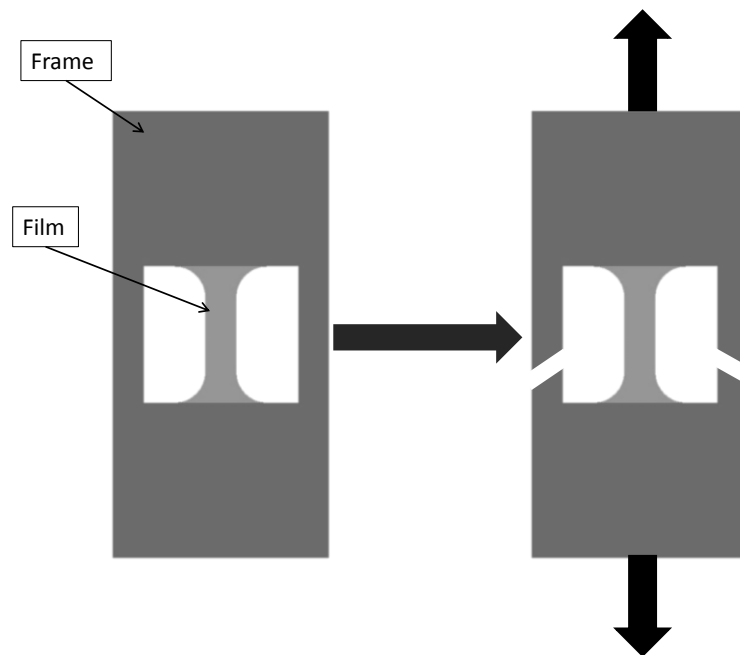


Figure 9 - Frame for tensile testing

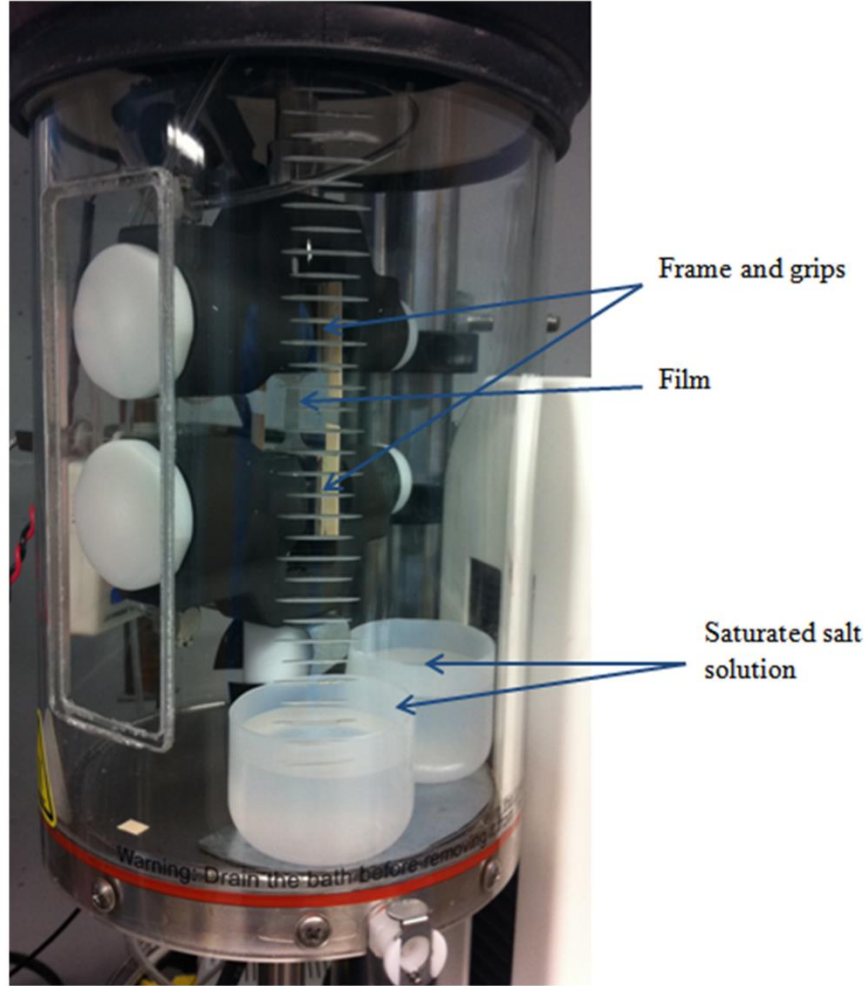


Figure 10 - Setup for tensile testing of chitosan films.

Table 1 - Mechanical properties of chitosan-alumina films at different relative humidities and platelet volume fractions.

Volume Fraction [%]	Relative Humidity [%]	Elastic Modulus [GPa]	Tensile Strength [MPa]	Strain at Failure [%]
0	35	3.66 ± 0.18	64.9 ± 5.04	4.6 ± 1.03
	55	2.77 ± 0.4	62.43 ± 3.03	12.3 ± 1.13
	75	1.9 ± 0.14	39.64 ± 1.62	19.85 ± 0.92
0.05	35	4.97 ± 0.42	74.42 ± 4.78	6.72 ± 0.79

	55	3.69 ± 0.29	65.64 ± 1.74	12.89 ± 0.51
	75	2.54 ± 0.28	44.55 ± 1.45	16.65 ± 1.48
<hr/>				
	35	5.54 ± 0.7	71.37 ± 6.27	4.98 ± 0.32
0.1	55	3.94 ± 0.24	58.86 ± 2.05	10.12 ± 1.29
	75	3.15 ± 0.17	38.54 ± 1.76	13.86 ± 0.96
<hr/>				
	35	7.18 ± 0.63	59.71 ± 4.03	2.66 ± 0.22
0.15	55	5.29 ± 0.4	45.83 ± 3.2	6.92 ± 0.5
	75	4.06 ± 0.4	37.32 ± 0.93	10.95 ± 0.66
<hr/>				

Appendix G: Spherical Nanoindentation Protocols for Extracting Micro-scale Mechanical Properties in Viscoelastic Materials

Mohammed T. Abba, Surya R. Kalidindi

George W. Woodruff School of Mechanical Engineering, Georgia Institute of Technology, Atlanta, Georgia, GA, USA

Introduction

Extensive advances in imaging and property measurement techniques, at the micro-scale, over the past few decades have allowed researchers to gain new insights into the mechanics of engineering materials, biological materials, and advanced composites. In the design of many advanced composite materials, the goal is to fabricate lightweight, strong, and tough materials, generally by reinforcing soft materials such as polymers. Composites are very popular in biomedical applications where they are used for bone replacements, cartilage replacement, bone cement, screws and many other applications [1]. There has been recent interest in the application of biological principles in the design of stronger, tougher, and “greener” materials [2-5]. Several studies fabricate materials with properties that match or are even stronger and tougher than certain natural material [4-11].

There is considerable ongoing research into how such composites achieve better properties than their individual constituents display on their own. To investigate this property amplification we have to understand the mechanical properties at the scale in which the separate constituents interact and not just at the macro-scale where the average property of the composite is defined. Successful application of devices at small length scales can only be guaranteed if their local mechanical properties are known. To understand the deformation behavior of materials requires knowledge of the local stress-strain behavior of individual microstructural phases and constituents. While there are tools to characterize mechanical response of materials at such scales [12-15], multiple data analysis procedures and assumptions lead to very different results even on the same materials.

One method that has been successfully applied to characterize mechanical properties of hard materials is nanoindentation. Nanoindentation has a high load resolution, depth sensing capabilities, and can be used to characterize the local mechanical behavior in material systems with heterogeneous microstructures. Indentation data analysis methods recently developed by our research group have demonstrated a great potential to transform the raw load-displacement data obtained using spherical indenters into indentation stress-strain curves [16]. These protocols have been able to capture the local loading and unloading elastic moduli, the local indentation yield strengths, and some post-yield behavior in some samples [17, 18]. The protocols have been used to critically evaluate the validity of different definitions of indentation strain and contact radius by using finite element models [19]. By recovering indentation stress-strain curves from the measured indentation load-displacement data we can get a more reliable comparison of material behavior between different samples even before recovering uniaxial mechanical

properties. These protocols have been shown to be sufficient for materials that do not experience significant time-dependent deformation.

To be able to apply this to polymer composites or hybrids that contain soft constituents, we have to first develop analysis techniques that will work for materials that exhibit viscoelasticity. Current methods that are used for viscoelastic materials are usually applied after the material has experienced some significant deformation. This does not give an accurate representation of the material properties of the undeformed sample. This study develops analysis protocols to extract stress-strain curves and viscoelastic properties from the load-displacement data generated from nanoindentation on time-dependent materials, at room temperature, from the initial loading segment. Once these protocols are developed they can then be applied, in the future, to study viscoelastic and viscoplastic properties of the constituents of composite material systems. We plan to demonstrate the validity of these new protocols through selected case studies on a range of materials including polymers, polymer blends, and a biopolymer used in novel hybrid thin films with highly aligned microstructures that our group has recently fabricated to mimic natural materials.

Viscoelastic Nanoindentation Protocol

While the focus of most elastic-plastic nanoindentation tests is to extract the modulus, hardness, or a stress-strain curve, the focus of viscoelastic tests is to extract the creep compliance, relaxation modulus, or storage and loss moduli. The objective of this work is to give any researcher a protocol to extract stress-strain curves from load-displacement curves from nanoindentation on viscoelastic materials. The protocol shall be laid out in steps, starting with an understanding of the material behavior, performing the indentation tests, and finally analyzing the data obtained.

Step 1: Material Viscoelasticity

The first step is to determine if the material has a big enough viscous component to affect its deformation behavior. The best example of this is if the material produces different load-displacement curves in the elastic or viscoelastic portion when different deformation rates are applied. This can be illustrated by performing indentation simulations on a viscoelastic material at different loading rates and comparing against an elastic material. The viscoelastic material properties used for the simulation were obtained from experiments done by Huang and Lu [20] on polymethyl methacrylate (PMMA) in terms of a two term Prony series representation. The elastic material properties were considered as just the steady state stiffness. A 13.5 μm radius indenter was indented into the material to a depth of 1 nm at 10^{-3} $\mu\text{m/s}$, 10^{-3} $\mu\text{m/s}$, and 10^{-3} $\mu\text{m/s}$. As can be seen from Figure 1, the material produces different responses as the displacement rate is reduced. At very high displacement rates, the response is the same as the elastic case. This is because the time it takes to reach the specified displacement is lower than the material's time constants thus not giving the material enough time to relax. This rate dependence is also shown experimentally when PMMA, polycarbonate (PC) and low-density polyethylene (LDPE) are indented at strain rates of 0.05 s^{-1} and 0.5 s^{-1} as shown in Figure 2 and Figure 3. From these

curves it is clear that LDPE and PMMA exhibit more viscoelasticity than PC. This means that while viscoelasticity may be negligible in models for PC, it cannot be ignored for PMMA or LDPE.

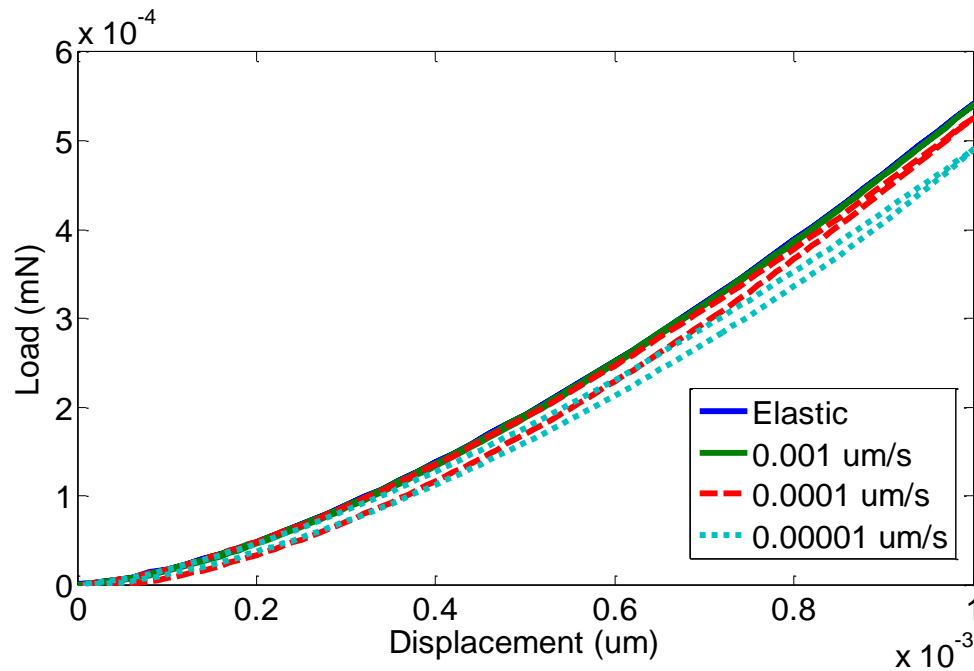


Figure 1 - FEM simulation on PMMA at different displacement rates

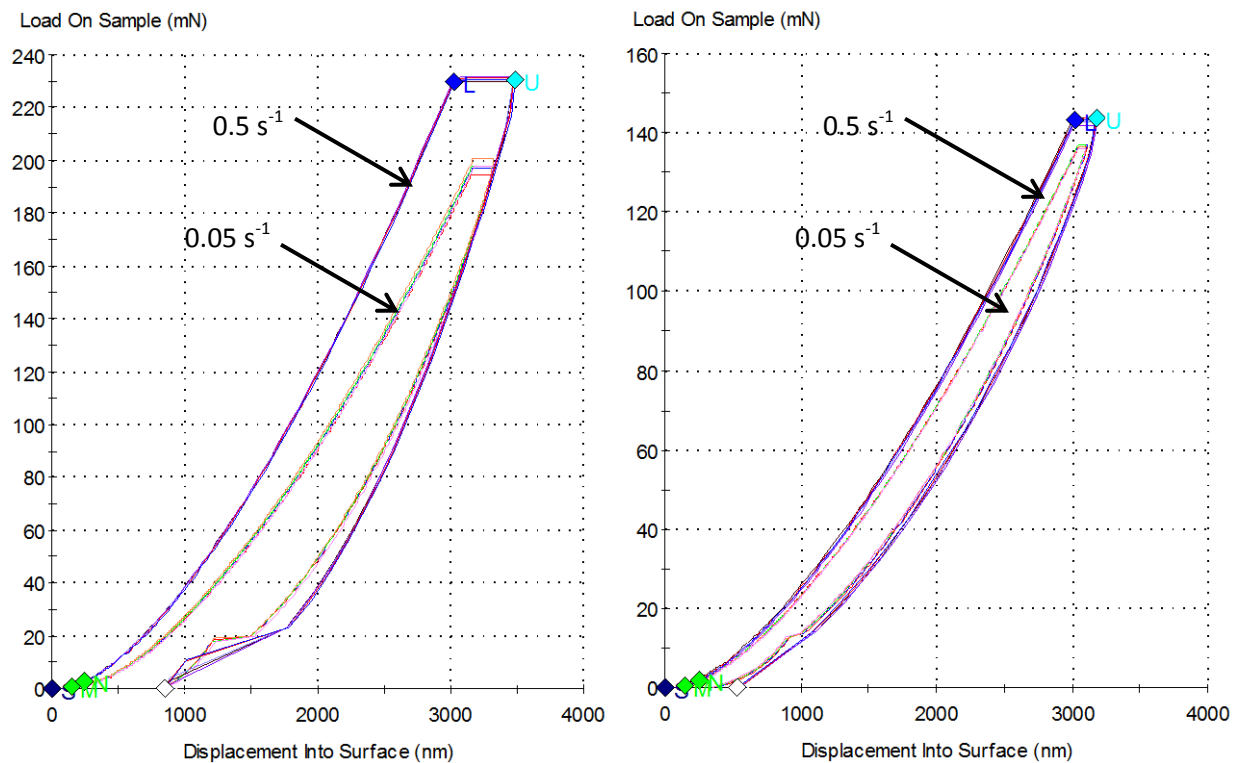


Figure 2 - Load-displacement curves of (a) PMMA and (b) PC at two different strain rates

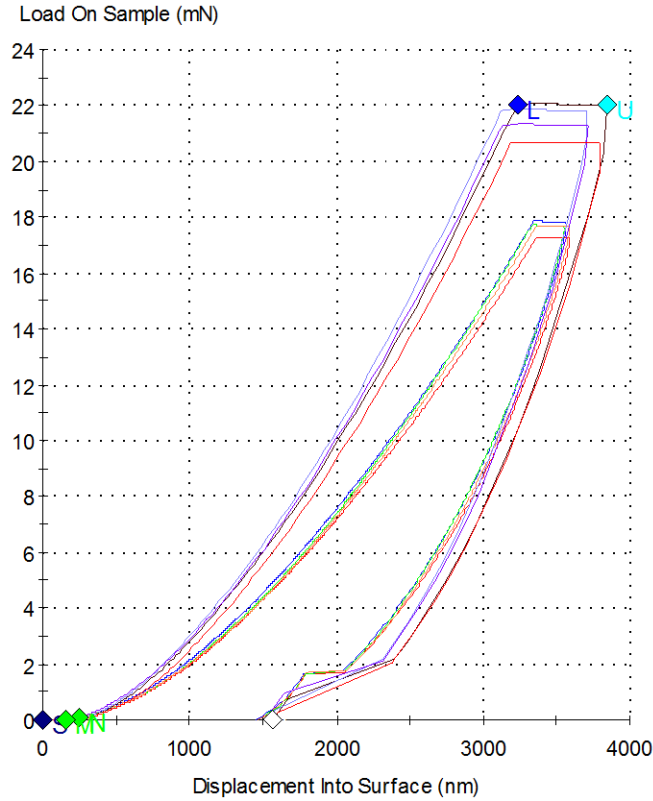


Figure 3 - Load displacement curves of LDPE at two different strain rates.

Another example of determining viscoelasticity is to perform a creep or relaxation test. The relaxation test can be performed by ramping to a specific displacement and holding the displacement for some time. For a viscoelastic material, load will decrease over the hold time. The creep test is performed by ramping to a specific load and holding the load for some time. For a viscoelastic material, displacement will increase over the hold time. Creep tests were performed on PMMA, PC, and LDPE by ramping to a specific load in 5 seconds, holding that load for 300 seconds, and then unloading in 5 seconds. The results are plotted in **Figure 4** and **Figure 5**. Displacement increases by about 100 nm for PMMA, 20 nm for PC, and 200 nm for LDPE. These results verify how viscoelastic each material is as seen in the load-displacement curves at different rates.

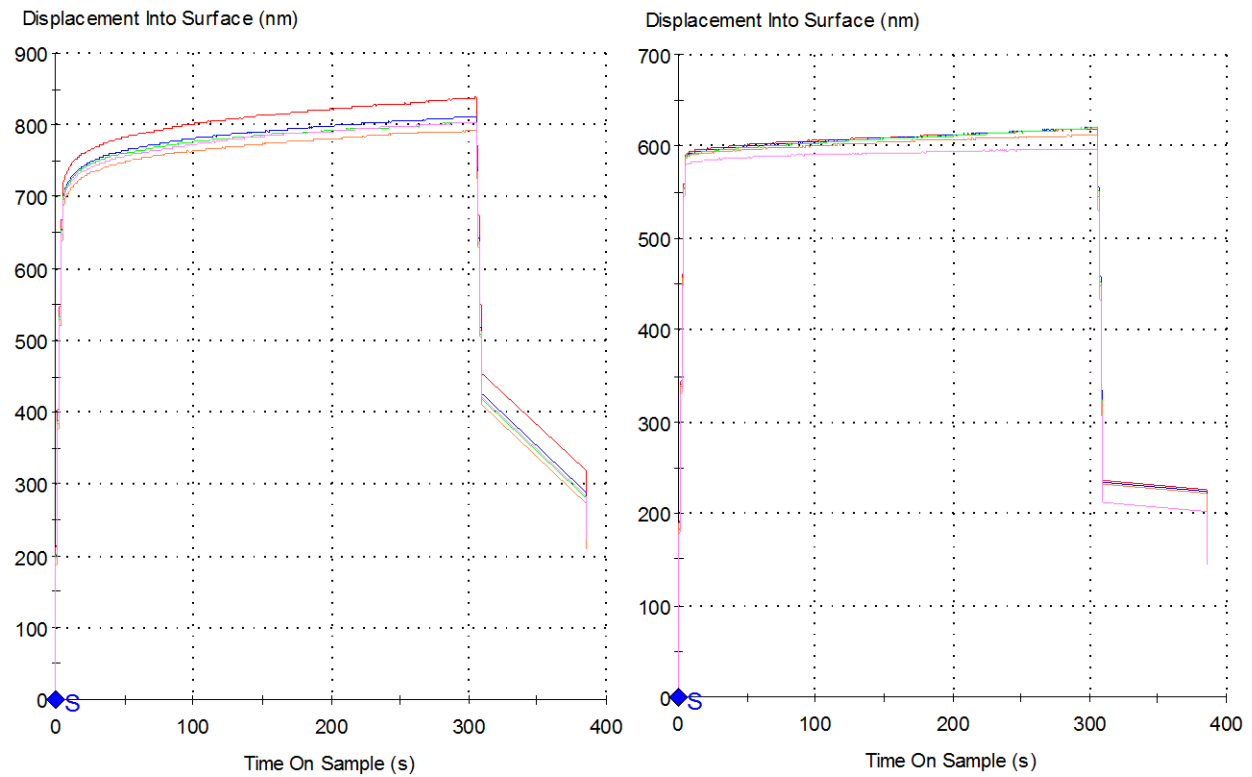


Figure 4 - Displacement vs time for creep tests performed on (a) PMMA and (b) PC.

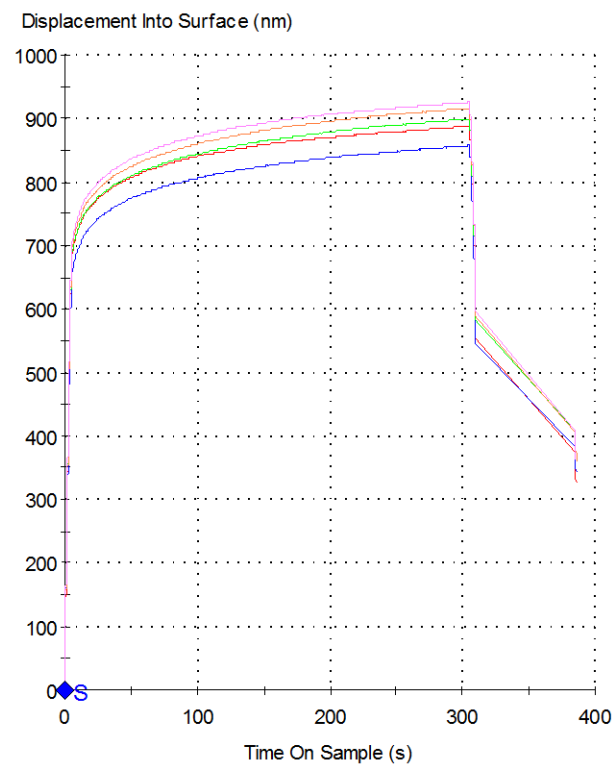


Figure 5 - Displacement vs time for creep tests performed on LDPE.

Step 2: Initiation of Plastic Deformation

The next step is to determine when the region being indented is no longer in the linear viscoelastic regime and starts experiencing plasticity. This is just an approximation to make sure that the zero point correction and viscoelastic properties are extracted within the linear viscoelastic region of the load-displacement curve. This can be determined by performing cyclic indentation on the material and observing the change in the load-displacement curves at each cycle. Since these are viscoelastic materials, hysteresis loops will be observed in the linear viscoelastic region which does not necessarily mean the material has experienced viscoelasticity. The goal is to observe where the unloading portion of the loop ends at a significant distance from the beginning of the loading curve. This suggests that the material is unable to return to its original position and has experienced plastic deformation.

Step 3: Indentation Tests

With an understanding of how much load should be applied, the indentation test can be performed to collect data that can be converted to stress-strain curves. The nanoindentation tests were performed on an Agilent Nano Indenter G200 with an XP head. The indenter can reach a maximum load of 500 mN and a maximum indentation depth of 500 μm with a load resolution of 50 nN and a displacement resolution of 0.2 nm. All tests were performed with diamond tipped spherical indenters. Important signals collected during the test are the displacement, load, and stiffness signals. For the CSM option, a target frequency and harmonic displacement is provided to the indenter as inputs and the indenter varies the harmonic load to achieve the required harmonic displacement. The indentations were performed as either a constant load rate test, a ramp and hold test, or a constant strain rate test as defined by the indentation machine. The constant strain rate as defined by the machine is achieved by setting the load rate divided by the load as a constant.

Step 4: Zero Point Correction

Once the data is collected the next step is to make sure that the initial portion of the load-displacement curve is corrected for the zero-point. The zero-point correction for the elastic nanoindentation case as explained in our previous work [16] can only be performed because Hertz's model can be rearranged in terms of the available signals; load, displacement, and contact stiffness. In the viscoelastic nanoindentation case, due to the convolution integrals in the equations, this cannot be done without extracting the creep compliance or relaxation modulus first, as shown by Cheng and Cheng [21]. Since in the experiments the stiffness is obtained from the small unloads performed by the CSM module, the viscoelastic response of these unloads would depend on the frequency applied. As shown in step 1, at faster rates the material starts responding like an elastic material. This means that at higher frequencies the CSM unloads can be thought of as being elastic. This can only be applied to the oscillations applied by the CSM module and not to the monotonic loading applied by the nanoindenter head itself. This can be visualized by performing FEM simulations at different frequencies and comparing the phase angle between the applied displacement and measured load. The results of these simulations on a

low-density polyethylene (LDPE) model are shown in Figure 6. These results show that increasing the frequency reduces the viscous response of the material. Since the zero-point correction is done on the first few nanometers of the data which can be considered elastic, the procedure described in [16] can be used to obtain the zero-point correction for viscoelastic materials.

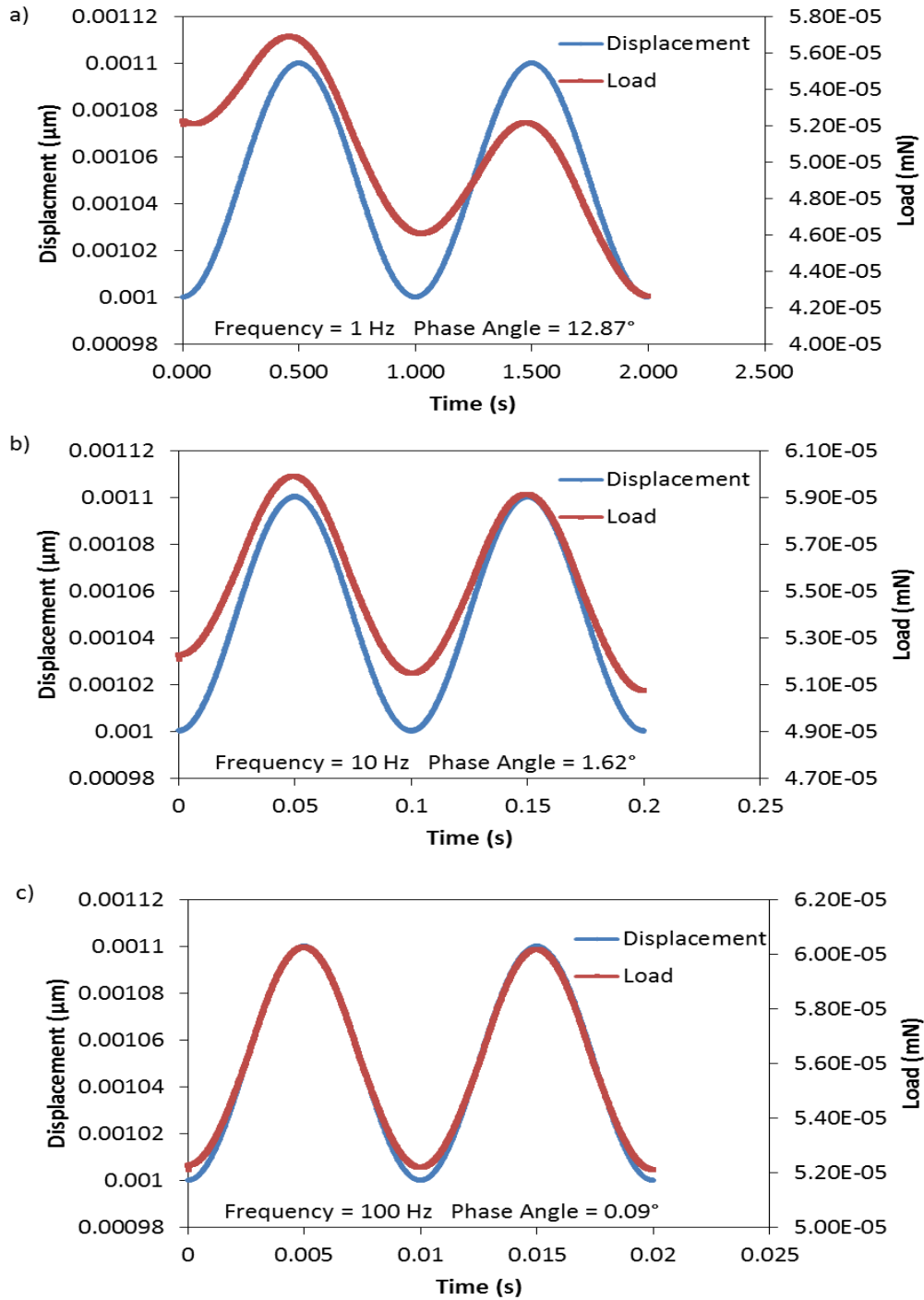


Figure 6 - FEM simulations of LDPE at different frequencies.

Step 5: Extract Viscoelastic Property

Now that the data has been corrected, the next step is to extract the material's viscoelastic property from the loading portion of the curve or from the ramp and hold tests. To extract the properties from the loading portion, a discrete deconvolution procedure can be used on the constitutive relationships for viscoelasticity:

$$P(t) = \frac{4\sqrt{R}}{3(1-\nu^2)} \int_0^t E(t-\tau) \frac{dh^{3/2}(\tau)}{d\tau} d\tau \quad (1)$$

$$h^{3/2}(t) = \frac{3(1-\nu)}{8\sqrt{R}} \int_0^t J(t-\tau) \frac{dP(\tau)}{d\tau} d\tau \quad (2)$$

where h , P , ν , R , E , and J are displacement, load, sample Poisson's ratio, indenter radius, sample relaxation modulus, and sample creep compliance. The unknown in this case is either the relaxation modulus or the creep compliance with the indentation either load controlled or displacement controlled. The output is then represented by the load as P or the displacement as $h^{3/2}$. Since the input and output is recorded by a discrete signal, noise and other perturbations will affect the solution obtained after approximation. This can be represented by the condition number of the input matrix, which measures how much the output will change for a small change in the input. A high condition number means the problem is ill-conditioned and small error in the output can cause a large error in the solution obtained. Whereas a low condition number means the error in the solution will not be much larger than the error in output [22]. We have found that the lowest condition number is obtained when the indentation input is a constant load rate, $dP/dt = \text{constant}$, giving us a good solution for the creep compliance. Once a solution is obtained as a discrete signal, it can be fit to a Prony series to be used in finite element analyses.

To extract from a ramp and hold test, the method presented by Oyen [23] can be used. The loading conditions can be written as:

$$\begin{aligned} P(t) &= kt & 0 \leq t \leq t_r \\ P(t) &= kt_r & t \geq t_r \end{aligned} \quad (3)$$

where t_r is the time it takes to reach the maximum load and k is the loading rate. This means that the viscoelastic equation for creep (equation (2)) must be solved twice, once for the ramp and again for the hold:

$$\begin{aligned} h^{3/2}(t) &= \frac{3(1-\nu)}{8\sqrt{R}} \int_0^t J(t-\tau) k d\tau & 0 \leq t \leq t_r \\ h^{3/2}(t) &= \frac{3(1-\nu)}{8\sqrt{R}} \int_0^{t_r} J(t-\tau) k d\tau & t \geq t_r \end{aligned} \quad (4)$$

If a Prony series representation of the creep compliance is used and the integrals are solved, we get:

$$\begin{aligned}
h^{3/2}(t) &= \frac{3(1-\nu)k}{8\sqrt{R}} \left[J_{\infty}t - \sum_{i=1}^N J_i\tau_i(1 - e^{-t/\tau_i}) \right] & 0 \leq t \leq t_r \\
h^{3/2}(t) &= \frac{3(1-\nu)k}{8\sqrt{R}} \left[J_{\infty}t_r - \sum_{i=1}^N J_i\tau_i e^{-t/\tau_i} (e^{-t_r/\tau_i} - 1) \right] & t \geq t_r
\end{aligned} \tag{5}$$

The hold portion of the nanoindentation test can then be fit to equation (5) to extract the constant terms and get the creep compliance function. This method takes into account the ramping it takes to achieve the holding load rather than assuming it is fast enough to be negligible.

3.6. Step 6: Extract Stress-Strain Curves

With the zero-point corrected for and the viscoelastic property extracted, the stress-strain curves can now be recovered from the load-displacement data. The indentation stress can simply be cast as load applied over the indentation contact area:

$$\sigma_{ind}(t) = \frac{P(t)}{\pi a(t)^2} \tag{6}$$

with the contact radius defined by Hertz's theory as:

$$a(t) = \sqrt{R_{eff}h(t)} \tag{7}$$

where R_{eff} is the effective radius of curvature of the combined indenter and sample system in contact, defined as:

$$\frac{1}{R_{eff}} = \frac{1}{R_s} + \frac{1}{R_i} \tag{8}$$

where the subscripts s and i refer to the sample and indenter respectively. Due to the confined area that the deformed region is in and the heterogeneous nature of the stress applied on it, an accurate definition of indentation strain is harder to define. One option is to use the viscoelastic stress-strain constitutive relationship:

$$\varepsilon_{ind}(t) = \int_0^t J(t-\tau) \frac{d\sigma_{ind}(\tau)}{d\tau} d\tau \tag{9}$$

Since the results are in discrete form and not a function, differentiation and integration induces significant errors on the final result. While this method may be used, it does not give reliable results for noisy data. Another option is to use the definition of strain defined in our previous work [16]:

$$\varepsilon_{ind} = \frac{4}{3\pi} \frac{h_t}{a} \approx \frac{h_t}{2.4a} \quad (10)$$

This definition of strain is idealizing the primary zone of indentation as a cylinder of radius a and length $2.4a$ which is compressed by the total indentation depth h_t . This definition was validated using both numerical simulations and experimental measurements [16, 17, 19, 24]. The next step in this study is to confirm this definition of strain for viscoelastic materials and produce stress-strain curves.

Bibliography

- [1] Ramakrishna, S., et al., *Biomedical applications of polymer-composite materials: a review*. Composites Science and Technology, 2001. **61**(9): p. 1189-1224.
- [2] Munch, E., et al., *Tough, Bio-Inspired Hybrid Materials*. Science, 2008. **322**(5907): p. 1516-1520.
- [3] Walther, A., et al., *Large-area, lightweight and thick biomimetic composites with superior material properties via fast, economic, and green pathways*. Nano Lett, 2010. **10**(8): p. 2742-8.
- [4] Bonderer, L.J., A.R. Studart, and L.J. Gauckler, *Bioinspired Design and Assembly of Platelet Reinforced Polymer Films*. Science, 2008. **319**(5866): p. 1069-1073.
- [5] Bonderer, L.J., et al., *Strong and ductile platelet-reinforced polymer films inspired by nature: Microstructure and mechanical properties*. Journal of Materials Research, 2009. **24**(9): p. 2741-2754.
- [6] Podsiadlo, P., et al., *Ultrastrong and Stiff Layered Polymer Nanocomposites*. Science, 2007. **318**(5847): p. 80-83.
- [7] Wegst, U.G.K., et al., *Biomaterials by freeze casting*. Philosophical Transactions of the Royal Society a-Mathematical Physical and Engineering Sciences, 2010. **368**(1917): p. 2099-2121.
- [8] Ebina, T. and F. Mizukami, *Flexible transparent clay films with heat-resistant and high gas-barrier properties*. Advanced Materials, 2007. **19**(18): p. 2450-+.
- [9] Malwitz, M.M., et al., *Layered structures of shear-oriented and multilayered PEO/silicate nanocomposite films*. Physical Chemistry Chemical Physics, 2004. **6**(11): p. 2977-2982.
- [10] Deville, S., et al., *Freezing as a path to build complex composites*. Science, 2006. **311**(5760): p. 515-518.
- [11] Dunlop, J.W.C. and P. Fratzl, *Biological Composites*, in *Annual Review of Materials Research, Vol 40*, D.R. Clarke, M. Ruhle, and F. Zok, Editors. 2010, Annual Reviews: Palo Alto. p. 1-24.
- [12] Haque, M.A. and M.T.A. Saif, *A review of MEMS-based microscale and nanoscale tensile and bending testing*. Experimental Mechanics, 2003. **43**(3): p. 248-255.
- [13] Bhushan, B., *Nano- to microscale wear and mechanical characterization using scanning probe microscopy*. Wear, 2001. **251**(1-12): p. 1105-1123.
- [14] Hemker, K.J. and W.N. Sharpe, *Microscale characterization of mechanical properties*, in *Annual Review of Materials Research*. 2007, Annual Reviews: Palo Alto. p. 93-126.
- [15] Fischer-Cripps, A.C., *Nanoindentation*. Mechanical Engineering Series, ed. F.F. Ling. 2002, New York: Springer.
- [16] Kalidindi, S.R. and S. Pathak, *Determination of the effective zero-point and the extraction of spherical nanoindentation stress-strain curves*. Acta Materialia, 2008. **56**(14): p. 3523-3532.
- [17] Pathak, S., et al., *Analyzing indentation stress-strain response of LaGaO₃ single crystals using spherical indenters*. Journal of the European Ceramic Society, 2008. **28**(11): p. 2213-2220.
- [18] Pathak, S., D. Stojakovic, and S.R. Kalidindi, *Measurement of the local mechanical properties in polycrystalline samples using spherical nanoindentation and orientation imaging microscopy*. Acta Materialia, 2009. **57**(Copyright 2009, The Institution of Engineering and Technology): p. 3020-8.

- [19] Donohue, B.R., A. Ambrus, and S.R. Kalidindi, *Critical evaluation of the indentation data analyses methods for the extraction of isotropic uniaxial mechanical properties using finite element models*. Acta Materialia, 2012. **60**(9): p. 3943-3952.
- [20] Huang, G. and H. Lu, *Measurement of Young's relaxation modulus using nanoindentation*. Mechanics of Time-Dependent Materials, 2006. **10**(3): p. 229-243.
- [21] Cheng, Y.-T. and C.-M. Cheng, *Relationships between initial unloading slope, contact depth, and mechanical properties for spherical indentation in linear viscoelastic solids*. Materials Science and Engineering: A, 2005. **409**(1-2): p. 93-99.
- [22] Kreyszig, E., *Advanced Engineering Mathematics*. 2010: John Wiley & Sons.
- [23] Oyen, M.L., *Spherical indentation creep following ramp loading*. Journal of Materials Research, 2005. **20**(08): p. 2094-2100.
- [24] Pathak, S., D. Stojakovic, and S.R. Kalidindi, *Measurement of the local mechanical properties in polycrystalline samples using spherical nanoindentation and orientation imaging microscopy*. Acta Materialia, 2009. **57**(10): p. 3020-3028.

Appendix H: Lamellar level correlations between mechanical behavior and composition in mouse bone

Vachhani, Shraddha J.^a, Pathak, Siddhartha^b, Burr, Thomas^c, Jepsen, Karl^d, Kalidindi, Surya R.^e and Goldman, Haviva M.^{f*}

^aMaterial Science and Technology, Los Alamos National Laboratory, Los Alamos, NM 87545, USA

^bCenter for Integrated Nanotechnologies, Los Alamos National Laboratory, Los Alamos, NM 87545, USA

^cStatistical Sciences, Los Alamos National Laboratory, Los Alamos, NM 87545, USA

^dDepartment of Orthopedic Surgery, University of Michigan, Ann Arbor, MI 48104, USA

^eGeorge W. Woodruff School of Mechanical Engineering, Georgia Institute of Technology, Atlanta, GA 30332, USA

^fNeurobiology and Anatomy, Drexel University College of Medicine, Philadelphia, PA 19129, USA

Abstract

We tested whether two inbred strains of mice – with known differences in the average mineralization of their long bones – also show differences in how their extracellular matrix is deposited and mineralized. Using the combined capabilities of Raman spectroscopy and spherical nanoindentation stress-strain analysis we further studied the lamellar level correlations between the local composition and local mechanical properties in these mouse bone. We utilized a total of 11 samples from two different inbred mouse strains at 16 weeks of age, A/J and C57BL/6J (B6). The local elastic moduli (E_s) and indentation yield strengths (Y_{ind}) were determined from spherical indentation stress-strain analysis, while Raman spectroscopy was used to determine the local composition around the indents in terms of the phosphate-to-CH₂ wag ratio, phosphate-to-Amide I ratio, phosphate-to-monohydrogen phosphate ratio and phosphate-to-carbonate ratio. In both mouse strains, Raman spectroscopy measurements showed that the new bone close to the bone-edge had a lower mineral-to-matrix (phosphate-to-CH₂ wag) ratio, lower mineral maturity (phosphate-to-monohydrogen phosphate ratio) and higher degree of carbonate substitution (phosphate-to-carbonate ratio) in the mineral. There was a significant difference in the mineral-to-matrix ratio of the two strains of mice, with the A/J mice showing an overall higher mineral-to-matrix ratio and lower carbonate substitution in the mineral. While

newer bone appeared to show evidence of difference in the mineral-to-matrix ratio ($p < 0.03$) between the mouse strains, the differences in composition appear to be far less significant as the bones matured ($p > 0.05$). Local mineral-to-matrix ratio appears to be a good indicator of the local mechanical properties and correlated well with the elastic modulus ($r^2 = 0.82$) and indentation yield strength ($r^2 = 0.53$). Other compositional aspects such as mineral maturity and carbonate substitutions did not significantly influence local mechanical properties. Intra-strain differences in both bone composition and relationship between composition and local mechanical properties were found to be statistically insignificant.

Introduction

Our ability to reliably predict the mechanical performance of bone is largely hampered by an inadequate knowledge of how bone's mechanical properties relate to the complex details of its internal hierarchical structure. Moreover details of bone's matrix level organization (at length scales on the order of $1\mu\text{m}$ and below, including details of collagen fibril and mineral crystal organization) have traditionally been difficult to characterize, as bone's mineral and collagen components are closely intertwined. The use of spectroscopic techniques such as Raman spectroscopy [1-3] and Fourier Transform Infrared Microspectroscopy (FTIR) [4-7] have shown considerable promise in quantifying bone's composition at this length scale. Examples include relating the mineral and collagen compositions measured using Raman and FTIR as a function of anatomical location [7] in both normal and diseased bone [4, 8-10]. These characterization studies are often carried out in conjunction with nanoindentation to measure local tissue-level properties [11-16]. However, despite the popularity of nanoindentation testing on bone [17], many of the assumptions and limitations inherent in current nanoindentation methodologies have limited the potential of the technique for elucidating quantitative structure-property relationships in bone [18]. In this paper, we utilize our novel data analysis protocols for spherical nanoindentation in combination with Raman spectroscopy to quantify the correlations between the lamellar level composition in bone and its local mechanical behavior in two strains of genetically inbred mice

The two mouse strains utilized in this study, A/J and C57BL/6J (B6), represent an important genetic tool for studying the local mechanical properties of bone [19-20]. The two inbred mouse strains selected for this study have the added advantage of their known inter-strain variability [21] and whole bone biomechanical properties [22]. In particular, the A/J and B6 strains have been shown to significantly differ in their matrix mineralization and whole bone brittleness [23]. For example, the bones of the A/J strain have been shown to have a higher ash content than those from the B6 strain [22]. Similarly whole bone mechanical tests have demonstrated a higher yield point and a more brittle post-yield behavior [21-23] for the A/J mice, although both strains recorded similar stiffness values. Other studies have also provided a detailed knowledge of the growth patterns in these mouse strains [23], which allow us to readily select specific areas of the bone cortex representing regions of older and newer bone deposition.

In this work we utilize a novel protocol for analyzing the local mechanical behavior in mouse bone using spherical nanoindentation. This technique uses our newly developed data analysis procedures to transform the entire load-displacement dataset, including both the loading and the unloading segments, into much more meaningful indentation stress-strain [24-26] curves. The use of these indentation stress-strain curves makes it possible to analyze the initial loading segments of spherical indentation, thereby allowing us to obtain measures of elastic modulus and indentation yield strength of the material prior to the damage introduced by the indentation itself. This is in contrast to most of nanoindentation studies conducted on bone which employ sharp indenters such as Berkovich and cube corner tips [18, 27-30] to estimate the modulus and hardness from the unloading segments of load-displacement curves of these tests [31-32]. Unfortunately, property estimates from the unloading segments often reflect values which have been changed by the experiment itself, due to the additional local plastic deformation imposed by the indenter. Thus many of these studies have shown mixed results, with some showing support for relationships between local properties and variables affecting tissue composition (e.g., [11-13, 16]), and others not supporting any such correlations [14]. On the other hand, indentation stress-strain curves have been successfully used to capture a wealth of information about the material including the elastic moduli measured in loading and unloading segments [24-25, 33-34], the elastic limit (which can be identified as yielding in metallic samples [34-35] or buckling in high aspect ratio materials such as vertically aligned carbon nanotube forests [36]), and aspects of the post-elastic behavior [34-35].

The ability to use the indentation stress-strain approach on bone was examined in a previous report [40]. In Ref. [40] a small sample size (2 samples per strain) of A/J and B6 mice were studied to show that bone with a higher mineral-to-matrix ratio (measured using Raman spectroscopy) had higher elastic modulus, E_s , and indentation yield strength, Y_{ind} (measured from spherical nanoindentation stress-strain analysis), suggesting that the newer bone regions in these mice exhibited lower moduli and yield strengths compared to the more mature bone. The B6 mice were also found to exhibit lower modulus and yield strength values compared to the more mineralized A/J strain. These results complemented another study on the local viscoelastic behavior observed in the same general locations of the above two mouse strains [41]. In this case dynamic nanoindentation techniques were used on hydrated femur bone tissues of A/J and B6 to demonstrate a trend towards a higher viscoelastic response in newer bone, while the response

was also greater for the B6 samples as compared to A/J. This suggests that bone having a lower mineral-to-matrix ratio (i.e., a higher collagen content) would demonstrate a trend towards a larger viscoelastic response, along with a lower stiffness and yield behavior.

Building upon these previous studies on the two mouse strains, in this work, we use a larger dataset to further the understanding of tissue level differences in composition and local mechanical properties of these two strains. Specifically, the first aim of this current study is to determine if there exists a statistically significant difference in the composition of the bone (as determined by Raman spectroscopy) and if so, do these differences originate as the bone was being laid down or do they develop at a later stage as the bone matures. Further, we investigate whether the higher ash content values previously identified in the A/J bones are reflected in a higher average mineral-to-matrix ratio (as determined by Raman Spectroscopy). The second aim of this study is to assess the correlations between the localized differences in the composition (mineral-to-matrix ratio, mineral maturation and collagen cross-linking) at the depositional surfaces of the femoral cortex to the localized variation in indentation elastic behavior and indentation yield strength.

Materials and Methods

Sample preparation

Eleven dry dehydrated mouse femora were used in this study. Femora were obtained from A/J (5 individuals) and B6 (6 individuals) strains of genetically inbred mice at 16 weeks of age. A/J and B/6 mice were purchased from Jackson Laboratory (Bar Harbor, ME, USA) at 4–6 weeks of age, and housed at the animal care facility of the Mount Sinai School of Medicine. They were maintained on a 12-hour light:dark cycle, fed a standard mouse chow (Purina Laboratory Chow 5001; Purina Mills, St. Louis, MO, USA) and given water ad libitum. All mice were injected with a fluorochrome dye (Calcein, 10mg/kg) to label the mineralization fronts at 7 and 2 days prior to sacrifice. All mice were sacrificed at 16 weeks of age. The Mount Sinai Institutional Animal Care and Use Committee approved all procedures for the treatment of mice [21].

Right femora from A/J (5 individuals) and B6 (6 individuals) were harvested, cleaned of soft tissue and fixed in 70% ethanol, dehydrated in ascending grades of ethanol and embedded in

polymethylmethacrylate (PMMA). Tissue blocks were removed by sectioning the bone transversely just distal to the 3rd trochanter (Fig. 1a). The superior surface of each block was prepared for Raman Spectroscopy and nanoindentation testing by grinding with increasingly fine sand papers up to 1200 grit, and polishing by means of a series of napped cloth impregnated with diamond pastes, finishing with a grain size of 0.05 μ m. The samples were cleansed in a distilled water ultrasonic bath after each successive step. The above preparation procedure is summarized schematically in Figs. 1a and 1b.

Analyses were carried out at the 16 week time-point because by this age the mice have achieved their peak bone mass, inter-strain differences have already been established and slow, lamellar, bone growth characterizes the endosteal and periosteal formative surfaces [23]. We chose one of these sites (the Antero-Medial or AM cortex) for our study. The growth of the femora in these mouse strains up until this time is characterized by a pattern of cortical drift as illustrated in Fig. 1a [23, 42]. As seen in this figure, instead of a uniform expansion of the cortex around the periosteal or endosteal surfaces, bone formation and resorption take place as a coordinated process across different bone surfaces (see the regions marked in Fig. 1a). Thus at the AM cortex, the newest bone is present closest to the endosteal surface and tissue age progressively increases with the distance from the endocortical surface. Fig. 1 also shows the location of the bone section with respect to the femur length and the region of interest for performing the Raman spectroscopy and nanoindentation measurements.

Before proceeding with the analyses described below, selected polished, embedded blocks were first carbon coated and imaged using backscattered electron microscopy (BSEM) (following the methods of Goldman et al. [21]) with an Amray 1845 field emission scanning electron microscope (FE-SEM) with 4pi digital interface (SEMTECH, North Billerica, MA). The BSEM images are shown in this work for illustrative purposes only (Fig. 2).

Spherical Nanoindentation

The procedures and methodologies used for nanoindentation testing are explained in detail in our previous publication [40]; a brief summary of the same is presented below. The MTS nanoindenter XP® equipped with the continuous stiffness measurement (CSM) attachment was used to carry out the nanoindentation experiments. Indents were made using a spherical diamond

tip of 13.5 μm radius up to a nominal depth of 300 nm and then unloaded after a 10 sec hold at the maximum load. Three rows of 15 indents were made on each sample, starting from the endosteal surface of the AM cortex and proceeding radially inwards (Fig. 1a). This generated a total indentation dataset of 495 data points ($3 \times 15 \times 5$ individuals = 225 data points for A/J, and $3 \times 15 \times 6$ individuals = 270 data points for B6). Two neighboring indents were separated by 10 μm to avoid any proximity effects. Indents that landed on any pores, cracks etc. on the sample surface were not included in the data analysis.

The raw nanoindentation load-displacement data was converted into indentation stress-strain curves following the procedures described by Kalidindi and Pathak [24] (Fig. 1c). This procedure follows a two-step approach consisting of (i) the determination of an effective zero point followed by (ii) the calculation of the contact radius used for generating the indentation stress and indentation strain values. The aim of the first step is to determine the effective point of initial contact, i.e., a clear identification of a zero-point that makes the measurements in the initial elastic loading segment consistent with the predictions of Hertz's theory [43-44]. Typically the default protocols in the vendor-provided analyses software do not perform adequately in this respect, mostly resulting in the overestimation of the sample surface [24, 45-46]. The data analyses task is often made worse by surface roughness issues and the effects of the surface preparation techniques [47]. In this work, we calculate the load and displacement corrections (P^* and h^* respectively) by performing a linear regression analysis of the expected relationship between the measured load signal, \tilde{P} , the measured displacement signal, \tilde{h}_e , and the continuous stiffness measurement, S , in the initial elastic loading segment in the spherical indentation of a flat isotropic sample surface as given by Hertz theory [24]:

$$S = \frac{3P}{2h_e} = \frac{3(\tilde{P} - P^*)}{2(\tilde{h}_e - h^*)} \quad \dots(1)$$

In the second step, we recast Hertz's theory [43-44] in the following set of equations for frictionless, elastic, spherical indentation in order to calculate the contact radius (a) and indentation stress (σ_{ind}) and indentation strain (ε_{ind}) values:

$$\sigma_{ind} = E_{eff} \varepsilon_{ind}, \quad \sigma_{ind} = \frac{P}{\pi a^2}, \quad \varepsilon_{ind} = \frac{4}{3\pi} \frac{h_e}{a} \approx \frac{h_e}{2.4a},$$

$$a = \frac{S}{2E_{eff}}, \quad \frac{1}{E_{eff}} = \frac{1 - \nu_s^2}{E_s} + \frac{1 - \nu_i^2}{E_i}, \quad \frac{1}{R_{eff}} = \frac{1}{R_i} + \frac{1}{R_s}, \quad \dots(2)$$

where a is the radius of the contact boundary at the indentation load P , h_e is the elastic indentation depth, S is the elastic stiffness described earlier, R_{eff} and E_{eff} are the effective radius and the effective stiffness of the indenter and the specimen system, ν and E are the Poisson's ratio and the Young's modulus, and the subscripts s and i refer to the specimen and the indenter, respectively.

The sample elastic modulus (E_s) and the 0.2% offset strain indentation yield strength (Y_{ind}) values reported in this work were calculated using Eq. (2) from the initial loading segment of the indentation stress-strain data, as shown in Fig. 1c.

Raman Spectroscopy

The procedure detailed in [40] was followed in this work for measuring the Raman spectra. Each polished bone block surface was analyzed in a Renishaw 1000 Raman micro spectrometer. A semiconductor diode excitation laser operating at the near-IR, 'red' laser 785nm wavelength was used in order to eliminate the auto-florescence of the bone proteins [48], along with a 50x objective lens (NA = 0.75) with a laser spot size of $\sim 2 \mu\text{m}$. A Renishaw silicon piece was used for x-calibration of the wavenumbers of the Raman spectra with a sensitivity of less than 1 cm^{-1} . No laser spot was focused directly on top of an indent, in order to avoid loss of focus and to avoid scanning bone damaged by indentation stresses. Spectra were taken point by point in extended mode from 750 to 1800 cm^{-1} using a grating of 1200 l/mm with a 60 sec detector interrogation time for each scan. Raman mapping was conducted over a $70 \mu\text{m} \times 70 \mu\text{m}$ area (instrument limit) using the spherical indents as markers (Fig 1a). Note that the Raman grid had a finer spacing ($5 \mu\text{m}$) between adjacent mapping points (as compared to the $10 \mu\text{m}$ spacing between indents), and thus completely overlapped the spherical indents. The indents outside of the Raman mapped area were not considered in the correlation analysis. The Raman data set consisted of a total of 1320 data points, with 600 (=8 columns x 15 rows x 5 individuals) and 720

(=8 columns x 15 rows x 6 individuals) Raman data points collected for the A/J and B6 strains respectively. Of this, a total of 1238 Raman data points were used in the statistical analysis, the rest were excluded since they landed on PMMA (outside the bone).

All analyses were performed using the Wire 2.0 Software as described in [40]. A pre-processing step was used to easily distinguish and analyze the mineral vs. matrix data. Thus the spectra (Fig. 1d) were divided into different sub regions based on methods used by Timlin et al. [49]. The first region (750-1150 cm^{-1}) contained bands arising from vibrations of the mineral component of bone, and the second region (1170-1800 cm^{-1}) contained mostly bands from bone matrix. After separation into the two sub regions, mineral and matrix, the data was further analyzed to subtract the background fluorescence using a baseline curve fit.

The peak intensities of the recorded spectra were analyzed to obtain the compositional characteristics of bone [61]. Peak intensity of the phosphate (P, $\sim 959 \text{ cm}^{-1}$), carbonate (CO_3 , 1070 cm^{-1}), monohydrogen phosphate (MHP, $\sim 1003 \text{ cm}^{-1}$), Amide I ($1616\text{-}1720 \text{ cm}^{-1}$) and CH_2 wag (1450 cm^{-1}) bands were calculated following protocols described in our previous work [6, 40]. The phosphate-to-monohydrogen phosphate (P-MHP) intensity ratios were assessed as a measure of mineral maturity. Phosphate-to-carbonate peak intensity ratios (P- CO_3) were used to investigate substitutions in the lattice of apatite, providing a measure of mineral composition. The mineral-to-matrix ratio, which relates to bone mineralization density [50], was determined using the phosphate-to- CH_2 wag (P- CH_2 wag) peak intensity ratio. While both the P- CH_2 wag peak intensity ratio and the phosphate-to-Amide I (P-Amide I) band intensity ratio can be used to denote the mineral-to-matrix ratio, the former (the CH_2 wag band) was chosen for two reasons: (a) the CH_2 wag band was more prominent than the Amide I band in the Raman spectra, and (b) ethanol fixation methods have been known to alter the Amide I band intensity, while the CH_2 wag intensity band is minimally affected by ethanol fixation [51]. Though PMMA bands do overlap the CH_2 wag band, its effects were found to be negligible [40] and no extra processing steps were taken to eliminate the effects of PMMA on the spectra. For comparative purposes we also report P-Amide I data, but analyses were performed only on the P- CH_2 wag dataset.

The Raman peak intensity ratios were also used to ascertain the location of the bone edge on the Raman grid and hence accurately determine distances in the Raman map. For each row of

data in the scan, the PMMA-bone interface was determined as the position where a linear interpolation of the P-CH₂ wag ratio reached a critical value of 1. The cut off value of 1 was chosen by comparing optical images that had a clear and sharp PMMA-bone interface with the corresponding Raman maps. Note that the optical images alone could not be used for bone edge determination since in some of the images the PMMA-bone interface was not sharp and hence hard to determine accurately. The P-CH₂ wag ratio was selected as the metric since these ratios had consistently low values outside the bone and then increased rapidly away from the bone edge (from the newer bone to the older bone regions). Use of the P-Amide I ratios for determining the edge instead of the P-CH₂ wag did not alter the edge position appreciably.

Methods of Statistical Analysis

In order to determine whether bone composition significantly differs between the two mouse strains, four separate *t*-tests were performed on the four Raman peak intensity ratios discussed above (P-CH₂ wag, P-Amide I, P-CO₃ and P-MHP). Estimated probability density plots and normal probability plots were used to verify approximate normality [54]. The distributions of the Raman bone compositions in this work were found to be only mildly non-normal, so we rely on simple *t*-tests to judge statistical significance. We assessed the statistical significance using a per-test *p*-value of $\alpha = 0.05/(\text{number of } t\text{-tests} = 4) = 0.0125$ (using the simple Bonferroni correction to adjust for multiple testing [54]).

In order to analyze differences in composition relative to bone age, Raman compositional data were binned into three groups: a new bone region defined as a region within 10 μm from the bone endosteal edge and an older bone region for bone greater than 50 μm away from the edge. All bone in between was binned as being of intermediate age. Here, distance from the bone-edge in the Raman data is used as a surrogate for bone age. A smooth curve was then fitted to the scatter plot for each bin for composition vs. distance from the bone edge. Four separate *t*-tests for each bin, one for each of the ratios of interest determined from the Raman Spectroscopy data, were used to determine the statistical significance in the compositional differences between the two mouse strains as a function of bone age.

Correlations between the local mechanical behavior (E_s and Y_{ind}) and bone composition (P-CH₂ wag, P-Amide I, P-CO₃ and P-MHP peak intensity ratios) were also evaluated using multiple t-tests.

The Bayesian Information Criterion (BIC) was used to test whether there was any statistically significant difference in bone composition (and local composition - mechanical property relationship) between individuals of the same strain. The BIC ($BIC = MSE + n\log(p)$, where MSE is the mean squared error, n is the sample size, and p is the number of parameters) is a common method to select the number of parameters in a model, and is a residual sum of squares that includes a penalty term to guard against over-fitting that can occur when one is using too many parameters.

Results

Figure 1c shows a representative indentation load displacement dataset (inset) and the corresponding indentation stress-strain curves for A/J and B6 femurs. These tests were performed at similar distances (~30 μ m) from the endosteal edge of the bone, as described in the methodology section. Fig. 1d shows a typical Raman spectra obtained from one of the embedded bone blocks.

Figures 2a and 2b contrast representative BSEM images obtained from A/J and B6 Femur sections at 16 weeks of age, and demonstrate the location of our region of interest (near the endosteal edge of the AM cortex) for obtaining Raman and indentation maps. Representative Raman maps, detailing the different aspects of the local bone composition as a function of distance from the endosteal edge in the AM cortex are shown in Figs. 2c-2j for the mineral-to-matrix ratio, defined as the P-CH₂ wag peak intensity ratio (Figs 2c and 2d); the P-Amide I ratio, which is another measure of the mineral-to-matrix differences (Figs. 2e and 2f); the P-CO₃ ratio, which is a measure of the mineral composition (Figs. 2g and 2h), and representative P-MHP peak intensity ratios, which represents mineral maturity (Figs. 2i and 2j). .

The Raman data is plotted in Fig. 3, which shows the variation in the bone composition (P-CH₂ wag peak intensity ratio Fig. 3a, P-Amide I peak intensity ratio Fig. 3b, P-CO₃ peak intensity ratio Fig. 3c and P-MHP peak intensity ratio Fig. 3d) as a function of distance from the

endosteal edge for A/J (n=5) and B6 (n=6) mice. For clarity and better visualization, the data were grouped into bins of 1 μm , starting at 0 μm from the edge of the bone. The average and standard deviation values for each bin are used in the plots. Note that for the statistical analysis reported below, the unbinned data was used.

The following observations can be made from these Raman measurements: (a) both mouse strains showed lower values of mineral-to-matrix ratio in the bone tested closer to the depositional edge (Figs. 2c -2f, and 3a, 3b), (b) the mineral is less mature (Figs. 2i, 2j and 3d) and has a higher degree of carbonate substitution (Figs. 2g, 2h and 3c) close to the endosteal edge, and (c) at a similar distance from the endosteal edge of the bone the A/J mice showed higher values for the mineral-to-matrix ratio as well as bone maturity accompanied with lower degree of carbonate substitution in the mineral.

To determine whether the differences in the bone composition between the two mouse strains were statistically significant, four separate *t*-tests were performed on the four Raman peak intensity ratios (P-CH₂ wag, P-Amide I, P-CO₃ and P-MHP, see Fig. 3). Two approaches were used. In the first case, individual mouse ID's were ignored and all the measurements from within the same mouse strain were pooled together and *t*-tests were applied. This approach is justified by the BIC tests which suggested that including a factor for individual mouse effects did not significantly improve the fits and were therefore not needed. In other words, BIC tests conclude that there is no statistically significant difference in the composition within individuals of the same strain. For this approach, all Raman peak intensity ratios yielded *p*-values of less than 0.01.

The second approach to performing the *t*-tests was more rigorous and took into account the individual mouse ID's. The resulting *p*-values were 0.02 for P-CH₂ wag, less than 0.001 for P-Amide I, 0.01 for the P-CO₃, and 0.40 for P-MHP ratios. Our analyses therefore imply statistically significant differences in the P-Amide I (*p* < 0.001) and P-CO₃ (*p* < 0.01) peak intensity ratios between the two mouse strains. Also, no significant difference (*p* = 0.4) in the P-MHP ratio between the two mouse strains was observed. For the P-CH₂ wag ratio, there is evidence of a mild difference between the two mouse strains. However, when adjusted for multiple *t*-tests *p* = 0.02 is not statistically significant; for multiple *t*-tests statistical significance is indicated only when *p* < 0.0125 (= 0.05/(number of *t*-tests = 4) = 0.0125). This may be a result

of the sample sizes in our work and follow-up studies with larger sample sizes may be able to provide more insights into this.

The BIC test was also applied to determine if the difference in composition between the two mouse strains was significant. When individual mouse IDs were taken into account, the BIC also provided the same conclusions as the t-tests performed using the second approach. Once again, moderately small p-value for P-CH₂ wag of 0.02, very small p-value less than 0.0125 for P-Amide I, and P-CO₃ and a large p-value for P-MHP were observed.

One of the objectives of this work was to determine if these compositional differences originate as the bone was being laid down, or whether they develop at a later stage as the bone matures through the secondary mineralization phase. In order to test these two alternatives, we binned the Raman data into three groups based on the distance from the endosteal edge, as described in the previous section. This approach inherently assumes that the measured distance from the bone-edge in the Raman data is a suitable surrogate for bone age. Confocal imaging studies were used to validate this assumption. These images can monitor the growth rate of the femora by visualizing the calcein labels along the endosteal aspect of the AM cortex (details of the confocal study are not included here). Results from the confocal imaging data show that both the A/J and the B6 mice lay down bone at very similar rates. This indicates that the measured distance from the bone-edge in the Raman data is a suitable surrogate for bone age. Note that the Raman measurements were equally spaced in all femur samples and all scans were of uniform size; hence data from similar distances from the bone-edge correspond to bone of same age. Therefore, the measured differences in composition can be directly related to inter-strain differences. This finding suggests that both the A/J and the B6 mice lay down bone at very similar rates till the measured 16 week time point. Note that the Raman measurements were equally spaced in all femur samples and all scans were of uniform size; hence data from similar distances from the bone-edge correspond to bone of the same age. Therefore, the measured differences in composition can be directly related to inter-strain differences.

Once again, multiple t-tests were used to determine if the differences were significant within each age group. The t-tests for the P-Amide I peak intensity ratio within the new bone region indicate that there is a evidence of small difference between the two mouse strains ($p = 0.03$)

between the two mouse strains. On the other hand the P-CH₂ wag ratio did not show significant differences ($p = 0.3$) between the two mouse strains. This may again be a result of the relatively small sample size and further studies on larger datasets may be needed to confirm these findings. In the intermediate age region however, the t-test suggests that the mineral-to-matrix ratio (both P-CH₂ wag and P-Amide I ratios) were significantly different ($p < 0.01$) between the two mouse strains. On the other hand, in the old bone region the differences in the mineral-to-matrix ratio were not significant ($p > 0.05$). These correlations show that bone, when first deposited, has different mineral-to-matrix ratios in the two mouse strains, but as the bone ages these differences become less prominent. Moreover, there were no significant differences ($0.28 < p < 0.57$) in the mineral maturity (P-MHP peak intensity ratios) in all of the three groups representing the different bone ages, indicating that mineral of roughly similar compositions are present in all cases. This would indicate that it is the relative amount of mineral that changes differently with the age of bone between the two mouse strains, but the mineral itself is similar in quality between the two strains.

Our final analysis was focused on determining whether correlations existed between the local mechanical behavior of the bone (E_s and Y_{ind}) and its local composition (mineral-to-matrix ratio, mineral maturation and collagen cross-linking) along the maturing bone surface of the antero-medial cortex. These results are illustrated in Figs. 4 and 5 respectively. All of the data collected from 5 individuals of A/J and 6 individuals of B6 mouse strain are included in these two figures.

As seen in these figures, there is a significant linear correlation between the mineral-to-matrix ratio (P-CH₂ wag peak intensity ratio) and E_s ($p < 0.001$). While the correlation between the mineral-to-matrix ratio (P-CH₂ wag peak intensity ratio) and Y_{ind} is also high, it is not statistically significant when considering individual mouse effects and accounting for multiple t-tests. Also, since the A/J samples show a more rapid increase in their mineral-to-matrix ratio (seen before in Figs. 2 and 3), there are far fewer data points for A/J in the mid-section of the scatter plot, as compared to B6. The A/J mouse samples also show the highest values of both E_s and Y_{ind} , as well as the mineral-to-matrix ratio. These observations were also pointed out in [40]. The relationships between the local mechanical properties (E_s and Y_{ind}) and the P-CO₃ and P-MHP ratios were found to be statistically insignificant.

Discussion

Previous studies of A/J and B6 strains have shown that A/J femora exhibit overall stiffness and strength values that are very close to the B6 femora despite a much smaller bone diameter (and therefore a smaller moment of inertia) in A/J as compared to B6 (see Figure 2a and 2b for an illustration of the differences in bone geometry between the two strains). This is contradictory, since one would expect the A/J mice femur to be less stiff (due to its smaller moment of inertia) if the bone composition in these two mice were the same. It has been hypothesized [21-22] that the A/J mice compensate for their less efficient mechanical structure of the femur by altering their bone quality. Here, we demonstrated that A/J not only has a significantly higher mineral-to-matrix ratio (P-CH₂ wag), but significantly lower P-CO₃ ratios (carbonate substitutions), and a slightly lower mineral maturity (P-MHP). Our findings support those of other researchers who have reported higher mineral-to-matrix ratios as measured by FTIR [52-53] and Raman spectroscopy [40] and a significantly higher whole bone ash content [22] in A/J mouse bone as compared to the B6 mouse.

Our results demonstrate some important differences in the composition of bone between the two mouse strains A/J and B6. Differences in the bone composition are also observed as a function of location within the bone cortex and relative to the growth pattern. At 16 weeks of age, when the mice were sacrificed, the femora had attained their peak bone mass, but also demonstrate strong differences between bone that has recently formed at the endosteal surface, vs. bone located deeper in the cortex. As mentioned earlier, the growth of these bones up until this time is characterized by a pattern of cortical drift as illustrated in Fig. 1b [23, 42]. At the AM cortex (our area of investigation) this translates into a region of newer primary lamellar bone close to the endosteal surface, while the bone is more mature (older) away from this surface. The mice do not secondarily remodel their bones to form osteons, thus the progressive increase of the mineral-to-matrix ratios away from the endosteal edge seen in Figs. 2 and 3 are indicative of an increased maturity of the bone tissue in the more intracortical regions. Correspondingly, similar increasing trends are also seen in the P-MHP peak intensity ratios which represent mineral maturity in the bone tissue.

We have previously shown in a smaller sample size [40] that the variation of local mechanical properties (E_s and Y_{ind}) follows the same pattern as the variation in the local mineral-to-matrix ratio, for both the mouse strains. Thus a lower mineral-to-matrix ratio in the newer bone region close to the endosteal edge correspond to lower values of E_s and Y_{ind} , while the higher mineral-to-matrix ratios in the older bone region (away from the bone edge) result in higher values of both E_s and Y_{ind} . Here we were able to confirm these associations using a statistical analysis in which BIC evaluations were used to conclude that including information, mouse strain and/or the individual mouse IDs in the model did not improve the correlations significantly. This suggests that the relationship between the lamellar level composition and the local mechanical properties is the same, irrespective of the mouse strain. In other words statistical significance of the results do not change if the fits are done separately for each mouse strain. We note that the analyses were carried out assuming a linear relationship between local microstructure and mechanical properties and the conclusions might change if other functional forms were to be used; this possibility is being investigated in continuing work.

It is worthwhile to re-emphasize here that the significant correlations calculated between the mineral-to-matrix ratio and the indentation measurements are made possible by the use of indentation data analysis protocols described earlier (Eqs. 1 and 2) which allow us to extract E_s and Y_{ind} from the initial loading segment of the indentation test. If the indentation properties are extracted from the unloading segments (such as values of unloading modulus and hardness, as typically done in most reported studies) they produce much weaker correlations ($R^2 \sim 0.3-0.4$, see Ref. [40]). These differences originate because the unloading data reflect the properties of the material subjected to additional plastic strain induced by the indentation itself. Moreover calculations performed on the unloading segment have various inherent approximations such as a non-flat surface (see [24] for a detailed review of the two analysis processes) which affect the accuracy of the data.

The underlying causes for the differences in composition and mechanical behavior noted above can be explained by considering the whole bone morphologies and the subsequent mechanical demands imposed on the bone due to weight bearing in the two mouse strains [21-22]. As mentioned before, the A/J femora have a smaller diameter and correspondingly a smaller moment of inertia compared to B6 (see Fig 2), but they do not differ in their cortical areas [21-

22]. This would have inevitably led to a less stiff structure in the A/J mice, if the bone compositions were identical across the two mouse strains. By biologically coupling a change in their bone quality, in terms of a higher mineral-to-matrix ratio, the A/J mouse strain appears to have satisfied the increased mechanical demands imposed by their particular bone morphology. This is confirmed by whole bone mechanical tests comparing the two strains, where A/J femora are found to possess similar overall stiffness and strength values, in spite of their smaller moment of inertia, as compared to B6 [21]. However this trade-off between the reduced diameter and an increased mineral content in the A/J mice is not without consequences – at the whole bone level the A/J femora were also found to have reduced toughness and they fracture in a more brittle manner than the B6 in whole bone bending tests [21-22]. Thus the increased mineral content in A/J femora makes them mechanically robust in terms of stiffness (in that they are similar to B6), but weaker with regard to their post-yield behavior.

Conclusion

Our investigations using Raman Spectroscopy and spherical nanoindentation establish that the bone composition in A/J mice is significantly different from the B6 mice. While the two strains lay down bone of different quality, in terms of its mineralization, the differences become less prominent as the bone matures. We also observed a statistically significant correlation between the mineral-to-matrix ratio (P-CH₂ peak intensity ratio) and the local mechanical properties (E_s and Y_{ind}), extracted from the initial loading segment of the nanoindentation data. The linkages between composition and properties at the lamellar level were found to be similar for both mouse strains. Intra-strain differences in both bone composition and relationship between composition and properties were found to be statistically insignificant.

Acknowledgements

This work was supported by grants from the National Institutes of Health (NIH AR044927). SK and SJV acknowledge funding from ARO grant W911NF-10-1-0409. SJV is currently at Los Alamos National Laboratory, operated by LANS for the NNSA of the US Department of Energy under Contract No. DE-AC52-06NA25396. SP gratefully acknowledges funding from the Los Alamos National Laboratory Director's Postdoctoral Fellowship for this work. The MTS XPs nanoindentation system and the Renishaw 1000 Raman micro spectrometer used in this study are maintained and operated by the Centralized Research Facilities in the College of Engineering at

Drexel University. The authors also wish to thank Dr. Phil Nasser and Dr. Hayden-William Courtland (both at Mount Sinai School of Medicine, New York, NY) for assistance with sample preparation, as well as Dr. Zhorro Nikolov and Ms. Melanie Patel (Drexel University) for help with Raman measurements.

References

1. Fan, Z. and J.Y. Rho, *Effects of viscoelasticity and time-dependent plasticity on nanoindentation measurements of human cortical bone*. Journal of Biomedical Materials Research Part A, 2003. **67**(1): p. 208-214.
2. Tai, K., H.J. Qi, and C. Ortiz, *Effect of mineral content on the nanoindentation properties and nanoscale deformation mechanisms of bovine tibial cortical bone*. Journal of Materials Science: Materials in Medicine, 2005. **16**(10): p. 947-959.
3. Goodwin, K.J. and N.A. Sharkey, *Material properties of interstitial lamellae reflect local strain environments*. Journal of orthopaedic research, 2002. **20**(3): p. 600-606.
4. Kazanci, M., P. Roschger, E. Paschalis, K. Klaushofer, and P. Fratzl, *Bone osteonal tissues by Raman spectral mapping: orientation–composition*. Journal of Structural Biology, 2006. **156**(3): p. 489-496.
5. Ager, I.J.W., R.O. Ritchie, R.K. Nalla, and K.L. Breeden, *Deep-ultraviolet Raman spectroscopy study of the effect of aging on human cortical bone*. Journal of Biomedical Optics, 2005. **10**(3): p. 034012-0340128.
6. Akkus, O., F. Adar, and M.B. Schaffler, *Age-related changes in physicochemical properties of mineral crystals are related to impaired mechanical function of cortical bone*. Bone, 2004. **34**(3): p. 443-453.
7. Ramasamy, J. and O. Akkus, *Local variations in the micromechanical properties of mouse femur: the involvement of collagen fiber orientation and mineralization*. Journal of biomechanics, 2007. **40**(4): p. 910-918.
8. Gamsjaeger, S., A. Masic, P. Roschger, M. Kazanci, J. Dunlop, K. Klaushofer, E. Paschalis, and P. Fratzl, *Cortical bone composition and orientation as a function of animal and tissue age in mice by Raman spectroscopy*. Bone, 2010. **47**(2): p. 392-399.
9. Grey, A., R. Ames, R. Matthews, and I. Reid, *Bone mineral density and body composition in adult patients with cystic fibrosis*. Thorax, 1993. **48**(6): p. 589-593.
10. Boskey, A. and N. Pleshko Camacho, *FT-IR imaging of native and tissue-engineered bone and cartilage*. Biomaterials, 2007. **28**(15): p. 2465-2478.
11. Gourion-Arsiquaud, S., J.C. Burket, L.M. Havill, E. DiCarlo, S.B. Doty, R. Mendelsohn, M.C. van der Meulen, and A.L. Boskey, *Spatial variation in osteonal bone properties relative to tissue and animal age*. Journal of Bone and Mineral Research, 2009. **24**(7): p. 1271-1281.
12. Burket, J., S. Gourion-Arsiquaud, L.M. Havill, S.P. Baker, A.L. Boskey, and M.C.H. van der Meulen, *Microstructure and nanomechanical properties in osteons relate to tissue and animal age*. Journal of biomechanics, 2011. **44**(2): p. 277-284.
13. Bala, Y., B. Depalle, T. Douillard, S. Meille, P. Clément, H. Follet, J. Chevalier, and G. Boivin, *Respective roles of organic and mineral components of human cortical bone*

- matrix in micromechanical behavior: an instrumented indentation study.* Journal of the Mechanical Behavior of Biomedical Materials, 2011. **4**(7): p. 1473-1482.
14. Zebaze, R., A.C. Jones, M.G. Pandy, M.A. Knackstedt, and E. Seeman, *Differences in the degree of bone tissue mineralization account for little of the differences in tissue elastic properties.* Bone, 2011. **48**(6): p. 1246-1251.
 15. Achrai, B. and H.D. Wagner, *Micro-structure and mechanical properties of the turtle carapace as a biological composite shield.* Acta Biomaterialia, 2013. **9**(4): p. 5890-5902.
 16. Donnelly, E., A.L. Boskey, S.P. Baker, and M.C.H. van der Meulen, *Effects of tissue age on bone tissue material composition and nanomechanical properties in the rat cortex.* Journal of Biomedical Materials Research Part A, 2010. **92A**(3): p. 1048-1056.
 17. Ebenstein, D.M. and L.A. Pruitt, *Nanoindentation of biological materials.* Nano Today, 2006. **1**(3): p. 26-33.
 18. Fan, Z., J.G. Swadener, J.Y. Rho, M.E. Roy, and G.M. Pharr, *Anisotropic properties of human tibial cortical bone as measured by nanoindentation.* Journal of Orthopaedic Research, 2002. **20**(4): p. 806-810.
 19. Beamer, W.G., L.R. Donahue, and C.J. Rosen, *Genetics and bone. Using the mouse to understand man.* J Musculoskelet Neuronal Interact, 2002. **2**(3): p. 225-31.
 20. Rosen, C.J., W.G. Beamer, and L.R. Donahue, *Defining the genetics of osteoporosis: using the mouse to understand man.* Osteoporos Int, 2001. **12**(10): p. 803-10.
 21. Jepsen, K.J., D.E. Pennington, Y.L. Lee, M. Warman, and J. Nadeau, *Bone brittleness varies with genetic background in A/J and C57BL/6J inbred mice.* Journal of Bone and Mineral Research, 2001. **16**(10): p. 1854-1862.
 22. Jepsen, K.J., O.J. Akkus, R.J. Majeska, and J.H. Nadeau, *Hierarchical relationship between bone traits and mechanical properties in inbred mice.* Mammalian Genome, 2003. **14**(2): p. 97-104.
 23. Price, C., B.C. Herman, T. Lufkin, H.M. Goldman, and K.J. Jepsen, *Genetic variation in bone growth patterns defines adult mouse bone fragility.* Journal of Bone and Mineral Research, 2005. **20**(11): p. 1983-1991.
 24. Kalidindi, S.R. and S. Pathak, *Determination of the effective zero-point and the extraction of spherical nanoindentation stress-strain curves.* Acta Materialia, 2008. **56**: p. 3523-32.
 25. Pathak, S., J. Shaffer, and S.R. Kalidindi, *Determination of an effective zero-point and extraction of indentation stress-strain curves without the continuous stiffness measurement signal.* Scripta Materialia, 2009. **60**: p. 439-42.
 26. Donohue, B.R., A. Ambrus, and S.R. Kalidindi, *Critical evaluation of the indentation data analyses methods for the extraction of isotropic uniaxial mechanical properties using finite element models.* Acta Materialia, 2012. **60**(9): p. 3943-3952.
 27. Rho, J.-Y., L. Kuhn-Spearing, and P. Zioupos, *Mechanical properties and the hierarchical structure of bone.* Medical Engineering & Physics, 1998. **20**(2): p. 92-102.
 28. Rho, J.Y., P. Zioupos, J.D. Currey, and G.M. Pharr, *Variations in the individual thick lamellar properties within osteons by nanoindentation.* Bone, 1999. **25**(3): p. 295-300.
 29. Hengsberger, S., J. Enstroem, F. Peyrin, and P. Zysset, *How is the indentation modulus of bone tissue related to its macroscopic elastic response? A validation study.* Journal of Biomechanics, 2003. **36**(10): p. 1503-1509.
 30. Oyen, M.L., *Nanoindentation hardness of mineralized tissues.* Journal of Biomechanics, 2006. **39**(14): p. 2699-2702.

31. Oliver, W.C. and G.M. Pharr, *Improved technique for determining hardness and elastic modulus using load and displacement sensing indentation experiments*. Journal of Materials Research, 1992. **7**(6): p. 1564-1580.
32. Oliver, W.C. and G.M. Pharr, *Measurement of hardness and elastic modulus by instrumented indentation: Advances in understanding and refinements to methodology*. Journal of Materials Research, 2004. **19**(1): p. 3-20.
33. Pathak, S., D. Stojakovic, and S.R. Kalidindi, *Measurement of the Local Mechanical Properties in Polycrystalline Samples Using Spherical Nano-Indentation and Orientation Imaging Microscopy*. Acta Materialia, 2009. **57**(10): p. 3020-3028.
34. Pathak, S., J. Michler, K. Wasmer, and S. Kalidindi, *Studying grain boundary regions in polycrystalline materials using spherical nano-indentation and orientation imaging microscopy*. Journal of Materials Science, 2012. **47**(2): p. 815-823.
35. Pathak, S., D. Stojakovic, and S.R. Kalidindi, *Measurement of the local mechanical properties in polycrystalline samples using spherical nanoindentation and orientation imaging microscopy*. Acta Materialia, 2009. **57**: p. 3020-8.
36. Pathak, S., Z.G. Cambaz, S.R. Kalidindi, J.G. Swadener, and Y. Gogotsi, *Viscoelasticity and High Buckling Stress of Dense Carbon Nanotube Brushes* Carbon, 2009. **47** p. 1969-76.
37. Basu, S., A. Moseson, and M.W. Barsoum, *On the determination of spherical nanoindentation stress-strain curves*. Journal of Materials Research, 2006. **21**(10): p. 2628-2637.
38. Field, J.S. and M.V. Swain, *A simple predictive model for spherical indentation*. Journal of Materials Research, 1993. **8**(2): p. 297-306.
39. Angker, L. and M.V. Swain, *Nanoindentation: Application to dental hard tissue investigations*. Journal of Materials Research, 2006. **21**(8): p. 1893-1905.
40. Pathak, S., S.J. Vachhani, K.J. Jepsen, H.M. Goldman, and S.R. Kalidindi, *Assessment of lamellar level properties in mouse bone utilizing a novel spherical nanoindentation data analysis method*. Journal of the Mechanical Behavior of Biomedical Materials, 2012. **13**(0): p. 102-117.
41. Pathak, S., J. Gregory Swadener, S.R. Kalidindi, H.-W. Courtland, K.J. Jepsen, and H.M. Goldman, *Measuring the dynamic mechanical response of hydrated mouse bone by nanoindentation*. Journal of the Mechanical Behavior of Biomedical Materials, 2011. **4**(1): p. 34-43.
42. Beamer, W.G., L.R. Donahue, C.J. Rosen, and D.J. Baylink, *Genetic variability in adult bone density among inbred strains of mice*. Bone, 1996. **18**(5): p. 397-403.
43. Johnson, K.L., *Indentation Contact Mechanics*. 1985: Cambridge University Press, Cambridge.
44. Hertz, H., *Miscellaneous Papers*. New York: MacMillan and Co., Ltd, 1896.
45. Fischer-Cripps, A.C., *A review of analysis methods for sub-micron indentation testing*. Vacuum, 2000. **58**(4): p. 569-585.
46. Basu, S.M., Alexander; Barsoum, Michel W., *On the determination of spherical nanoindentation stress-strain curves*. Journal of Materials Research, 2006. **21**(10): p. 2628-2637.
47. Pathak, S., D. Stojakovic, R. Doherty, and S.R. Kalidindi, *Importance of surface preparation on the nano-indentation stress-strain curves measured in metals*. Journal of Materials Research, 2009. **24**: p. 1142-55.

48. Carden, A. and M.D. Morris, *Application of vibrational spectroscopy to the study of mineralized tissues (review)*. Journal of Biomedical Optics, 2000. **5**(3): p. 259-268.
49. Timlin, J.A., A. Carden, and M.D. Morris, *Chemical microstructure of cortical bone probed by Raman transects*. Applied Spectroscopy, 1999. **53**(11): p. 1429-1435.
50. Boskey, A.L., Pleshko, N., Doty, S.B., Mendelsohn, R, *Applications of Fourier transform infrared (FT-IR) microscopy to the study of mineralization in bone and cartilage*. Cells and Materials and Corrosion, 1992(2): p. 209-220.
51. Yeni, Y.N., J. Yerramshetty, O. Akkus, C. Pechey, and C.M. Les, *Effect of Fixation and Embedding on Raman Spectroscopic Analysis of Bone Tissue*. Calcified Tissue International, 2006. **78**(6): p. 363-371.
52. Courtland, H.-W., P. Nasser, A. Goldstone, L. Spevak, A. Boskey, and K. Jepsen, *Fourier Transform Infrared Imaging Microspectroscopy and Tissue-Level Mechanical Testing Reveal Intraspecies Variation in Mouse Bone Mineral and Matrix Composition*. Calcified Tissue International, 2008. **83**(5): p. 342-353.
53. Courtland, H.W., M. Spevak, A.L. Boskey, and K.J. Jepsen, *Genetic variation in mouse femoral tissue-level mineral content underlies differences in whole bone mechanical properties*. Cells Tissues Organs, 2009. **189**(1-4): p. 237-40.
54. Miller, R.G., *Beyond ANOVA, Basics of Applied Statistics*. 1986, New York: Wiley.

Figures

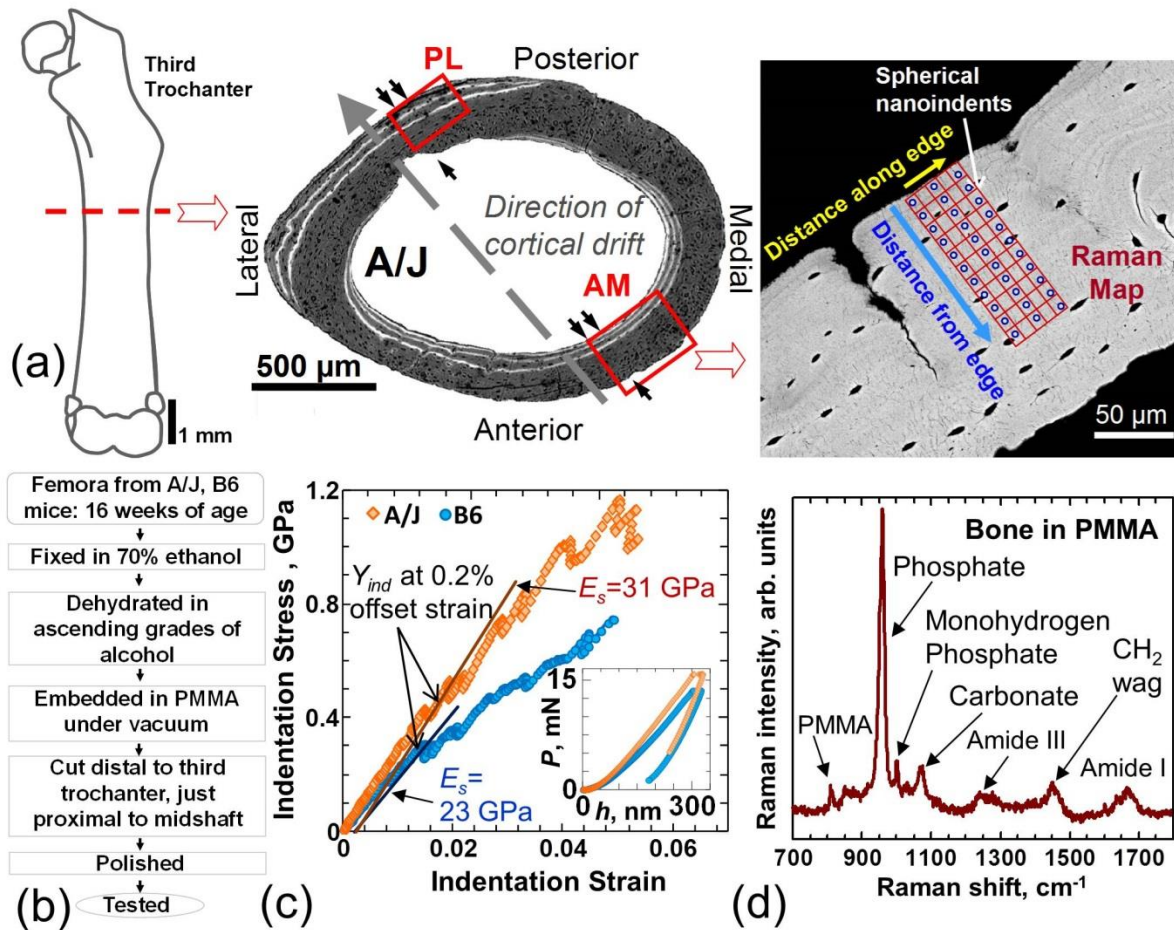


Figure 1. (a) For indentation and Raman testing the mouse femora were sectioned transversely, distal to the third trochanter. During post-natal growth, bone is deposited (double arrows) and resorbed (single arrows) at different sites around these regions of the femoral cortex resulting in a net cortical drift (large arrow). Spherical nanoindentations (shown as blue dots in the SEM image) at the antero-medial (AM) cortex thus probe newer bone closer to the endosteal edge while the bone is more mature away from this surface. Three rows of indentations were performed on each sample. The region surrounding the indents was then mapped by Raman Spectroscopy (shown by the red grid around the indented region). Figure adapted from Ref [44] with permission.

(b) Flow diagram for sample preparation of 'dry'/dehydrated-embedded mouse bone samples.

(c) Comparison of typical indentation stress-strain responses extracted from the measured load-displacement curves (inset) on A/J vs. B6 mice bone. These examples were taken from indents well away from the bone edge. E_s and Y_{ind} at 0.2% offset strain were both calculated from the loading portions of the indentation stress-strain curves.

(d) A typical Raman spectra obtained from bone embedded in PMMA

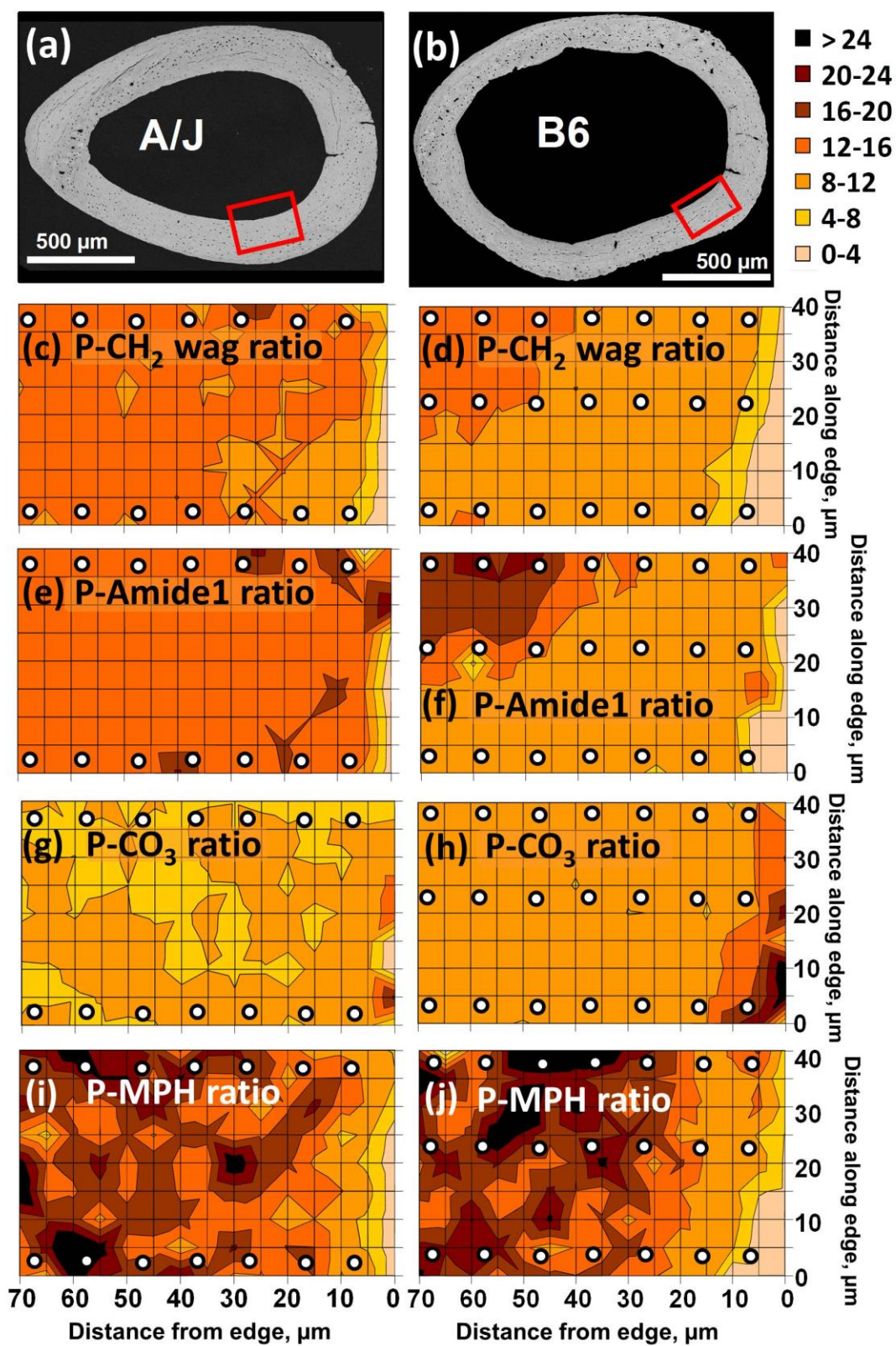


Figure 2. Representative BSEM images for (a) A/J and (b) B6 mice, and 2D surface maps obtained using Raman spectroscopy, showing the various aspects of the composition information extracted from a scan over a 70 μ m by 40 μ m region close to the endosteal edge of the AM cortex of (c, e, g and i) A/J mouse and (d, f, h and j) B6 mouse samples. The white circles within the maps denote the approximate size and location of the spherical indents with respect to the Raman map.

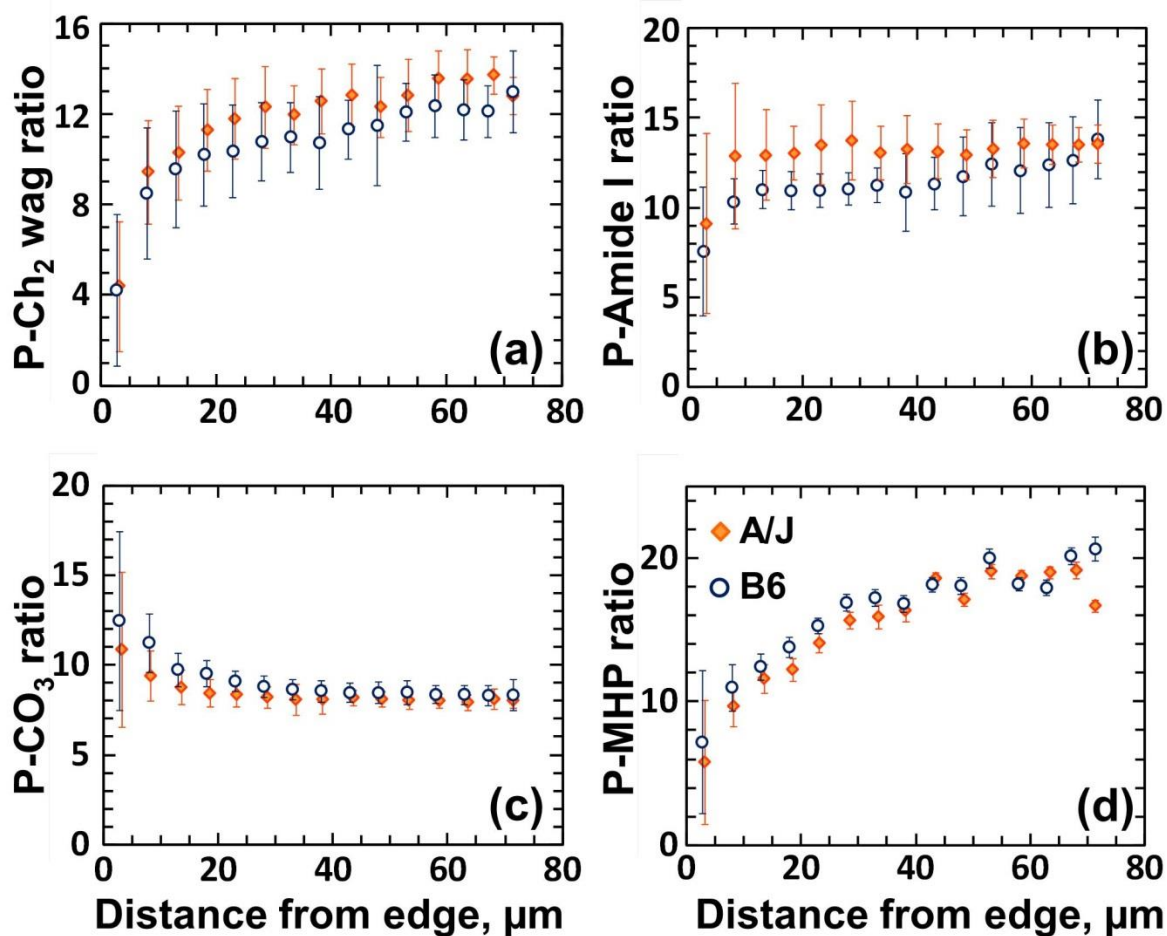


Figure 3. Variations in bone composition measured using Raman spectroscopy with respect to distance from the bone-edge: (a) phosphate-to-CH₂ wag peak intensity ratio, (b) phosphate-to-Amide1 peak intensity ratio, (c) phosphate-to-CO₃ peak intensity ratio and (d) phosphate-to-monohydrogen phosphate peak intensity ratio.

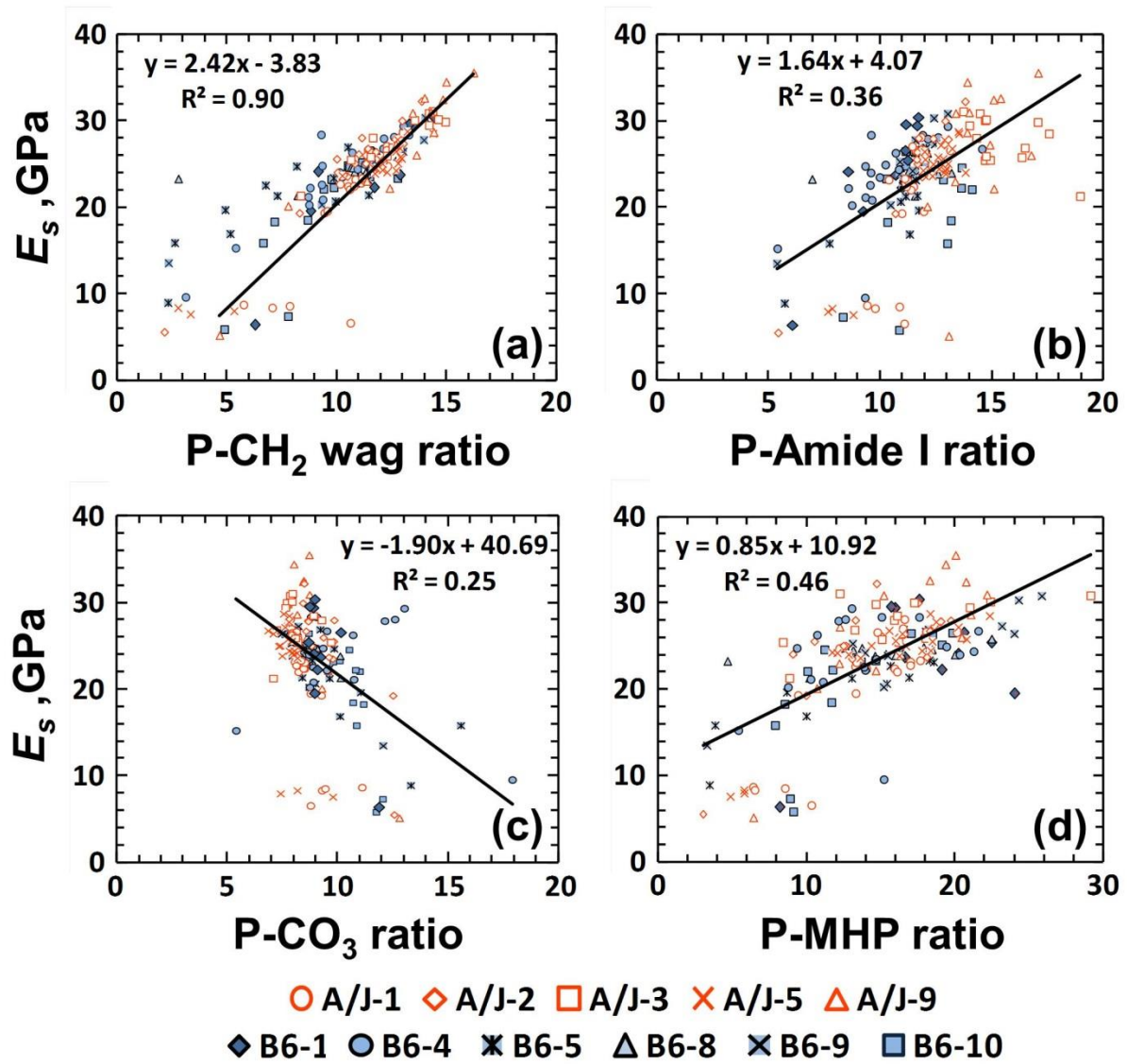


Figure 4. Scatter plots showing the variation of the elastic modulus as a function of the (a) phosphate-to-CH₂ wag peak intensity ratio, (b) phosphate-to-Amide1 peak intensity ratio, (c) phosphate-to-CO₃ peak intensity ratio and (d) phosphate-to-monohydrogen phosphate peak intensity ratios for A/J and B6 mice.

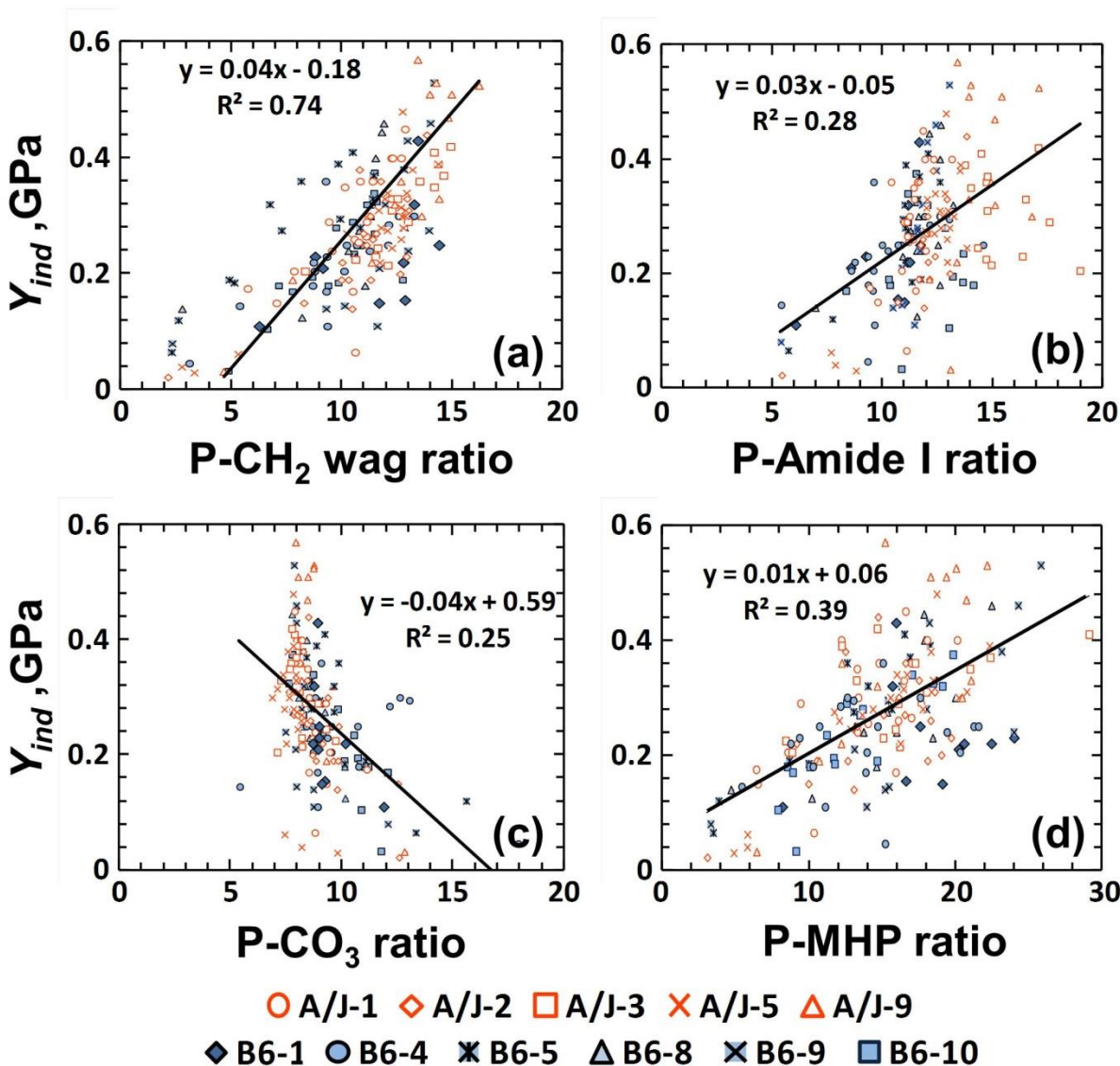


Figure 5. Scatter plots showing the variation of the 0.2% offset strain indentation yield strength (Y_{ind}) as a function of the (a) phosphate-to-CH₂ wag peak intensity ratio, (b) phosphate-to-Amide1 peak intensity ratio, (c) phosphate-to-CO₃ peak intensity ratio and (d) phosphate-to-monohydrogen phosphate peak intensity ratios for A/J and B6 mice.